

Crystallisation behaviour of PCDTBT in thin films

Fabio Pontecchiani

Submitted for the degree of Doctor of Philosophy

Department of Physics and Astronomy, The University of Sheffield

November 2018



The
University
Of
Sheffield.

Declaration

The work described in this thesis was undertaken at The University of Sheffield between October 2013 and November 2018 under the supervision of Professor Richard Jones. Unless stated, it is the work of the author and has not been submitted in whole or in part for any other degree at this or any other institution.

Fabio Pontecchiani November 2018

Crystallisation behaviour of PCDTBT in thin films

Fabio Pontecchiani

Summary of Thesis

Chapter 1 introduces the reasons behind this study, the importance and applications of PCDTBT in organic electronic devices, thus the importance of understanding how confinement in thin films influences the crystallisation of this polymer which will have an impact on the electronic properties of the material. Chapter 2 describes the analytical techniques used (ellipsometry, atomic force microscopy and grazing incidence X-ray scattering) and their importance for this study. In chapter 3 is reported the thermal protocol that allowed the understanding of the crystallisation of PCDTBT; ellipsometry, GIWAXS and AFM results are reported in order to understand the importance of the protocol and also aid the comprehension of the rest of the thesis. Chapter 4 describes how different annealing temperatures influence the crystallisation kinetics and the amount of crystallinity in a sample. Chapter 5 looks in detail at a phenomenon occurring in the film that was quite unpredicted: the ellipsometry data are used to follow the change of the thickness of the film under the thermal treatment explained in chapter 3; an initial shrinking at the ellipsometry shows the crystallisation phenomenon, but what is causing a second expansion which is following the crystallisation? In chapter 6 is finally reported the influence of the film thickness on the crystallisation properties of the material; the influence of the two interfaces on its ordering is key in understanding how to improve the efficiency of organic electronic devices. Chapter 7 is a general discussion of results and theoretical points, drawing conclusions and opening the way to future work.

Publicly presented work

- IOP Polymer Physics Group Biennial Conference, The University of Manchester, UK, 2015. Talk entitled “Behaviour of semiconducting polymers confined in thin films”.
- Puzzel Student Conference, Uniwersytet Wrocławski, Poland, 2015. Talk entitled “Behaviour of semiconducting polymers confined in thin films”.
- 10th European Summer School (2014) on “Scattering Methods Applied to Soft Condensed Matter” Vacation Centre “Les Bruyères”, Carcans-Maubuisson, Gironde, France. Talk entitled “Behaviour of semiconducting polymers confined in thin films”.

Acknowledgements

First of all I would like to thank Richard Jones for his supervision and his faith in me, and incredible patience to accompany and advice me until the end of this journey. He has dedicated a lot of time and support to me during the writing phase of this thesis in spite of his busy work schedule.

Special thanks as well to my second supervisor Mark Geoghegan who always managed to give me very useful advice and support during these years, especially during the most difficult times.

A great thanks also to Andrew Parnell for his guidance and assistance during this PhD, especially for the time he dedicated helping me with the collection of GIWAXS data and answering to all my questions and doubts.

I would like to thank Oleksandr Mykhaylyk who allowed the collection of X-ray scattering data just next door from the physics department.

I am also very grateful to Tao Wang and Andrew Pearson for helping me with ellipsometry experiments and analysis of the ellipsometry data. Cheng Wang from ALS, Berkley California for the analysis of PCDTBT with Soft X-ray scattering.

Last but not least I would like to thank my family and friends for never ceasing to believe in me and their constant support through these 4 years.

I would like to thank all the other PhD students, PostDocs, academics in the physics department, that were there in difficult emotional and technical moments. All the international and local friends, who made Sheffield feel like home. Special thanks finally go to the closest friends who have shared with me the best and worst moments of this life chapter.

Symbols and abbreviations

α_g	Expansion coefficient of the glassy phase	
α_l	Expansion coefficient of the visco-elastic phase	
α_i	Grazing angle	
α_r	Refracted angle	
Δg	Change in free energy	
ΔH_m	Latent heat of melting per unit volume	
ϕ	Crystallinity degree	
Ψ, Δ	Ellipsometry angles	
ρ	Polymer density	
ρ_a	Density of the amorphous phase	
ρ_c	Density of the crystalline phase	
σ	Interfacial energy of the lamella surface	
σ	Standard deviation	
a	Molecule stem diameter	
B	Positive coefficient	
c	Speed of light in vacuum	299, 792, 458 m/s
J_{SC}	Short-circuit current	
L	Coherence length = $\frac{2\pi}{FWHM}$	
l	Crystal lamella thickness	
$M_c^{Solution}$	Molecular weight at which the entanglements start to influence the macroscopic properties of the polymer solution.	
M_n	Number average molecular weight	
M_w	Weight average molecular weight	

p	Basis vector used to express the polarization state parallel to the ellipsometry plane of incidence.
q, Q	X-ray scattering vector = $\frac{4\pi \sin \theta}{\lambda}$
R_p, R_s	Fresnel's reflection coefficients of the p and s components of the polarized light.
s	Basis vector used to express the polarization state perpendicular to the ellipsometry plane of incidence. From <i>Senkrecht</i> , German for perpendicular.
T_c	Crystallisation temperature
T_g	Glass transition temperature
T_i	Annealing temperature, temperature of the isotherm
T_m	Melting temperature
$T_m(\infty)$	Ideal thermodynamic value of the melting temperature
T_o	Ordering temperature
v	Optical impedance
x_0	Full width at half maximum
a, b	Primitive unit cell length
AFM	Atomic force microscopy
FET	Field Effect Transistor
FWHM	Full width at half maximum
GIWAXS	Grazing incidence wide angle X-ray scattering
GIXD	Grazing incidence X-ray diffraction
HWHM	Half width at half maximum
MEH-PPV	Poly[2-methoxy-5-(2-ethylhexyloxy)-1,4-phenylenevinylene]
OLEDs	Organic light-emitting diodes
OPVs	Organic photovoltaics
P3HT	Poly(3-hexylthiophene-2,5-diyl)
PCBM	Phenyl-C61-butyric acid methyl ester
PCDTBT	Poly[N-9'-heptadecanyl-2,7-carbazole-alt-5,5-(4',7'-di-2-thienyl-2',1',3'-benzothiadiazole)]
PCE	Power conversion efficiency
PET	Polyethylene Terephthalate
PVK	Poly(9-vinylcarbazole)

Contents

Summary of Thesis	iii
Publicly presented work	v
Acknowledgements	vii
1 Introduction and literature review	1
1.1 Background of this study	1
1.2 Organic electronic devices	4
1.2.1 The importance of crystallisation for conduction	4
1.2.2 Interplay between crystallisation and phase separation	6
1.3 Classical views on polymer crystallisation	8
1.4 New views on polymer crystallisation - the intermediate state of order	14
1.5 Crystallisation for conjugated polymers	16
1.5.1 Orientation of crystalline domains	17
1.5.2 Crystallisation in PCDTBT	20
1.5.3 Liquid crystal phases	29
1.6 Polymers in thin films: the consequences of confinement on the material	30
1.6.1 Consequences of confinement on the glass transition temperature	30
1.6.2 Consequences of the confinement on the crystallisation kinetics and orientation of the chains	32

2	Experimental techniques	37
2.1	Spectroscopic ellipsometric studies of thin films relaxation	37
2.1.1	Introduction	37
2.1.2	Polarization states	39
2.1.3	Jones matrix analysis of the rotating analyser	40
2.1.4	Refraction in bulk material	40
2.1.5	Single films on thick substrates	42
2.1.6	Optical constants and the Cauchy model	46
2.1.7	Ellipsometry components and sample configuration	47
2.2	AFM - Atomic Force Microscopy	50
2.2.1	Apparatus and condition	52
2.3	GIWAXS - Grazing Incidence Wide Angle X-ray Scattering	52
2.3.1	Experimental facility, instruments and apparatus	56
3	Sample preparation and methodologies	59
3.1	Introduction	59
3.2	Polymer solution and spin coating	60
3.3	Thermal protocol	61
3.3.1	Melting and quenching	64
3.3.2	Ellipsometry isotherms	64
3.4	Effect of annealing on the surface morphology - Atomic Force Microscopy	67
3.5	Thermal protocol seen at GIWAXS	72
3.5.1	Effect of the thermal protocol on 90 nm thick PCDTBT films	72
3.5.2	Effect of the thermal protocol on 200 nm thick PCDTBT films	78
3.6	Conclusions	84

4	Ordering as a function of temperature	85
4.1	Introduction	85
4.2	Ordering as a function of temperature - an ellipsometry analysis	89
4.2.1	Time-Temperature superposition	90
4.2.2	Ellipsometry data for samples annealed at temperatures $> 200^\circ$	102
4.3	Ordering as a function of temperature - an AFM analysis	104
4.4	Ordering as a function of temperature - a GIWAXS analysis	106
4.4.1	GIWAXS on 50 nm thick films	106
4.4.2	GIWAXS on 75 nm thick films	114
4.5	Discussion - Temperature dependence in PCDTBT films	118
5	Expansion during the isotherms	121
5.1	Introduction	121
5.2	Comparison between samples annealed for different time-lengths	124
5.2.1	UV-vis spectroscopy and GIWAXS analysis of 90 nm thick films (expanded vs not expanded)	124
5.2.2	AFM analysis of films annealed for different time-lengths	131
5.3	Comparison between samples annealed at different temperatures	139
5.3.1	Absorption spectra comparisons	142
5.4	Discussion	150
6	Ordering as a function of thickness	153
6.1	Introduction	153
6.2	Existence of a threshold thickness	153
6.3	Thickness dependence of the isotherms - Ellipsometry	157
6.4	GIWAXS for different thicknesses	161
6.5	AFM for different thicknesses	167
6.6	Discussion - Thickness dependence of PCDTBT thin films	168

7 Discussion	171
7.1 Ordering as a function of thickness	171
7.2 Ordering as a function of temperature	179
7.3 Conclusions	183
7.4 Future Work	185

Chapter 1

Introduction and literature review

1.1 Background of this study

The current concern about sustainability and the environmental impact of fossil fuels has increased the necessity to find low cost materials and methods for large-scale production of photovoltaic devices. Semiconducting polymers are finding numerous potential applications in the form of thin films, for the production of field effect transistors (FETs), light emitting diodes (LEDs) and photovoltaic. As their inorganic counterparts require very expensive (especially in terms of energy) processing technologies, there is a clear benefit in substituting them with organic devices [1]. The advantageous trait of organic thin films is the possibility that they can be deposited easily and cost-effectively, whereas conventional silicon technologies require ultrahigh vacuum equipment for deposition on a thin layer form, and then if the manufacturing process has to be scaled up the cost will be enormous, compounding the risk for any company. On the other hand, polymers are much easier to manipulate and process, as they do not usually require special environments after synthesis, so they can be stored before the application, without degradation [2]. Plastic electronics are a promising field because they put together diverse interesting features: the wide range of semiconducting polymers, their low-cost processing methods (spin-coating and inkjet printing), their interesting optoelectronic properties, such as high-charge transport mobilities, electroluminescence, and their flexibility and light weight. The problem of these materials is that their current efficiency and lifetime are not enough for

large-scale production.

One of the major parameters controlling efficiency is the molecular order that controls charge mobility at different scales. At a smaller scale, intrachain transport is affected by the conformation of the chain and its defects. Interchain transport depends instead on the π - π stacking between two different chains, where the interaction between electronic orbitals allows a better delocalisation of electrons. At larger scale the connectivity between crystalline domains still influences the charge transport [3–5]. The chains of certain semiconducting polymers are sufficiently “flexible” to allow folding as classical polyolefins. This folding has a large impact on charge transport mechanisms.

While the mechanism and structure of crystallisation in classical polyolefins is rather established, the field of conjugated polymers is much less well studied due to the fact that their stiffness does not allow the same degree of crystallisation of regular polyolefins and that there are no available techniques to directly probe non-crystalline organization at high resolution and over large length scale (apart from polarized X-ray scattering, which is an early technique) [6, 7]. Being polymers, large entangled molecules, they can be easily perturbed by a near surface or interface. The confinement into a thin layer causes a deviation from their bulk physical properties [8]. Dynamics of polymer chains are then modified, and so therefore is the glass transition temperature. Different dynamics is translated also into a change of the crystallisation kinetics, while the interface’s influence may result in a different, unusual, crystal structure. All these parameters have a huge impact on the performance of electronic devices.

The purpose of this thesis is to understand how a semiconducting polymer developed for high performance photovoltaics Poly[N-9'-heptadecanyl-2,7-carbazole-alt-5,5-(4',7'-di-2-thienyl-2',1',3'-benzothiadiazole)] (PCDTBT) crystallises in thin films. This means studying how the confinement influences the crystallisation and molecular orientation. The thesis can be considered being a continuation of the work on PCDTBT by Wang *et al* [8] and Masaharu Ibaragi [9]. The latter was trying to understand the effect of confinement on the crystallisation of an important commercial polymer, polyethylene terephthalate PET, following important work on the reduction of T_g in thin films [10].

When a polymer is confined in a thin film it presents deviations from its bulk properties. As

it has been observed in many papers, of which the first was the Keddie paper from 1994 [10], there is a depression in T_g as the polymer film shrinks. This is because of the proportion of polymer chains entering in contact with the free surface of the film and gaining more freedom of movement. In contrast to the air/polymer interface, is the interface with the substrate, where a positive interaction with the polymer slows down the movement of the chains, competing with the air/polymer interface effect on T_g , if the proximity to the surface gives the material more degrees of freedom, the proximity to the substrate tends to increase the glass transition temperature for that material. Below a certain thickness the substrate effect on T_g may overcome the surface effect, stopping the further depression of T_g as a function of the film thickness and create a plateau below that thickness [8].

The confinement in thin films not only modifies the mobility of a polymer material, but also the molecular packing is influenced by a near interface as described in the paper by Wang *et al.* [8] where different packing structures as a function of the depth were detected within a PCDTBT film. The different behaviour as a function of the depth is caused by confinement of this important semiconducting polymer employed in optoelectronic devices like OPVs and OLEDs. The group exploited ellipsometry and X-ray scattering at grazing incidence (GI-WAXS) to study this phenomenon. Scanning all the film thickness through changing the incidence angle of the X-ray beam, the GI-WAXS analysis perhaps revealed an increased π - π stacking near the substrate and an increased lamella ordering near the top surface. Ellipsometry was used instead to study the effect of the change in thickness on the T_g depression. My study aims to bring this work further in a more extended and complete way, confirming these hypotheses and possibly add more.

In this thesis I used spectroscopic ellipsometry to gain an understanding of the film response to thermal annealing, studying the thickness change of PCDTBT films as a function of different temperatures. The change in thickness is an important parameter as it contains information about the degree of crystallinity of the polymer films. Moreover, ellipsometry can give information about the change in absorption spectra of the material, being PCDTBT a semiconducting polymer and absorbing light in the UV-vis region. Atomic force microscopy was used to check the change in surface morphology of the films, as a complementary result

to what ellipsometry data might have been suggesting. Finally, GIWAXS was used to study the packing structure of PCDTBT and its orientation in function of a thermal protocol and the film thickness. This makes it possible to study the films with some depth resolution and gaining some more understanding about the influence of the air and substrate interfaces on the crystallisation of PCDTBT.

1.2 Organic electronic devices

Organo-electronic devices are formed usually by blends of a hole and an electron transport polymers. Polymers usually phase separate because of their immiscibility generating interfaces that promote crystallisation, which influences charge transport properties in these materials. This is why crystallisation becomes crucial for the efficiency of optoelectronic devices. Bulk heterojunction solar cells, for example, are usually blends of a donor and an acceptor material such as a conjugated polymer and a fullerene, where a high interfacial area is formed, necessary for the dissociation of photogenerated excitons in separate charges.

In the next paragraphs it will be described the importance of studying and understanding the crystallisation of these polymers and its impact on the conduction properties of organic devices, which is often driven by the phase separation of the binary blends constituting the devices.

1.2.1 The importance of crystallisation for conduction

Usually in organic solar cells, made of a photoactive conjugated polymer, an increase in the polymer crystallinity is highly desirable since it is generally accepted to improve device performance. One reason is because light absorption increases with crystallinity and consequently more excitons are formed. In different works [11, 12], it has been reported how charge-carrier mobility improves when the material is more crystalline. It has been shown that charge transport depends strongly on the alignment direction of the backbone in semiconducting polymers [13], and on the orientation of the grain boundaries [14]. How electrons and holes move within a polymer

is of considerable importance for the design of polymer transistors and opto-electronics devices and two mechanisms are to be considered, hopping and band transport [2]. Band transport happens exclusively for intrachain motion because it has to occur without interruptions such as defects, while hopping occurs in both intrachain and interchain transports. Band transport occurs thanks to conjugation. The wave function of the charge is affected by an applied field and so the polaron travels along the chain in a direction defined by the field. The limit to conduction due to band transports are due to the localization of the charge carriers. Even if a pure polymeric crystal were synthetically possible there would be limitations on charge transport. The chain has to be aligned with the electric field, as a polaron on a chain aligned perpendicularly to the applied field cannot contribute to band transport without hopping onto another chain. Also, a perfect crystal will have polaron transport disrupted by phonons.

On the other hand, hopping, which is also called activated tunnelling, is a mechanism by which the charge carrier jumps from one monomer to another through a quantum-mechanical tunnelling process, rather than travelling coherently (band transport). Hopping can occur also in intrachain transport, even for conjugated polymers, a kink or defect will give rise to the opportunity to move from one part of the chain to another without travelling along the chain. Some non-conjugated materials are characterised by charge transport due exclusively to hopping, such as poly(vinyl carbazole), PVK. In this polymer the charge carrier cannot travel coherently because the chain is not conjugated, but the hole can move between aromatic rings without passing through the chain backbone. The key point is that hopping transport does not give rise to mobilities as large as those for pure band transport. In the case of PVK, the hole needs enough energy to leave one carbazole unit and move to another, as the backbone does not present double bonds.

Therefore, now it is easier to understand why the morphology of polymeric materials plays an important role in charge transport. Differently from saturated polymers, conjugated polymers are stiff by nature, and they cannot bend as frequently as the formers, making it more difficult to form chain-folded lamella. However, the presence of π electrons promotes the interaction of adjacent chains and therefore packing, consequently making the material semi-crystalline, which has a great impact on the charge transport. Intrachain (within a chain) transport is the

easiest form of transport to explain, happening in polyacetylene, for example. Different from intrachain transport, is interchain (between chains) charge transport, that happens in polymers like polycarbazoles that have non-conjugated backbones. A strong interchain charge transport mechanism is hopping, however it can take place along the chain too, being called intrachain hopping and can be significant in polycarbazoles and other similar polymers.

Most devices are dominated by hole transport, which is usually more efficient than electron transport. Hole-transporting polymers (like PCDTBT) tend to have better mobility and stability. The presence of oxygen is one explanation, been highly electronegative and being present on many impurities (e.g. water), it acts as an electrons trap and inhibits electron mobility.

Taking a widely used semiconducting polymer as an example, P3HT, it has been reported in two works that its crystallization improves J_{sc} (short-circuit current) for two reasons: the crystallization leads to a better absorption in the near-infrared region of the solar spectrum and second, it yields to a higher hole mobility that prevents geminate-pair recombination [15, 16]. While aggregation of PCBM assists charge collection through the formation of a network for efficient electron transport, thus preventing losses due to bimolecular recombination. In the Agostinelli et al. paper [15] they demonstrated that the initial increase of power conversion efficiency in the blend P3HT:PCBM solar cells during thermal annealing correlates with the crystallization of P3HT in an initial fast time window. Then PCE continues to increase, but at a slower pace, perhaps due to the diffusion of PCBM.

1.2.2 Interplay between crystallisation and phase separation

The active layer of opto-electronic devices is composed of phase-separated blends of two different materials as said above, a hole and an electron transport polymer. The two phases interpenetrating each others represent the ideal morphology in order to reach the highest device efficiencies. The structure of the interface between the two materials for both light emitting diodes and photovoltaics, is essential in order to form a continuous path of n-type or p-type material from any point on the interface to the appropriate electrode.

The fact that most conjugated polymers crystallise, leads to an interplay of crystallisation

and phase separation as it has been studied in the work by Agostinelli et al. [15], where the common P3HT/PCBM blend has been studied. The blend of P3HT with PCBM is one of the most studied material system for organic solar cells, where the high efficiency is obtained after a thermal-annealing process that leads to crystallisation of the polymer and consequent higher holes mobility. The crystallisation of P3HT facilitates then phase segregation, expelling PCBM from the polymer domains. Viceversa, phase separation creates a large amount of interface that promotes crystallisation. In the work by Kline et al. [17] the buried interface with the substrate induces highly oriented crystals in P3HT and in the same way, an interface with another polymer can promote crystallisation.

Another group [18], investigated the interplay between crystallisation and phase separation through two-step quenching experiments in polyolefin blend systems. They showed that almost all the nuclei appear in the interfacial regions of phase separation. This is because the spinodal decomposition process occurring orients the polymer chains at the interfacial regions, which decreases the nucleation energy barrier for crystallization. The interfacial area was found to be constant during the early stage of phase separation, while the interface thinned faster than the phases getting rougher. The nucleation in this case was proportional to the interfacial thickness.

Terrill et al. [19] studied the crystallisation of isotactic polypropylene and based on simultaneous SAXS and WAXS measurements, they suggested that long-range density fluctuations developed via spinodal decomposition - precursor of the phase separation mechanism - occurs prior to the development of crystalline peaks. As a last example, Deribew et al. [11] used grazing incidence X-ray diffraction (GIXD), UV-vis absorption and scanning force microscopy (SFM) to confirm that the addition of a diblock copolymer, P3Ht-b-PI (polyisoprene) was responsible for the increase in crystallisation. The PI blocks mixed with P3HT promoted P3HT crystallization through heterogeneous nucleation with a 31% enhancement in nucleation efficiency and acting as a plasticizer increasing the segmental mobility of P3HT. It was demonstrated with GIXD that the improvement in crystallinity was not due to larger crystallites but by a larger number of nucleation centres in the film, caused by the copolymer acting as a nucleation agent, offering more interface for the nucleation to take place.

Classically, the complex mechanism of polymer crystallization is understood on the basis of nucleation-followed-by growth. Nevertheless, the recently observed behaviour for the early stage of polymeric crystallization challenged this classical view. This topic will be explored in section 1.4.

1.3 Classical views on polymer crystallisation

For most polymers, crystallisation is a relatively slow process, starting with a density fluctuation in the melt, a nucleation forming a spherulite and its growth that can be followed by optical microscopy to determine the crystallisation kinetics. Differently from small molecules, polymers melt over a range of temperatures. The crystallisation for small molecules might occur rapidly at temperatures just slightly below the melting point (low degrees of undercooling). On the other hand, cooling down a polymer sample from above T_m , the crystallisation does not happen at T_m , but at a much lower temperature. There is a critical temperature, at which the formation of a stable primary nucleus occurs. The formation of this nucleus is the critical stage in all materials, and especially in polymers: it defines the first slow part of the crystallisation kinetics, called the induction period. The formation of the nucleus occurs heterogeneously, which means that it occurs thanks to impurities, usually on the surface of low molar mass molecules present in the melt. This contributes to decrease the interfacial free energy of the lamellae as we will see later in this section. The first stage after nucleation is the formation of an embryo (through concentration fluctuations), a particle with an enhanced inner order. The embryo can surpass a critical size and become a nucleus of a growing crystal, while smaller embryos disappear. Nucleation is a bulk property and it can be described by a rate τ_{nucl}^{-1} per unit volume.

Crystallisation could start in principle at the equilibrium melting point, T_m^∞ , which is the temperature where the chemical potential of a monomer in the melt, μ_m^a equals the chemical potential of a perfect infinite crystal composed of extended chains, μ_m^c :

$$\mu_m^a(T_m^\infty) = \mu_m^c(T_m^\infty). \quad (1.1)$$

In practice, however, a sufficient supercooling below T_m^∞ is necessary to start the crystallisation process. The driving force for the crystallisation process is given by the chemical potential difference

$$\Delta\mu_m = \mu_m^a - \mu_m^c. \quad (1.2)$$

For low supercooling is possible to write, in linear approximation,

$$\Delta\mu_m \approx \Delta s_m^f (T_m^\infty - T) = \frac{\Delta h_m^f}{T_m^\infty} (T_m^\infty - T) \quad (1.3)$$

where Δs_m^f and Δh_m^f are the entropy and heat of fusion per monomer. From equation 1.3 it is possible to obtain a temperature dependence for the nucleation rate:

$$\tau_{nucl} \sim exp - \frac{const \cdot \sigma^3 \nu_m^2}{kT (\Delta h_m^f)^2 (T_m^\infty - T)^2} \quad (1.4)$$

where σ is the excess free energy per unit area of the nucleus surface, and ν_m is the monomer volume. From equation 1.4 it is possible to predict a rapid change of the nucleation rate with an increase of supercooling. From here the nucleation rate is proportional to the surface energy of the nucleus. The existence of nucleating agents in the melt largely reduces the interfacial free energy σ and thus the supercooling. Although equation 1.4 can be applied in rare cases, *i.e.* when polymers are really pure and the nucleation occurs homogeneously, which is rarely the case. As has already been stated, nucleation usually occurs on the surface of impurities which strongly reduce the necessary supercooling by a consistent reduction in interfacial free energy σ . The initial stages of crystallisation have been described by the Avrami equation,

$$\phi_c(t) \sim 1 - e^{-(zt)^\beta} \quad (1.5)$$

which describes spherulites growing independently. The equation relates the ‘Avrami exponent’ β and the rate coefficient z to the particular shape of the particles, their growth rate and the time distribution of the nucleation events. The equation was developed on the basis of statistical geometrical considerations dealing with a sample of a certain volume that gets covered by

growing objects of different shapes.

The chain-folded lamella is the basic unit of semi-crystalline polymer and it is not an equilibrium structure. The difficult part in the formation of a stable nucleus derives from the fact that the folding of the chains into lamellae contributes to a substantial interfacial energy at the lamella surface, called σ_f . The lamellar thickness l is independent of the molecular weight, a typical value can be 10 nm. Lamellae are ordered regions, separated by amorphous regions (figure 1.1). The lamellae are then organised in sheaves that grow out from the nucleus into spherulites, which are of μm size.

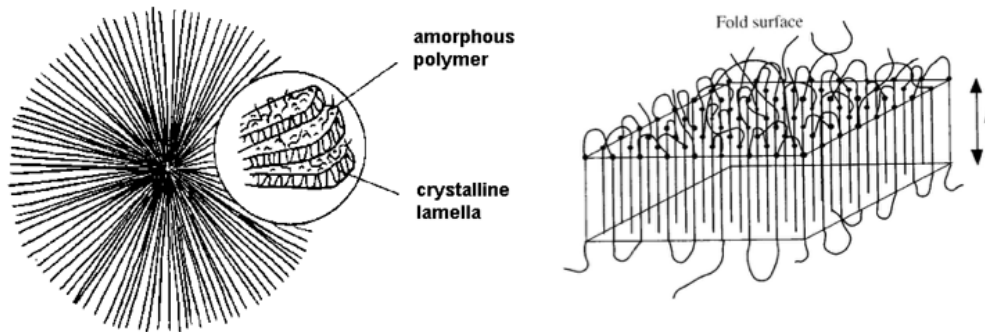


Figure 1.1: A spherulite on the left hand side and a chain-folded lamella on the right hand side. The lamella has thickness l which is typically 10 nm. A spherulite can reach several μm up to some cm in diameter, depending on the nucleation density. Figure reproduced from “Soft Condensed Matter” by Jones [20].

Typical graphs describing the crystallisation rate have a sigmoidal shape (figure 1.2): are obtained plotting the crystallinity $\phi(t)$ against the time. The crystallinity of a polymer is calculated from equation 1.3 knowing ρ , ρ_c and ρ_a , the density of the polymer and of the crystalline and amorphous phase respectively.

$$\phi = \frac{\rho - \rho_a}{\rho_c - \rho_a}. \quad (1.6)$$

Section 1.6.2 will describe the kinetics of crystallisation in thin films, therefore it is important to understand the temperature dependence of the crystal growth in the bulk. The growth rates

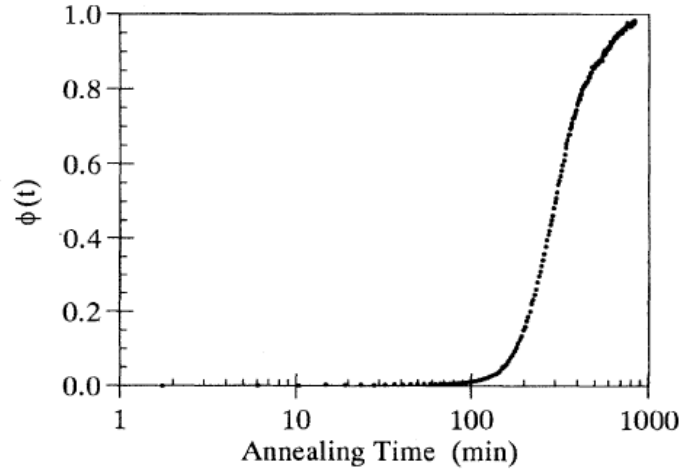


Figure 1.2: Crystallisation kinetics of PET annealed isothermally at 80°C. Figure reproduced from Imai *et al* [21].

of the spherulites, u depend strongly on the temperature and usually have a bell shape as represented in figure 1.3 for three polymers. In proximity of T_g the strong reduction in rate is

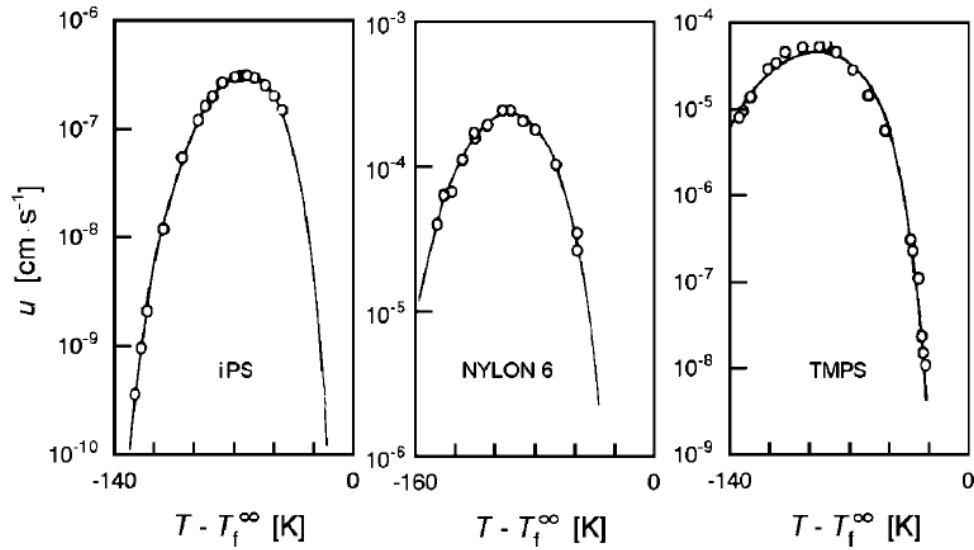


Figure 1.3: Temperature dependence of the growth rate u of spherulites in i-PS, nylon-6 and TMPS. Data from different authors taken from “Methods of Experimental Physics” by Ross and Frolen [22].

given by the slowing down of the segmental mobility in the melt, mainly due to the frictional forces during the reorganisation of the chains that increases progressively on cooling. These frictional forces are defined by the parameter ζ and their increase is well described by the empirical ‘Volger-Fulcher law’, as

$$\zeta \sim \exp \frac{T_A}{T - T_V} \quad (1.7)$$

$$\log u \sim \log \zeta^{-1} \sim -\frac{T_A}{T - T_V} + \text{const} \quad (1.8)$$

ζ^{-1} is the segmental mobility. Findings on PE [23] also show that the crystal growth in proximity of T_m decreases and it is possible to write down the equation for the high temperature counterpart of equation 1.8:

$$u \sim \exp -\frac{T_A}{T - T_V} \cdot \exp -\frac{B_0}{T_m^\infty - T}. \quad (1.9)$$

This equation was obtained by multiplying equation 1.8 with the function $\zeta(T)$ as given by the Vogel-Fulcher law, in order to extract the effect of the supercooling and eliminating the temperature dependence of the mobility. Secondly, the crystallisation temperature T was replaced by the inverse of the supercooling. So the temperature dependence of the crystal growth is similar on both the low temperature and the high temperature side, but for different physical reasons. Findings exhibit a general trend: crystallite thickness l and supercooling $T_m^\infty - T$ are inversely related and the relation can be described by

$$l(T) = \frac{B_1}{T_m^\infty - T} + B_2. \quad (1.10)$$

This means that approaching the equilibrium melting point the crystallising chains become progressively extended and a consequent decrease in the crystallisation rate occurs [24, 25]. This derives from the selection rules that determine the thickness of the growing crystallites. The change in free energy for a polymer stem of length l and cross-sectional area a^2 that joins the crystal is

$$\Delta g = -\frac{\Delta H_m \Delta T}{T_m^\infty} l a^2 + 2\alpha^2 \sigma_f. \quad (1.11)$$

The change in free energy of a polymer stem joining a growing crystal is represented in figure 1.4: the loss in entropy has to be covered by the free energy gained with the crystallisation process of a straightened stem that joins the growing crystal. Then the thickness of the polymer lamella arises from kinetics considerations, rather than equilibrium thermodynamics. There is an optimal lamellar thickness that allows the crystal to grow the fastest: it can be considered

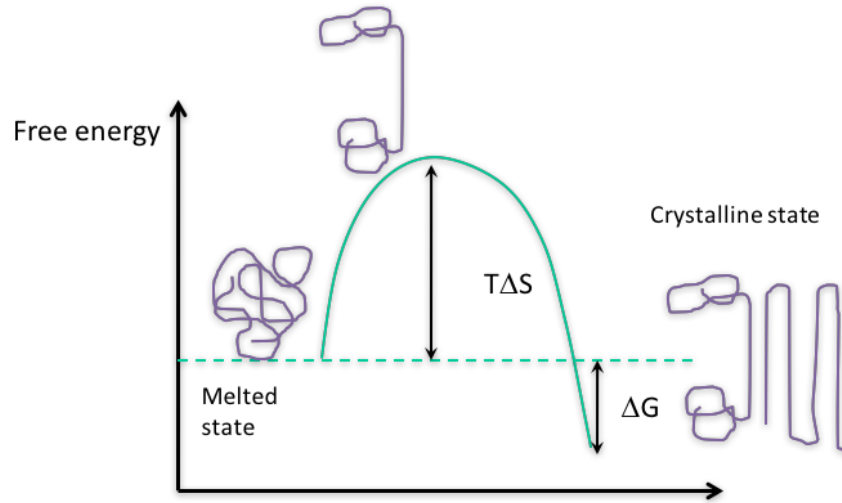


Figure 1.4: Free energy changes of a polymer stem joining a growing crystal from the melt. Figure reproduced with permission from Jones [20].

to be a length scale selection process. Crystals that are too thick grow slowly because the probability of a long enough polymer chain to straighten itself out is too small. While crystals that are too thin involve too much unfavourable energy deriving from their fold surfaces, which constitutes smaller thermodynamic force for the growth of the crystal. The rate of the straightened stem that joins the crystal from the melt depends on an entropic loss given by

$$\tau^{-1} \exp\left(-\frac{\Delta S}{k_B}\right). \quad (1.12)$$

While the rate of the segment that leaves the crystal to rejoin the melt depends in the loss in entropy and the free energy gained from the joining of the crystal:

$$\tau^{-1} \exp\left(-\frac{(T\Delta S - \Delta g)}{k_B T}\right). \quad (1.13)$$

The difference between these two rates gives the net crystallisation rate u :

$$u = \tau^{-1} \exp\left(-\frac{\Delta S}{k_B}\right) \left[1 - \exp\left(\frac{\Delta g}{k_B T}\right)\right]. \quad (1.14)$$

Assuming that $\Delta g/k_B T$ is small enough, it is possible to expand the exponential and write the speed of the crystal growth as

$$v = a\tau^{-1} \exp\left(-\frac{\Delta S}{k_B}\right) \frac{\Delta g}{k_B T}. \quad (1.15)$$

After some considerations on the relation between the crystal growth, the crystallite thickness and the temperature it is possible to write down a total equation representing the temperature dependence of the crystal growth velocity [20]:

$$v = \frac{a\tau_0^{-1}}{ek_B T} \frac{a^3}{\mu} \frac{\Delta H_m \Delta T}{T_m^\infty} \exp\left(\frac{-B}{T - T_0}\right) \exp\left(-\frac{2\mu\sigma_f T_m^\infty}{a\Delta H_m \Delta T}\right). \quad (1.16)$$

This equation shows that the temperature dependence of the growth rate is dominated by two exponentials. At low temperatures the approaching of the glass transition, means that the segmental mobility is slowed down, therefore suppressing the crystal growth. At high temperatures, the thermodynamic driving force controls the growth rate through the second exponential. The two exponentials combined give the strong peak responsible for the bell shape of the growth rate as a function of temperature.

1.4 New views on polymer crystallisation - the intermediate state of order

A number of works have shown that in some cases crystallisation in polymers proceeds via a state of intermediate state of order. In between the amorphous and the crystalline states, there is a polymer structure that is ordered in a very small length scale prior to crystallisation, but it is very difficult to observe experimentally. An intermediate state of order or mesomorphic state could be stabilised in ultrathin polymer films by the proximity to a surface and/or interface.

To prove this hypothesis it is necessary to use techniques that analyse the degree of order at the free surface and, with more difficulty, at buried interfaces.

Intermediate states of order are states of partial crystallinity, called mesomorphic states, which may be stabilised at equilibrium by the proximity to a surface or interface. An example could be the surface-induced ordering of liquid crystals in isotropic phases [26, 27]. The mesomorphic state could be present as one stage in the kinetic mechanism of crystallisation, which could be different then from the mechanism of the bulk of the film. Keller *et al* were emphasising that polymers might not nucleate from a totally amorphous phase, but they could go via an intermediate metastable mesophase [28]. This view is still seen as controversial by some physicists, but it actually recalls Ostwald's rule of stages and the classical understanding of the formation of Guiner-Preston zones in Cu/Al alloys [29].

The physics explaining this new view on polymers crystallisation has been summarised by a body of work by Strobl [30]. This intermediate state of order could preferentially be nucleated if the interfacial energy between the intermediate state and the melt is lower than other more ordered phases: the intermediate state may not be the lowest energy phase in the bulk. This has been considered to explain some findings from Imai *et al* [21], who were reporting small X-ray scattering patterns suggesting the kinetics of spinodal decomposition, which is explained by Olmsted *et al* [31] as a coupling of density and molecular orientation in a precursor mesophase.

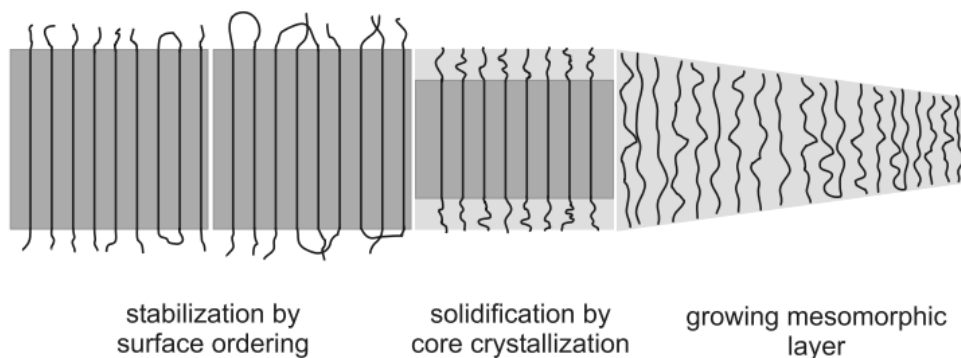


Figure 1.5: Multistage model of the polymer crystal growth through a mesophase as suggested by Strobl [30]. The crystal does not grow by chain segments directly attaching to the crystal front, but from the melt are first incorporated in a thin layer with mesomorphic structure in front of the crystallite. A critical thickness is then reached and a crystal block forms by first order transition. In this last step the excess energy of the fold surface is reduced. Figure reproduced with permission from Strobl [30]

1.5 Crystallisation for conjugated polymers

In semiconducting polymers the repeat unit usually contains aromatic or heterocyclic rings and their electrical properties are intimately related to their molecular structure and intermolecular interactions in the films. The conjugation of the π -orbitals in the repeat units promotes electrical transport along the polymeric chain, and it also leads to nearly planar backbones. Saturated sidechains are added to the repeat units to facilitate solubility in common solvents. Conjugated and non-conjugated regions put together, lead to a phase separation into highly ordered structures [32]. The resulting material has a complex thermal phase behaviour as it can contain isotropic, liquid crystalline and crystalline phases all together.

High-performance semiconducting polymers form semicrystalline films that are typically more disordered than other molecular compounds used in organic electronics, such as pentacene [33]. Usually the molecular structure of the polymer is known in detail and together with X-ray scattering information, optical spectroscopy and modeling methods it is possible to have an understanding of the packing structure [34–36]. Semiconducting polymers may crystallise in lamellar or hexagonal structures depending on the sidechains (figure 1.6) [37]. Most studied semiconducting polymers are polyfluorenes and polythiophenes, where usually the former have been observed crystallising in hexagonal unit cells and orthorhombic in others [38–41]. Polythiophenes preferentially form lamellar structures [34]. Semiconducting polymers can

be schematised as 2D sheets with the side-chains that separate layers of conjugated moieties strongly interacting with each others [42, 43]. Electrical transport happens preferably along the direction of the π - π stacking, while it is very weak along the side-chains, which mainly constitute saturated bonds. The type of alkyl chains between the backbones is an important factor that influences the probability of tunnelling from backbone to backbone. Lamellar packing structures (figure 1.6a) present usually larger separations between the backbones in comparison to the hexagonal structures (figure 1.6b). Different factors influences the intermolecular electronic coupling; the mixture of ordered and disordered regions is also a very important parameter to consider [44].

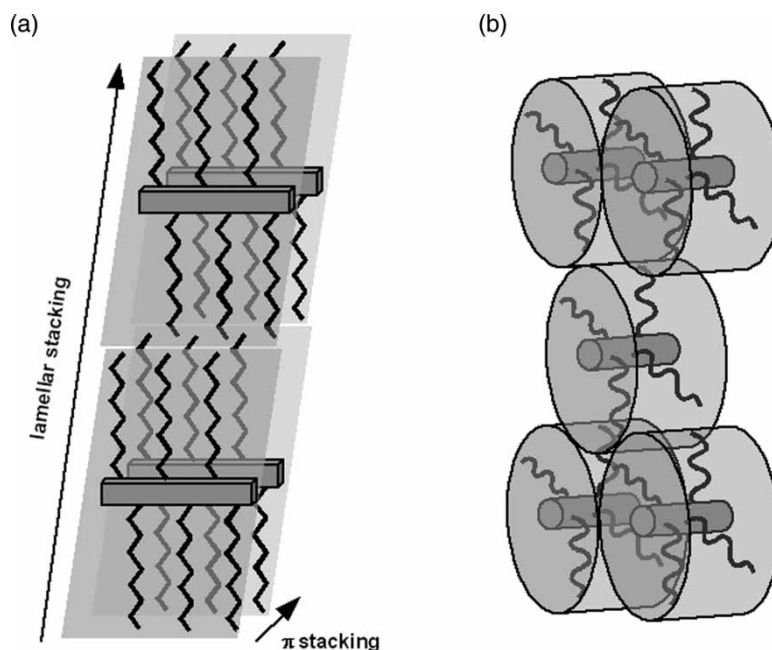


Figure 1.6: (a) Lamellar and (b) hexagonal packing structures typical in semiconducting polymers. Figure reproduced with permission from Chabinyč [45].

1.5.1 Orientation of crystalline domains

The spin-coating procedure leads to polycrystalline samples with crystalline domains oriented in different directions, and since the electric transport is anisotropic in ordered domains it is important to know the orientations of these regions relative to each others and the substrate. The crystalline regions of P3HT for examples have the a-axis (lamellar stacking-alkyl chains) oriented within 10° of the normal to the substrate, in this way the surface energy is minimised

as non-polar sidechains are oriented towards the surface of the film [43, 46–48].

An experiment was done on P3HT with two different regioregularity and molecular weights: 96% with low molecular weight and 81% with low molecular weight [49]. The high regioregularity one had an edge-on preferential orientation, while the low regioregularity one had a flat-on preferential orientation. The cause of this change in orientation was not fully understood, but it must have been the fast spin-coating process (fast evaporating solvent, chloroform was used) that has been affected by either the different regioregularity or molecular weight. These orientations might have been the kinetic structures rather than thermodynamically favoured orientations because of the fast evaporating solvent used [50, 51].

An important fact is that highly oriented domains are usually found at the substrate interface, data suggest that nucleation of crystalline domains in P3HT occurs at the substrate interface [17]. From a number of works [52–56] it is possible to draw a general result: conjugated polymers tend to have their backbone lying parallel to the substrate surface in spin-coated films, driven by the process forces. The second reason is that the length of the polymer is usually longer than the thickness of the film, so the lower energy solution is this orientation instead of chain folding, which is unfavoured due to the rigidity of the backbone [57–60].

So orientation, crystal domain size and packing strongly depend on the processing methods used to fabricate the devices, due to the non-equilibrium nature of the techniques. Additional parameters influencing orientation, domain sizes and packing are the boiling point of the solvent, the phase transitions of the material and the film thickness.

A number of studies highlighted how important it can be to have a thermal annealing treatment post spin coating to re-organise the molecules and remove packing defects. This is because during the deposition process there is an interplay between molecular aggregation and evaporation (for example) that might hinder the formation of crystalline domains [61].

Important details about the ordering of polymer chains can be deduced by probing the d -spacing between lamella as a function of temperature. This is because the d -spacing is set by the end to end interaction of the side chains. It is believed that ordered alkyl side-chains starts to disorder before any larger conformational change involving the more rigid backbones. This disordering process of the side-chains confers more mobility to the polymer molecules and

could be the starting stage of the ordering process. This ordering model has been supported by optical spectroscopies and calorimetric data [62, 63].

Concluding, there is a wide understanding of crystallisation for saturated polymers in thin films [64], but much less is known about conjugated polymers, which present more chain stiffness and an intermediate level of order like $\pi - \pi$ stacking, that can be defined as a shorter range order, as chains are unable to fold and form lamellae. Reduction of $\pi - \pi$ stacking involves a compromised hole-mobility and a worse device efficiency [65–67].

Most conjugated polymers are not sufficiently flexible to allow folding in lamellae as the saturated ones tend to show, but some other ordered structure can be found. For example P3HT films can present a network of crystalline nanofibrils embedded in a matrix of amorphous material [68].

As mentioned at the beginning of this section, conjugated polymers are often characterised by a chemical incompatibility controlled by the intermix of alkyl chains and conjugated backbones, that gives origin to layered “self-assembled structures” of $\pi - \pi$ stacked backbones alternated with more or less ordered alkyl chains (an example is P3HT in figure 1.7 where the backbone is constituted by conjugated polythio-phenes) [4, 34, 69, 70]. The main chains are then separated by side chains giving origin to a typical diffraction peak that is known as lamellar ordering peak and a second peak at larger Q s given by the scattering of the $\pi - \pi$ stacked backbones.

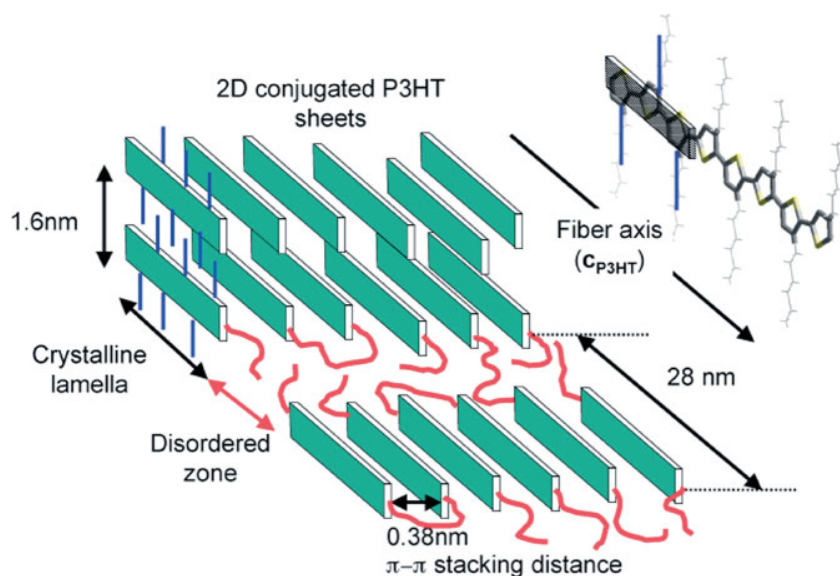


Figure 1.7: In this figure is possible to distinguish three different length scales: (a) the lamellar structure that involves layers of π - stacked polythiophene backbones separated by the hexyl side chains (1.6 nm), (b) the π - π stacking distance, 0.38 nm and (c) the periodicity related to the alternation of crystalline and amorphous zones (28 nm). The P3HT chains in the amorphous zones are represented as red segments. Figure reproduced with permission from Brinkmann [4].

1.5.2 Crystallisation in PCDTBT

PCDTBT is a relatively stable semiconducting polymer: FETs fabricated with PCDTBT show stability in air up to 150°C and in nitrogen up to 350°C [71]. No change in the chemical bonding within the backbone is observed neither with UV-vis absorption spectra nor XPS, up to the temperature mentioned above. The stability of PCDTBT is due to the large ionization potential because of its very low energy HOMO [72, 73].

PCDTBT has also a very high internal quantum efficiency, an operating lifetime of > 6 years and a 6 - 7 % PCE that typically surpasses the PCE of P3HT-based devices.

Although PCDTBT devices present more efficiency than P3HT based devices, P3HT is a much more crystalline polymer than PCDTBT. The latter is thought to reach a short range order packing, without organising in chain folded lamellae. A very exhaustive description of the packing has been described in the paper by Lu et al. [74], which is described later in this section. In earlier work [71], XRD spectra on PCDTBT were registered for annealed and unannealed samples and neither of them show any crystalline peaks (figure 1.9), meaning the polymer is amorphous, either as cast and post annealing. The films were 60 nm thick, but XRD was carried out in air with the X-ray source being a Cu-K α source ($\lambda=1.5 \text{ \AA}$), which might not

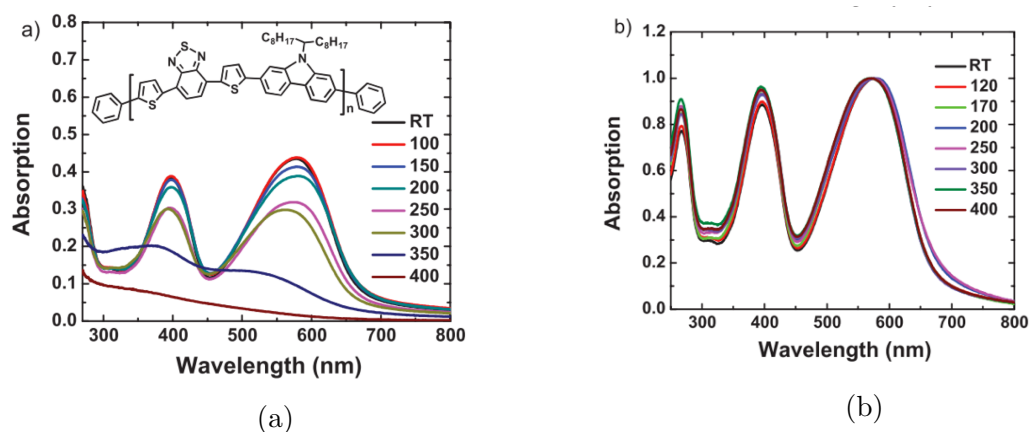


Figure 1.8: Absorption spectra for PCDTBT annealed at different temperatures in air (a) and under nitrogen (b). It is possible to see that the optical properties of the polymer are already influenced above 150°C in air (a). Figures reproduced with permission from Cho *et al* [71].

have been energetic enough to generate scattering in this very weakly crystalline polymer.

In another work [72] different poly(2,7-carbazole) derivatives have been tested and it was found

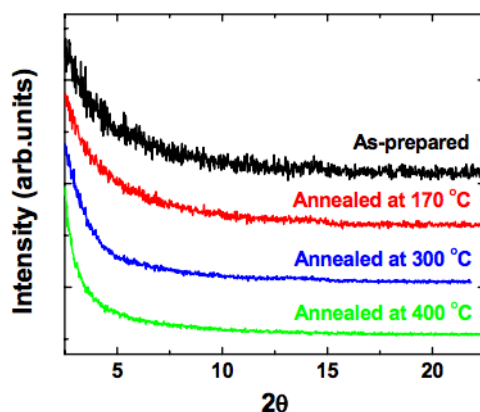


Figure 1.9: X-ray Diffraction data for PCDTBT polymer films annealed and as-cast. Figure reproduced with permission from Cho *et al* [71].

that all the co-polymers were stable up to 340°C with a T_g over 100°C, apart from PCDTPX. PCDTPX is a variation of PCDTBT, where the sulfur in the benzothiazole has been substituted with another nitrogen, and an oxygen has been added in between the two nitrogens. Sulfur-containing polymers like PCDTBT show higher thermal stability than polymers where an oxygen atom has been added to the benzothiazole unit (figure 1.10).

Employment of crystalline P3HT fibrils in active layers of BHJ solar cells avoids the need for post-processing thermal annealing to improve polymer crystallisation [68], that is why PCDTBT fibrils have been studied by Wang *et al* [75]. They studied nanoscale PCDTBT fibrils prepared

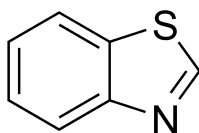


Figure 1.10: Chemical structure of benzothiazole.

in solution, which have been then characterised by AFM, TEM and GI-WAXS. It is interesting to compare the AFM and GI-WAXS results for PCDTBT fibrils observed by this group, with the results presented in this thesis for non-fibrils films. In this work [75], the same procedure used to crystallise P3HT has been used for PCDTBT and it has been unsuccessful. PCDTBT was dissolved in a poor solvent, anisol, at elevated temperature and allowed to cool slowly. If it is dissolved in a good solvent instead, such as chloroform and then the poor solvent is added, random aggregates or featureless structures can be observed by electron microscopy. While heating the polymer in dichloromethane at elevated temperatures in a sealed vessel gave 60-80 nm thick fibres.

The substructure of the fibrils is given by π - π stacking (010) and alkyl-alkyl interaction (100), called also lamellar packing. These X-rays scattering analysis brought to hypothesize coexistence of face-on and edge-on lamellar stacking. These GIWAXS data are more similar to the results presented in this thesis, compared to the previous GIWAXS data showed in figure 1.9, where no structures were observable. The GIWAXS data presented in figure 1.11 show an interchain separation of 16.5 Å (0.38 \AA^{-1}) for the lamellar packing and 4.3 Å (1.46 \AA^{-1}) for the π - π stacking.

Absorption and fluorescence emission spectroscopy surprisingly showed little change between the fibrils and the polymer in solution, while for P3HT a significant red-shift of more than 50 nm was showed for the fibril absorption spectrum maximum, with the appearance of vibronic bands [75]. The authors justify this observation saying that “ π - π stacking and alkyl interactions in the fibrils have little influence on the electronic structure of the polymer chains or between neighbouring chains.”

The crystallisation in this promising conjugated polymer is fairly ambiguous, as it is not easy to reveal the degree of order of its polymer chains. Studying PCDTBT with grazing-incidence wide-angle X-ray scattering (GIWAXS) (figure 1.13), Wang *et al* [8] found an enhanced scat-

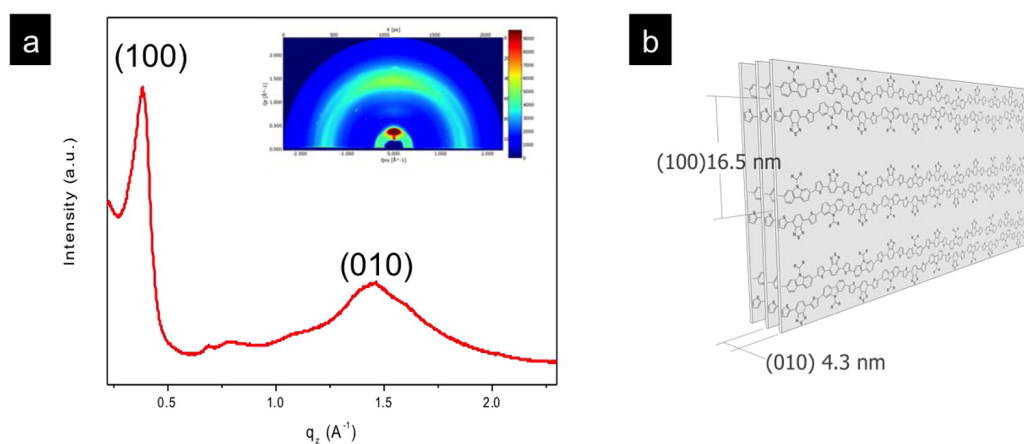


Figure 1.11: (a) GIWAXS data and line-cuts out-of-plane from [75]. (b) The corresponding crystal lattice. Reprinted with permission from [75]. Copyright 2017 American Chemical Society.

tering for the π - π stacking peak at $q = 1.57 \text{ \AA}^{-1}$, at high depths of the film (figure 1.13c). This might suggest the positive contribute of a substrate to the formation of π - π stacking. Then scattering at $q = 0.63 \text{ \AA}^{-1}$ has been seen; this has been assigned to the 2nd-order diffraction of the bi-layer lamella spacing in a previous paper from Lu *et al* [74].

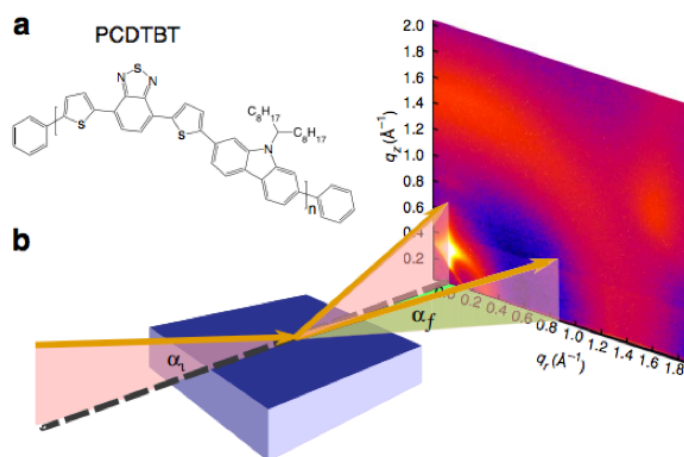


Figure 1.12: (a) Molecular structure of PCDTBT and the experimental geometry of the GIWAXS (b). Figure reproduced with permission from Lu *et al* [74].

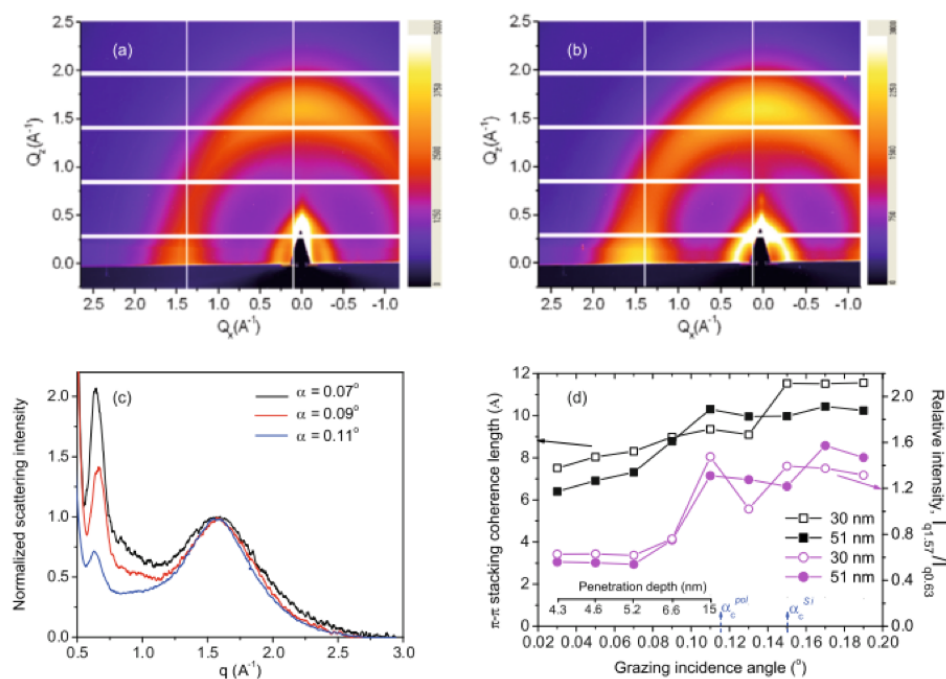


Figure 1.13: 2D GIWAXS images before (a) and after heating/cooling cycle for T_g measurement (b). (c) raw scattering data at three different grazing incidence angles in the out-of-plane direction. (d) π - π Stacking coherence length as a function of the g.i. angle, and the relative intensity changes of peaks at $q = 0.63 \text{\AA}^{-1}$ and $q = 1.57 \text{\AA}^{-1}$. Figure reproduced with permission from Wang *et al* [8].

An interesting approach used by Wang *et al* [8] was to study the depth profile structure, using GIWAXS, as a function of the grazing-incidence angle, that allowed the calculation of the $\pi - \pi$ stacking coherence length of the polymer and the relative $\pi - \pi$ stacking intensity to the lamellar packing as a function of depth (figure 1.13d).

In the work from Lu *et al* [74] more details about the crystallisation of PCDTBT emerged. The

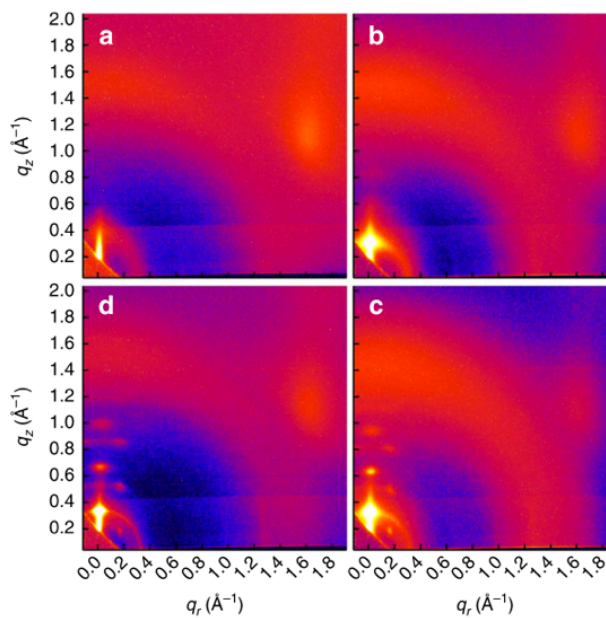


Figure 1.14: GIWAXS scattering images of PCDTBT. The images were obtained at (a) 25°C before annealing; (b) 140°C; (c) 200°C; (d) 25°C after annealing. Figure reproduced with permission from Lu *et al* [74].

GIWAXS images of PCDTBT (figure 1.14) revealed a layer spacing of $\sim 17.5 \text{ \AA}$ and $\sim 19.0 \text{ \AA}^{-1}$ (from the slightly elliptical ring located at 0.36 \AA^{-1} along the q_z axis and at 0.33 \AA^{-1} along the q_r axis). The elliptical nature of the scattering before annealing indicates that the chains are packed closer along the Q_z axis and different polymorphs co-exist. After annealing at 140°C the scattering rings become circular with a uniform radius of 0.302 \AA^{-1} suggesting that the polymorphs have vanished. The ring at 1.42 \AA^{-1} corresponds to an average $\pi - \pi$ stacking distance of 4.4 \AA , which, together with the 0.302 \AA^{-1} are identical to the values obtained for bulk samples [72] and to the one obtained by Wang *et al* [8]. This $\pi - \pi$ stacking is although larger than the one measured for P3HT of 3.8 \AA , which generally translates in a worse electron coupling and device performance [76]. However PCDTBT based devices present an excellent efficiency, which is probably related to additional structural features of this polymer.

The images 1.14a and b at 25°C and 140°C present similar features, however scattering rings are sharper and more intense at 140°C indicating an enhanced order. At 200°C (figure 1.14c) well-defined Bragg peaks were observed, indicating the formation of a crystalline phase, that remains after the film is cooled to 25°C.

It was thus possible to obtain a very detailed diffraction pattern from the scattering profiles

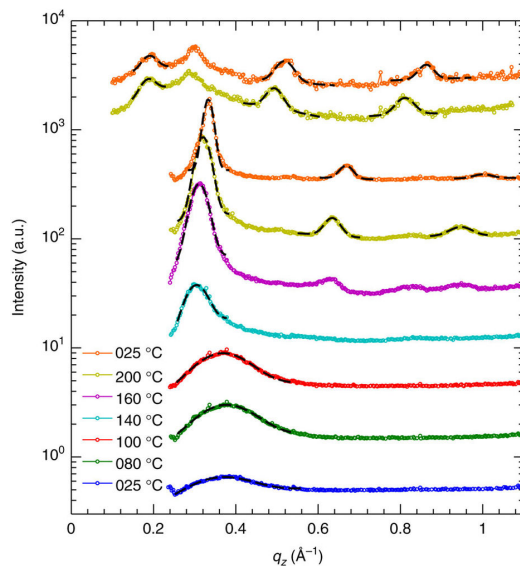


Figure 1.15: Scattering profiles along q_z . The lower seven curves have been obtained along $q_r \sim 0$ and the top two curves along $q_r = 0.15 \text{ \AA}^{-1}$. The orange 25°C curves are measured before the thermal treatment and the blue one, after the thermal treatment. Figure reproduced with permission from Lu *et al* [74].

(reported in figure 1.15) and this can be represented by an oblique unit cell with $b_1 = (0, 0.333) \text{ \AA}^{-1}$ and $b_2 = (0.150, 0.190) \text{ \AA}^{-1}$ (figure 1.16a). The real-space primitive unit cell vectors are then $a_1 = (-23.9, 18.9) \text{ \AA}$ and $a_2 = (41.9, 0) \text{ \AA}$ (figure 1.16b), where the x axis is in-plane and the y axis is out-of-plane. The 41.9 Å length corresponds to the length of two linear backbone segments with a constant shift of 23.9 Å between backbone chains separated by the 18.9 Å layer spacing. Differently from another conjugated polymer like P3HT, PCDTBT packs with a backbone pairing mode, with all the side-chains on the the same side in order to minimise their interactions, while in P3HT (regio-regular) all the side-chains are alternate as shown in figure 1.7. In P3HT the alkyl chains must alternate from either side due to steric constraints. As, for PCDTBT, the alkyl chains are all anchored on the same segment, this allows the alkyl-free side of the PCDTBT backbones to pair as in figure 1.16. This arrangement is favoured, because it minimizes the interfacial energy between the nonpolar alkyl side chains and the polar

backbones.

As proposed by Lu et al [74] in the schematics of figure 1.16d, lamella stacking is happening perpendicular to the plane of the film (edge-on), and π - π stacking, perpendicular to the lamellar stacking. The two being perpendicular to each other can then orient themselves in different directions within the film. But the constraint is that π - π has to be perpendicular to the lamellar stacking. π - π Stacking is simply given by attractive non-covalent interactions between the aromatic rings parallel to each other, the p-orbitals interact overlapping and minimizing the internal energy of the system.

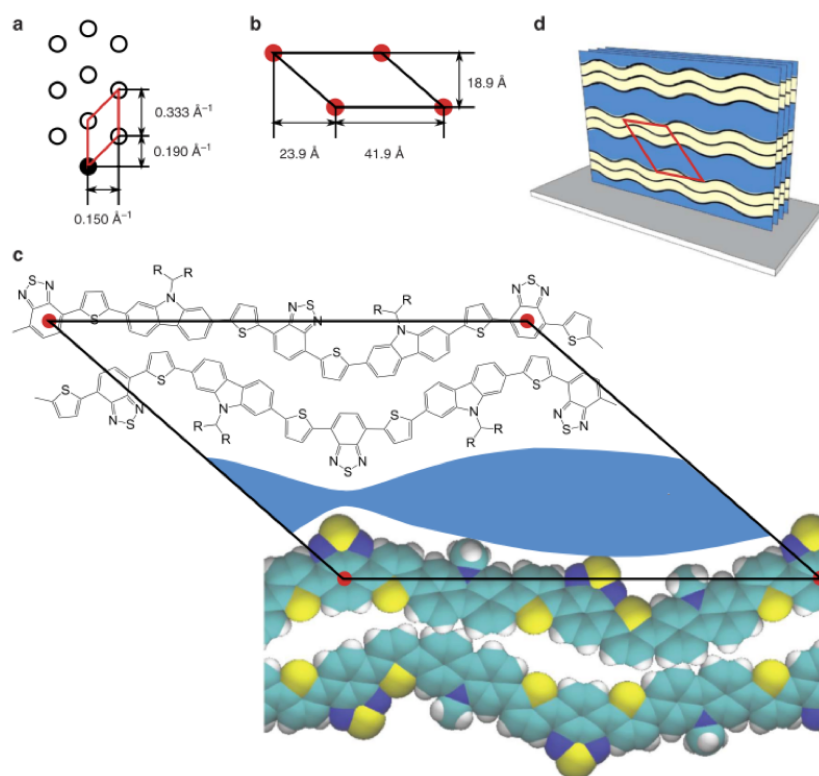


Figure 1.16: PCDTBT thin-film diffraction pattern, unit cell and bilayer motif. (a) Diffraction pattern obtained from the Bragg peaks shown in figure 1.15d. The filled circle corresponds to the origin. (b) The corresponding oblique real-space lattice obtained from the scattering pattern. The π - π direction is normal to this plane. (c) Backbone configuration for one of possible conformations of a backbone obtained by *ab-initio* calculations. Figure reproduced with permission from Lu *et al* [74].

Influencing the packing of PCDTBT is the entanglement of the polymer chains, as polymers are long molecules, it is inevitable. There is a paper [77] where the number of chain entanglements N for P3HT are calculated with an equation, but the molecular weight at which the entanglements start to influence the macroscopic properties of the polymer solution, has to be known. For P3HT, this molecular weight $M_c^{solution}$ measured by a change in viscosity

of the polymer solution was found when $M_w \geq M_c^{solution} \approx 35\text{kDa}$. From there is calculated the number of entanglements ($N = 2M_w/M_c^{solution}$) in low and high M_w solutions, finding $N = 1-2$ for the low M_w P3HT and $N = 4$ for the high M_w P3HT. In the work by Shao et al. [78] PCDTBT is thought to be interacting with himself from 24 kDa (around 33 repeat units) and above. $M_c^{solution,PCDTBT} < M_c^{solution,P3HT}$ as PCDTBT presents larger repeat units which causes a PCDTBT chain to be stiffer than a P3HT one, giving then a lower $M_c^{solution}$. During this PhD, it has been used PCDTBT with molecular weight, M_w of 35.4 kDa, $M_n = 14.5$ kDa and polydispersity, $\text{PDI} = 2.44$. The estimate for the number of chain entanglements in solution for this molecular weight of PCDTBT is therefore ~ 3 .

The backbone of PCDTBT has many degree of rotational freedom and as showed by quantum chemical calculations the backbone conformation of PCDTBT is not planar at the ground state; the carbazole (the electron donor group) and thiophene units are twisted with a torsion angle of $25-27^\circ$, while the thiophene and benzothiadiazole (the electron acceptor group) units are slightly twisted with a torsion angle of $3-5^\circ$ [79].

Counting that 24 kDa corresponds to 33 repeat units, 35.4 kDa means a larger number of repeat units and this would require a dramatically large conjugation length especially given the size of the monomer unit. For this reason, charge transport in PCDTBT would be a mix of of intrachain and interchain hopping and band transport. The latter will be in those points where the backbone is completely conjugated. The monomer size of a PCDTBT alone is much larger than homopolymers such as poly(phenylene-vinylene)s (~ 3 times) and polythiophenes (~ 9 times). This is equivalent to ~ 99 repeat units for MEH-PPV, whose conjugation lengths are believed to only be ~ 8 repeat units. It is unlikely that a conjugation can sustain such long distance as structural factors such as curvatures and kinks in the polymer chain would disrupt conjugation. From a molecular dynamics study, PCDTBT in solution tends to have a wide range of dihedral angles, suggesting planar structures are not thermodynamically favoured for low concentrations in solution, on the other hand the higher concentration reached in solid phases might support π - π stacking which might support to reach a better planarity [80]. This rotational freedom around the backbone would explain the different orientations described by the X-ray scattering rings, for both the π - π stacking and the lamellar packing.

1.5.3 Liquid crystal phases

In what is called hard condensed matter physics, metals, semiconductors and ceramics materials are generally crystalline, where atoms and molecules are arranged with near-perfect long ranged order over distances that are orders of magnitude greater than the distance between molecules. For soft condensed matter the situation is different as for most soft matter systems the degree of molecular ordering is intermediate between the full positional order of a single crystal and the complete positional disorder of liquid or glass. The equilibrium phases in which molecules are arranged with a degree of order intermediate between the complete disorder of a liquid and the long-ranged, three dimensional order of a crystal is called liquid crystallinity. Polymers composed by units with a high degree of rigidity either in the backbone or as side chains, show a liquid crystalline behaviour. When the solid melts, some aspects of the long range order characteristic of the solid may be retained, and the new phase may be a liquid crystal, a substance having a liquid-like imperfect long-range order in at least one direction in space but positional or orientational order in at least one other direction. There are different types of liquid crystals, a smectic phase, when molecules align themselves in layers, some smectic phases at high temperatures, lack the layered structure but retain a parallel alignment, so then it is called nematic phase. The cholesteric phase is when the molecules lie in sheets at angles that change slightly between each sheet, forming helical structures. Nematic liquid crystals have anisotropic optical properties, as their optical properties depend on the relative orientation of the molecular aggregation with respect to the polarization direction of the light beam.

A topic to consider is the liquid crystallinity of polyfluorenes, as a fluorene moiety is contained in PCDTBT. It has been shown that Poly-(9,9-dioctylfluorene) (PFO) and fluorene copolymers display liquid crystalline phases with high order parameters above their melting points and at temperatures that are well below those for thermal decomposition. These phases were found to align readily into monodomains [39, 81, 82].

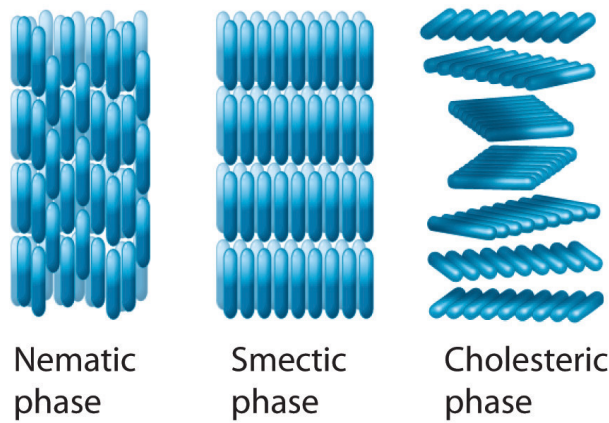


Figure 1.17: Schematic of three types of liquid crystals, nematic, smectic, cholesteric. In the nematic phase the long axis of the molecules are parallel to each others. In the smectic phase, the molecules are parallel to each others and also organised in planes. In the cholesteric phase the molecules are organised in layers which are tilted forming a spiral, which gives chiral properties to this type of phase. The degree of order increases from nematic to cholesteric and the liquid becomes also more opaque.

1.6 Polymers in thin films: the consequences of confinement on the material

1.6.1 Consequences of confinement on the glass transition temperature

Semicrystalline polymers contain an amorphous part where the chains are entangled and thus, in a random disordered state. The entanglement gives rise to typical viscoelastic properties of polymeric materials. These amorphous regions present a transition phase defined by the glass transition temperature. Below this temperature, polymer chains are frozen in a disordered glassy state, where any motion is blocked. Many studies [10, 83–91] have confirmed the trend in chain mobility within a polymer film confined between a substrate, *e.g.* a silicon wafer, and air. It can be summarised in a three layer T_g model [92]:

- polymer chains has enhanced mobility near the free surface, resulting in a glass transition temperature lower than in the bulk;
- polymers in contact with the substrate, where the specific interactions between the polymer and the material, *e.g.* PMMA with SiO_2 [93], will reduce the mobility of the chains,

increasing T_g .

- finally in the middle layer, polymer chains show the bulk value of T_g .

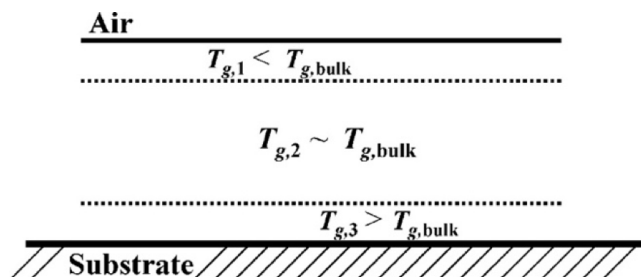


Figure 1.18: A polymer film can be seen as constituted by three layers with different characteristics. The top air/polymer interface layer with enhanced mobility with enhanced T_g , the bottom substrate/polymer interface with hindered mobility and decreased T_g , the bulk-like layer in the middle. Figure reproduced with permission from Wang *et al* [92].

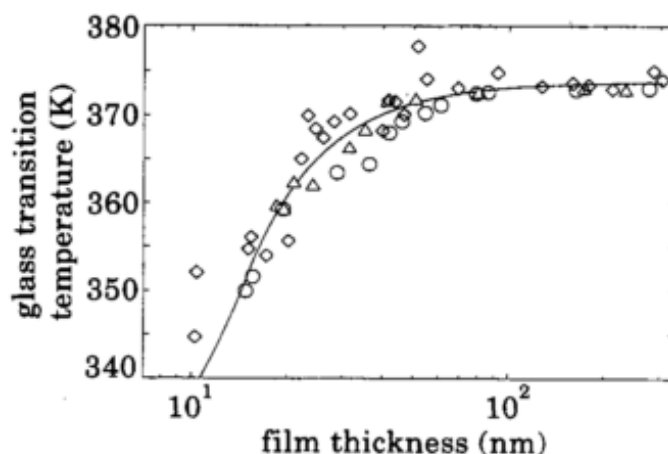


Figure 1.19: Glass transition temperature T_g in function of the film thickness for different molecular weights of polystyrene. Figure reproduced from Keddie *et al* [10].

One of the first works about the deviation of the T_g as a function of thickness is the paper from Keddie *et al* [10] (figure 1.19), where a remarkable depression of T_g for films below a certain value of film thickness was observed, showing that the role of the polymer/air interface becomes predominant in determining the properties of the entire film.

The glass transition temperature T_g was studied as a function of film thickness and molecular weight for polystyrene. There are then two defined opposite behaviours (at the air/polymer and polymer/substrate interface) that are competing in a film, giving an enhanced or decreased T_g . For example, the effect of the substrate can overcome the effect of the free surface, like in

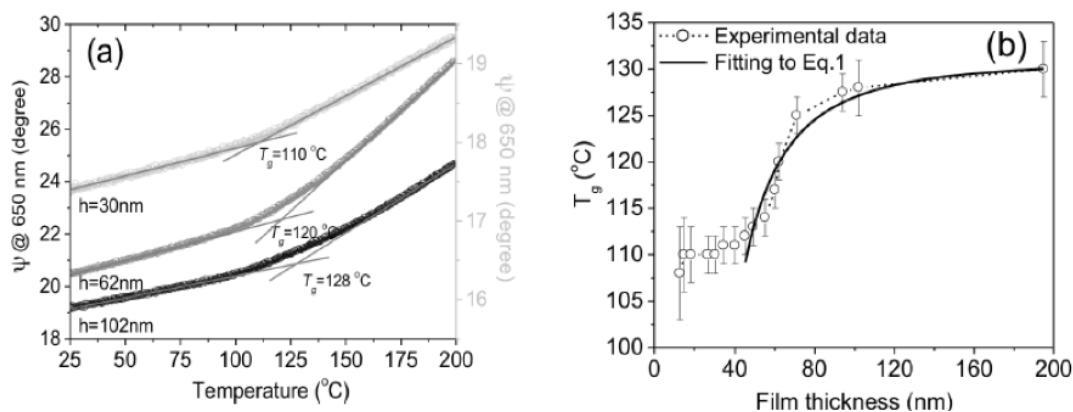


Figure 1.20: (a) Represents the T_g for three different film thicknesses, measured during cooling by ellipsometry. (b) Direct effect of π - π stacking is observed on the T_g : it converges to 110°C at a film thickness of 40 nm and it does not decrease anymore. Figure reproduced from Wang *et al* [8].

the case of the Wang *et al* paper [92], where a sharp increase in the T_g is observed for thickness less than 30 nm (figure 1.22). In the work by Wang *et al* [92], the polymer used was the poly(bisphenol A hexane ether) (BA-C6) (figure 1.21).

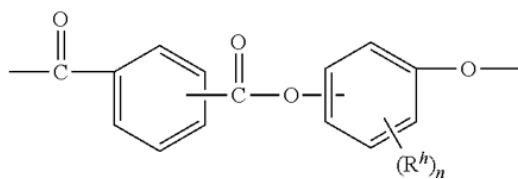


Figure 1.21: Chemical structure of the poly(bisphenol A hexane ether) (BA-C6).

There are different factors to be considered, like the kind of substrate used and its degree of interaction with the polymer chains which defines the length-scale at which this interaction has an influence.

1.6.2 Consequences of the confinement on the crystallisation kinetics and orientation of the chains

Different dynamics caused by the confinement of the chains results in different nucleating rates and then in different crystallisation kinetics [92, 94–96]. It seems legitimate to consider the kinetic effect of nucleation in determining the orientation of the lamellae formed in thin films [96, 97]. It is shown from the bell-shaped curve of the primary nucleation rate (figure 1.23), that the critical temperature T_c , indicating the maximum of the crystallisation rate, changes in each

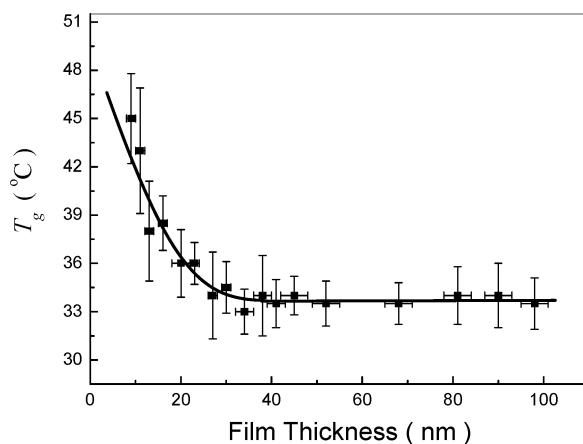


Figure 1.22: Measured T_g of ultrathin BA-C6 films as a function of film thickness. Differently from the curve from Keddie *et al* in here T_g increases for very thin films suggesting that the substrate influence prevails on the air/polymer interaction. Figure reproduced with permission from Wang *et al* [92].

layer.

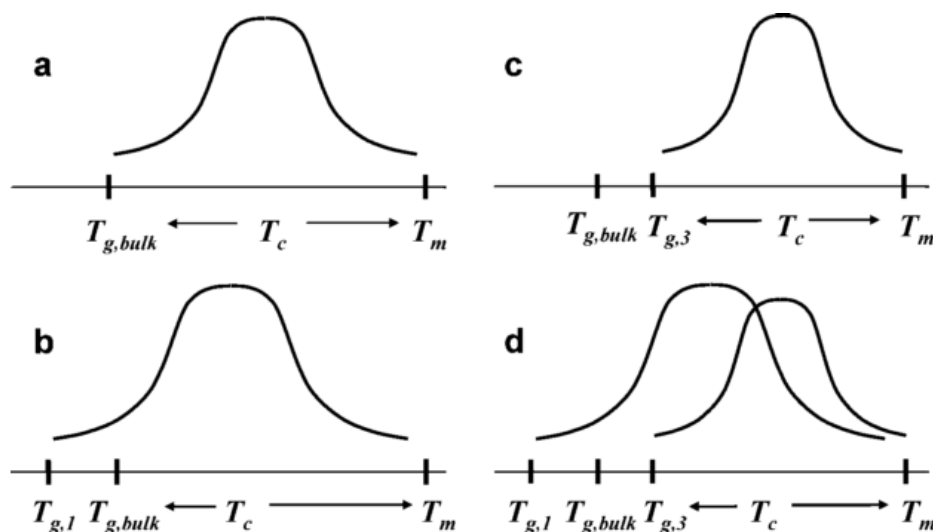


Figure 1.23: (a) A bell-shaped curve shows the primary nucleation rate as a function of temperature. (b) T_{g1} is the characteristic T_g near the surface and the curve shows that the T_c will decrease. (c) T_{g3} is the characteristic T_g near the substrate and the consequent increase in T_c . (d) Shows the combination of the two. Figure reproduced with permission from Wang *et al* [92].

Wang *et al* [92] (supported by ellipsometry, AFM and computer simulations from other groups [98–101]) claim that the temperature and proximity to the air or substrate interface both have an active role on the preferential nucleation and thus on the orientation of the crystals:

- at lower temperature, homogeneous nucleation is the quickest at the surface of the film, and gives birth to edge-on lamellae;

- at higher temperatures, heterogeneous nucleation rate near the substrate is higher than the homogeneous nucleation rate at the surface, so flat-on lamellae at the surface are observed;
- at very high temperatures, homogeneous nucleation becomes very slow at the surface, thus flat-on lamellae are observed at the surface (figure 1.24).

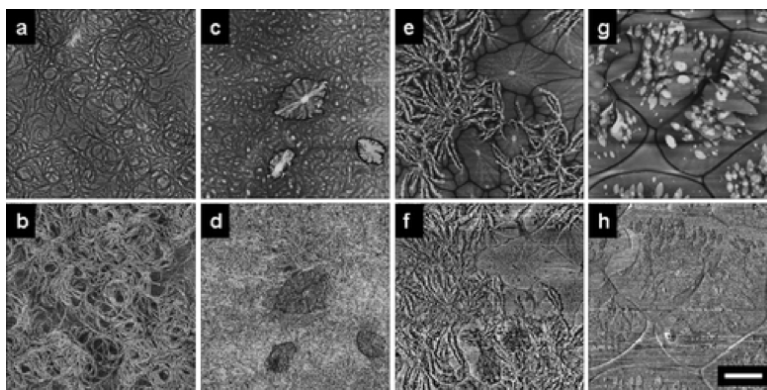


Figure 1.24: AFM images from Wang *et al* work [92]. Height images in the upper row, phase images in the lower row. Crystalline morphologies for BA-C6 are shown in these about 30 nm films crystallised for 84 hours at 45°C (a), 60°C (b), 75°C (c) and 90°C (d). It is possible to see that edge-on lamellae are visible at the surface for the lower annealing temperatures, while for higher annealing temperature, mainly flat-on lamellae are visible. The scale bar in (h) is 10 μm . Figure reproduced with permission from Wang *et al*.

Given that the chains are more free to move near the surface, they can nucleate faster at lower temperatures.

The orientation is then determined by three parameters: temperature, film thickness and interaction with the substrate. For large thicknesses, flat on lamellae, growing near the substrate, do not have time to show up at the surface (figure 1.25). But if the interaction with the substrate is very high, flat-on lamellae will dominate, thickness allowing obviously.

As for the T_g , also the kinetics of crystallisation are determined by the two opposite effect of the air surface and the substrate effect.

Different groups [57, 102–105] have followed the kinetics of crystallisation in isothermal (between T_g and T_m) and non-isothermal conditions, using spectroscopic techniques. The general trend, is that the kinetics decrease with the shrinking of the films, and in one of the works [105] it is pointed out that the reduction of the crystal growth factor by 2 orders of magnitude in PEO

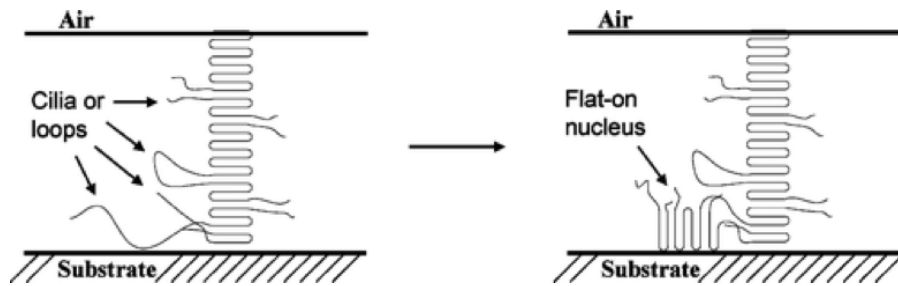


Figure 1.25: Schematic illustration proposed by Wang *et al* [92] showing the formation of flat-on lamellae in contact with the substrate. Figure reproduced with permission from Wang *et al*.

(polyethylene oxide), is due to the interaction with the substrate that perhaps increases the glass transition temperature by 30°C. Another group [106], who studied crystallisation kinetics for PEO thin films with optical microscopy techniques, observed substrate-induced-inhibition of the amorphous material transport to the growth front of the lamellae. Other works based on grazing incidence X-ray diffraction point out that random orientation is characteristic of bulk regions or however of thick films (200 nm) and preferred orientations, typically edge-on are characteristic of thin film, below 20nm, which they present also enhance crystallinity [17, 107–109]. Using Monte Carlo simulations it has been found that there is a threshold thickness defined transition thickness $d(t)$, for which, films thinner than it have growth rates that decrease as the thickness is decreased and for thickness greater than $d(t)$ the growth rate is constant [110].

Chapter 2

Experimental techniques

2.1 Spectroscopic ellipsometric studies of thin films relaxation

2.1.1 Introduction

Spectroscopic Ellipsometry has been used in a number of works to follow the properties of thin films because it has high sensitivity and precision. In this thesis for example I could follow very small changes in thickness every 0.9 s produced by thermal expansion or crystallization. Thermal expansion reduces the density of the films, while crystallization increases it, producing changes in the thickness and the refractive index of the film, which can be followed by the instrument. A risk common to some techniques is that they cannot distinguish between a thickness change and a refractive index change, but spectroscopic ellipsometry gets around this problem, by measuring over a wide range of wavelengths and using model fitting.

Ellipsometry measures the change of polarization between the incident and the reflected light-beam from the sample, being able to describe the optical system (sample) that modifies the polarization state of the beam of light.

The instrument measures the ratio of the two Fresnel reflection coefficients R_p and R_s which represents the components p - and s - of the polarized light (parallel and perpendicular to the

plane of incidence), which are related through equation 2.1 to Ψ and Δ , the ellipsometry angles. Δ contains phase informations, making the measurements very sensitive. The ratio is given by

$$\rho = \frac{R_p}{R_s} = \tan(\psi)e^{i\Delta} . \quad (2.1)$$

In order to understand the relation between the ellipsometry angles and the Fresnel reflection coefficients, the first step is to understand an electromagnetic plane wave, which is a solution of Maxwell's equations for electromagnetic fields. The wave equation for the electric field, derived from Maxwell's equations for a non-conducting, non-dispersive medium is:

$$\vec{\nabla}^2 \vec{E} - \frac{1}{v^2} \frac{\partial^2 \vec{E}}{\partial t^2} = 0 , \quad (2.2)$$

where v is the optical impedance $v = \frac{c}{\sqrt{\epsilon\mu}}$, where μ being the permeability and ϵ is the permittivity.

A solution to equation 2.2 is the electromagnetic plane wave:

$$\vec{E}(\vec{r};t) = \vec{E}_o \exp\left(\frac{i2\pi\tilde{n}}{\lambda} \vec{q} \cdot \vec{r}\right) \exp(-i\omega t) , \quad (2.3)$$

where \vec{q} is the unit vector along the direction of the propagation of the wave (\vec{r}), \tilde{n} is the complex index of refraction, ω is the angular frequency of the wave, \vec{E}_o is the complex vector constant specifying the amplitude and polarization state of the wave. \tilde{n} is given by $\tilde{n} = n + ik$: when the material is absorbing the complex part is non-zero and the amplitude of the wave decays exponentially as it propagates through the media. Materials with very large k , like metal films, are not suitable for ellipsometer measurements because the beam can penetrate only few tens of nm. To characterise the film, the beam has to penetrate all the sample film and also to come back out from the sample after reflection from the interface.

2.1.2 Polarization states

As the electric and the magnetic fields and the direction of propagation are all orthogonal to one another, it is possible to define a plane wave just with the electric field components and the propagation. The electric field vector is constituted of two components, s and p parallel and perpendicular to the surface of incidence and it can be expressed with a Jones vector which is formed by the parallel and perpendicular complex components of the electric field

$$\vec{E} = \begin{bmatrix} \tilde{E}_p \\ \tilde{E}_s \end{bmatrix}. \quad (2.4)$$

The propagating beam can be expressed by a 2×2 Jones matrix, where any optical components of the instrument or the sample change the polarization state of the wave. The matrix diagonal elements constitute by the change in amplitude Ψ and phase Δ of the p and s components of the beam. While off-diagonal elements represent the energy transfer from p to s and vice versa.

The key feature in ellipsometry is the polarization state of the light beam, which is the path that the electric field vector traces as it propagates through space and time, and it can be linear, circular and elliptical.

A linear polarization is obtained when \tilde{E} lies in one line at all times; this happens when the phase angle ϕ is identical for both component p and s ,

$$\vec{E} = \begin{bmatrix} E_p e^{i\phi} \\ E_s e^{i\phi} \end{bmatrix}. \quad (2.5)$$

Circular polarized light is obtained when the two components are $\pi/2$ out of phase. The linear and circular polarizations are just special types of elliptically polarized light, so out of these two special cases, the electric field vector will trace out an ellipse as a function of time. So ellipsometry measures Ψ and Δ by determining the polarization ellipse of the reflected beam after interaction with the sample.

2.1.3 Jones matrix analysis of the rotating analyser

What the ellipsometer actually measures is the time dependent intensity at the detector, which is proportional to the magnitude of the electric field of the beam $I_p \propto |E_p|^2$. The incident beam on the sample can be represented by the input polarizer Jones matrix (2.6), that describes the rotation of the plane of incidence axis of a P angle produced by the polariser,

$$\begin{bmatrix} \cos P & -\sin P \\ \sin P & \cos P \end{bmatrix} \begin{bmatrix} 1 \\ 0 \end{bmatrix}. \quad (2.6)$$

For an isotropic and not too rough sample is possible to define a sample Jones matrix,

$$\begin{bmatrix} \tilde{R}_p & 0 \\ 0 & \tilde{R}_s \end{bmatrix}. \quad (2.7)$$

The ratio between the two complex Fresnel reflection coefficients is defined by the parameter $\tilde{\rho} = \frac{\tilde{R}_p}{\tilde{R}_s}$, which is also expressed in terms of the real values Δ and Ψ (equation 2.1). From equation 2.1 $\tan \Psi \propto \tilde{\rho}$. While Δ represents the phase difference between the p - and s -refraction coefficients, as the two components are reflected out of phase from the sample.

2.1.4 Refraction in bulk material

Considering an optically thick sample it is important to calculate the Fresnel reflection coefficients of the sample. From their ratio, $\tilde{\rho}$ it is possible to calculate the value of Δ and Ψ :

$$\tan \Psi e^{i\Delta} \equiv \tilde{\rho}. \quad (2.8)$$

Writing down the relation between incident, reflected and transmitted beams in matrix form,

$$\begin{bmatrix} \tilde{E}_p \\ \tilde{E}_s \end{bmatrix}^{reflected} = \begin{bmatrix} \tilde{r}_p & 0 \\ 0 & \tilde{r}_s \end{bmatrix} \begin{bmatrix} \tilde{E}_p \\ \tilde{E}_s \end{bmatrix}^{incident}$$

$$\begin{bmatrix} \tilde{E}_p \\ \tilde{E}_s \end{bmatrix}^{transmitted} = \begin{bmatrix} \tilde{t}_p & 0 \\ 0 & \tilde{t}_s \end{bmatrix} \begin{bmatrix} \tilde{E}_p \\ \tilde{E}_s \end{bmatrix}^{incident}$$

it is possible to obtain the equations that define the Fresnel reflection/transmission coefficients,

$$\tilde{r}_p = \frac{\tilde{E}_p^{reflected}}{\tilde{E}_p^{incident}}, \quad (2.9)$$

$$\tilde{r}_s = \frac{\tilde{E}_s^{reflected}}{\tilde{E}_s^{incident}}, \quad (2.10)$$

$$\tilde{t}_p = \frac{\tilde{E}_p^{transmitted}}{\tilde{E}_p^{incident}} \quad \text{and} \quad (2.11)$$

$$\tilde{t}_s = \frac{\tilde{E}_s^{transmitted}}{\tilde{E}_s^{incident}}. \quad (2.12)$$

It is now possible to write the p and s components of the incident, reflected and transmitted electromagnetic waves as follows:

$$\vec{E}_{p,s}^{incident}(\vec{r}, t) = \tilde{E}_{0p,s}^{incident} \exp\left(\frac{i2\pi\tilde{n}_0}{\lambda} \hat{q}_{incident} \cdot \vec{r}\right) \exp(-i\omega t), \quad (2.13)$$

$$\vec{E}_{p,s}^{reflected}(\vec{r}, t) = \tilde{E}_{0p,s}^{reflected} \exp\left(\frac{i2\pi\tilde{n}_0}{\lambda} \hat{q}_{reflected} \cdot \vec{r}\right) \exp(-i\omega t), \quad (2.14)$$

$$\vec{E}_{p,s}^{transmitted}(\vec{r}, t) = \tilde{E}_{0p,s}^{transmitted} \exp\left(\frac{i2\pi\tilde{n}_0}{\lambda} \hat{q}_{transmitted} \cdot \vec{r}\right) \exp(-i\omega t). \quad (2.15)$$

Substituting these expression into the Fresnel coefficients and requiring the phase quantities to be identical at all points on the interface, it is possible to conclude three useful points:

1. the reflection angle must be equal to the angle of incidence: the reflection beam will be specular,

2. from the phase identity we obtain Snell's law, $\tilde{n}_0 \sin \phi_0 = \tilde{n}_1 \sin \phi_1$, where $_0$ corresponds to the incident beam and $_1$ to the refracted/transmitted beam in the sample.

3. If $k = 0$ (the sample is absorbing), \tilde{n}_1 is complex and $\tilde{\phi}_1$ will be complex as well.

From these conclusions the Fresnel reflection and transmission coefficients can be defined as,

$$\tilde{r}_p = \frac{\tilde{n}_1 \cos \phi_0 - \tilde{n}_0 \cos \tilde{\phi}_1}{\tilde{n}_1 \cos \phi_0 + \tilde{n}_0 \cos \tilde{\phi}_1}, \quad (2.16)$$

$$\tilde{r}_s = \frac{\tilde{n}_0 \cos \phi_0 - \tilde{n}_1 \cos \tilde{\phi}_1}{\tilde{n}_0 \cos \phi_0 + \tilde{n}_1 \cos \tilde{\phi}_1}, \quad (2.17)$$

$$\tilde{t}_p = \frac{2\tilde{n}_0 \cos \phi_0}{\tilde{n}_1 \cos \phi_0 + \tilde{n}_0 \cos \tilde{\phi}_1} \quad \text{and} \quad (2.18)$$

$$\tilde{t}_s = \frac{2\tilde{n}_0 \cos \phi_0}{\tilde{n}_0 \cos \phi_0 + \tilde{n}_1 \cos \tilde{\phi}_1}. \quad (2.19)$$

Inserting equations 2.16 and 2.17 into the equation 2.8 it is possible to evaluate Δ and Ψ for bulk samples.

2.1.5 Single films on thick substrates

One then needs to find an analytical solution for the particular case treated in this thesis: a semi-transparent film on a thick substrate. An incident beam will be split in a reflected and a transmitted beam from the surface of the sample film; the transmitted part will reach the substrate interface and reflected again to the air-sample interface which will bounce it back towards the substrate interface. Ideally an infinite number of reflection and transmitted beams will occur, the splitting of the beam at each reflection quickly reduces the amplitude of the wave, until it dies out (the attenuation is accelerated of course by the absorbance of the film, which is generally non-zero).

It is useful to define the Fresnel reflection coefficients, in order to treat the $-s$ and $-p$ polarized incident beams independently, so that any incident beam can be described as a linear combination of the $-p$ and $-s$ polarization states, and it simplifies the nomenclature without adding the labels s and p to the coefficients. For example, \tilde{r}_{01} will be a coefficient of reflection for an incident beam coming from the medium 0 (air) and hitting the film (1). As a consequence, \tilde{t}_{12}

and so on.

A general form for the reflected beam can easily be written as:

$$\tilde{E}_n^{reflected} = \tilde{t}_{10}\tilde{t}_{01}(\tilde{r}_{10})^{n-2}(\tilde{r}_{12})^{n-1}e^{-i(2n-2)\beta} \quad (2.26)$$

and the sum on all the infinite reflected beams:

$$\tilde{E}_{total}^{reflected} = [\tilde{r}_{01} + \tilde{t}_{10}\tilde{t}_{01}e^{i2\beta} \sum_{n=2}^{\infty} (\tilde{r}_{10})^{n-2}(\tilde{r}_{12})^{n-2}e^{-i2n\beta}] \tilde{E}^{incident} . \quad (2.27)$$

From equations 2.16-2.19 it is possible to derive these identities:

$$\tilde{r}_{01} = -\tilde{r}_{10} \quad \text{and} \quad (2.28)$$

$$\tilde{t}_{10}\tilde{t}_{01} = 1 - \tilde{r}_{01}^2 . \quad (2.29)$$

Inserting 2.28 and 2.29 into 2.27 and evaluating the resulting convergent series, it is possible to write the equation for the total reflected beam

$$\tilde{E}_{total}^{reflected} = \left(\frac{\tilde{r}_{01} + \tilde{r}_{12}e^{-i2\beta}}{1 + \tilde{r}_{01}\tilde{r}_{12}e^{-i2\beta}} \right) \tilde{E}^{incident} \quad (2.30)$$

which is valid for $-s$ and $-p$ polarized beams.

Now there are the tools to define the “pseudo” Fresnel reflection coefficients for any arbitrary sample. If the p - polarised Fresnel coefficients are used for the evaluation of 2.30, it is possible to obtain the p - polarised pseudo Fresnel reflection coefficient \tilde{R}_p :

$$\tilde{R}_p = \frac{\tilde{E}_{total}^{reflected}}{\tilde{E}^{incident}} = \frac{\tilde{r}_{01} + \tilde{r}_{12}e^{-i2\beta}}{1 + \tilde{r}_{01}\tilde{r}_{12}e^{-i2\beta}} \quad (2.31)$$

and it will be similar for the s - polarised case.

The reflection coefficients are called “pseudo” because the material optical properties resulting from an ellipsometry experiment are quantitatively valid only if the sample does not

have:

- a surface oxide layer,
- any surface roughness,
- or any other films or overlayer.

Since these assumptions are rarely met, the term “pseudo” is used to describe reflection coefficients derived by these analytical transformations.

It is possible now to see how to derive Ψ and Δ for a sample exhibiting pseudo Fresnel $-p$ and $-s$ polarised reflection coefficients:

$$\tilde{\rho} = \tan \Psi e^{i\Delta} = \frac{\tilde{R}_p}{\tilde{R}_s}. \quad (2.32)$$

Summarising the steps to calculate Ψ and Δ for a thin film:

1. Calculate the phase thickness of the film (β) with equation 2.21.
2. Calculate the $-p$ and $-s$ plane reflection coefficients for a beam incident on the film from the ambient using 2.16 and 2.17.

$$r_{01}^p = \frac{n_1 \cos \phi_0 - n_0 \cos \phi_1}{n_0 \cos \phi_1 + n_1 \cos \phi_0}, \quad r_{01}^s = \frac{n_0 \cos \phi_0 - n_1 \cos \phi_1}{n_0 \cos \phi_0 + n_1 \cos \phi_1} \quad (2.33)$$

3. Calculate the $-p$ and $-s$ plane reflection coefficients for a beam incident on the substrate from the film using 2.16 and 2.17.

$$r_{12}^p = \frac{n_2 \cos \phi_1 - n_1 \cos \phi_2}{n_1 \cos \phi_2 + n_2 \cos \phi_1}, \quad r_{12}^s = \frac{n_1 \cos \phi_1 - n_2 \cos \phi_2}{n_1 \cos \phi_1 + n_2 \cos \phi_2} \quad (2.34)$$

4. Calculate the $-p$ and $-s$ polarized pseudo-reflection coefficient for the sample from equation 2.31 using the interfacial reflection coefficients calculated in steps 2 and 3.
5. Obtain Ψ and Δ from the $-p$ and $-s$ polarized pseudo-reflection coefficients via equation 2.32.

2.1.6 Optical constants and the Cauchy model

For any angle of incidence between 0° and 90° , the two components p - and s - will be reflected differently, originating an elliptically polarized beam with the Fresnel coefficients $R_p \neq R_s$ (as in figure 2.2).

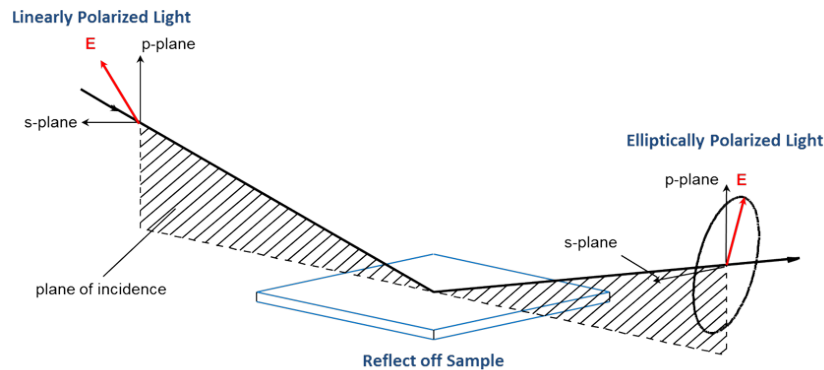


Figure 2.2: Schematic diagram of an ellipsometry experiment. The linearly polarised beam is reflected from the sample becoming elliptically polarised. [112]

The term Spectroscopic Ellipsometry refers to the use of multiple wavelengths of light. The Fresnel coefficients vary with λ , which makes Ψ and Δ change across the spectrum, so ellipsometry requires an accurate model of the measurement process to analyse the measured data. The key components of all ellipsometric models are the optical constants (refractive index and extinction coefficient) of the substrate and sample layers and the thicknesses of the layers. To obtain good model fits to the measured data, the optical constants are required to be highly accurate. It is a good technique to measure optical constants of materials and they are expressed as a complex dielectric function, $\varepsilon = \varepsilon_1 + i\varepsilon_2$ or as a complex refractive index, $\tilde{n} = n + ik = \sqrt{\varepsilon}$.

Spectroscopic ellipsometry has an iterative history: first, simple samples are measured and optical constants are obtained from the data. Then these optical constant are used in modelling more complicated samples that in turn yield optical constants for additional materials. In this way a large base of optical constants has been accumulated. So most optical constants are tabulated as wavelength functions and there is a causality relationship between the real and imaginary part, the Kramers-Kronig relationship. What is tabulated for the materials is the

dispersion relation $n(\lambda)$. If the explicit knowledge of $n(\lambda)$ is not available, it is possible to use a mathematical approximation, the Cauchy equation. [113]

$$n(\lambda) = A_n + \frac{B_n}{\lambda^2} + \frac{C_n}{\lambda^4} \quad (2.35)$$

A_n , B_n and C_n are called ‘‘Cauchy coefficients’’. A_n is dimensionless and represents the refractive index as $\lambda \rightarrow \infty$, B_n and C_n have units of nm^{-2} and nm^{-4} respectively. So Ψ and Δ are directly measured. Film thickness and refractive index calculated from Ψ and Δ using a model fitting that matches the actual configuration of the sample and the experiment. Validity and accuracy can be assessed by the goodness of fit of a model to the experimental set-up.

The model is based on tabulated refractive indexes of PCDTBT and the Si substrate and the incident angles between N_2 and PCDTBT ϕ_0 , between PCDTBT and Si wafer ϕ_1 . Using equations 2.33 and 2.34 is possible to calculate Ψ_{mod} and Δ_{mod} that are compared to Ψ_{exp} and Δ_{exp} measured by the instrument and a Mean Squared Error (MSE) calculated:

$$\chi^2 = (\Psi_{exp} - \Psi_{mod})^2 + (\Delta_{exp} - \Delta_{mod})^2 \quad (2.36)$$

$$\text{MSE} = \frac{1}{2N - M} \sum_{i=1}^N \left[\left(\frac{\Psi_i^{mod} - \Psi_i^{exp}}{\sigma_{\Psi_j}^{exp}} \right)^2 + \left(\frac{\Delta_i^{mod} - \Delta_i^{exp}}{\sigma_{\Delta_j}^{exp}} \right)^2 \right]. \quad (2.37)$$

Here, N is the number of measured points, M the number of parameters, and σ the standard deviation. The calculation is iterative until a minimum value of χ or MSE is reached, changing the values for the refractive index n and the film thickness d of the model, that will then be the value closest to the real n and d of the PCDTBT film.

2.1.7 Ellipsometry components and sample configuration

The ellipsometer used during this PhD was a J. A. Woollam M-2000V using a rotating compensator that illuminates the sample with light of a constantly varying polarisation state. Incidence and reflection angles were fixed at 65° and the range of wavelengths between 370 nm and 1000

nm.

There are different kind of ellipsometry configurations and the one with a rotating compensator after the polariser offers different advantages with respect to the rotating polariser or rotating analyser ellipsometry. It offers an accurate measurement of Ψ and Δ over the complete range of wavelength, with equal sensitivity, $\Psi=0-90^\circ$ and $\Delta=0-360^\circ$. There is no residual polarisation in input due to a fixed polariser, or in output due to a fixed analyser. The rotating compensator offers then the possibility of measuring depolarisation effects.

The light source used was a 50W quartz tungsten halogen lamp (QTH). A polariser (calcite or quartz crystal) after the QTH lamp converts the light beam into linearly polarised light oriented along the transmitting axis. Between the polariser and the sample there is then the compensator that introduces a phase delay converting the linearly polarised into circularly polarised light. The compensator is made of thin plates of birefringent material or polished crystals which ideally have a retardation of exactly 90° (1/4 wave). Compensators can then distinguish unpolarised from circular polarisations.

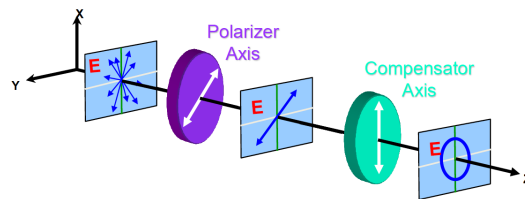


Figure 2.3: The polariser linearly polarise the light coming from the QTH lamp and the rotating compensator introduces a phase delay of 90° producing a circularly polarised light. [111]

The sample (PCDTBT film spin-cast onto Si wafer) was positioned on a Linkam stage. The sample is covered by a metal cell with two transparent windows for the incident and refracted beams. The cell was used in order to create an inert N_2 atmosphere around the sample. The nitrogen is sucked into the cell by the Linkam stage attached to a liquid nitrogen dewar and a pump (figure 2.4).

This is the configuration of the instrument used during this PhD:

QTH lamp \Rightarrow Polariser \Rightarrow Rotating Compensator \Rightarrow Sample \Rightarrow Analyser \Rightarrow Detector.

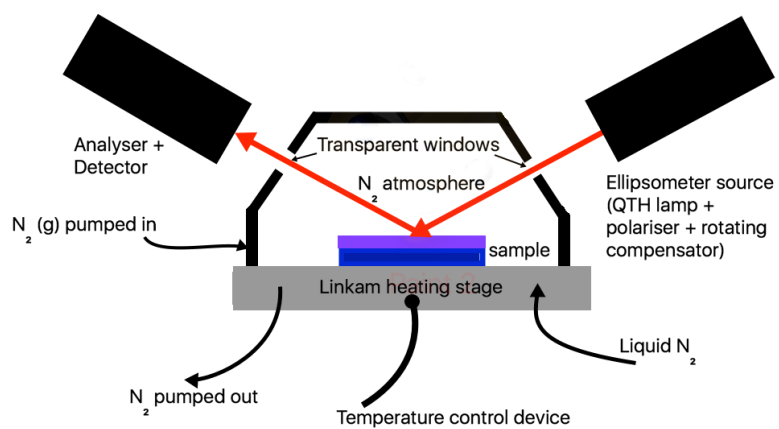


Figure 2.4: Schematic diagram of the ellipsometry experimental setup.

2.2 AFM - Atomic Force Microscopy

PCDTBT is a low crystallinity material and a method able to provide an analysis in the 100 nm - 1 μm size range was necessary. Atomic force microscopy (AFM) has a good resolution of nanoscale features, being similar to the resolution of electron microscopy [24]. One characteristic that is not possible to measure with electron microscopy is the precise height of a sample surface, which on the other hand is possible with AFM. This is why AFM is often used to analyse the crystallinity in polymer materials.

In an AFM experiment a nm scale tip is mounted on a flexible cantilever with a typical spring constant of 0.1 to few tens of Nm^{-1} . [85]

There are three imaging modes in AFM: contact, tapping and non-contact mode. The tapping mode is the one adopted in this study because of its non-destructive and high resolution nature.

In tapping mode the cantilever oscillates up and down near its resonance frequency. The

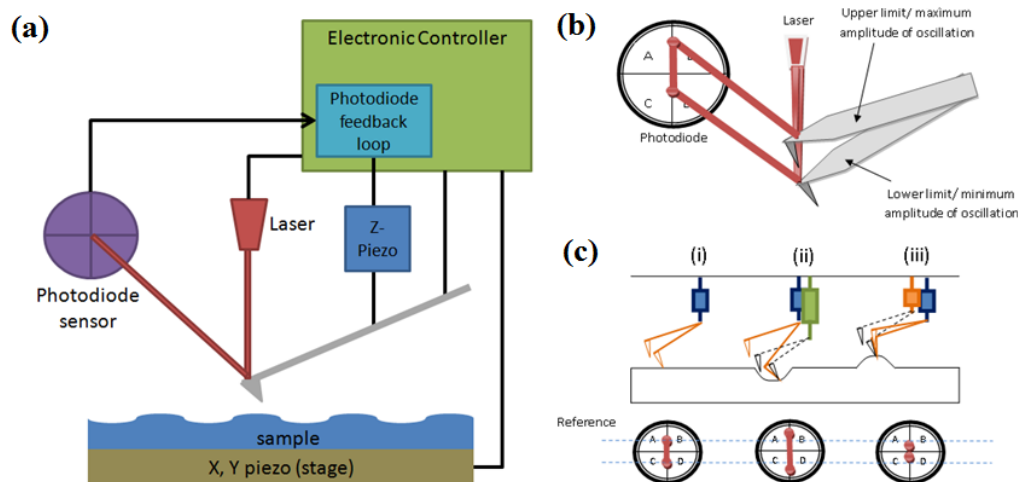


Figure 2.5: (a) Schematic representation of atomic force microscopy in tapping mode. (b) Cantilever deflection and feedback system through a laser reflected on the cantilever. (c) Schematic representation of the relation of the surface morphology with the cantilever oscillations. [114]

vertical oscillation is imposed by a small piezo-electric element in the cantilever holder. The amplitude of the oscillation is usually from several nm to 200 nm. The frequency and amplitude of the driving signal are kept constant, producing a constant amplitude of the cantilever oscillation as long as there is no interaction with the surface. The tip does not touch the surface of the sample, but long-range weak forces (Van der Waals, dipole-dipole interactions, electrostatic

forces) act on the cantilever tip causing the oscillation amplitude of the cantilever usually to decrease. This amplitude is kept constant by a feed-back system as the cantilever is scanned over the sample. The feedback system consists of a laser reflected by the cantilever onto a four-quadrant photodiode. An AFM image is then produced from the force that the feed-back system has to use in order to keep that constant oscillation amplitude. The peak forces applied during the contacting part of the oscillation can be much higher than the ones applied in contact mode. Differently from contact mode, tapping mode generally does not damage the sample surface and the tip. This because the applied force in tapping mode is of very short duration and the lateral forces between tip and sample are significantly lower in tapping mode, compared to contact mode.

The tip can be scanned in the horizontal plane using two additional piezo-electric drivers. The quadrant photodiode detects the the displacement of the tip with bending a cantilever by displacement of the reflected laser beam and translate the information to a current signal. The feedback system maintains the tip close to the surface and the centre position of the four-quadrant photodiode using highly precise piezo-electric drives during the scan. These integrated scan lines becomes a two dimensional figure indicating detailed height information of the sample surface and morphology.

In general very stiff cantilevers are used with high spring constants of about 20 to 50 N/m to ensure the cantilever does not stick to the sample. An amplitude setpoint of the cantilever may be established to be 10 nm less than the free oscillation amplitude, which may be on the order of 100 nm. Therefore, the energy in the oscillation is much higher than the energy lost striking the sample in each cycle. The oscillation amplitude changes after each cycle and is then expressed by:

$$\Delta A = (A_0 - A_s)/Q \quad (2.38)$$

where A_0 is the amplitude of the free oscillation of the amplitude and A_s the amplitude setpoint. Q is the quality factor defined as

$$Q = m\omega_0/b , \quad (2.39)$$

where m is the mass of the cantilever, ω_0 is the resonance frequency and b the damping coefficient. Usually cantilevers with high Q (100 - 1000) together with the high spring constant are employed in tapping mode to ensure the cantilever does not stick to the sample.

2.2.1 Apparatus and condition

Atomic force microscopy analysis was performed using the Digital Instruments Nanoscope III Dimension 3100 using tapping mode. The cantilevers were Bruker MPP-11100 made of Si nitrate, with resonant frequency of 300 Hz and spring constant of 40 N/m. The tip radius was under 1 Å.

The scanning frequency used was from 0.5 to 1.5 Hz and the image size from 500 nm to 10 μm . An optical microscope is incorporate into the instrument in order to focus the target position onto the sample surface.

The instrument has also a damped air suspension system in order to remove any low frequency vibrations and oscillations from the surrounding environment.

2.3 GIWAXS - Grazing Incidence Wide Angle X-ray Scattering

A branch of X-ray analysis is grazing incidence X-ray scattering, which can be split into GIWAXS and GI-SAXS. The two techniques differ from the sample-detector distance as shown in figure 2.6. In wide-angle X-ray Scattering (WAXS) the detector is close to the sample so the X-rays scattered at wide angles are detected, corresponding to sub-nanometres-sized structures. On the other hand, in small-angle X-ray scattering (SAXS) the detector is moved further away from the sample, detecting X-rays scattered at smaller angles 0.1 - 10°. SAXS is used to study for example nanoparticle size distributions and to resolve the size and shape of monodisperse macromolecules. In ordinary X-ray diffraction the signal is mainly from the substrate because of high incident angles. When the angles of incidence is very small, near the critical angle of the analysed material, there is total reflection and a strong signal from the surface of thin films.

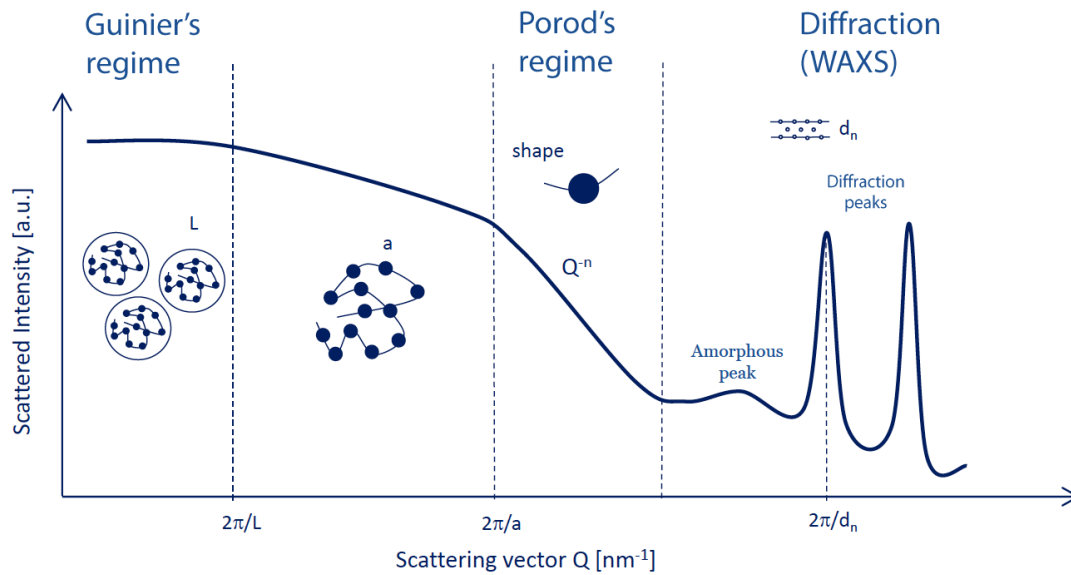


Figure 2.6: Scattering intensity in function of the scattering vector and representation of the length-scales that is possible to analyse in SAXS (larger lengthscales, 1 - 100 nm) or WAXS (shorter lengthscales, 10 - 1 Å). [115]

Polymer thin films give relatively weak X-ray scattering due to the weak scattering strength of carbon due to its low atomic number and the disorder of the films. The usual geometry used is then with the beam incident at grazing incidence. Semiconducting polymers usually give the strongest scattering in the specular direction because they form ordered layers relative to the substrate.

The difference between reflection and refraction at interfaces in the case of X-rays is related to the refractive index, which is 1 for vacuum, for visible light in glass is between 1.5 to 1.8. For X-rays it is of order of 0.99999 and can be expressed as $n = 1 - \delta + i\beta$, where $\delta \approx 10^{-5}$ in solids and 10^{-8} for air. The imaginary part β is usually much smaller than δ and for X-rays, n is smaller than unity, which implies that below a certain incident grazing angle $\alpha_{critical}$ we have total external reflection of the X-rays. This arises from Snell's law which relates the incident grazing angle α_i to the refracted angle α_r , $\cos\alpha = n\cos\alpha_r$. When the condition of total external reflection is valid, the penetration depth of the incident X-ray beam is only a few tens of Å, and the reflectivity is near unity. Naturally, as the angle is increased past the critical angle, the reflectivity decreases rapidly, while the penetration depth increases.

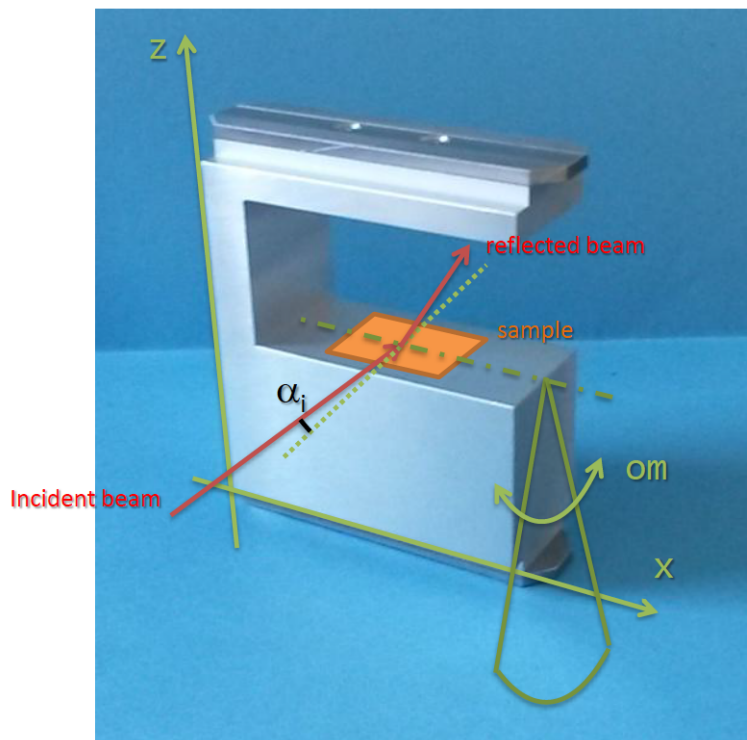


Figure 2.7: Schematic representation of the sample stage utilised on the XeuSS for the GIWAXS experiments reported in this thesis. [115]

The critical angle can be calculated using [8]

$$\alpha_c = \sqrt{\frac{2\lambda^2 r_e N_A Z}{2\pi A}}, \quad (2.40)$$

where r_e is the classical electron radius (2.814×10^{-14} nm), N_A is the Avogadro's number, Z_p the averaged atomic number and A the averaged atomic mass. There are three regimes in GIWAXS depending whether the incident angle is below, at or above the critical angle of the analysed material:

1. The evanescent regime is when the incident angle of the X-ray beam is smaller than the critical angle of the (polymer) material. The beam does not penetrate the polymer film, but there is an evanescent wave penetrating the first few nanometres of the film and revealing information at the surface. Total reflection occurs and the evanescent wave decays exponentially with distance from the surface.

With $\alpha_i < \alpha_c$ we can use this equation [8, 116] to calculate the penetration depth l .

$$l = \frac{\sqrt{2}\lambda}{4\pi} \sqrt{[(\alpha_i^2 - \alpha_c^2)^2 + (\lambda\mu_m\rho/4\pi)^2]^{-1/2} + \alpha_c^2 + \alpha_i^2} \quad (2.41)$$

- The dynamical regime is in between the critical angles of the polymer and the substrate, $\alpha_{cpol} < \alpha_i < \alpha_{cSi}$. In this regime the X-ray beam penetrates the bulk of the film and the interference between the incident X-rays and the portion of the beam reflected from the polymer-substrate interface generates a standing wave (figure 2.8). In this case it is not possible to calculate the penetration depth, but we need to solve the problem for the X-rays in a cavity. The experiment will probe then an average of the molecular structures through the whole film. [117]

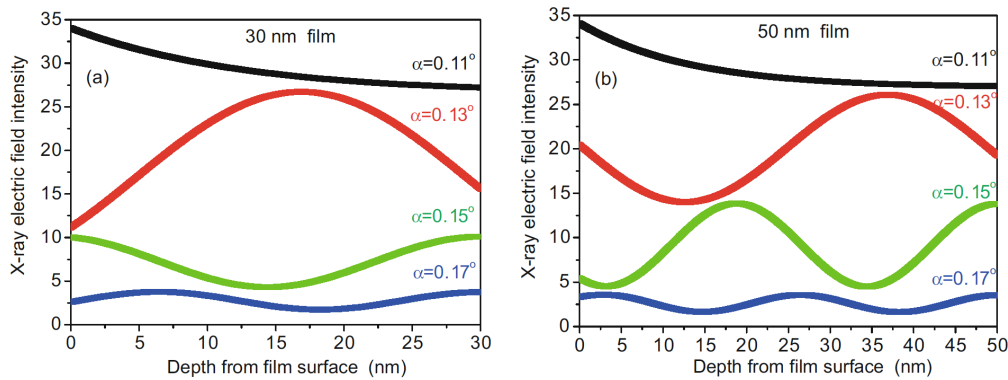


Figure 2.8: X-ray electric field intensity for incident angles above the critical angle of the polymers for two PCDTBT films, 30 nm and 50 nm thick. The plots of the electric fields represent the standing waves at different angles, produced from the interference of the incident beam with the reflected beam from the polymer-substrate interface. Figure reproduced from Wang *et al* [8].

- The kinematical regime is when the incident angle is above the critical angle of the substrate, *i.e.* $\alpha_i > \alpha_{cSi}$ and the beam can penetrate both the film and the substrate, giving information about the film and substrate.

One of the first works using Grazing Incidence X-ray diffraction (GIXRD) applied to polymer films [118] was an investigation of the near surface structures in aromatic polyimide films as function of thermal treatment and film thickness. The flat-on structure was found to be more ordered at the air surface than in the bulk, for thick films. Also Macdonald *et al.* [119] have studied the molecular ordering for different depths in thin films, varying the incidence of the

X-ray beam near the critical angle.

The other advantage of GIWAXS is that it can detect out-of-plane and in-plane orientation of the molecules, as shown in figure 2.9.

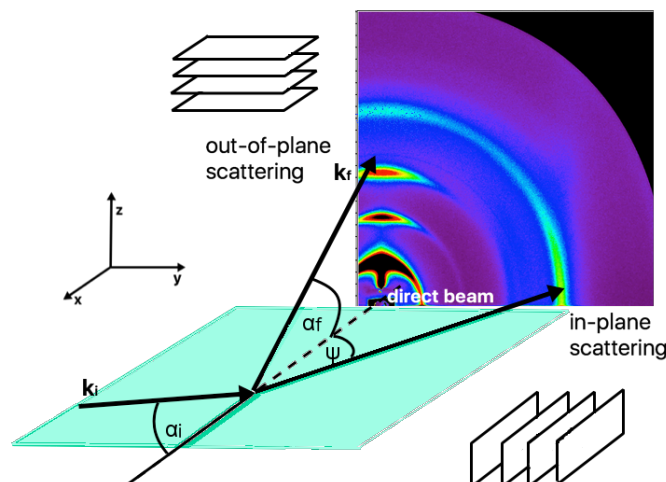


Figure 2.9: Schematic diagram of the geometry for a GIWAXS experiment. Q_z is the component of the scattering vector perpendicular to the sample surface and Q_{xy} is the component lying on the sample surface. Material features that present a periodicity which is parallel to the substrate (plane xy) will show a scattering signal in the in-plane direction. Periodicity perpendicular to the substrate (along the z axis) will show scattering in the out-of-plane direction.

2.3.1 Experimental facility, instruments and apparatus

The GIWAXS measurements reported in this thesis were taken on I07 beamline at Diamond Light Source (UK national synchrotron science facility located at the Harwell Science and Innovation Campus in Oxfordshire) and on Xeuss 2.0 SAXS/WAXS laboratory beamline in the Department of Chemistry, University of Sheffield (figure 2.10).

The beamline I07 at Diamond Light Source uses a detector Pilatus 2M with long camera lengths and the beam energy is $10.5 \text{ KeV} = 1.18 \text{ \AA}$.

The critical angle of PCDTBT for this energy is about 0.12°



Figure 2.10: Photography of the Xeuss chamber in GIWAXS mode of the instrument at the department of chemistry, University of Sheffield. [115]

The Xeuss instrument at the Department of Chemistry uses a liquid gallium MetalJet (Excillum) X-ray source (9.2 keV, 1.34 Å). The detector is a hybrid photon counting (HPC) Pilatus3R 1M with cadmium telluride sensors. The critical angle of PCDTBT for this energy is about 0.14°

Chapter 3

Sample preparation and methodologies

3.1 Introduction

As it was emphasised in the introductory chapter, the aim of this thesis is to have a better understanding of how PCDTBT crystallises. What is already known has been described in the first chapter: PCDTBT presents two ways of ordering: lamellar packing responsible for the 1st scattering peak at around 0.31 \AA^{-1} and π - π stacking responsible for the 2nd scattering peak at about 1.53 \AA^{-1} . It is not very clear how sample thickness and different annealing temperatures influence the weak, although existing crystallisation, of this polymer.

To study the crystallisation mechanism, the polymer needs to be completely amorphous at the beginning of the study, this is because any residual crystallinity would promote further crystal growth and perhaps change the kinetics, making the study not very accurate. The ideal starting state of the samples should be in an equilibrium melt-like configuration, although the spin-coating process produces films that are far from equilibrium. The spin-coating process produces some chain alignment (shown later in this chapter) that constitutes the driving force for further ordering.

The easiest way to make the system amorphous is to heat up the polymer at or just above its melting temperature (but before it degrades), and cool it down fast enough so that the chains do not have the time to crystallise.

There is the need to know the T_m of PCDTBT, and at what temperature it starts degrading, so

it is sure that it melts, but not degrade. Once the polymer is amorphous, it will be possible to study the crystallisation mechanism and so the second task is to choose the right temperature to anneal the polymer so it crystallises.

What is the right temperature? There will be a temperature between T_g and T_m where the crystallisation rate is maximum, as explained in Chapter 1 (figure 1.23), showing the bell-shaped curve of the rate as a function of the temperature. Starting from there, then the study can proceed at different temperatures (as will be covered in Chapter 4) so to have a complete understanding of the crystallisation rate in function of the annealing temperature. But there is the need to check that each step of the thermal protocol does its job, and this is the purpose of this chapter, *i.e.* to analyse the effect of each thermal step by ellipsometry, AFM and GIWAXS, that are the three suitable techniques that has been chosen for the reasons explained in chapter 2. Once the consequences of the thermal protocol on the material are clear, it will be possible to have a better knowledge of PCDTBT and more importantly to proceed towards the understanding of the influence of different annealing temperatures and the thickness on the crystallisation of the material.

3.2 Polymer solution and spin coating

PCDTBT was synthesized by Ossila; it was in the form of dark brown crystals with a purple colour. The crystals were then weighed, dissolved in chlorobenzene (CB) and left at circa 75°C for 12 hours for complete dissolution. The solution, left to cool, was then spin coated onto clean Si/SiO_x wafers. The range of PCDTBT thicknesses used in this thesis was from 5 to 300 nm, corresponding to 2 - 30 mg of polymer per litre of CB.

A film was made spin-coating the relevant solution at 2000 rpm for 60 s. All the films had to be prepared with the same spin-coating speed and same drying time of 60 s in order to minimize the factors that could influence the crystallisation of the polymer, as the film starts to crystallise upon drying on the substrate [120]. The concentration of the solution was the only parameter used to control the film thickness.

3.3 Thermal protocol

In order to study polymer ordering, there is the need to eliminate any form of order that has been induced by the spin-coating process. The method to do so is to melt and quench the polymer fast enough in order to prevent crystallisation. The crystallisation of PCDTBT has been described in Chapter 1, and as it is possible to notice from the literature, it does not present a large crystalline phase, Cho et al. [71] stated that the polymer is amorphous when casted and remain amorphous after annealing at high temperatures. Another research group [72] was able to observe the melting and crystallisation peaks with DSC, and declared that the polymer melts to a liquid crystalline state at around 268°C and recrystallises at around 259°C which has been verified with polarized light microscopy. The DSC I have done on the PCDTBT I used (figure 3.1) does not present any sign of crystallisation, but the presence of liquid-crystal structures observed from Blouin et al. [72] cannot be excluded.

In this other work [75] a $T_m = 250^\circ\text{C}$ was reported. Anyway the melting process occurs in a

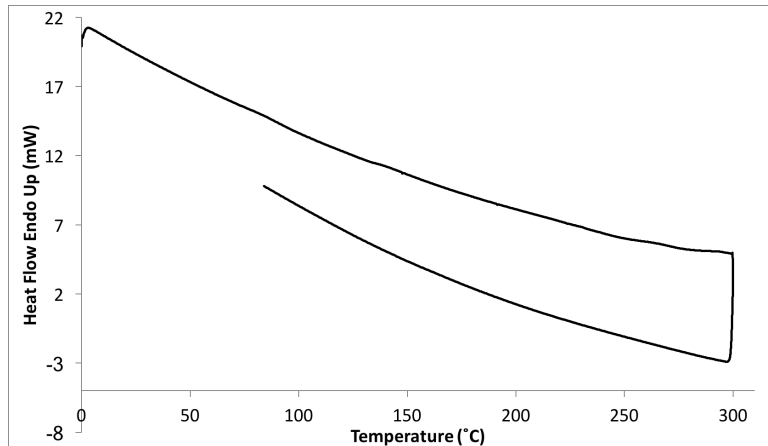


Figure 3.1: Differential Scanning Calorimetry of PCDTBT. No crystallisation peaks are observed.

window of temperatures as it depends from the size of the crystals that are melting. Other factor that influences T_m is the confinement, which reduces the value of T_m , as reported elsewhere [97, 121–125].

An easy way to measure T_m was to use ellipsometry, measuring the thermal expansivity of the material. This method has already been used to determine the glass transition temperature T_g [8, 126] and T_m [123]. The latter, which is a first order transition, has been measured for the first time by Kim *et al* [121] and later by others, such as [123] where they confirmed the

fact that confinement in thinner films reduces the melting temperature of the polymer.

In figure 3.2, it is possible to see the change in expansivity between the glass and the viscoelastic

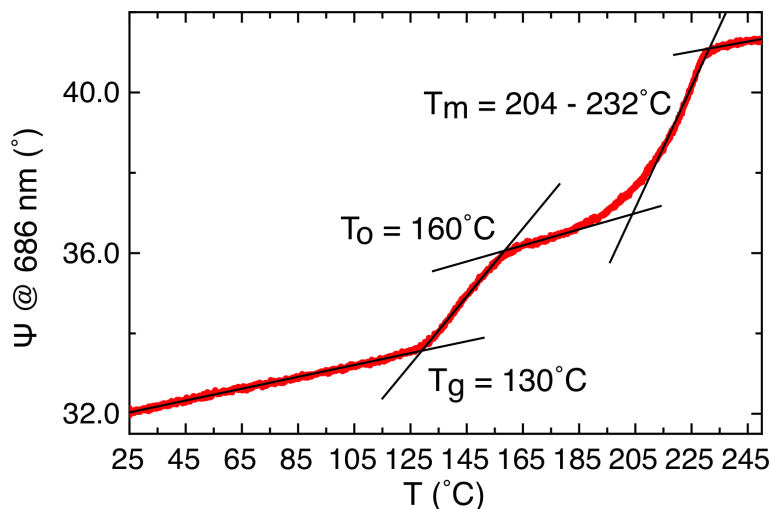


Figure 3.2: Ellipsometry experiment heating up a 68 nm film from 25°C to 310°C at 5°C/min. It is possible to recognise the glass transition, T_g , the shoulder where the polymer presumably tends to order spontaneously, at the temperature T_o (it will be explained in chapter 4) and the shoulder corresponding to the melting point.

phase. Then the film expands again until T_o is reached, where presumably the polymer starts to shrink because it reaches its crystallisation temperature: the chains have acquired enough kinetic energy to start the ordering process, resulting in a phase of higher density.

The crystallisation would continue if the system were left at the optimal temperature (optimal kinetics). Although, as the temperature increases, the film expands, but a little more slowly, because the ordering of the polymer constitutes a driving force in the opposite direction (tends to shrink). The slope of the curve in figure 3.2, dictated by T_o , starts changing when T_m is reached. Ideally, the melting point, as a first order transition, would look like the enthalpy graph in figure 3.3, as the latent heat given to the system is used exclusively for melting. After all is melted, the system keeps absorbing heat, increasing faster, as the heat capacity of the melted state is greater than the heat capacity of the crystalline state.

The transition in the case of a polymer, does not look like a jump, but it is more smeared out because there is a range of crystal thicknesses, that melt at different temperatures. Thus, we can see the melting occurs in the interval 204°C - 232°C.

From the graph in figure 3.2, $T_g = 130^\circ\text{C}$, in agreement with the literature [8, 71–73] and the TGA analysis in figure 3.5 shows that the degradation starts at around 290°C.

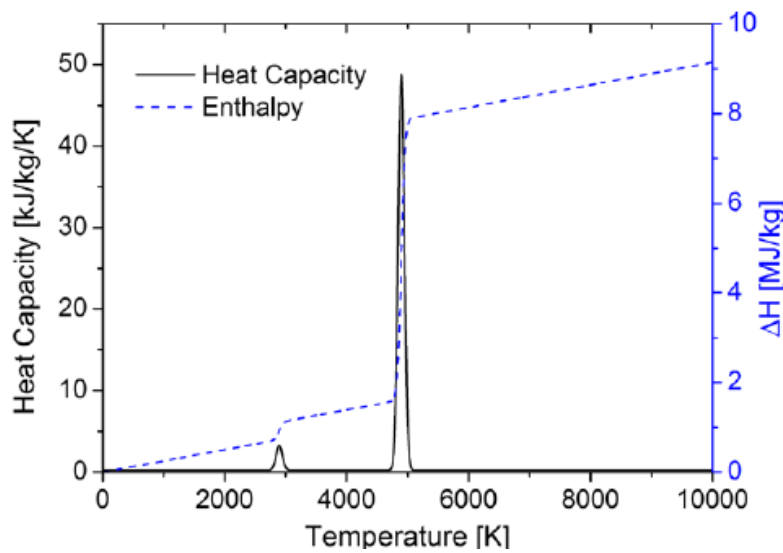


Figure 3.3: Heat capacity and enthalpy vs. temperature. The latent heat for melting and evaporation is modeled by a Gaussian distribution.

In the light of these results, it is possible to define a temperature of 250°C for the melting-quenching procedure, in order to be sure to melt all the crystals. 250°C is also slightly above the range that has been verified with ellipsometry (figure 3.2), and in agreement with the literature [75]. It is better to do not go too near 290°C because that is where the degradation processes starts (figure 3.5).

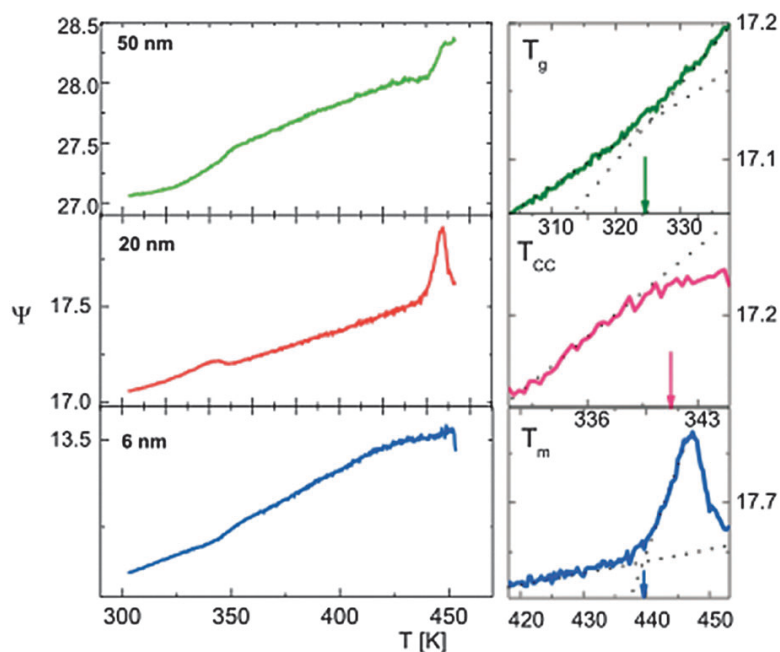


Figure 3.4: Glass transition, crystallisation and melting for PLLA films. Right panels: an example of the determination of the phase transition temperatures. Reproduced from [123] with permission of The Royal Society of Chemistry.

3.3.1 Melting and quenching

As already mentioned at the beginning of section 3.3, the thermal protocol consisted of heating the sample at 250°C under nitrogen atmosphere for 4-5 min and then dipping it into liquid nitrogen for a rapid cooling. After this stage the film was usually much thicker than before because the amorphous phase is much less dense than the crystalline phase.

The validity of this protocol can only be confirmed after having analysed the results presented in this chapter.

3.3.2 Ellipsometry isotherms

In order to analyse the ordering process of PCDTBT, it has to be in its visco-elastic state, so above T_g (130°C) and below T_m (250°C). Taking as an example a sample heated up to 200°C (figure 3.6), the film will expand as the temperature rises from 25°C, until a certain temperature is reached: in the example in figure 3.6 this temperature is 176°C. At this point a driving force brings the polymer film to shrink while the temperature is still increasing. It could possibly be a crystallisation peak: the chains have acquired enough kinetic energy and space to be able to

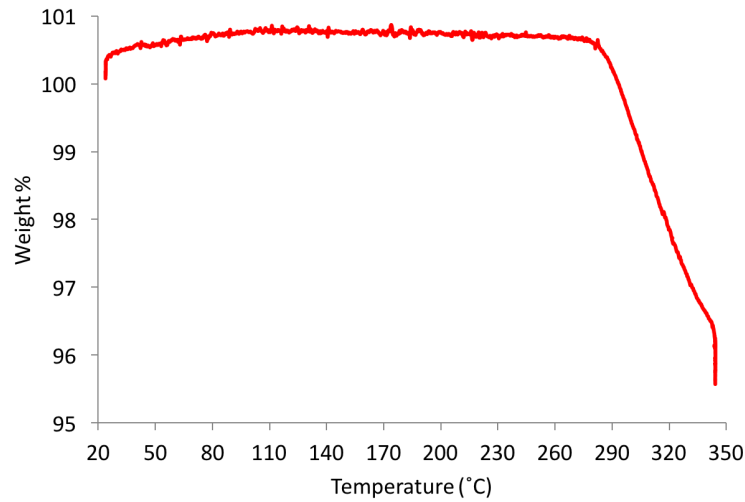


Figure 3.5: Thermal Gravimetric Analysis for PCDTBT.

attain a better order, which produce this jump in thickness. The phenomenon will be anyway verified in the course of this thesis.

The ellipsometry experiment shown in figure 3.6, consists of five parts:

1. the initial flat part at 25°C
2. the 90°C/min heating that corresponds to an expansion in thickness of the polymer film;
3. the isotherm part: the film is heated up to a temperature T_i (temperature of the isotherm or annealing temperature), 200°C in this case) which is $T_m < T_i < T_g$ and that correspond to the point of maximum expansion of the film. Most of the time, as already said, this T_i is not reached and the polymer starts shrinking at a temperature T_o (176°C in this case). This sudden shrinking is in some cases followed by a slow expansion (as in this example);
4. a fast cooling from T_i to 25°C;
5. a final flat part at 25°C.

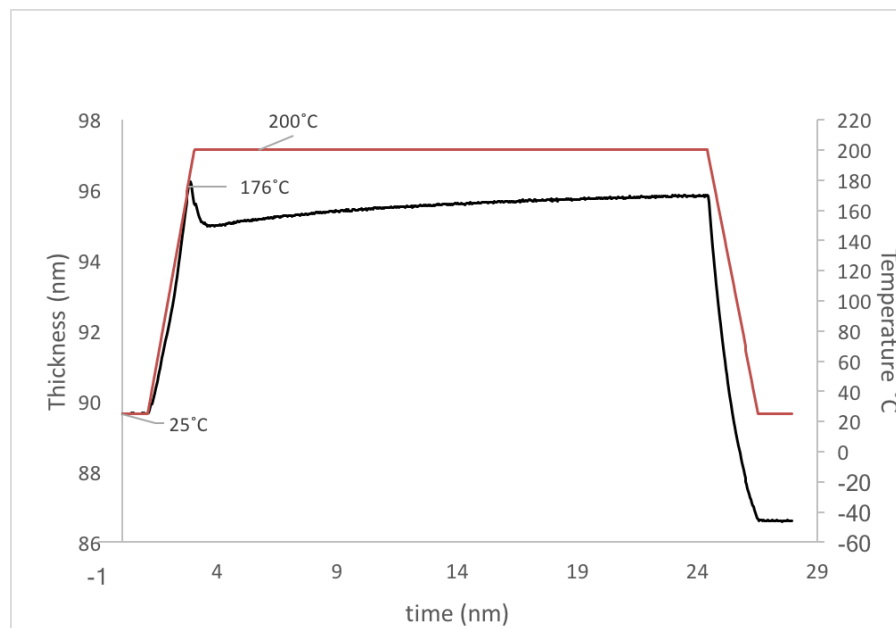


Figure 3.6: Thickness profile (black line) of a PCDTBT film as a function of time, measured by ellipsometry. The temperature profile is represented by the red line. The difference in thickness between the beginning and the end of the experiment is due to the polymer molecules reorganising during the isothermal annealing and packing in a different conformation that occupies less space.

3.4 Effect of annealing on the surface morphology - Atomic Force Microscopy

Analysing the samples with AFM made it possible to see that very thin films did not show as much difference after each thermal treatment as the thicker ones. In figures 3.8, 3.9, 3.10 and 3.11 AFM images for different film thicknesses, respectively 8 nm, 40 nm, 85 nm and 200 nm, are shown. For each thickness the AFM analysis has been made on an as cast film, on a film after the melting-quenching at 250°C and on a film after the isotherm at 180°C. The different thicknesses are reported because they have an additional effect on the surface morphology together with the thermal treatment. What is happening throughout the entire film thickness has clear repercussions on the surface morphology of the sample. The plots on the right handside are the roughness profiles of the corresponding height image, with the root mean squared roughness stated (RMS).

Figures 3.8c, 3.9c, 3.10c and 3.11c are for samples taken after the isothermal annealing procedure and are all taken at similar times, after 20 - 40 min of annealing at 180°C, always past the shrinking peak seen at ellipsometry (figure 3.6) and reached the lowest point in thickness.

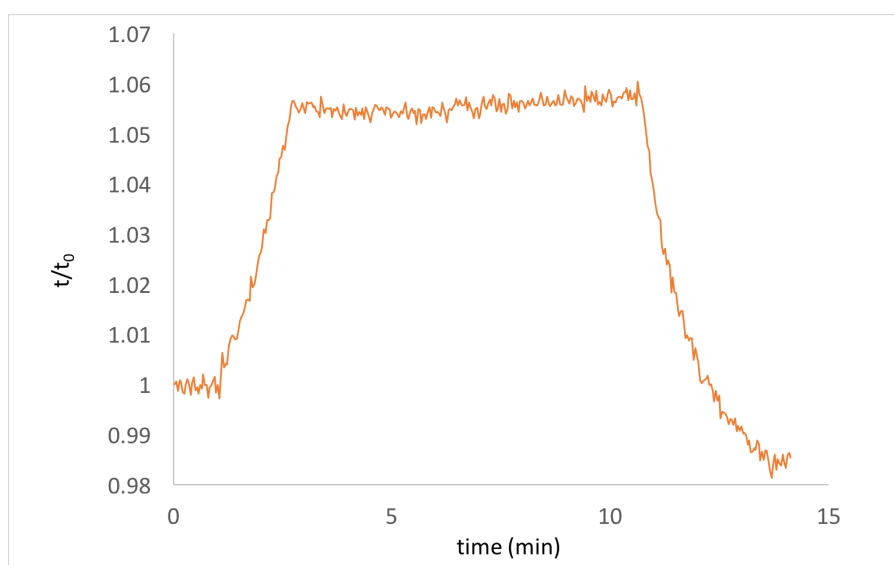


Figure 3.7: Thickness profile of the 8 nm PCDTBT film annealed at 180°C, after melting and quenching at 250°C.

The very thin film, 8 nm, presents very small features, 0.1 μm wide (figure 3.8a), which are slightly increasing after the melting-quenching procedure (figure 3.8b) and then after the isotherm (figure 3.8c). But the difference between the three samples is not very evident, as the ellipsometry curve in figure 3.7 suggests.

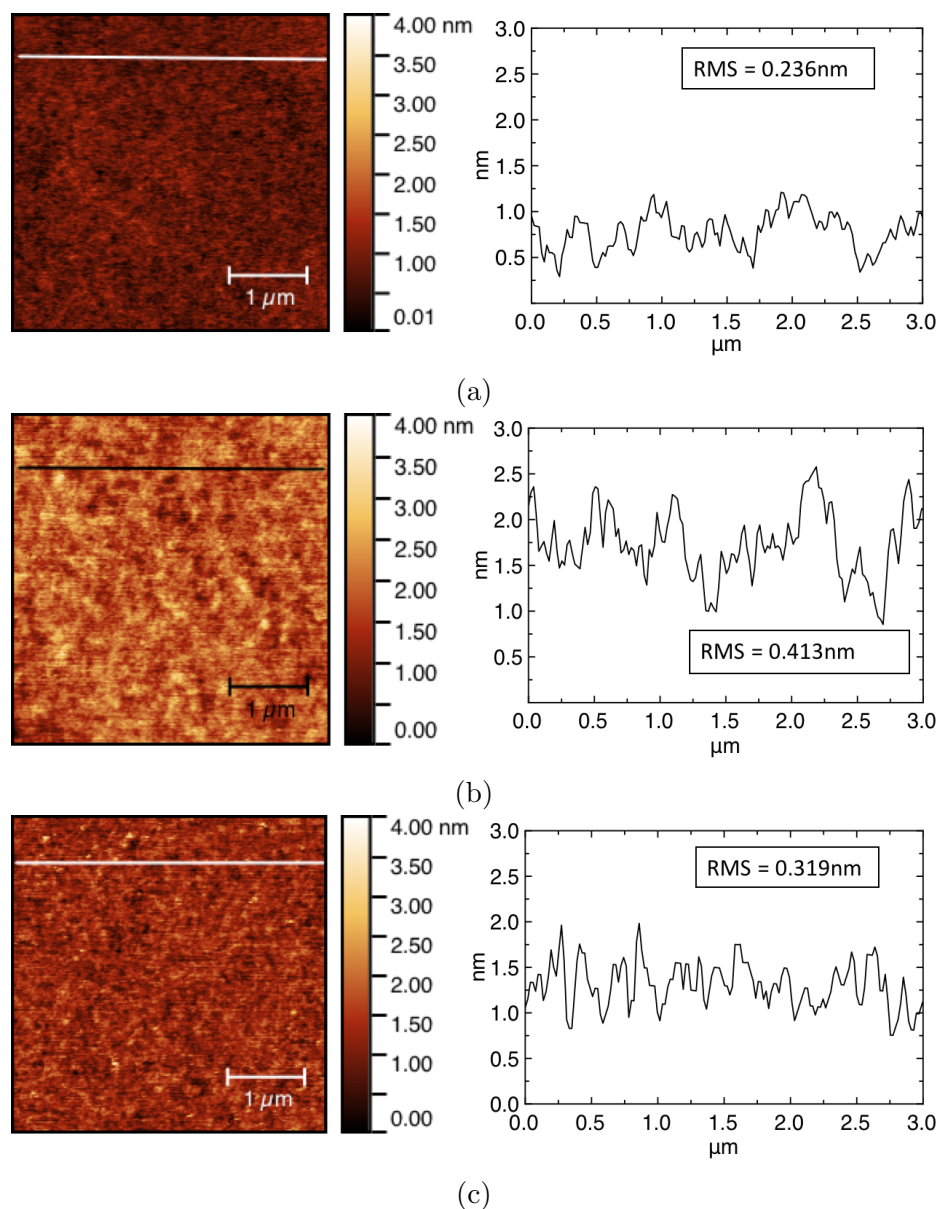


Figure 3.8: Height images for a 8 nm film of PCDTBT as cast (a), after melting-quenching at 250°C (b), and after an isotherm at 180°C (c).

Increasing the thickness to 40 nm, it is possible to notice a more defined difference between the as cast (figure 3.9a) and annealed samples (figure 3.9b and c). Very small textures for the as-cast and then the melting-quenching increases the size and the definition of the texture, which becomes larger after leaving the film at 180°C for an hour.

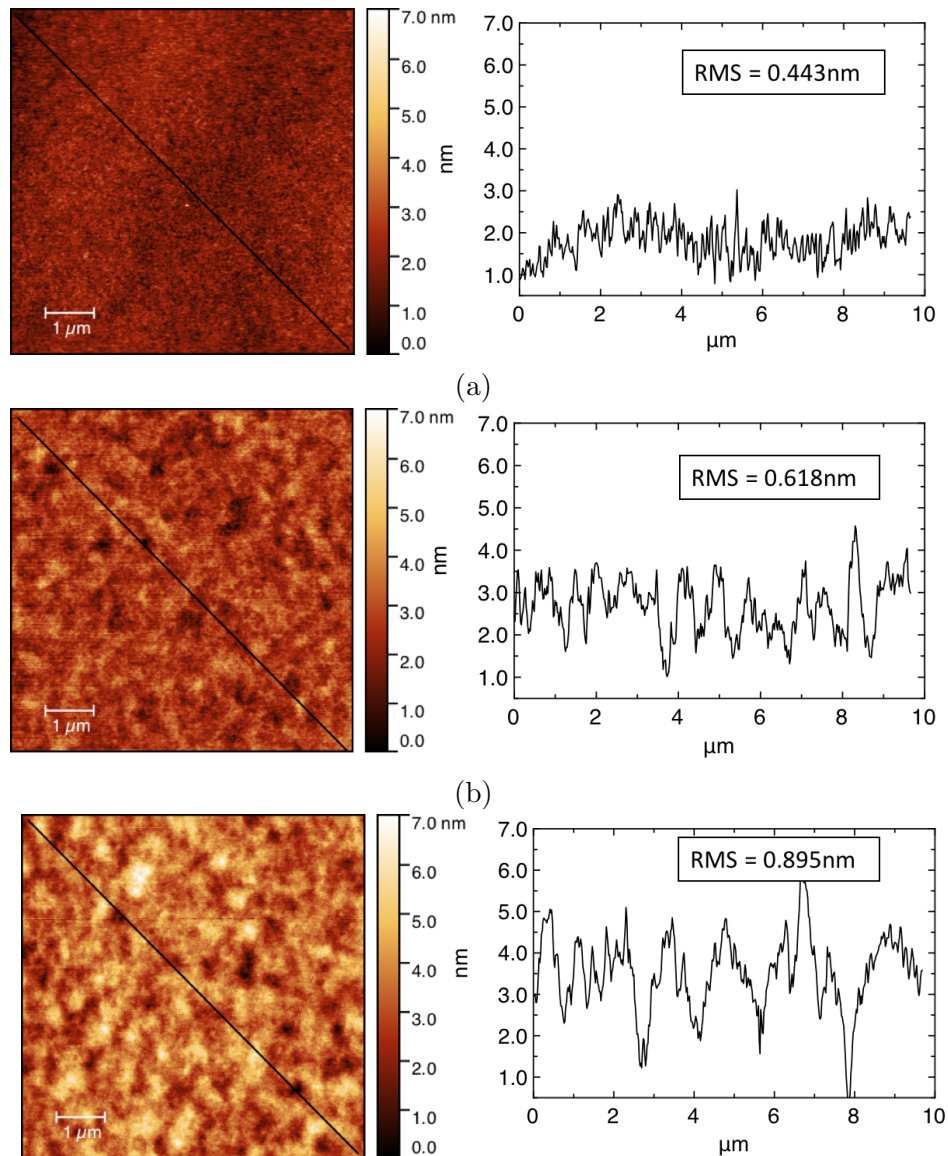


Figure 3.9: Height images for 40 nm PCDTBT films, as cast (a), after melting-quenching at 250°C (b) and after an isotherm at 180°C (c).

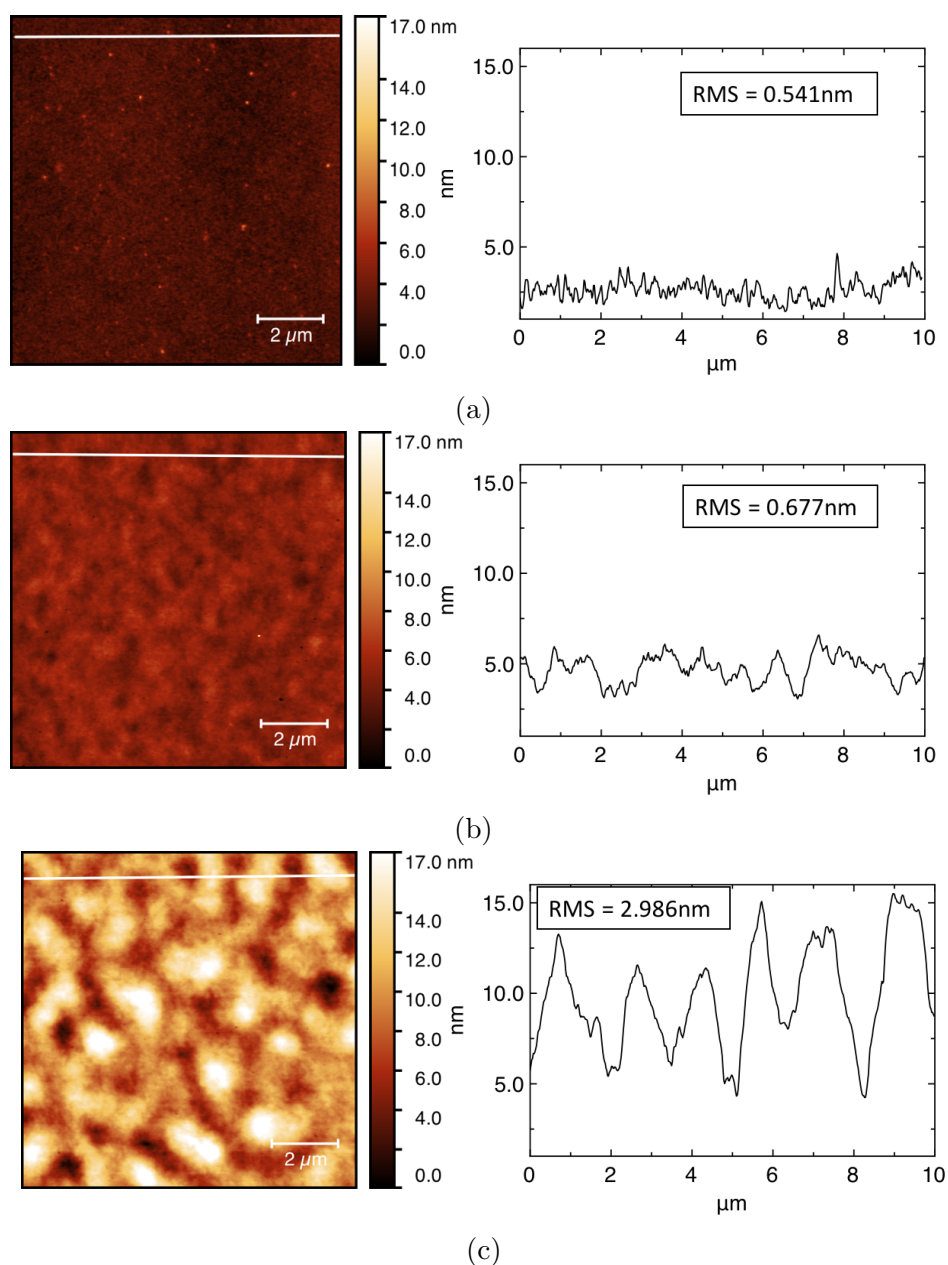


Figure 3.10: Height images for 85 nm PCDTBT films, as cast (a), after melting-quenching at 250°C (b) and after an isotherm at 180°C (c).

The 80 nm film presents a further development; not only the melted-quenched sample (figure 3.10b) presents larger features compared to the as cast one (figure 3.10a), but the isothermal annealing at 180°C (figure 3.10c) also creates a well defined set of aggregates on the surface of the polymer, drastically increasing the roughness and waviness of the film.

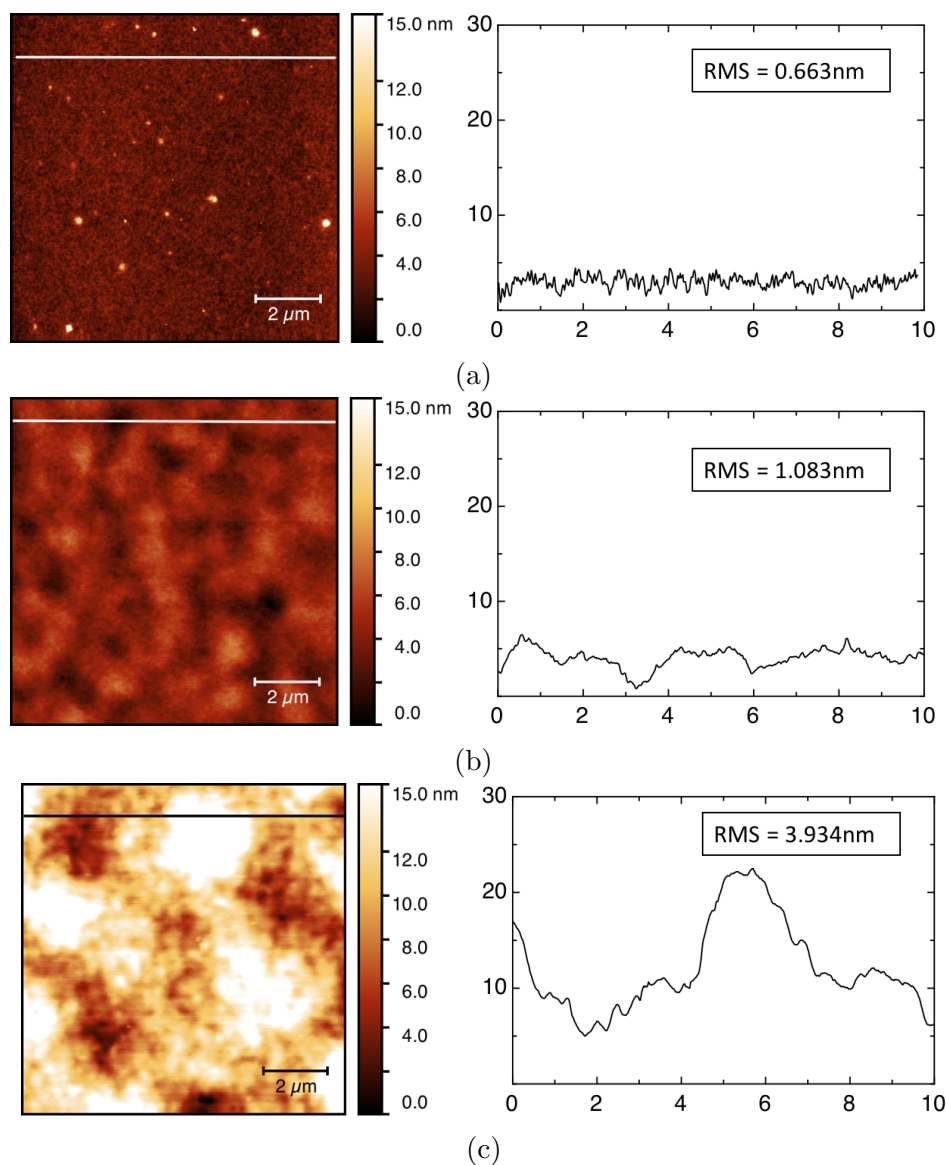


Figure 3.11: Height images for 200 nm PCDTBT films, as cast (a), after melting-quenching at 250°C (b) and after an isotherm at 180°C (c).

Finally, the 200 nm film, presents a similar development to the 80 nm one, but the features appearing on the surface after the isothermal annealing (figure 3.11c) are about 2 μm in size, while they were about 1 μm for the 80 nm sample (figure 3.10c).

Concluding this analysis of the AFM results: annealing causes the surface to roughen and aggregates of material are visible on the surface of the polymer films. Especially in thicker samples, the surface of a film processed at 180°C presents more surface roughness and larger areas of aggregation, whereas for the thinner films, 8 and 40 nm, the difference is less evident. The ordering causes an increase of density with a consequent decrease in thickness. In the thickest films larger masses of material may be able to move around, creating consequently

larger aggregates. It is clear that something is happening in the bulk of the film and this is reflected on the surface. It might be that the overall film shrinks, as if empty spaces under the surface are filled and the ordered polymer aggregates appear on the surface.

3.5 Thermal protocol seen at GIWAXS

The GIWAXS data reported in this section show that annealing increases the space between out-of-plane chains (responsible for the scattering along Q_z), which are the chains stacked face-on: face parallel to the substrate (the geometry of the instrument is explained in chapter 2). Contrarily, the chains oriented edge-on (producing scattering along Q_{xy}) show a decreased interchain distance compared to the pre-annealed sample.

There is also a decrease in the out-of-plane intensity upon annealing, meaning that the amount of face-on ordering decreases with annealing. The details of the GIWAXS analysis are presented in sections 3.5.1 and 3.5.2 for PCDTBT films of two different thicknesses 90 nm and 200 nm. For each thickness, three samples: as cast, after melting-quenching and after isothermal annealing have been analysed.

3.5.1 Effect of the thermal protocol on 90 nm thick PCDTBT films

The ellipsometry profile of the isotherm in figure 3.12 for the 90 nm sample analysed at GIWAXS, shows that the shrinking takes place at 176°C, so before the temperature of the heating stage reaches 200°C (target temperature that has been set up for the isothermal experiment). From a first look at the GIWAXS 2D images in figure 3.13 the straightforward message is the low scattering intensity for the melted-quenched sample in both the in-plane and out-of-plane directions, which constitutes a positive result as we wanted to eliminate the crystallinity from the as-cast sample. However the sample after the isotherm (figure 3.13c) does not look more crystalline than the as-cast one (figure 3.13a). Probably the crystallisation after the isotherm reaches about the same degree of crystallinity of the as-cast film and cannot improve any further.

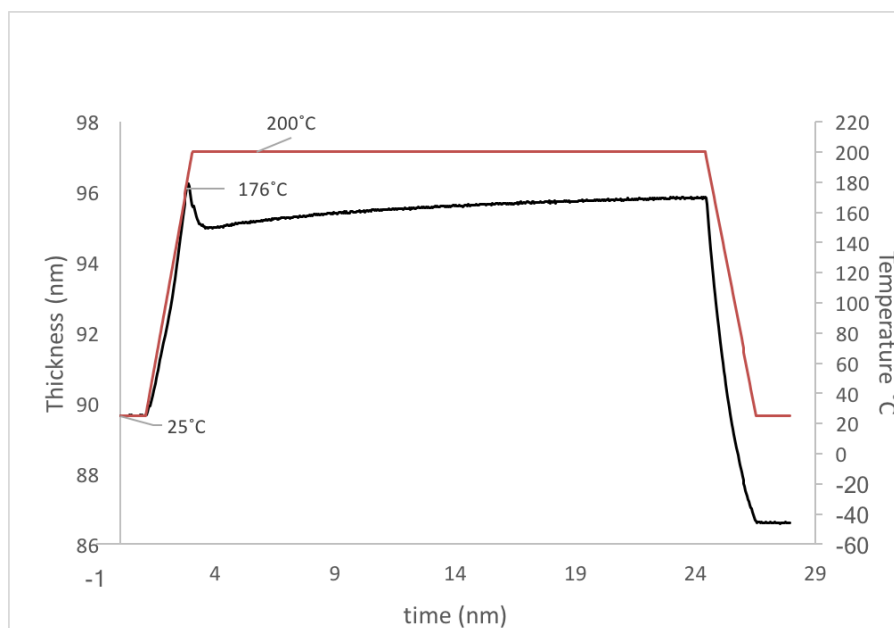


Figure 3.12: Thickness profile of the 90 nm PCDTBT sample heated at 200°C.

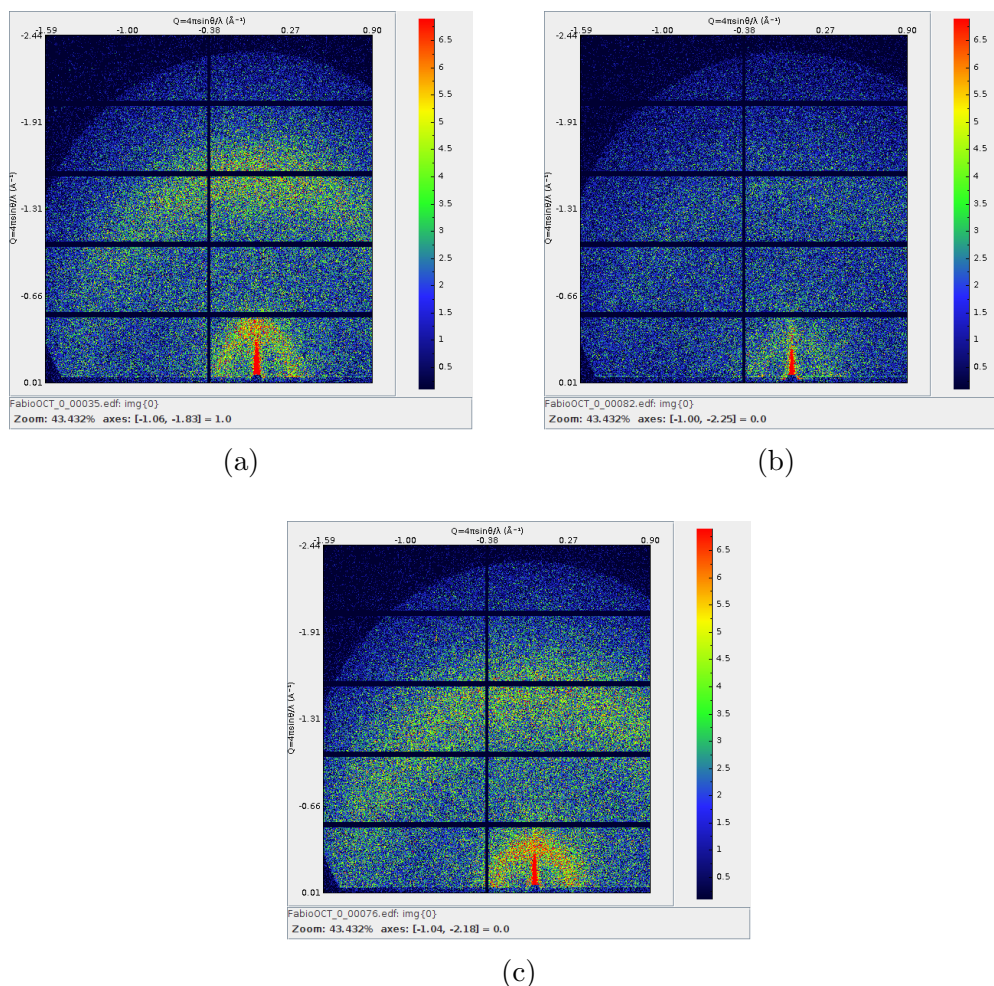


Figure 3.13: GIWAXS data verifying the thermal protocol on a 90 nm film. 2D images for an as cast sample (a), a sample that has been just melted and quenched at 250°C (b), and a sample that has been heated at 200°C (c). The two scattering rings at $Q = 0.33 \text{ \AA}^{-1}$ and the π - π stacking at $Q = 1.53 \text{ \AA}^{-1}$ correspond to the lamellar packing.

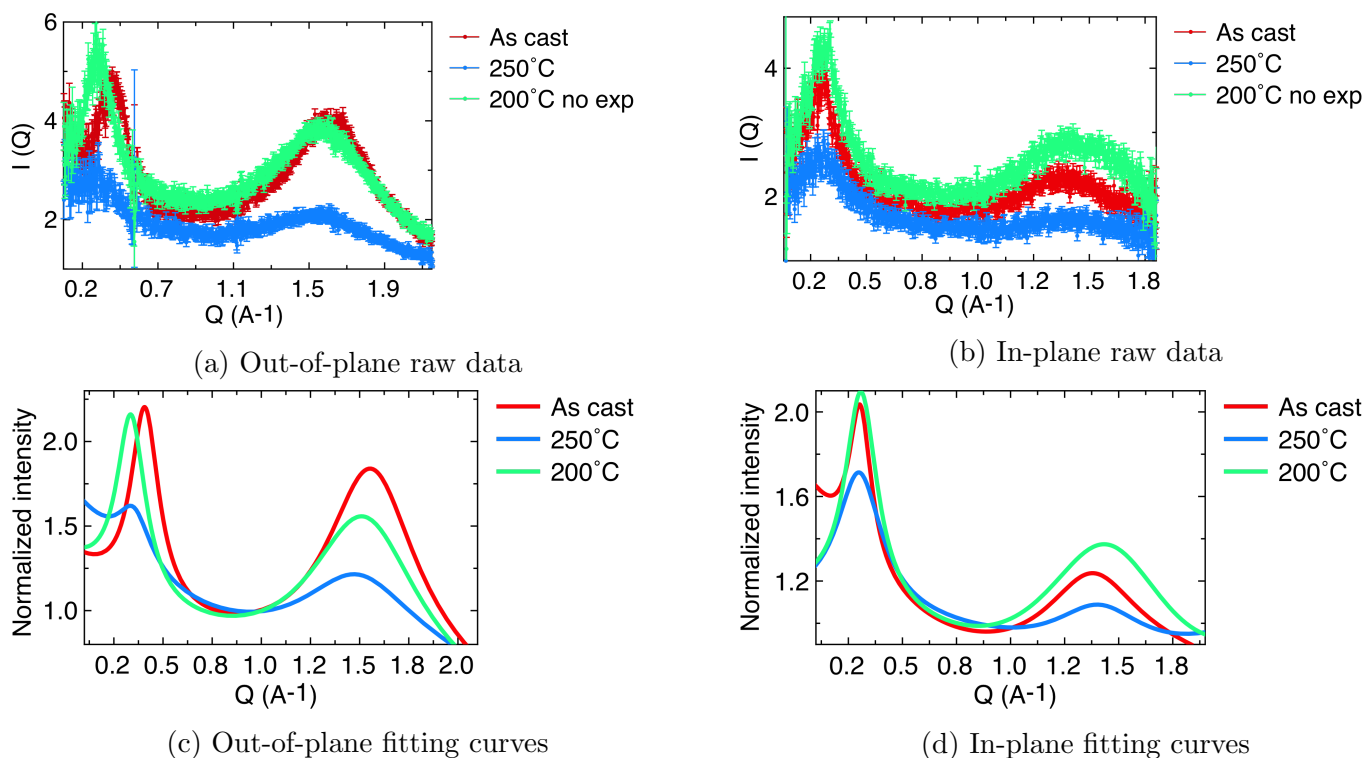


Figure 3.14: (a) and (b) show the out-of-plane and in-plane GIWAXS scattering data for a 90 nm PCDTBT film after each step of the thermal protocol. (c) and (d) are the functions that best fit the data in figures (a) and (b). The data were re-scaled, so that they could be represented on a single plot helping the comparison between the different peaks. The peaks were fitted to Gaussian functions. (a) and (b) have been created by integrating the signal intensity within delimited circular sectors centred at the beamstop, of the 2D data represented in figure 3.13. For the out-of-plane sections were taken regions 30° wide centred along Q_z , while for the in-plane data, regions 30° wide were taken along Q_{xy} with the bottom radius lying horizontally coinciding with the bottom border of the 2D image.

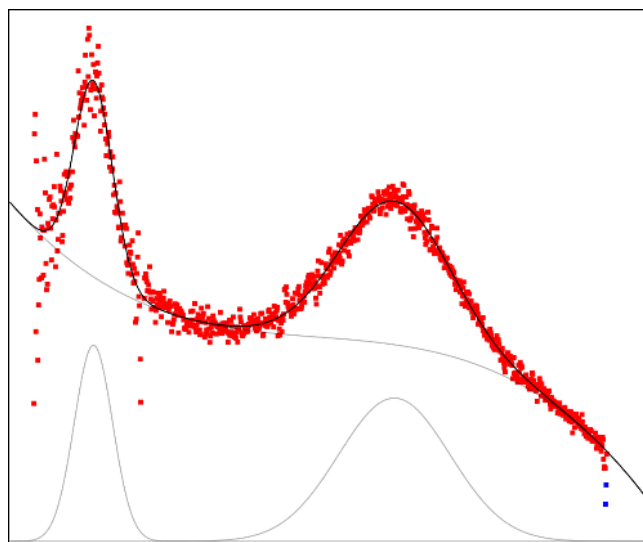


Figure 3.15: This figure is showing how the data fitting has been performed to obtain height and position of a scattering peak. The red squares are the line cuts taken from the GIWAXS data showed in figure 3.13. The grey lines represent the third degree polynomial and the Gaussian functions used to fit the experimental data. The black line is the sum of the two function. The distances between the polynomial and the maximum of the peaks are then the intensity at x_0 reported in table 3.1.

1st peak (lamellar packing)					
	x_0 (\AA^{-1})	$2\pi/Q$ (\AA^{-1})	μ (\AA^{-1})	L (\AA)	$I(x_0)$
as-cast _{OOIP}	0.42 (0.003)	15	0.11 (0.012)	28	2.4 (0.1)
as-cast _{IP}	0.30 (0.003)	21	0.09 (0.009)	34	1.6 (0.1)
250°C _{OOIP}	0.35 (0.022)	18	0.14 (0.106)	23	0.5 (0.1)
250°C _{IP}	0.31 (0.007)	20	0.11 (0.019)	30	1.0 (0.2)
200°C _{OOIP}	0.34 (0.004)	19	0.11 (0.018)	29	2.7 (0.1)
200°C _{IP}	0.31 (0.003)	20	0.10 (0.008)	32	1.4 (0.1)
2st peak (π - π stacking)					
as-cast _{OOIP}	1.54 (0.001)	4	0.21 (0.002)	15	2.6 (0.04)
as-cast _{IP}	1.38 (0.013)	5	0.24 (0.056)	13	1.0 (0.2)
250°C _{OOIP}	1.51 (0.008)	4	0.29 (0.08)	11	1.1 (0.1)
250°C _{IP}	1.40 (0.071)	4	0.36 (0.483)	9	0.3 (0.1)
200°C _{OOIP}	1.52 (0.002)	4	0.34 (0.009)	9	2.8 (0.2)
200°C _{IP}	1.35 (0.015)	5	0.50 (0.06)	3.5	1.4 (0.4)

Table 3.1: Fitting parameters for the GIWAXS data shown in figure 3.14. x_0 is the position of the maximum of the Lorentzian peak on the x-axis, $2\pi/Q$ is the corresponding length to the Q -coordinate, μ the half width at half maximum of the peak, L is the coherence length and I the amplitude of the peak which counts for the scattering intensity excluded the background noise. The values in brackets are the standard errors. The first lines are the out-of-plane values, the second lines are the in-plane values.

The preferable orientation of the chains seems to be the parameter that changes the most: in the as-cast sample (figure 3.13a) the scattering rings looks more intense along the out-of-plane direction, compared to the scattering rings in figure 3.13c relative to the isothermal annealed sample. In the annealed sample the rings show less preferable orientation and more homogeneity. The as-cast sample presents also a higher Q than the annealed samples in the out-of-plane direction (figure 3.14c, table 3.1). This means that the chains are closer together, and it can explain why the as-cast film is thinner than the annealed one. The film thickness after the melting and quenching step results expanded compared to the as-cast sample (not shown). Then the isothermal annealing produces a decrease in thickness and the film is 3 nm thinner

(figure 3.12) than the as-cast sample (as-cast sample thickness not shown).

More intensity is noticeable in the out-of-plane direction in the as-cast sample (figure 3.13a), meaning there is a larger quantity of chains oriented flat-on in the as-cast sample, *i.e.* the isothermal annealing might homogenise the orientation of the chains, distributing them equally between edge-on and flat-on. Moreover, from the line-cuts in figure 3.14 the difference in intensities for the peaks between the isothermal and the as-cast sample is greater in the out-of-plane (figure 3.14c) than in the in-plane direction (figure 3.14d).

The coherence length of the π - π stacking peak (table 3.1), suggests it decreases with annealing in the out-of-plane direction, as found elsewhere [8], confirming that annealing disrupts it. In the in-plane direction, the π - π stacking peaks generally look broader than in the out-of-plane direction, suggesting this feature orients preferably face-on the surface and almost not edge-on, as the peaks have an amorphous shape.

Lamellar stacking seems to have larger aggregates in the in-plane respect to the out-of-plane direction (larger in-plane coherence length): lamellar stacking is probably constituted by larger aggregated disposed edge-on. However more lamellar stacking is oriented flat-on. Comparing

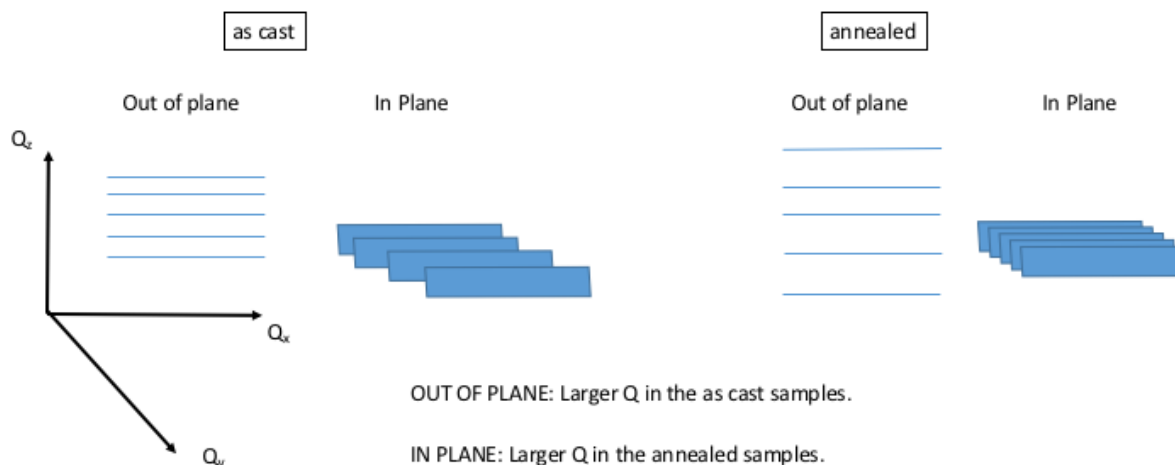


Figure 3.16: Schematic diagram representing the changes in the molecular ordering and spacing between an as cast and an annealed sample.

the out-of-plane and in-plane intensities for the as-cast and the 200°C annealed samples (ta-

ble 3.1), we can see that the most difference between the in-plane and out-of-plane directions, meaning that they are the sample with the most inequality between edge-on and flat-on orientation. Then for the film after the melting-quenching, the inequality is reduced for both the π - π stacking and the lamellar packing.

These results indicate that the as-cast sample has a preferential orientation, while the melting-quenching step removes it, before being restored with the isothermal annealing.

3.5.2 Effect of the thermal protocol on 200 nm thick PCDTBT films

The 200 nm sample was heated to 200°C and kept for approximately 25 min at this temperature, as can be seen from the ellipsometry graph in figure 3.17. The thickness profile upon annealing for this sample does not look like the thickness profile for the 90 nm sample presented in section 3.5.1 and the shrinking here is very mild. Other difference is that T_o (the crystallisation temperature as in figure 3.12) is not visible as it might coincide with the annealing temperature or it might have not been triggered by it yet. This might be due to the fact that these 200 nm films (the only ones in this thesis) have been prepared from a different batch of PCDTBT with $M_w = 57.0$ kDa, while for all the other thicknesses the PCDTBT used had a molecular weight of 35.4 kDa (as specified in section 1.5.2). This increase of 21.6 kDa would mean a greater number of chain entanglements (section 1.5.2) which would hinder the crystallisation process more than for the lower molecular weight and it would explain the milder shrinking observed in this batch. The only difference in the two batches is the molecular weight as purification and synthesis have been the same. It is well known that molecular weight has an impact on the physical properties of polymers [127]. For example it has been seen a decrease of the crystallisation temperature with a decreasing molecular weight [128], which is exactly what is observed with T_o in this case.

Another 200 nm film annealed at 200°C is represented in figure 3.20a, where T_o still coincides with the annealing temperature, but more shrinking is visible.

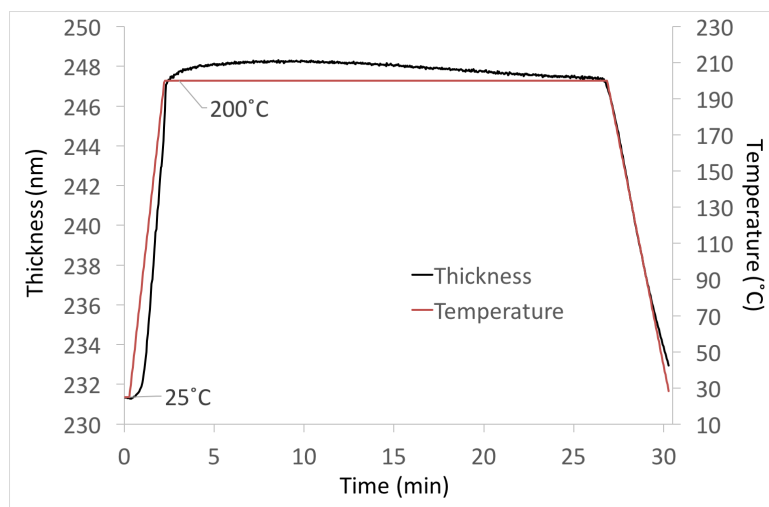


Figure 3.17: Thickness profile of the 200 nm PCDTBT sample heated at 200°C.

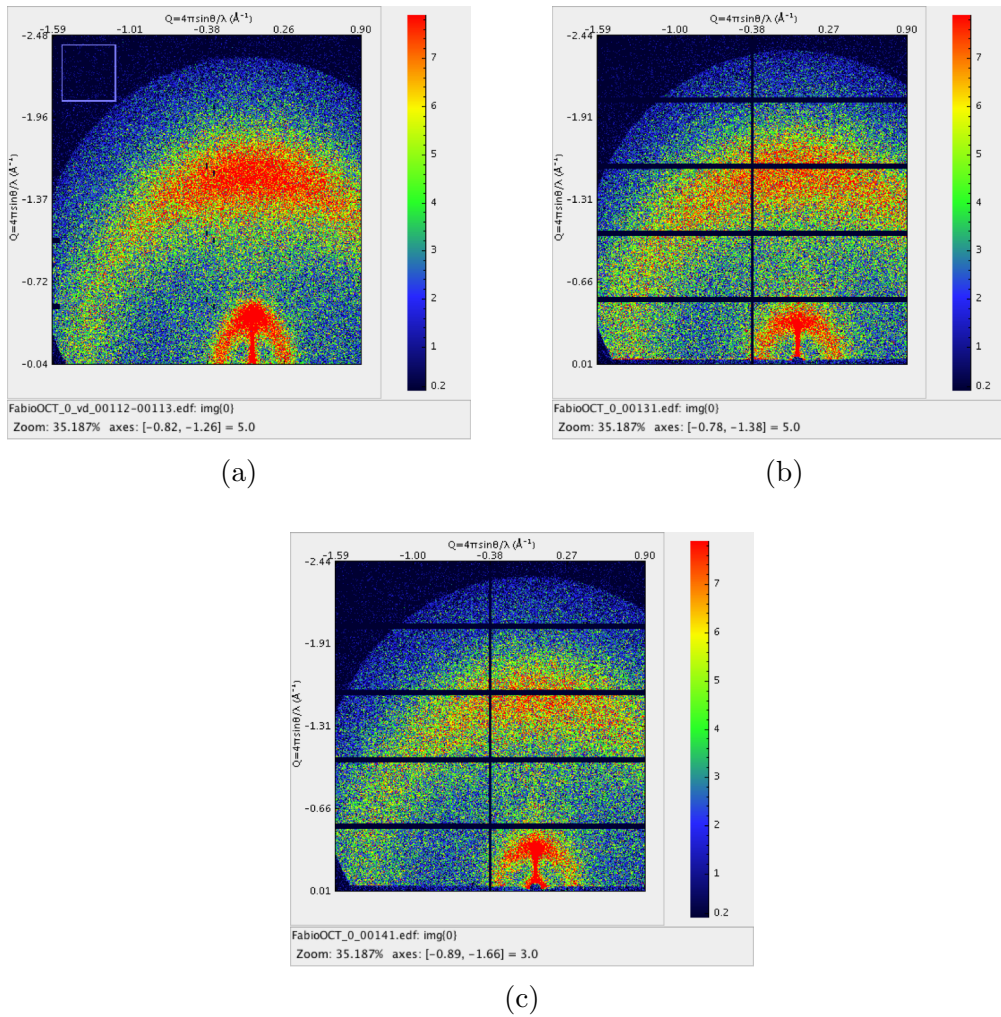


Figure 3.18: GIWAXS 2D images for 200 nm thick films of PCDTBT: as-cast (a), after melting and quenching at 250°C (b) and after isothermal annealing at 200°C (c). The inner scattering rings are from the lamellar packing distance, which is about 15 Å for the as-cast sample in the out-of-plane direction and 18 Å for the annealed samples. While, along the in-plane direction the distance is 22 Å for the as-cast sample and 20 Å for the annealed samples. The outer rings are from the π - π stacking distance of 4 Å in the out-of-plane direction for all the samples and 5 Å in the in-plane direction.

It is easily noticeable from the 2D images that the as-cast image (figure 3.18a) presents the elongated rings in the Q_z direction, as for the 90 nm film, and a reduction along Q_z for the annealed samples (figure 3.18b and 3.18c). Also the intensity changes: there is much more intensity in the out-of-plane direction for the as-cast sample, compared to the annealed films, but it is easier to understand the effect of the annealing on this sample from the fitted data in figures 3.19c and 3.19d.

The most intense scattering signal is the one from the as-cast sample (red line in figure 3.19a) in the out-of-plane direction, and very similar are the scattering intensities for the melted-

quenched at 250°C and the sample annealed at 200°C (blue and green lines). This very little difference before and after the isotherm was expected, as the ellipsometry profile does not show a concrete shrinking peak. On the other hand, the in-plane line cuts in figure 3.19d present much less difference in intensity between the annealed and the as-cast samples. Looking at the π - π stacking peaks in figure 3.19d it is possible to notice that the as-cast sample has the sharpest peaks, while the green and blue peaks appear very broad, meaning that the ordering lost after the melting-quenching process is then not recovered with a 200°C isotherm.

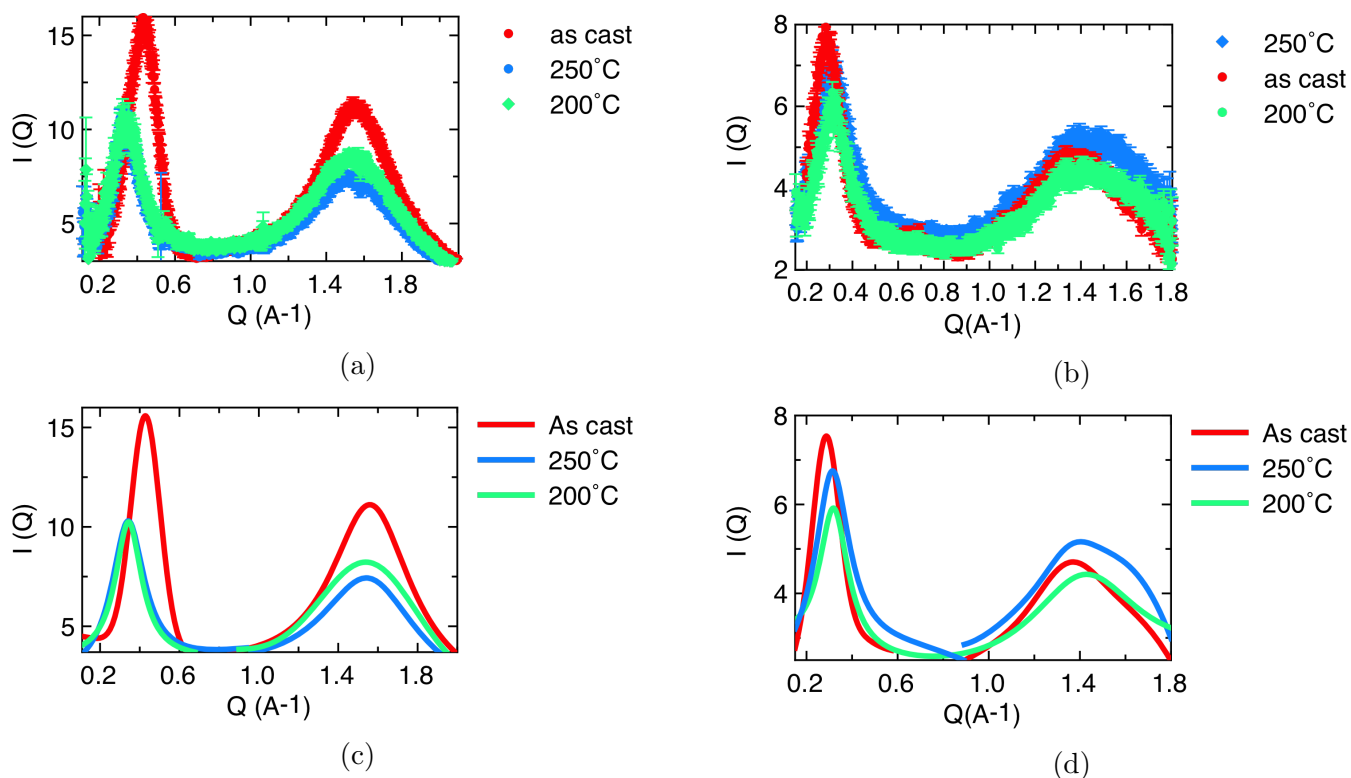


Figure 3.19: (a) and (b) show the out-of-plane and in-plane scattering data for a 200 nm PCDTBT film after each step of the thermal protocol. (c) and (d) are the functions that best fit the data in figures (a) and (b).

1st peak (lamellar packing)					
	x_0 (\AA^{-1})	$2\pi/Q$ (\AA^{-1})	μ (\AA^{-1})	L (\AA)	$I(x_0)$
as-cast	0.43 (0.001)	15	0.07 (0.001)	42	11.7 (0.09)
	0.28 (0.003)	22	0.06 (0.001)	50	4.4 (0.04)
250°C	0.34 (0.002)	18	0.10 (0.004)	31	7.5 (0.17)
	0.32 (0.001)	20	0.09 (0.004)	33	4.3 (0.09)
200°C	0.34 (0.001)	18	0.08 (0.002)	39	6.9 (0.11)
	0.32 (0.001)	20	0.08 (0.004)	39	3.5 (0.09)
2st peak (π - π stacking)					
as-cast	1.56 (0.001)	4	0.20 (0.001)	16	9.2 (0.02)
	1.35 (0.004)	5	0.12 (0.007)	26	2.3 (0.04)
250°C	1.55 (0.001)	4	0.24 (0.001)	13	5.4 (0.02)
	1.36 (0.005)	5	0.34 (0.014)	9	3.4 (0.18)
200°C	1.55 (0.001)	4	0.30 (0.002)	11	5.6 (0.03)
	1.35 (0.006)	5	0.32 (0.015)	10	2.6 (0.14)

Table 3.2: Fitting parameters for the GIWAXS data shown in figure 3.19. x_0 is the position of the maximum of the Lorentzian peak on the x-axis, $2\pi/Q$ is the corresponding length to the Q -coordinate, μ the half width at half maximum of the peak, L is the coherence length and I the amplitude of the peak which counts for the scattering intensity excluded the background noise. The values in brackets are the standard errors. The first lines are the out-of-plane values, the second lines are the in-plane values.

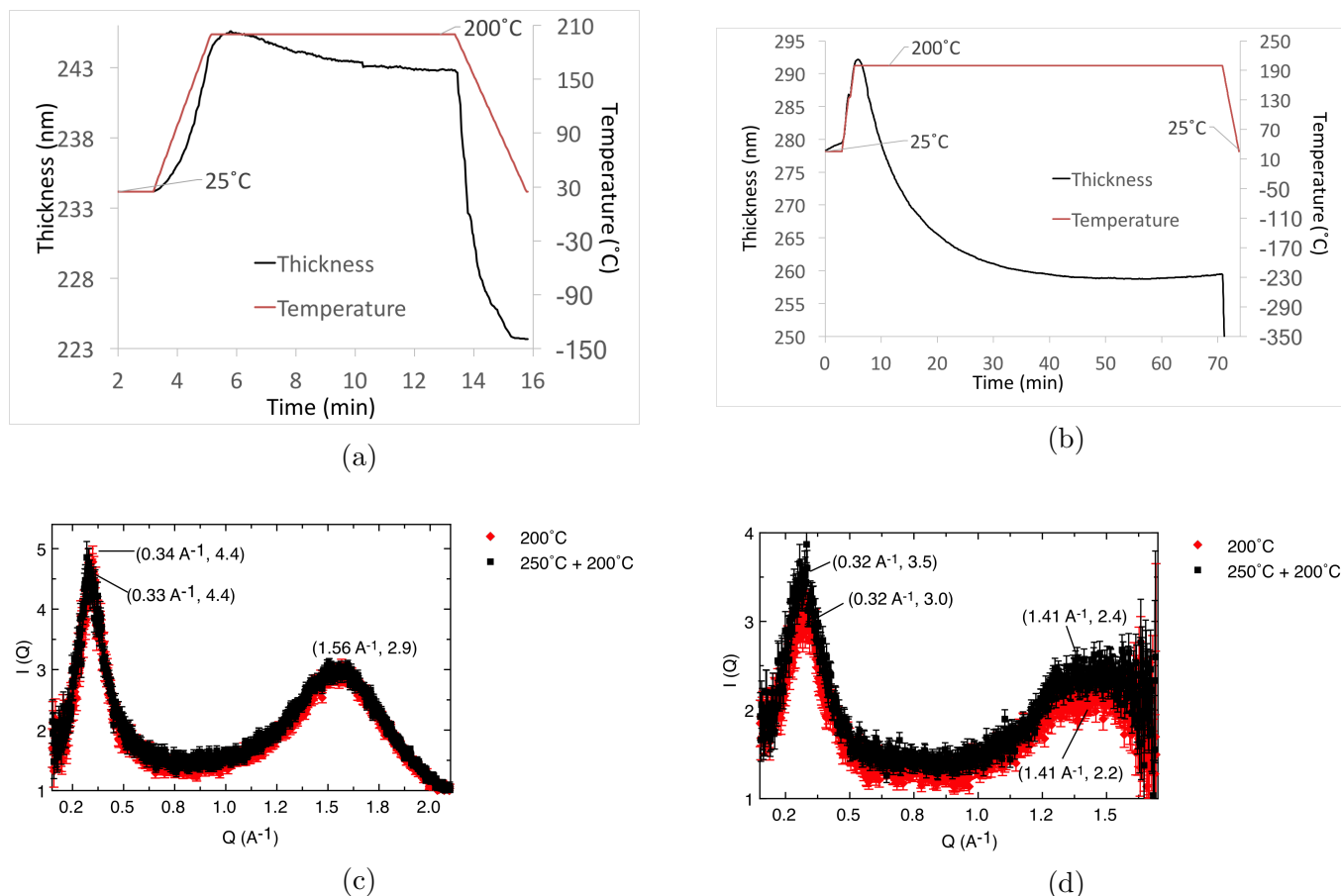


Figure 3.20: Thickness profiles for two 200 nm PCDTBT samples: with (a) and (b) without a previous melting-quenching process. (c) and (d) are the out-of-plane and in-plane scattering data for the two samples. The ellipsometry curve in (a) shows more shrinking compared to the curve for a film of the same thickness, reported in figure 3.17. The only difference between the two samples is that they have been prepared from different solutions, prepared on different dates, but material and experimental conditions were exactly the same.

Finally, a control experiment has been done, to see the difference between a sample that has been exposed to the regular protocol and one that has not been melted-quenched before annealing at 200°C. The ellipsometry results are surprising as the not melted-quenched sample (figure 3.20b) shows a substantial shrinkage of the film. Then the GIWAXS data do not present any particular difference: it might indicate that the melting-quenching step does not modify the maximum order achievable from the isotherm. A peculiar difference is that the plateau in the isotherm in figure 3.20a is reached in only ten minutes, while in figure 3.20b is reached in approximately 30 minutes, suggesting that the melting-quenching might have already crystallized a portion of the sample and that is why it does not occur or at least it occurs mildly with an isothermal annealing done afterwards.

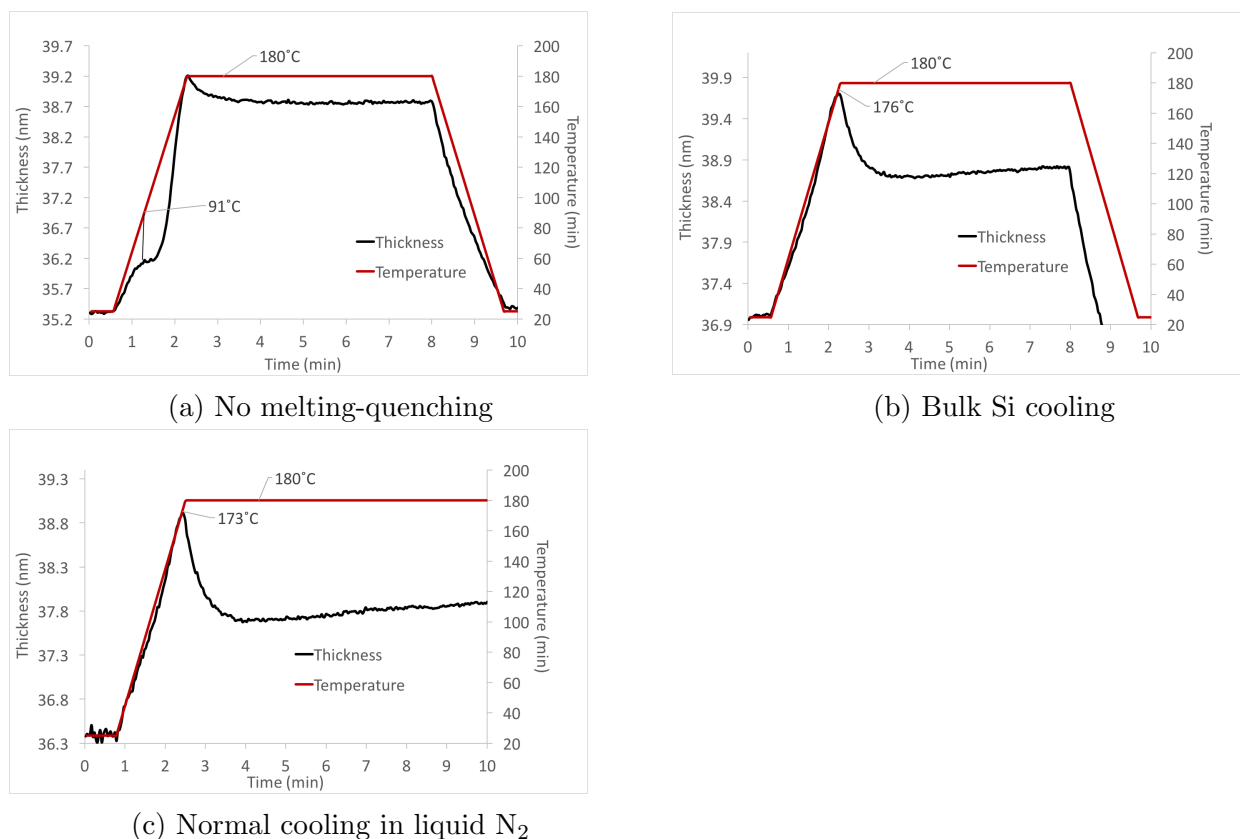


Figure 3.21: Thickness profiles for three 35 nm PCDTBT samples, studying the impact on isothermal annealing for a sample that has not been previously melted and quenched (a); a sample that has been cooled on a cold piece of Si (b); and a sample normally cooled by being dipped in liquid nitrogen.

In figure 3.21 ellipsometry graphs for three 35 nm samples that have been exposed to different treatments are shown. These are the details:

- spin casted and 180°C annealing without melting and quenching in between (figure 3.21a);
- spin casted, melting-quenching at 250°C and cooled on bulk Si (figure 3.21b);
- spin casted, melted-quenching at 250°C and cooled in liquid nitrogen (figure 3.21c).

It is possible to notice an unexpected behaviour for the not melted/quenched sample in figure 3.21a, where the heating ramp has a bump at 91°C, which might be the ordering process partially starting there. Then the remaining two figure 3.21b and 3.21c, have the usual behaviour, with T_o at 173°C-176°C where the polymer starts the ordering before reaching the

temperature of the isotherm, 180°C. This shows that cooling on a bulk piece of Silicon (although much slower) and cooling in liquid nitrogen after the melting-quenching step, does not make any appreciable difference.

3.6 Conclusions

It is clear from the atomic force microscopy analysis that the surface morphology changes a lot with the thickness and the thermal protocol, getting rougher and presenting larger aggregates for thicker, annealed films.

From the X-ray scattering data, the low intensity of the melted-quenched samples confirms that the melting-quenching step did what it was introduced for, *i.e.* eliminate the crystallinity. Then the post-isotherms results are surprising, because the reduction of the film thickness seen at ellipsometry might suggest an increase order of the films, however, the as cast films are the ones with a preferable orientation. It is possible that the melting and quenching causes the loss of this preferable orientation which is not possible to restore with an isothermal annealing at 200°C that was thought to promote the crystallisation process.

For now, it is not possible to conclude any further and the designed protocol might have worked only partially, as the GIWAXS data for the melted-quenched samples still show some residual ordering of the chains. However it has been a useful tool to understand the property of PCDTBT. It will be possible to understand more about the crystallisation of PCDTBT studying the ordering process as function of the film thickness and annealing temperature in the following chapters.

Chapter 4

Ordering as a function of temperature

4.1 Introduction

In chapter 3 the annealing protocol necessary to study the ordering of PCDTBT in thin films has been described. The samples are annealed isothermally, in a temperature range between 140°C and 250°C, between the T_g and T_m of the polymer and the change in thickness is measured by ellipsometry to understand the effect of the temperature on the kinetics of the ordering process.

As described in chapter 3, it is possible to notice some systematic phenomenon happening. The polymer film expands until it reaches a certain temperature, $T_o < T_i$, where T_i is the target temperature for the isotherm: 200°C in the example in figure 4.1. The film starts to shrink at a temperature, defined as T_o (ordering temperature, 176°C in the example in figure 4.1 where the heating rate was 90°C). At T_o the film presumably starts to crystallise spontaneously, demonstrated by the fact that there is a reduction in thickness, meaning the material becomes more dense. Solvent evaporation can be excluded, as the boiling point of CB is 130°C and where we see the transition T_o is 166 - 180°C. As the polymer is in a viscous state above 130°C, it is not likely that any mechanism would keep the solvent trapped between 130°C and 166°C, and in any case, if the solvent was present, we would observe a decrease in T_g , as it acts as plasticizer. The issue has been addressed by Wang et al. [126], who confirmed that the solvent evaporates quickly as soon as the film reaches a temperature of 135°C, the boiling temperature of CB. Solvent evaporation was also found to be independent of the heating rate,

as the chloroform (CF) film was heated at $90^{\circ}\text{C min}^{-1}$ while the CB one at $5^{\circ}\text{C min}^{-1}$ and still the change in slope of the heating curve corresponded to the boiling points of the solvents. The Linkam stage temperature has also been verified using some standard samples with well defined melting temperatures and an optical microscope, to confirm there was no difference between the actual silicon wafer temperature and the value read by the Linkam stage.

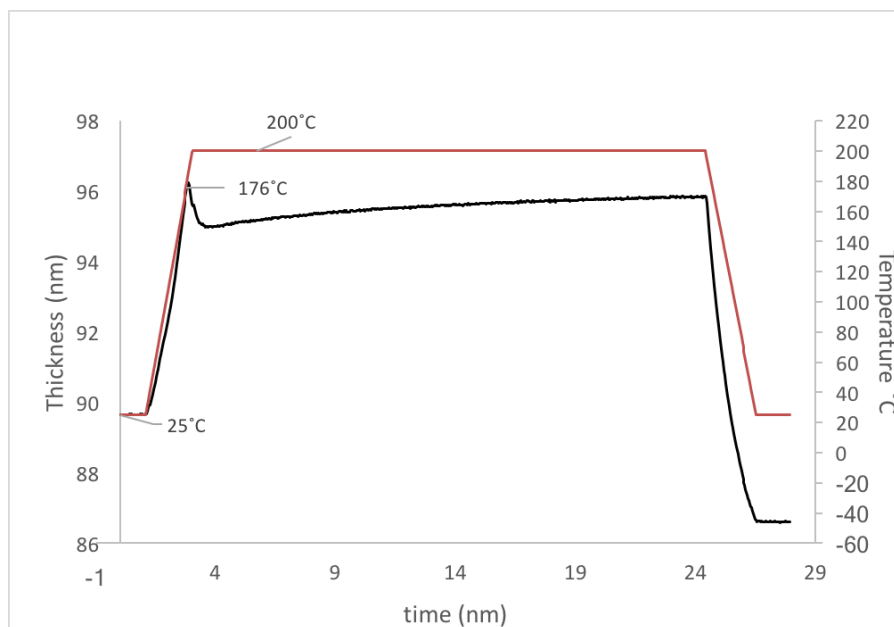


Figure 4.1: Thickness profile (black line) of a PCDTBT film as a function of time, measured by ellipsometry. The temperature profile is represented by the red line.

Generally then, if the set up temperature is 200°C , the film would start shrinking at a temperature $\leq 190^{\circ}\text{C}$. It has been noticed that this temperature of spontaneous ordering is constant, falling in the range of temperatures $166 - 169^{\circ}\text{C}$.

If T_o is a temperature at which spontaneous ordering begins, we expect it to depend on heating rate. It has then been decided to vary the heating rate, doing an experiment at 30°C/min and one at 130°C/min (the maximum allowed from the instrument), when the usual heating rate used for all the isotherms was 90°C/min .

Figure 4.2c shows that in the case of a faster (130°C/min) heating rate the temperature reached is higher: 172°C instead of 166°C for 90°C/min (figure 4.2b). In the slowest case, 30°C/min in figure 4.2a the temperature at which the film starts to shrink is the lowest, 155°C . The shrinking seen with ellipsometry seems then to be then rate dependent which makes the ordering process both thermodynamically and kinetically controlled. The polymer chains need to reach a certain

temperature, *e.g.* 166°C (like in figure 4.2b) in order to start what appears to be an ordering process. But if the heating rate is faster (130°C/min), the chains are not able to start the ordering process before a higher temperature (172°C) is reached.

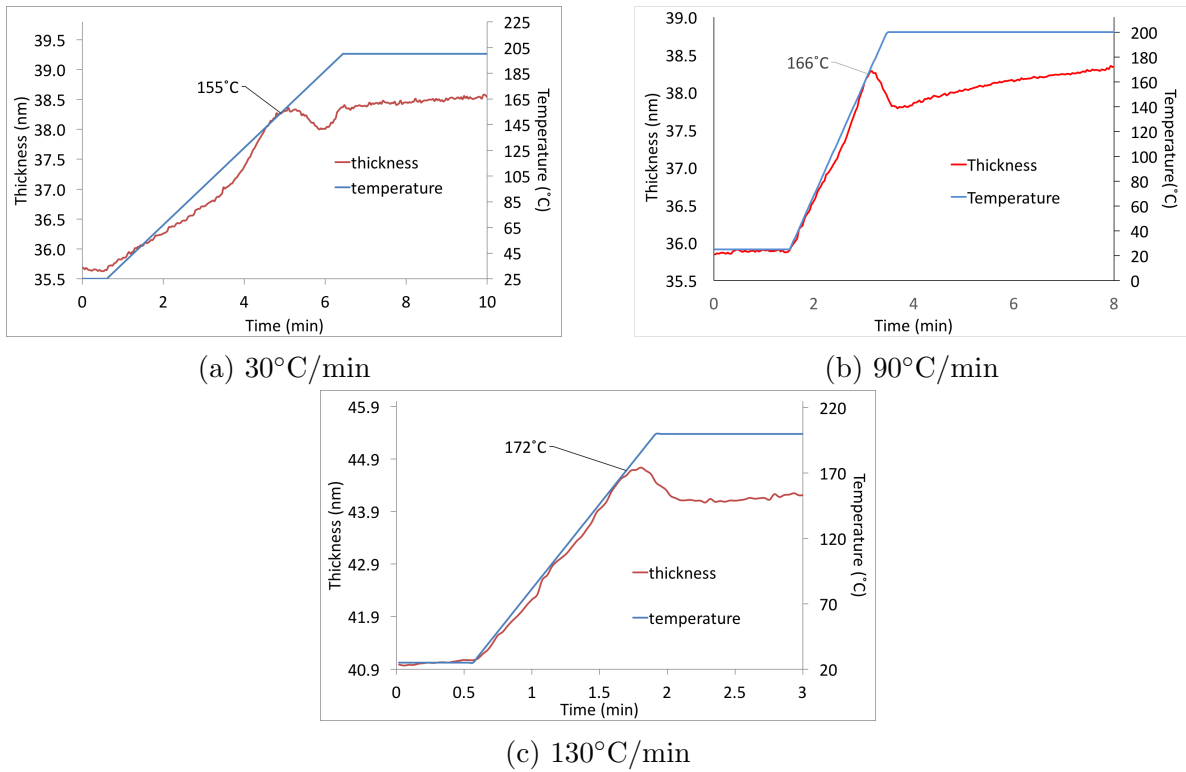


Figure 4.2: Ellipsometry data for 30°C/min (a), 90°C/min (b) and 130°C/min (c) heating rates. The faster the heating rate, the higher is T_o , temperature where the shrinking starts.

There is one situation where the polymer starts to shrink at the target temperature T_i and not at $T_o < T_i$, like shown in figure 4.3b. The sample in figure 4.3b has been melted and quenched a second time after a first isotherm: during the second time the film reaches the target temperature T_i . This suggests that T_o might not simply correspond to a crystallisation temperature, but it might correspond to a preordering process that is overcome the first time an isotherm is applied to a sample. Then, even if the sample is melted-quenched a second time, this preordering is zero.

To recall the annealing protocol results in chapter 3 - section 3.5, the melting-quenching step removes the ordering of the film induced by spin-coating (figure 3.13b), then a first isotherm, improves the crystallinity, as seen from stronger X-ray scattering rings (figure 3.13c). It was expected that the second melting-quenching would remove the crystallinity induced by the first isothermal annealing. This is what the second melting-quenching appears to do looking at the

jump in thickness in figure 4.3b. However it still remains puzzling that $T_o < T_i$ in figure 4.3a and in the second curve in figure 4.3b $T_i \equiv T_o$.

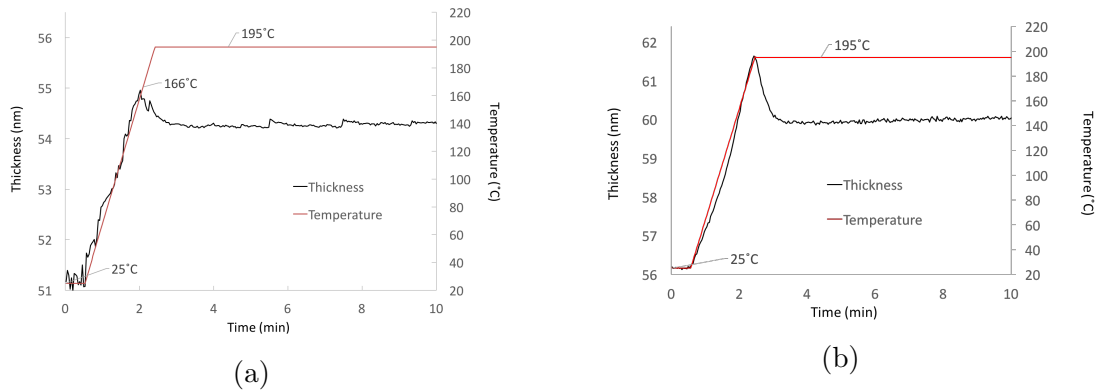


Figure 4.3: Ellipsometry experiment showing two isotherms at 195°C, heating rate 90°C/min. a) The film annealed at 195°C the first time after one melting-quenching, starts shrinking spontaneously at 166°C. In this case $T_o < T_i$ where $T_o = 166^\circ\text{C}$ and $T_i = 195^\circ\text{C}$. (b) the same sample of figure (a) has been then melted-quenched a second time and brought again at 195°C for more than 10 minutes, in this case $T_o = T_i$, the film does not start shrinking before reaching the set up temperature of 195°C

Both types of samples - those for which $T_o < T_i$ and for which $T_o = T_i$ - have been analysed with AFM and GIWAXS; these results are shown in chapter 5, and are also used to understand the expansion that follows the initial shrinking. Samples that were heated at low temperatures, $T_i \leq T_o$ usually do not show any further expansion and this will be analysed in chapter 5.

4.2 Ordering as a function of temperature - an ellipsometry analysis

As discussed in the first chapter, it is well known that the crystallisation rate for a polymer follows a bell-shaped curve with the maximum in the middle between the T_g and the T_m .

In this section typical thickness plots for PCDTBT measured by ellipsometry while annealed at different temperatures are described. Some examples of these ellipsometry data of PCDTBT films annealed at different temperatures are shown in figure 4.4 for three different film thicknesses 30, 50 and 75 nm, in order to have an overview before analysing the temperature dependence in more detail in the next section.

For all the samples it is possible to see how the shrinking process is different for 200°C and

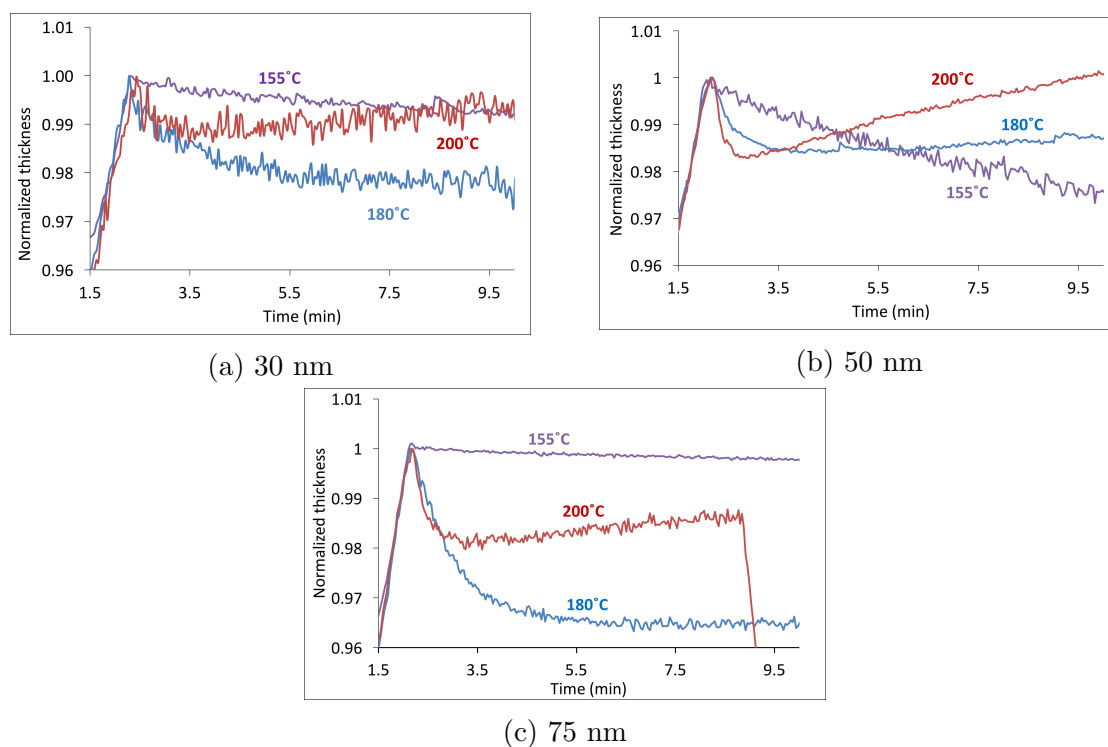


Figure 4.4: Thickness profiles measured by ellipsometry are shown for three different PCDTBT film thicknesses: 30 nm (a), 50 nm (b) and 75 nm (c). For each film thickness are reported the thickness profiles of samples annealed at three different temperatures, 155°C, 180°C and 200°C.

180°C compared to the 155°C one. The kinetics for the 155°C is very slow, while 180°C and 200°C are very similar, slightly faster for the 200°C compared to the 180°C. It is also possible to see how the shape of the curve changes for the samples that have been heated above the T_o (200°C and 180°C). Moreover, the 30 nm and the 75 nm samples shrink less at 200°C than at

180°C and they then start expanding.

4.2.1 Time-Temperature superposition

Time-temperature superposition is a concept in polymer physics, that is used to determine the temperature dependence of the mechanical properties in linear viscoelastic materials. It accounts for changes in mobility of the chain segments; it holds just if all the possible chain motions have the same temperature dependence.

Considering the crystallisation kinetics of a polymer, it might crystallise faster at a temperature $T_2 > T_1$. The principle of the time-temperature superposition states that the change in temperature from T_1 to T_2 is equivalent to multiplying the timescale by a constant factor c_T (a shift factor) which is only a function of the two temperatures, *i.e.*

$$V(t, T) = V(c_T t, T_0)$$

where V defines the crystallisation kinetics, in as much as they are controlled by chain mobility.

The principle has been applied as follows:

- experimental determination of the crystallisation kinetics at different temperatures,
- calculation of a shift factor to make the curves at different temperatures overlap to a reference temperature curve.
- The shift factor is then plotted for all temperatures, to study the relationship between the temperature and the ordering kinetics of the polymer. The crystallisation rate would be expected to be faster at a mid temperature between T_g and T_m . If T_g is 130°C and T_m 240°C, the fastest kinetics would be at 180°C - 190°C.

4.2.1.1 Shift factors and activation energies

The shift factors necessary for the overlap of the ellipsometry curves registered at different temperatures have been plotted taking 170°C as reference temperature (figure 4.5). All the ellipsometry curves from 140°C to 200°C (presented in figures 4.8-4.12) have been shifted by multiplying a constant number (shift factor) to the time-axis in order to bring all the curves to overlap to the 170°C one. This has been done for different film thicknesses, 25, 35, 60, 75 and 90 nm.

The shift factors in function of the annealing temperatures seem to follow an exponential behaviour (figure 4.5), increasing exponentially with the annealing temperature and it could be described by an Arrhenius type equation:

$$c_T = Ae^{\alpha T}, \quad (4.1)$$

The term α can be defined as the activation energy for the crystallisation process, which is the amount of energy required by the polymer to start the ordering process: it describes the exponential dependence of the shift factor c_T from the annealing temperature. The shift factor increases exponentially with the temperature rising, it is 1 for the reference temperature 170°C because it would be the curve compared to itself. Above 170°C, until 185°C the film thickness shrinks much faster and a larger shift factor is needed to make the two ellipsometry curves overlap. For annealing temperatures $\geq 185^\circ\text{C}$, the polymer starts shrinking before reaching T_i (the target annealing temperature), so temperatures between 190°C and 200°C are not included in the fit because they might influence the crystallization kinetics differently compared to temperatures $\leq 185^\circ\text{C}$. It is possible to notice that the points for $T \geq 185^\circ\text{C}$ do not follow the exponential trend but create a plateau (figures 4.5d and e) or have a more linear behaviour. This might be expected, as at higher temperatures the decreasing driving force for crystallisation competes with the increasing chain mobility as the melting temperature is approached.

If the relation between annealing temperatures and shift factors is really exponential we would expect the logarithmic forms to be a linear correlation and the slopes of the curves to correspond

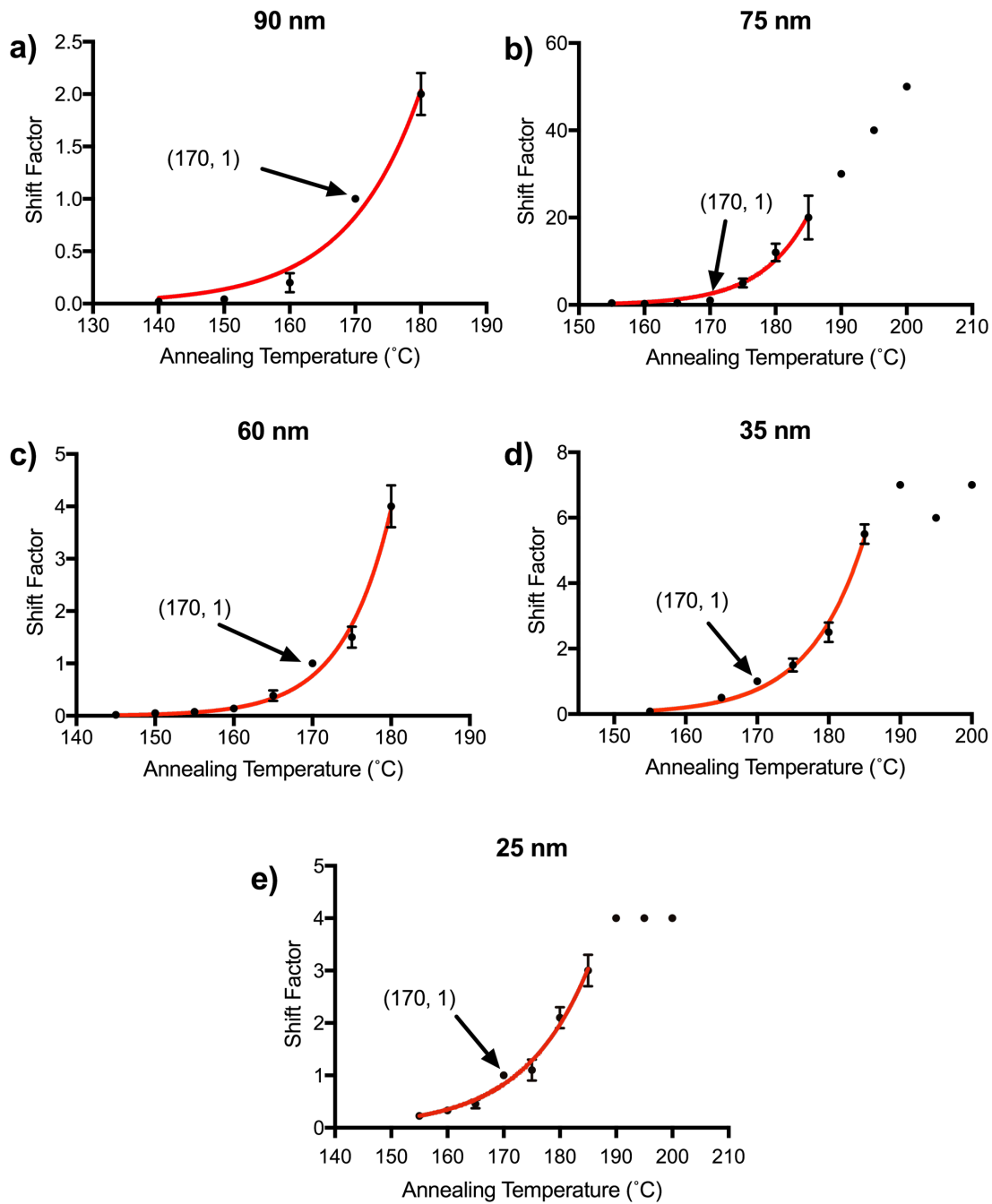


Figure 4.5: The shift factors have been plotted against the annealing temperatures. All the ellipsometry curves have been compared to the ellipsometry curve of the film annealed at 170°C, which has been chosen as reference temperature. That is why is highlighted in the graphs with an arrow. The red lines represent the best exponential fit for the data points. The data points for temperatures > 185° have not been included in the fitting because is believed they follow a different law.

to the activation energy for the crystallisation of the polymer for different film thicknesses.

$$\ln(c_T) = \ln(A) + \alpha T, \quad (4.2)$$

The logarithmic forms of the exponential plots in figure 4.5 have been plotted in figure 4.6 and the correlation seems to be perhaps linear.

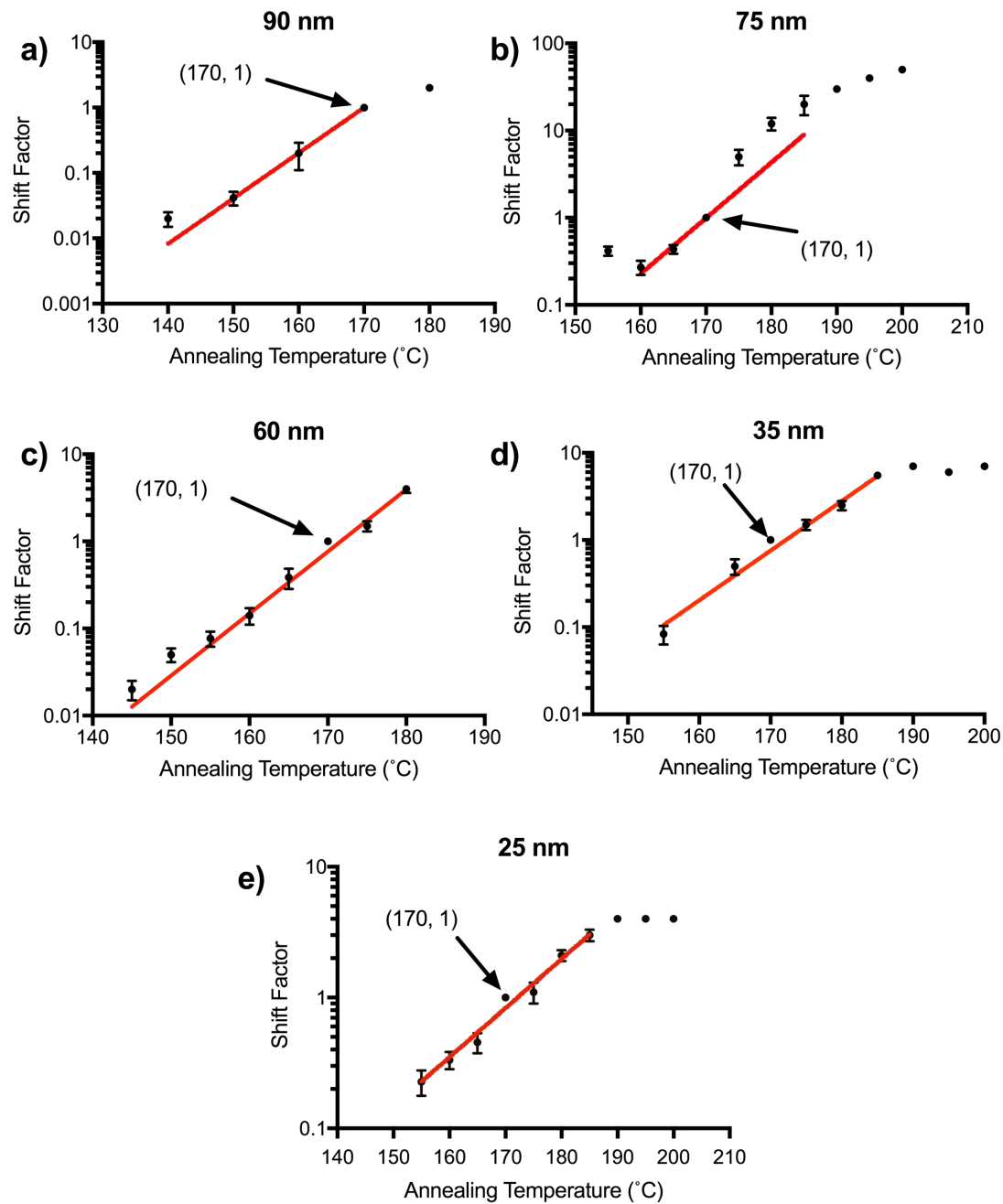


Figure 4.6: Logarithmic forms of the plots in figure 4.5. 170° is the reference temperature taken in the time-temperature superposition analysis. The red lines represent the best fit to the data points and they are described by the equation $\ln(c_T) = \ln(A) + \alpha T$, where α is the slope of the linear fits.

The logarithm of the exponential curves produces then a linear correlation between the annealing temperatures and shift factor, the which slope correspond to the activation energy of the crystallisation process. It is possible to analyse the change of the activation energy in function of the film thickness. The trend is not very clear, as it seems that the thinnest samples (25 nm) have the slowest change as a function of the temperature. The slope is maximum for the 60 nm and 90 nm samples, although the 90 nm thick film has been analysed until 180°C, so the missing 185°C data point could have made a large difference in slope and make it decrease. The result of this study, reported in figure 4.7, shows a transition point (≈ 40 nm) between thin and thick films. Thin films have a lower crystallisation energy than thick films, as in thin films, a larger relative quantity of the polymer film is in contact with the air interfaces, that is known to increase chain mobility and therefore helping the crystallization process. The activation energy linearly increases with the film thickness because relatively fewer of the polymer chains are exposed to the air interface and the bulk-like layer behaviour takes over. The flat line for thicknesses above 40 nm might represents then a constant activation energy for thick films governed by a bulk-like behaviour.

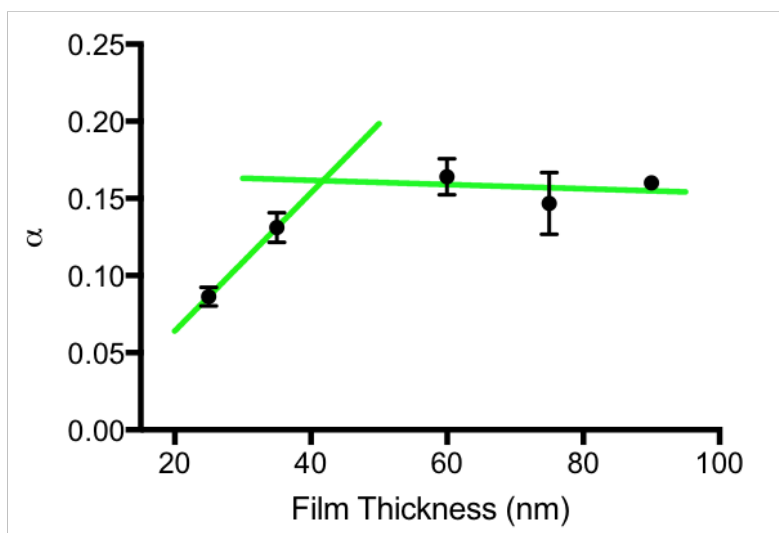


Figure 4.7: Plot showing two trends of the crystallisation activation energy α in function of the film thickness. α varies for film thinner than 40 nm and it is constant for films thicker than 40 nm.

4.2.1.2 Time-temperature superposition analysis

The analysis of the time-temperature superposition curves proceeded in two stages:

1. in section 4.2.1.1 we analysed the temperature dependence of the shift factors to look for any thickness dependence in the kinetics;
2. in this section a detailed analysis of the curve shapes is presented, to look for where the time-temperature superposition fails.

For each film thickness there is a $\log(\text{time})$ plot that highlights the difference in shape of the isotherms at different annealing temperatures. The remaining two plots show the shifted isotherms by application of the shift factor, to allow the overlap of the curves.

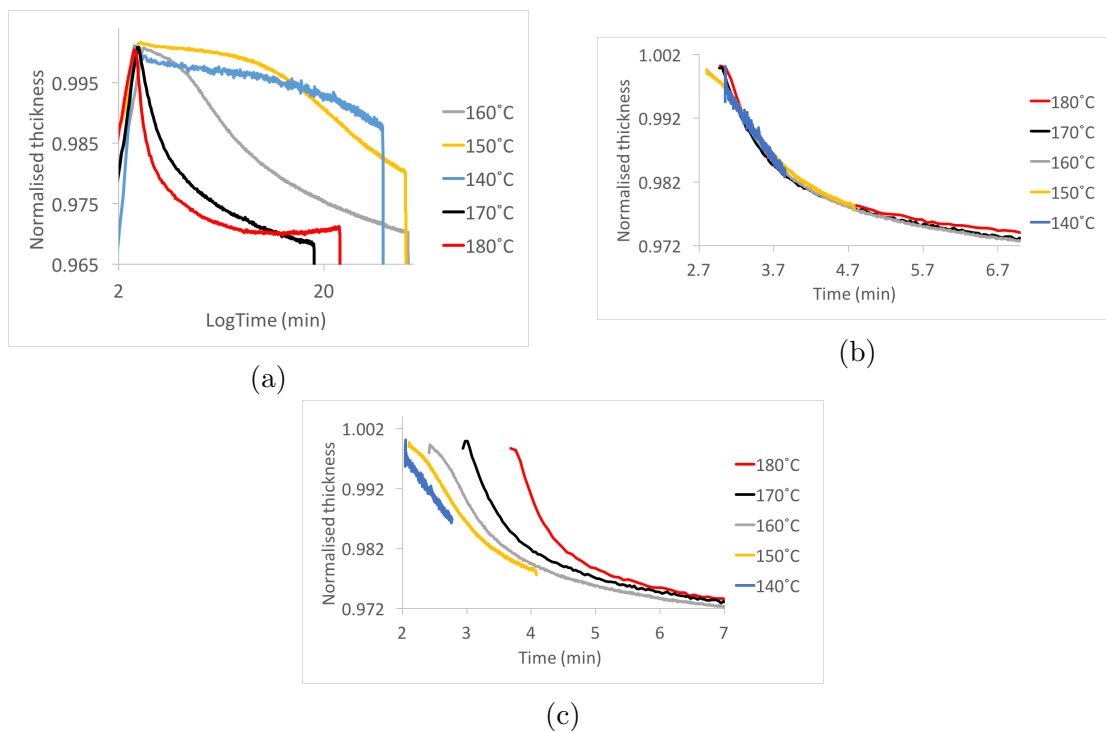


Figure 4.8: 90 nm film thickness. (a) The normalised thickness profiles at different temperatures, as recorded by the ellipsometry. (b) The curves have been multiplied by a shift factor in order to make them overlap. (c) The curves once again multiplied by a shift factor and then 'shifted' along the x-axis, so it is possible to distinguish the three different shapes of the isotherms: 140°C is one shape, different from 150°C and 160°C, which are different from 170°C and 180°C.

For a 90 nm thick film in figure 4.8, the range tested was only 140°C - 180°C, but it is possible to see, 180°C (red curve) to be the fastest temperature, which is also followed by an expansion. It is noticeable that the shape of the curve is the same for 170°C and 180°C, while 160°C and

150°C (grey and yellow curves) present a slower shrinking phase followed by a steeper part on the graph. It might be possible that there are three different processes distinguishable in the grey and yellow curves:

1. a slower pre-ordering stage that starts as soon as the target temperature T_i is reached;
2. a fast ordering stage that is the one that starts spontaneously at the temperature T_o when $T_i \geq T_o$;
3. a third stage is the plateau after the ordering when the film is not influenced anymore by the temperature of the isotherm.

Finally, the 140°C (blue curve) is different from the previous two: there is a very quick but small shrinking at the beginning and then a slow linear shrinking that follows until the quench to 25°C is applied at the end. At 140°C the preordering and the ordering processes seems then to be merged together in an averaged ordering process that is slower than the process at higher temperatures.

The crystallisation kinetics could be defined as made of two temperature-dependent contributes:

$$V(t, T) = M(T)C(T)f(t)$$

where M is the mobility contribution, responsible for the pre-ordering process, the C is the crystallisation driving force, then there is the purely time-dependent part given by f . Since the time-temperature superposition principle approximates the processes to the same temperature dependence, here is where the approximation falls, revealing the impossibility of making the curves to overlap perfectly.

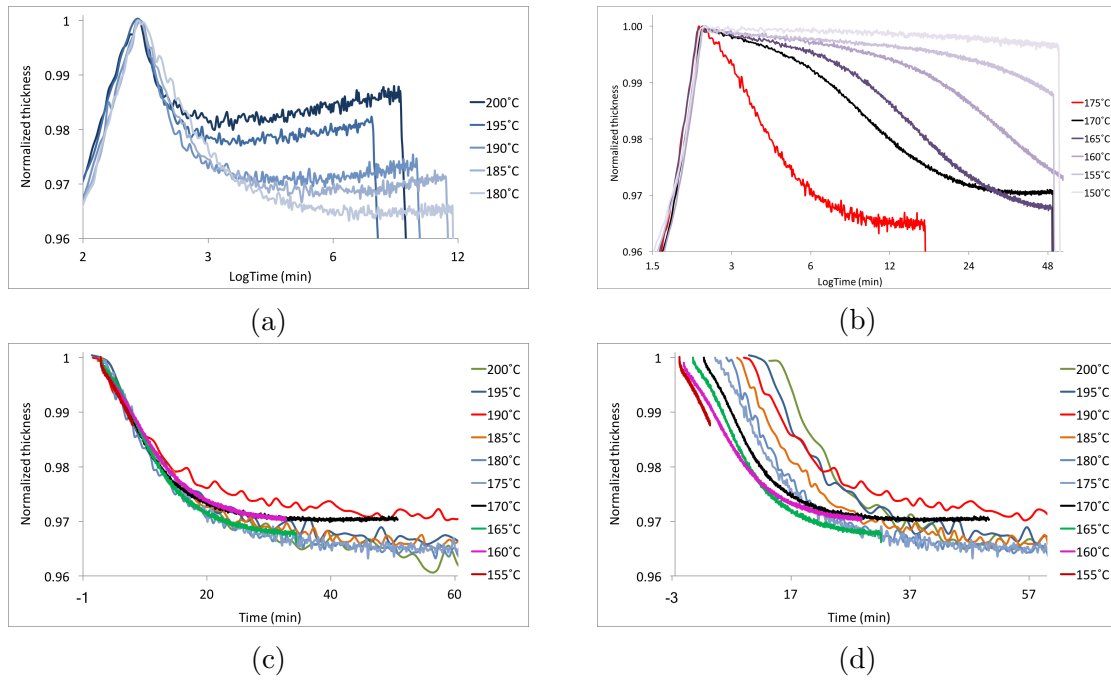


Figure 4.9: 75 nm film thickness. (a) and (b) The normalised thickness profiles at different temperatures, as recorded by the ellipsometry. (c) The curves have been multiplied by a shift factor in order to make them overlap. (d) The curves once again multiplied by a shift factor and then 'shifted' along the x-axis. One shape for 150°C - 155°C, a different one for 160°C - 175°C and another one for 180°C - 200°C.

A very similar argument can be made for the 75 nm thickness (figure 4.9), but here a wider range of temperature is available, 200°C - 150°C and every 5°C. Below 150°C the shrinking was just too slow to be detected and it has been omitted. Again for this sample it is possible to appreciate a change in shape, when $200^{\circ}\text{C} \geq T_i \geq 180^{\circ}\text{C}$ ($T_i \geq T_o$) the shrinking is immediate after the maximum thickness is reached, with a consequent expansion. From 175°C to 160°C there is a three stage ordering process, which is slightly visible at 155°C as well. Then at 150°C the shrinking is just linear as for the 140°C in the case of the 90 nm film (figure 4.8a).

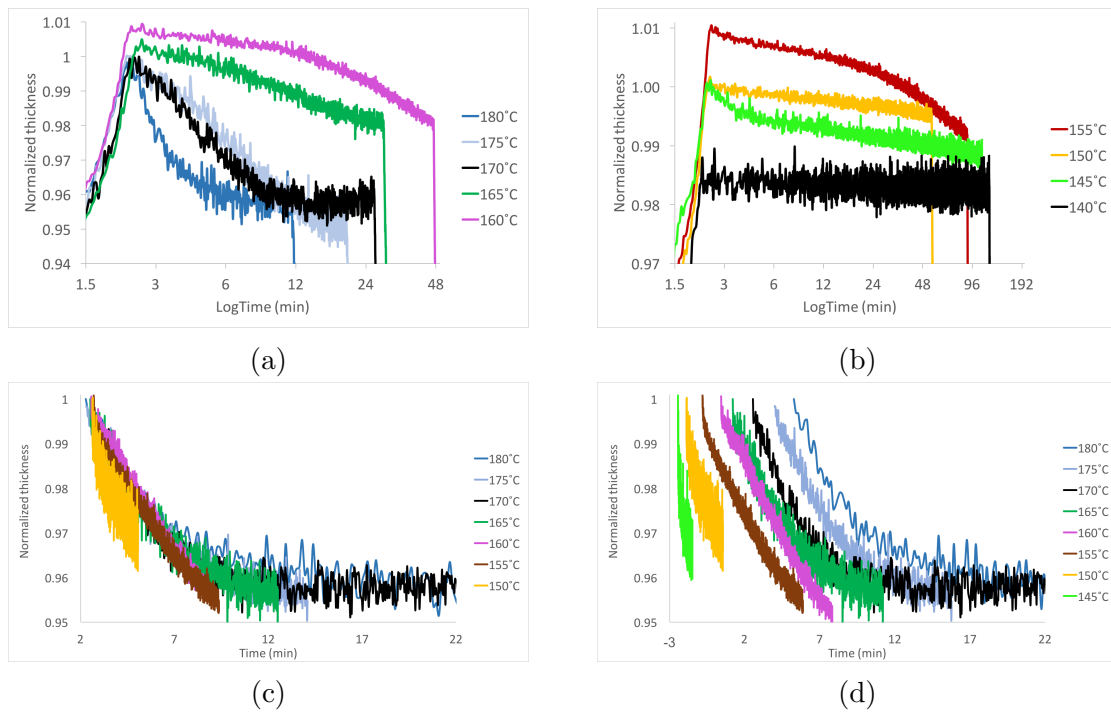


Figure 4.10: 60 nm film thickness. (a) and (b) The normalised thickness profiles at different temperatures, as recorded by the ellipsometer. (c) The curves have been multiplied by a shift factor in order to make them overlap. (d) The curves once again multiplied by a shift factor and then 'shifted' along the x-axis.

For the 60 nm film (figure 4.10), temperatures higher than 180°C are missing, but it is possible to predict how they will be, given the results for the 75 nm film. Curves for annealing temperatures from 180°C to 200°C will very probably have an expansion following the minimum reached by the shrinking like in figure 4.9a for $200^\circ\text{C} \geq T_i \geq 180^\circ\text{C}$. The second shape usually seen in intermediate temperatures (called earlier in this section three stage ordering), might be present for $175^\circ\text{C} \geq T_i \geq 155^\circ\text{C}$. Finally the last type of curve, with the slowest linear ordering, is present for $T_i \leq 150^\circ\text{C}$ (figure 4.10b); the green curve (145°C) seems to have a faster ordering at the beginning, while for the black curve (140°C) the shrinking is not very visible. The lack of shrinking for the 140°C curve shows the limit of the ordering kinetics just near the T_g of 130°C.

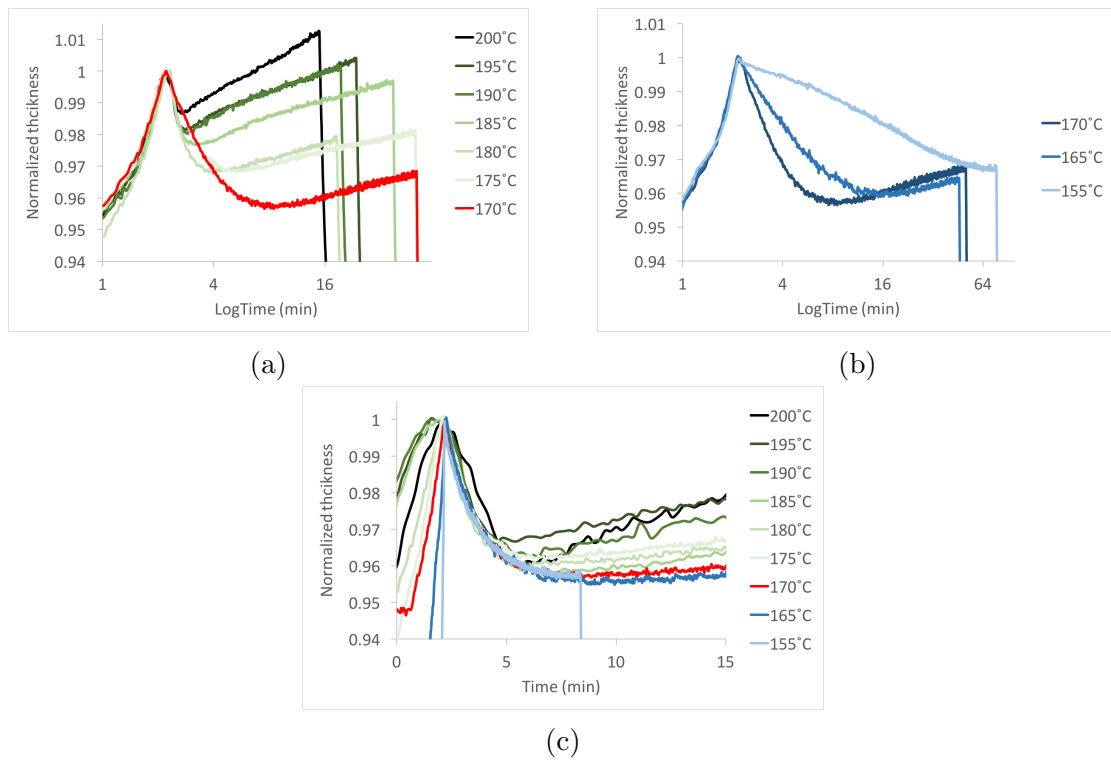


Figure 4.11: 35 nm film thickness. (a) and (b) The normalised thickness profiles at different temperatures, as recorded by the ellipsometer. (c) The curves have been multiplied by a shift factor in order to make them overlap.

In figure 4.11b (35 nm film) it is possible to see that the 155°C curve is the first with a different shape: three stage ordering and the expansion starts already at a temperature $\geq 165^\circ\text{C}$.

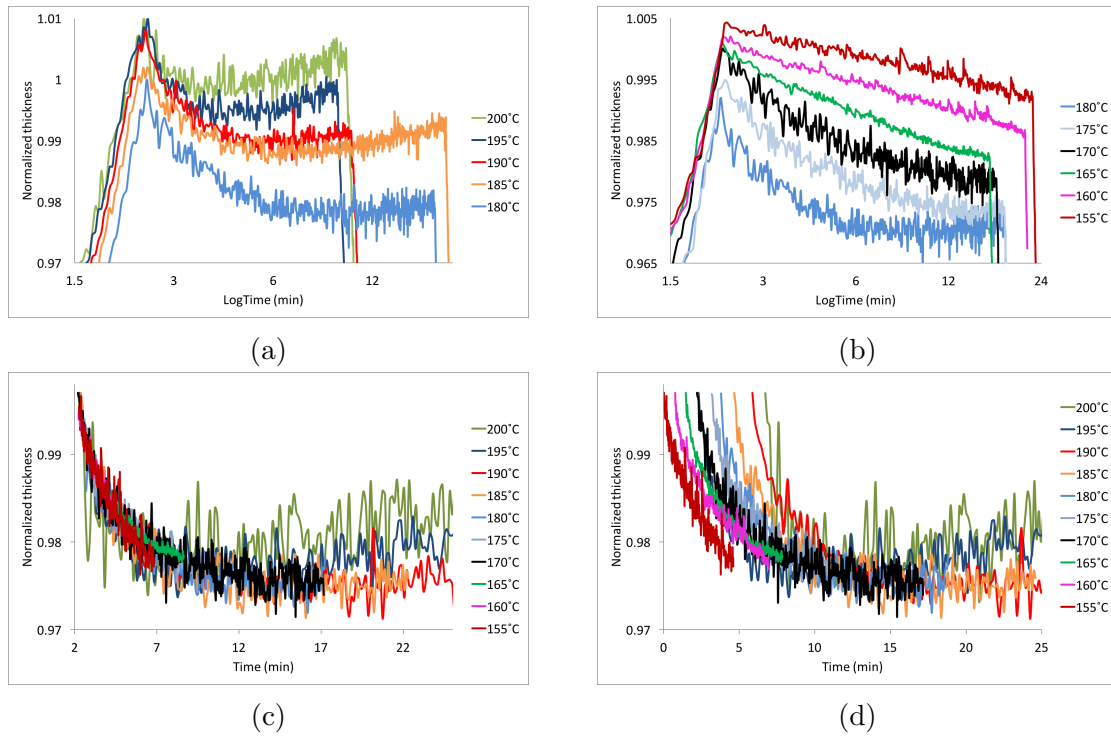


Figure 4.12: 25 nm film thickness. (a) and (b) The normalised thickness profiles at different temperatures, as recorded by the ellipsometer. (c) The curves have been multiplied by a shift factor in order to make them overlap. (d) The curves once again multiplied by a shift factor and then 'shifted' along the x-axis.

For the last thickness of 25 nm (figure 4.12), for $200^{\circ}\text{C} \geq T_i \geq 170^{\circ}\text{C}$ there is an expansion that follows the first shrinkage and for $165^{\circ}\text{C} \geq T_i \geq 155^{\circ}\text{C}$ the maximum shrinkage is not reached in the time the annealing has been recorded, but the shrinkage would have gone further if the sample was left at the annealing temperature for longer. However it is very difficult to recognise the three stage process from these curves for the 25 nm sample because of the noise. The fact that is possible to notice looking at the ordering processes for different thicknesses showed in figures 4.8 - 4.12 for different thicknesses, is that it seems like the change in curve-shape is shifted at higher temperatures for thinner films. For example, going from lower to higher temperatures in the 90 nm film, the first temperature at which the three stage ordering process disappears is 170°C , while is 180°C for the 75 nm and 60 nm samples, 165°C for the 35 nm sample and 170°C again for the 25 nm sample. In the 60 nm films, the faster kinetics are reached at higher temperatures, which might mean higher activation energies for the ordering process, as specified in section 4.2.1.1. In the thinnest film (25 nm) the pre-ordering phase that usually appears at intermediate temperatures, disappears, which can mean that a layer

(referring to the three layers model [92]) that was present in thickest samples is not there anymore. The relationship between ordering and thickness will be discussed further in chapter 6.

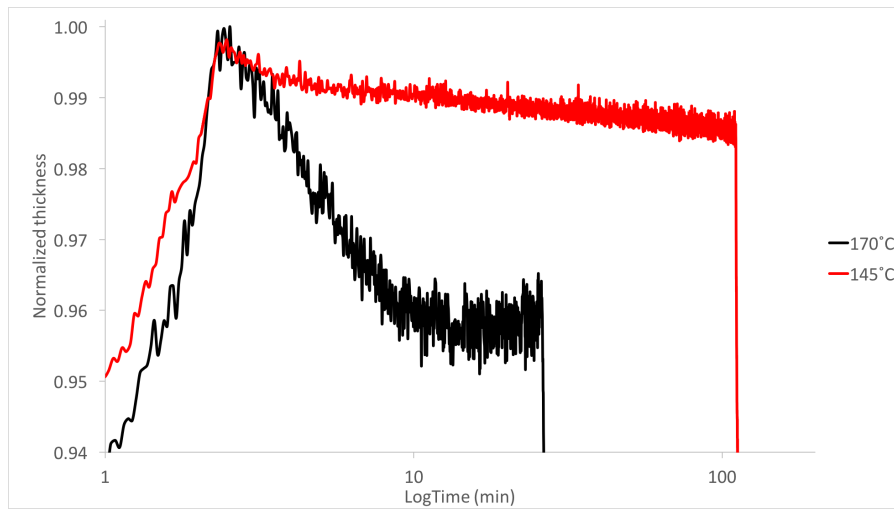


Figure 4.13: Example of a 170°C and a 145°C isotherm for a 60 nm film, illustrating the different shape of the two curves. The 170°C (black curve) shrinks 0.04 units in 5 minutes, while at 145°C (red curve) for the same time the shrink is of 0.01 unit and then it continues a slow shrinking for a long time. It is impossible to overlap these curves completely as they both are divided in two stages, but for the 140°C the first step is much shorter than the 170°C.

4.2.2 Ellipsometry data for samples annealed at temperatures $> 200^\circ$

Samples annealed at temperatures $> 200^\circ$ presented an unusual behaviour, so their ellipsometry data are reported in this section. In figures 4.14, 4.15 and 4.16 the ellipsometry curves for isotherms at temperatures $> 200^\circ\text{C}$ are reported. At 210°C and 220°C (figures 4.14a, 4.15a, 4.16a and b) $T_o = 153 - 186^\circ\text{C}$ but then the ordering does not start at T_o : the film expands until it reaches T_i (220°C or 210°C) and then it undergoes a minor shrinkage, which is smaller than the shrinkage happening at 200°C . At 200°C the shrinkage occurs at T_o , followed by an expansion, phenomenon that will be studied in chapter 5.

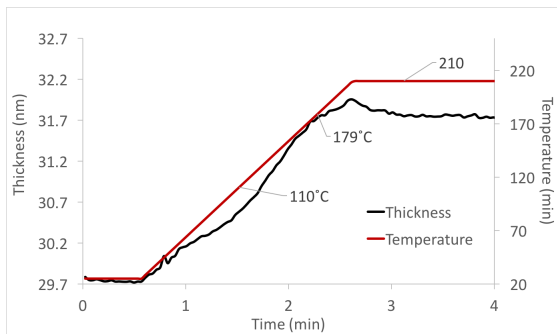
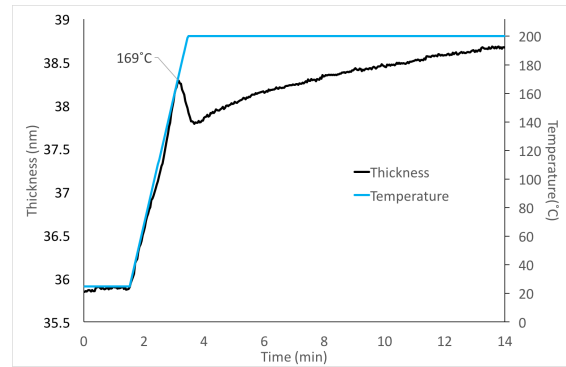
(a) 35 nm 210°C (b) 35 nm 200°C

Figure 4.14: Thickness profiles measured by ellipsometry for 35 nm films annealed at 210°C (a) and 200°C (b). (a) The change in expansivity at 110°C it is probably due to the T_g and 179°C denotes T_o : the ordering does not start at T_o but it starts when the film reaches T_i (210°C).

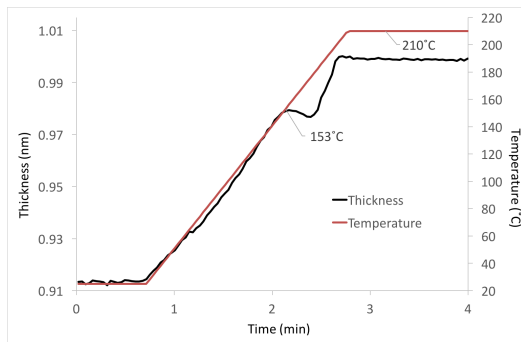
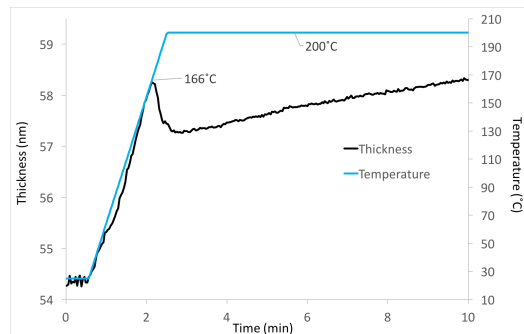
(a) 50 nm 210°C (b) 50 nm 200°C

Figure 4.15: Thickness profiles measured by ellipsometry for 50 nm films annealed at 210°C (a) and 200°C (b).

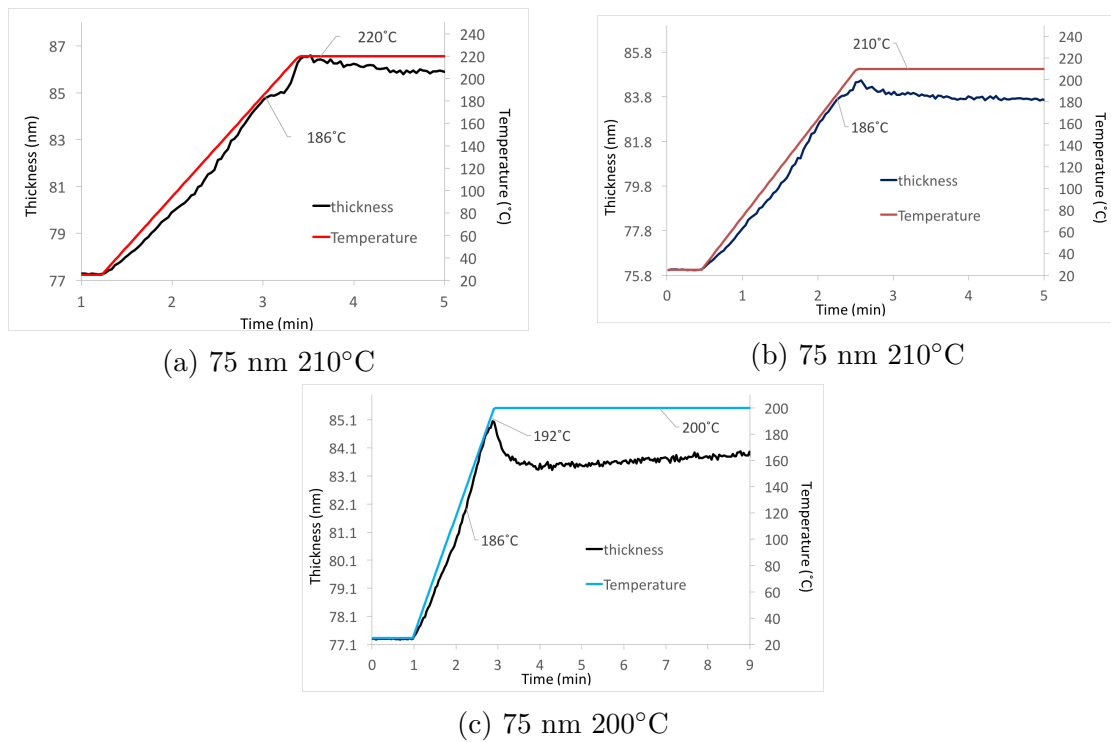


Figure 4.16: Thickness profiles measured by ellipsometry for 75 nm films annealed at 220°C (a), 210°C (b) and 200°C (c).

This behaviour is puzzling, as it would be expected that the shrinking would start at T_o as for annealing temperatures $\leq 200^\circ$. This change in behaviour is not really explainable at this stage and it could be important to study it in the future maybe with X-ray scattering.

4.3 Ordering as a function of temperature - an AFM analysis

In this section some AFM data are shown. These data were obtained in order to see if annealing a sample above or below T_o (200° and 155°) would produce any difference in the surface morphology of the film, in order to shed more light on the existence of T_o . This AFM analysis reported in figures 4.18 and 4.19 refers to the 50 nm samples, the ellipsometer curves of which were shown in the previous section in figure 4.4b where T_o was around 169°C . The AFM measurements were taken for two samples that have been annealed at 155°C and 200°C .

Well defined aggregates are noticeable (figures 4.18a and 4.19a) for the sample annealed at 155°C . It is possible that the fast ordering occurring at 200°C does not allow the formation of good aggregates as for the 155°C case. As the sample is 50 nm thick, it can be compared with the AFM image for the 40 nm sample annealed at 180°C showed in figure 3.9c of chapter 3; it can be noticed perhaps that the aggregates size are similar. The two samples have been stopped at two different stages of the ordering process, moreover the 200°C shows expansion whilst the 155°C do not show it (figure 4.17). From the different definition of the aggregates in the AFM images can be possible that 200°C is damaging for the ordering of the polymer, as the 200°C annealed sample shows a minor definition of the aggregates. But well-defined aggregates on the surface does not necessarily correspond to a more ordered film. The only way to find out is through X-ray scattering probing the entire film, which is reported in the next section.

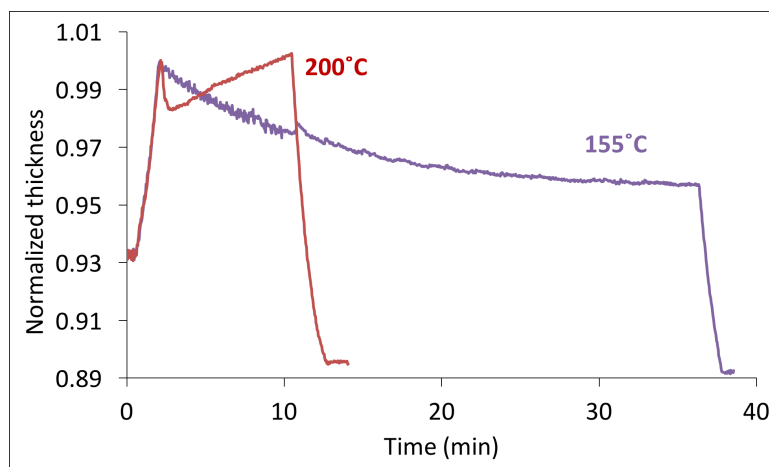


Figure 4.17: Thickness profiles of the two 50 nm PCDTBT samples annealed at 155°C and 200°C the which AFM images are shown in figures 4.18 and 4.19

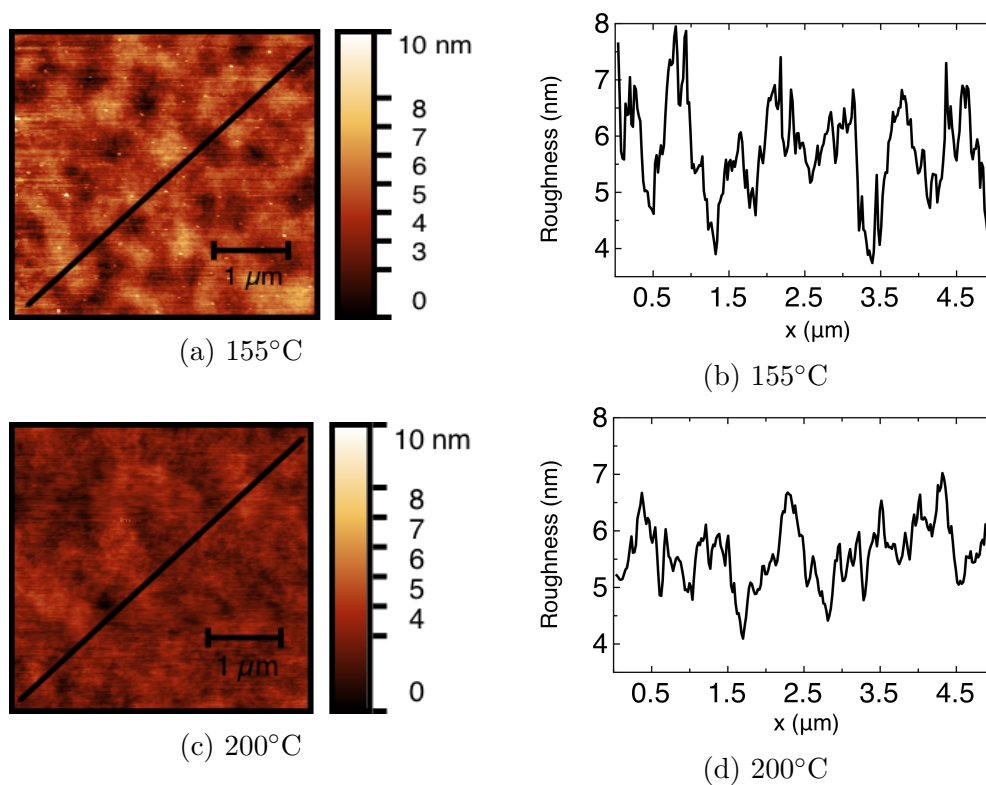


Figure 4.18: AFM comparison of 50 nm PCDTBT films annealed at 155°C (a) and 200°C (b). Scale: 10 μm .

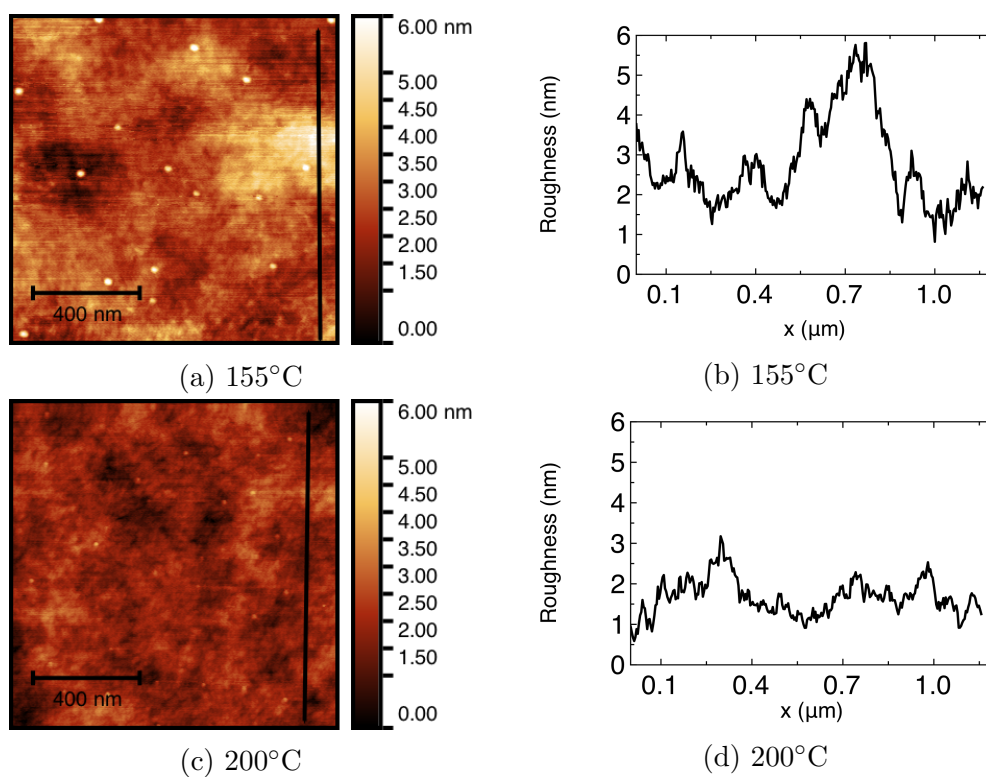


Figure 4.19: AFM comparison of 50 nm PCDTBT films annealed at 155°C (a) and 200°C (b). Scale: 2 μm .

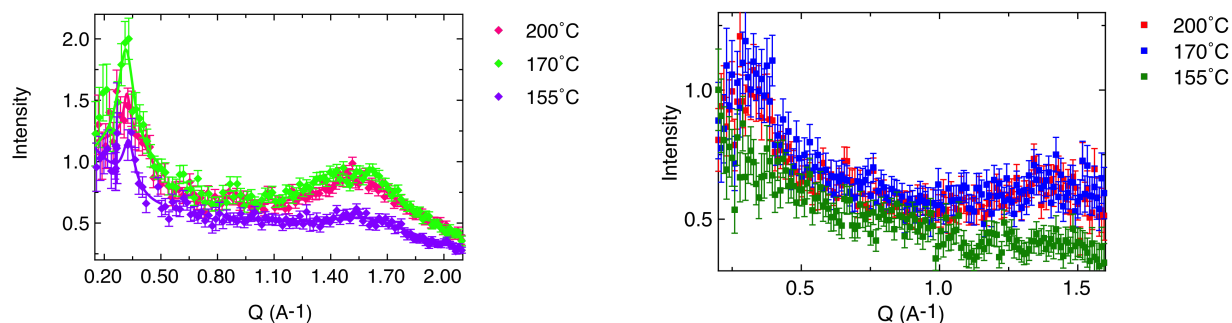
4.4 Ordering as a function of temperature - a GIWAXS analysis

GIWAXS was used to see if different annealing temperatures impact on the final crystal ordering in the films, as the different ellipsometry curves discussed in section 4.2 might suggest. Therefore the polymer films have been analysed using X-rays after having been annealed at different temperatures. The thickness is constant within a comparison, in order for the temperature to be the only variable. Two different thicknesses have been analysed in detail at GIWAXS (50 and 75 nm) in order to verify the reproducibility of the results for different thicknesses.

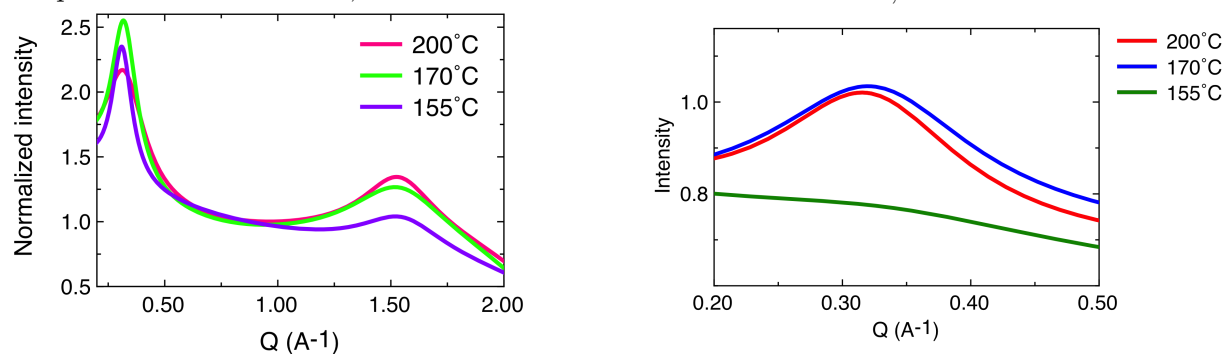
4.4.1 GIWAXS on 50 nm thick films

50 nm samples have been analysed at three different grazing incident angles, 0.18° , 0.16° and 0.14° to see how the interfaces influence the ordering process at different depths. The samples have been analysed out-of-plane and in-plane, to study not only the packing, but also the different orientation of the chains. As stated in the GIWAXS section of chapter 2 the critical angle for PCDTBT on the instrument used is 0.145° , so 0.16° and 0.18° are expected to be both at bulk values.

The 50 nm film displays the least scattering when annealed at 155°C (figure 4.20), which just indicates that there is less crystallinity in the film. This is consistent with the limited shrinkage of this film at this temperature as seen from the ellipsometry results in figure 4.4b although the AFM analysis (figure 4.18a) was showing well-defined aggregates. This to demonstrate that the presence of aggregates in AFM do not correlate with the high degree of ordering as measured by X-rays. Then, there is a difference of 1 \AA between the lamellar packing for samples annealed at 155°C and 200°C (table 4.1). As said in section 3.5 of the previous chapter, annealing seems to increase the distance between chains, so it is here: 20 \AA in the 200°C and 170°C annealed film that becomes 19 \AA in the film annealed at 155°C .

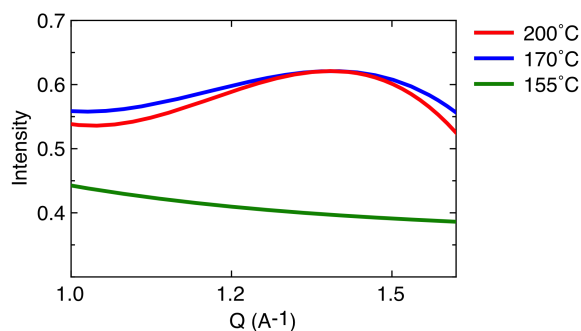


(a) Out-of-plane line cuts for scattering data of samples annealed at 200°C, 170°C and 155°C. (b) In-plane line cuts for scattering data of samples annealed at 200°C, 170°C and 155°C.



(c) Lorentzian and cubic polynomial functions fitting the out-of-plane scattering data.

(d) Lorentzian functions fitting the in-plane lamellar packing peaks.



(e) Lorentzian functions fitting the in-plane π - π stacking peaks.

Figure 4.20: Raw scattering data (a,b) and fitting curves (c-e) for GIWAXS experiments on 50 nm samples annealed at 200°C, 170°C, 155°C at a grazing incident angle of 0.18°. The π - π stacking peaks in the in-plane direction are extremely weak and no fitting is possible.

The most crystalline sample is the one annealed at 170°C (highest intensities in the out-of-plane direction). It might indicate that annealing samples at 200°C is too high and it could cause some chemical degradation that disrupts the crystal structure. This could in turn provoke that secondary expansion at the ellipsometry that happens after the first shrinking part.

The fact that the π - π stacking peaks in the in-plane direction are very weak and almost zero for the 155°C means that this temperature is not high enough to change the orientation of the chains from flat-on to edge-on: the as-cast sample presents mainly flat-on orientations as demonstrated in chapter 3. It can be that the edge-on orientated π - π stacking is the less energetically favoured and requires higher energies to be achieved, which is why the as-cast films present mainly flat-on orientated π - π stacking.

1st peak (lamellar packing)						
T (°)	x_0 (Å ⁻¹)	$2\pi/Q$ (Å ⁻¹)	$I(x_0)$	μ (Å ⁻¹)	L (Å)	$Area$
200°C	0.31 (0.005)	20 (0.32)	0.62 (0.13)	0.11 (0.04)	28 (10)	0.21 (0.09)
	0.32 (0.009)	20 (0.56)	0.15 (0.04)	0.07 (0.04)	45 (26)	0.03 (0.02)
170°C	0.32 (0.012)	20 (0.75)	0.90 (0.11)	0.07 (0.02)	45 (13)	0.20 (0.06)
	0.32 (0.011)	20 (0.69)	0.13 (0.05)	0.09 (0.03)	35 (12)	0.04 (0.02)
155°C	0.33 (0.002)	19 (0.12)	0.56 (0.14)	0.05 (0.02)	63 (25)	0.09 (0.04)
	0.34 (0.010)	18 (0.53)	/	/	/	/
2st peak (π - π stacking)						
200°C	1.53 (0.012)	4.0 (0.03)	0.29 (0.04)	0.19 (0.04)	16 (3)	0.17 (0.04)
	1.42 (0.050)	4.4 (0.15)	0.15 (0.03)	0.17 (0.09)	18 (10)	0.08 (0.04)
170°C	1.54 (0.015)	4 (0.04)	0.30 (0.08)	0.25 (0.03)	12 (1)	0.24 (0.07)
	1.42 (0.072)	4.4 (0.22)	0.07 (0.04)	/	/	/
155°C	1.55 (0.020)	4 (0.05)	0.15 (0.06)	0.22 (0.10)	14 (6)	0.10 (0.06)
	/	/	/	/	/	/

Table 4.1: Fitting parameters for the GIWAXS data shown in figure 4.20 for a grazing angle of 0.18°. The values in brackets are the standard errors. The first lines are the out-of-plane values, the second lines are the in-plane values.

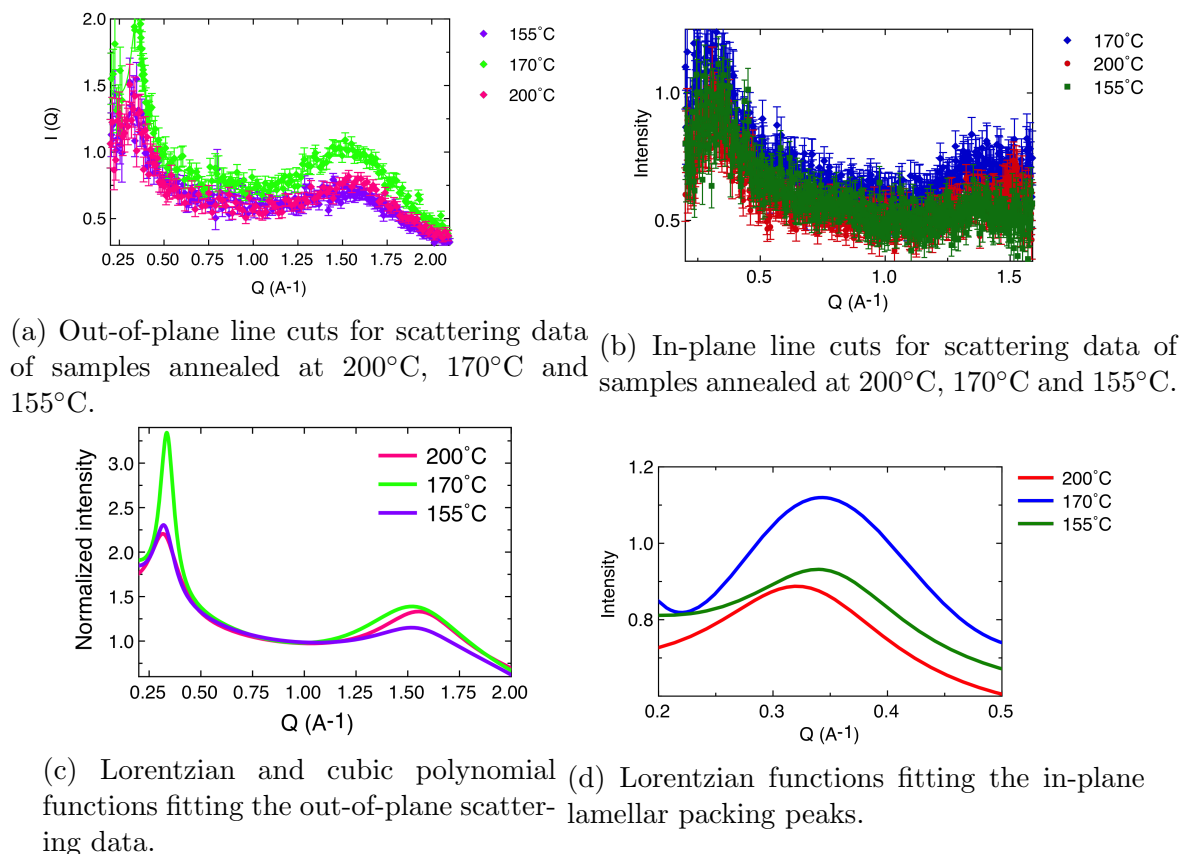
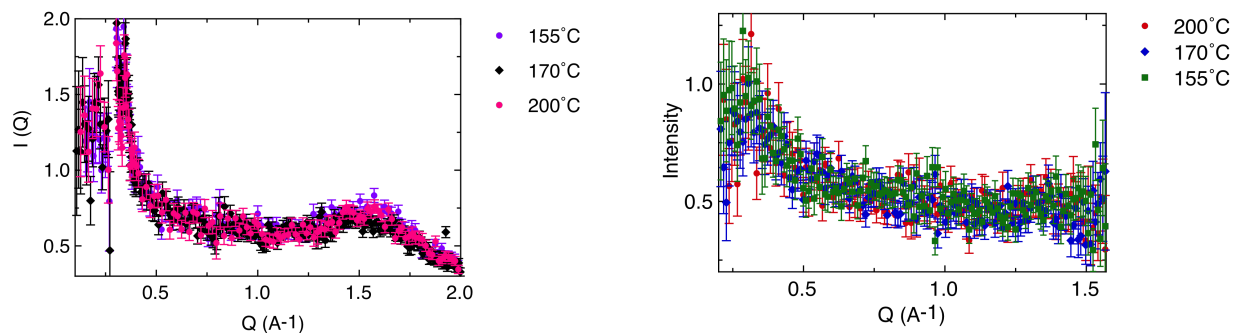


Figure 4.21: Raw scattering data (a,b) and fitting curves (c-e) for GIWAXS experiments on 50 nm samples annealed at 200°C, 170°C, 155°C at a grazing incident angle of 0.16°

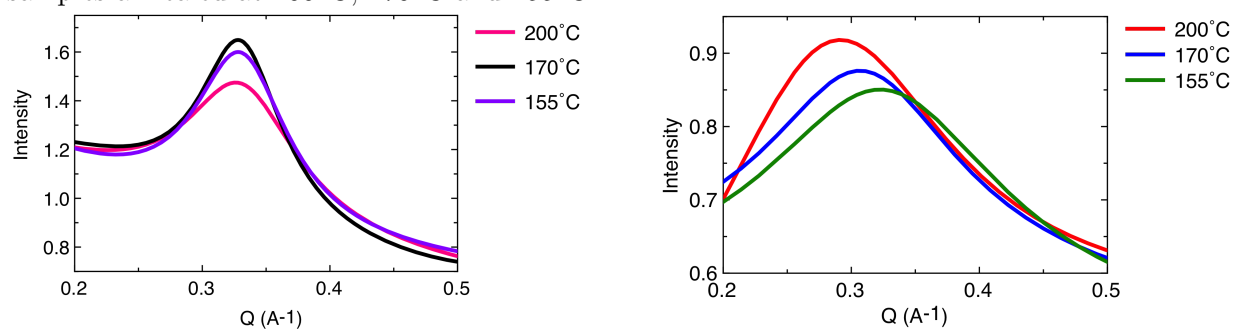
Moving towards the surface of the film, as the angle gets shallower, the trend stays the same for the lamellar packing in the out-of-plane direction: the most crystalline sample is the one annealed at 170°C, although 200°C and 155°C this time have very similar low intensities (looking at figures 4.21a and c). The in-plane lamellar packing in figure 4.21d has the highest intensity in the 170°C annealed sample.

1st peak (lamellar packing)			
T ($^{\circ}$)	x_0 (\AA^{-1})	$2\pi/Q$ (\AA^{-1})	$I(x_0)$
200 $^{\circ}$ C	0.32 (0.005)	20 (0.31)	0.52 (0.08)
	0.32 (0.007)	20 (0.44)	0.34 (0.07)
170 $^{\circ}$ C	0.35 (0.005)	18 (0.26)	1.36 (0.05)
	0.33 (0.060)	19 (3.4)	0.50 (0.19)
155 $^{\circ}$ C	0.32 (0.006)	20 (0.38)	0.51 (0.08)
	0.34 (0.006)	18 (0.32)	0.28 (0.08)
2st peak (π - π stacking)			
200 $^{\circ}$ C	1.57 (0.009)	4.0 (0.02)	0.35 (0.07)
	/	/	/
170 $^{\circ}$ C	1.54 (0.008)	4 (0.02)	0.59 (0.1)
	/	/	/
155 $^{\circ}$ C	1.57 (0.018)	4 (0.04)	0.15 (0.06)
	/	/	/

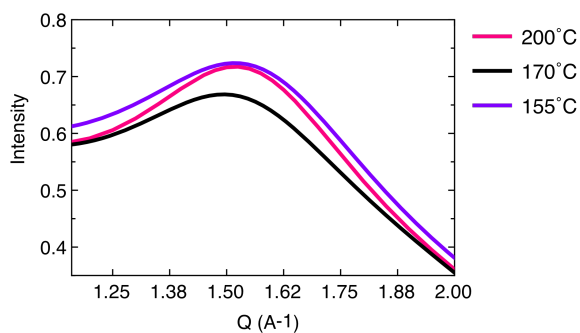
Table 4.2: Fitting parameters for the GIWAXS data shown in figure 4.21 for a grazing angle of 0.16° . The values in brackets are the standard errors. The first lines are the out-of-plane values, the second lines are the in-plane values.



(a) Out-of-plane line cuts for scattering data of samples annealed at 200°C, 170°C and 155°C. (b) In-plane line cuts for scattering data of samples annealed at 200°C, 170°C and 155°C.



(c) Lorentzian and cubic polynomial functions fitting the out-of-plane lamellar packing peaks. (d) Lorentzian functions fitting the in-plane lamellar packing peaks.



(e) Lorentzian functions fitting the out-of-plane π - π stacking peaks.

Figure 4.22: Raw scattering data (a,b) and fitting curves (c-e) for GIWAXS experiments on 50 nm samples annealed at 200°C, 170°C, 155°C at a grazing incident angle of 0.14°

1st peak (lamellar packing)			
T ($^{\circ}$)	x_0 (\AA^{-1})	$2\pi/Q$ (\AA^{-1})	$I(x_0)$
200 $^{\circ}$ C	0.33 (0.004)	19 (0.23)	0.50 (0.01)
	0.29 (0.012)	22 (0.91)	0.42 (0.04)
170 $^{\circ}$ C	0.33 (0.005)	19 (0.29)	0.50 (0.05)
	0.31 (0.009)	20 (0.58)	0.38 (0.06)
155 $^{\circ}$ C	0.33 (0.002)	19(0.12)	0.40 (0.04)
	0.32 (0.010)	20 (0.622)	0.35 (0.09)
2st peak (π - π stacking)			
200 $^{\circ}$ C	1.55 (0.007)	4(0.02)	0.12 (0.03)
	/	/	/
170 $^{\circ}$ C	1.52 (0.011)	4(0.03)	0.06 (0.02)
	/	/	/
155 $^{\circ}$ C	1.55 (0.009)	4 (0.02)	0.11 (0.02)
	/	/	/

Table 4.3: Fitting parameters for the GIWAXS data shown in figure 4.22 for a grazing angle of 0.14° . The values in brackets are the standard errors. The first lines are the out-of-plane values, the second lines are the in-plane values.

The 0.14° data have a rather low intensity, which is surprising given that the critical angle is expected to be close to this value. The raw scattering curves seem to overlap and the error bars are very large (figures 4.22a and b), thus the fittings in figures 4.22c-e are likely to be not very trustworthy. Although for the in-plane direction (figure 4.22d), the trend is once more respected: the higher annealing temperature increases the distance within the lamellar packing (table 4.3).

For all the three angles, the π - π stacking peaks in the in-plane direction are extremely weak and they could not be fitted. It is very difficult to assign a Q -value for the maximum, as the peak is also very broad, meaning that the π - π stacking might be present mainly in the flat-on orientation.

Concluding, annealing at higher temperature seems to increase the distance between chains, as concluded at the end of chapter 3. The most crystalline are the samples annealed at 170°C ; slightly less crystalline are the samples annealed 200°C . This confirms that an annealing temperature of 200°C is too high and it disrupts the crystallinity, as the expansion at the ellipsometry might show. On the other hand, annealing at 155°C for one or two hours does not allow the polymer to crystallise as much as annealing at 170°C for just 20 minutes.

4.4.2 GIWAXS on 75 nm thick films

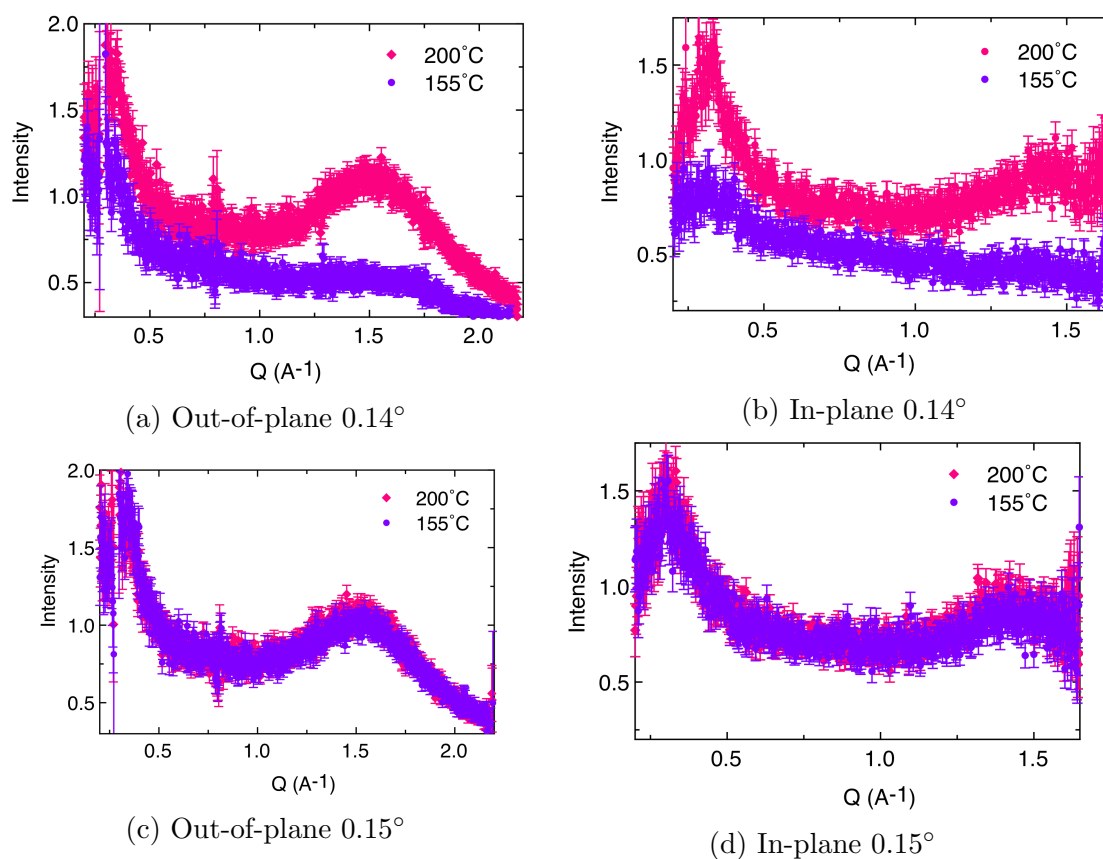


Figure 4.23: 75nm out-of-plane and in-plane for two different incident angles 0.14° and 0.15°.

In figure 4.23 the two annealing temperatures have the same intensities and Q values for the 0.15° angle (figure c and d). Figures 4.23a and b have different intensities (0.14° angle). This is because the scattering data come from two different samples: one annealed at 155°C and the second at 200°C, so they went through two different calibrations on the GIWAXS stage. In the case of the 0.14° angle (figures a and b) probably the angle of incidence was not exactly 0.14° for one of the two samples and the scattering intensity results to be lower. Otherwise it would not be possible to explain the intensity difference with the data for the 0.15° incident angle. In order to understand the issue with the incidence angle, the most intense scattering profiles for each sample have been compared in figure 4.24. Also in these scattering data there is no significant interchain difference between the two annealing temperatures, but the greatest scattering is for the sample annealed at 155°C, contrary to the results found in section 4.4.1 for the 50 nm films. A more complete study is then presented with angle scans for the different annealing temperatures.

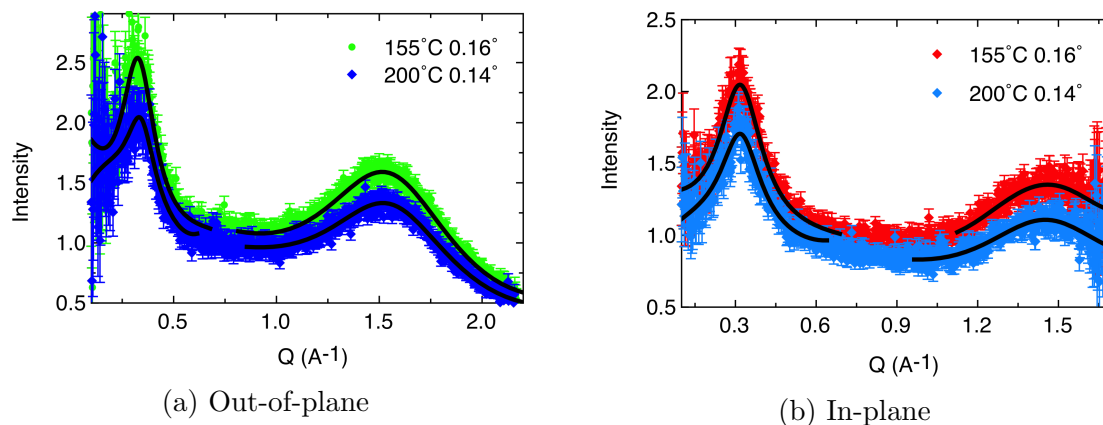


Figure 4.24: 75nm out-of-plane (a) and in-plane (b), grazing angle of 0.14° for 200°C and 0.16° for 155°C . The black lines correspond to the Lorentzian fitting of the peaks, the values with the error estimates are reported in table.

1st peak (lamellar packing)			
T ($^\circ$)	x_0 (\AA^{-1})	$2\pi/Q$ (\AA^{-1})	$I(x_0)$
200 $^\circ\text{C}$	0.34 (0.006)	18 (0.32)	0.6 (0.02)
	0.32 (0.005)	20 (0.31)	0.5 (0.05)
155 $^\circ\text{C}$	0.33 (0.004)	19 (0.23)	1.1 (0.03)
	0.32 (0.002)	20 (0.12)	0.7 (0.04)
2st peak (π - π stacking)			
200 $^\circ\text{C}$	1.55 (0.007)	4 (0.02)	0.3 (0.02)
	1.45 (0.111)	4 (0.31)	0.3 (0.03)
155 $^\circ\text{C}$	1.54 (0.005)	4 (0.01)	0.6 (0.02)
	1.55 (0.132)	4 (0.34)	0.3 (0.04)

Table 4.4: Fitting parameters for the GIWAXS data shown in figure 4.24. The values in brackets are the standard errors. The first lines are the out-of-plane values, the second lines are the in-plane values.

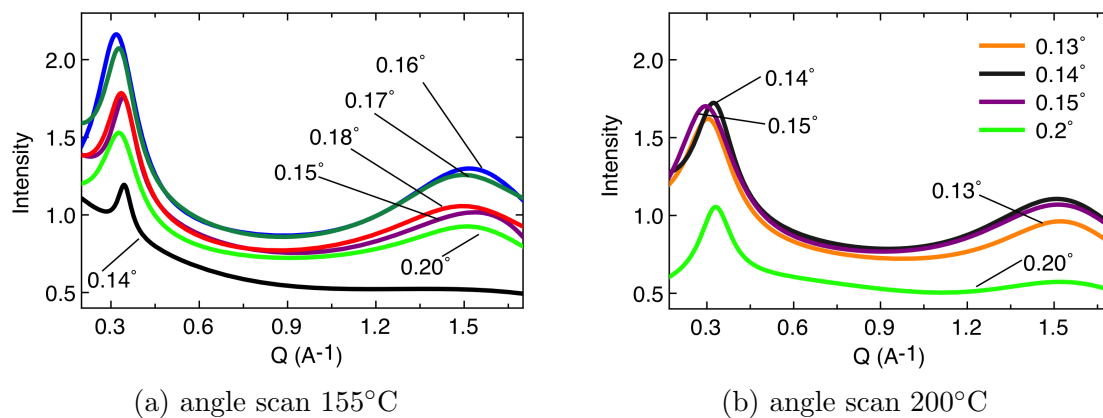


Figure 4.25: Fitting plots for the two temperatures out-of-plane line-cuts.

The angle scans presented in figure 4.25 were made to verify the value of the critical angle for the two samples. The result is that for the 155°C annealed film, the greatest scattering intensity is at the angle of 0.16° (explaining the higher intensity at this angle in figure 4.24) and at 0.14°/0.15° for the 200°C annealed sample. This last result (0.14°) is consistent with the mathematical calculation for the critical angle value. It is possible that the angle calibration for the 155°C annealed sample was not exact. As can be seen from figure 4.25a, the scattering at 0.14° is surprisingly low for a critical angle, but it might correspond instead to a 0.12° value.

In figure 4.26 is presented a study of the lamellar, π - π stacking distance and the π - π stacking

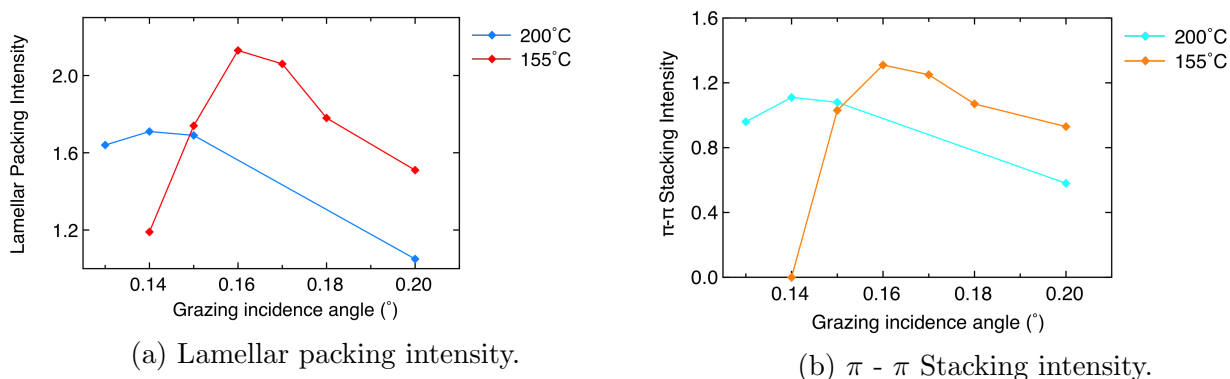


Figure 4.26: Out-of-Plane scattering intensities, comparison between the two temperatures, absolute intensities as function of the incidence angles (a,b), indicating the critical angles in the two samples.

relative scattering intensity as a function of depth; the plots in figure 4.26 present the change of these crystal characteristics as a function of the grazing incidence angle. From figure 4.26a it can be seen that for the sample annealed at 200°C the lamellar packing distance has generally a larger value than the sample annealed at 155°C, while the opposite is the case for the π - π stacking. It is very difficult to evaluate the location (Q value) of the maximum for the π - π

stacking peaks, as generally are very wide peaks. It might be wise to say the π - π stacking is approximately constant along all the depth of the film, probably larger towards the substrate in the case of the 155°C annealing experiment.

The relative intensities plot (figure 4.27c) does not show very significant differences between the two scattering peaks as measured in previous work [8] where the interval of ratios was 2.0 - 0.4 although the peak found for the lamellar stacking was at a Q value of 0.63 \AA^{-1} which is attributed to a second order lamellar packing while the peak at 0.33 \AA^{-1} here is a first order scattering.

The in-plane scattering curves in function of the angle (not shown), have a very similar intensity trend to the out-of-plane, so they are omitted. The in-plane data present, although, larger distances for the π - π stacking. Flat-on π - π stacking is more densely packed than the edge-on π - π stacking. .

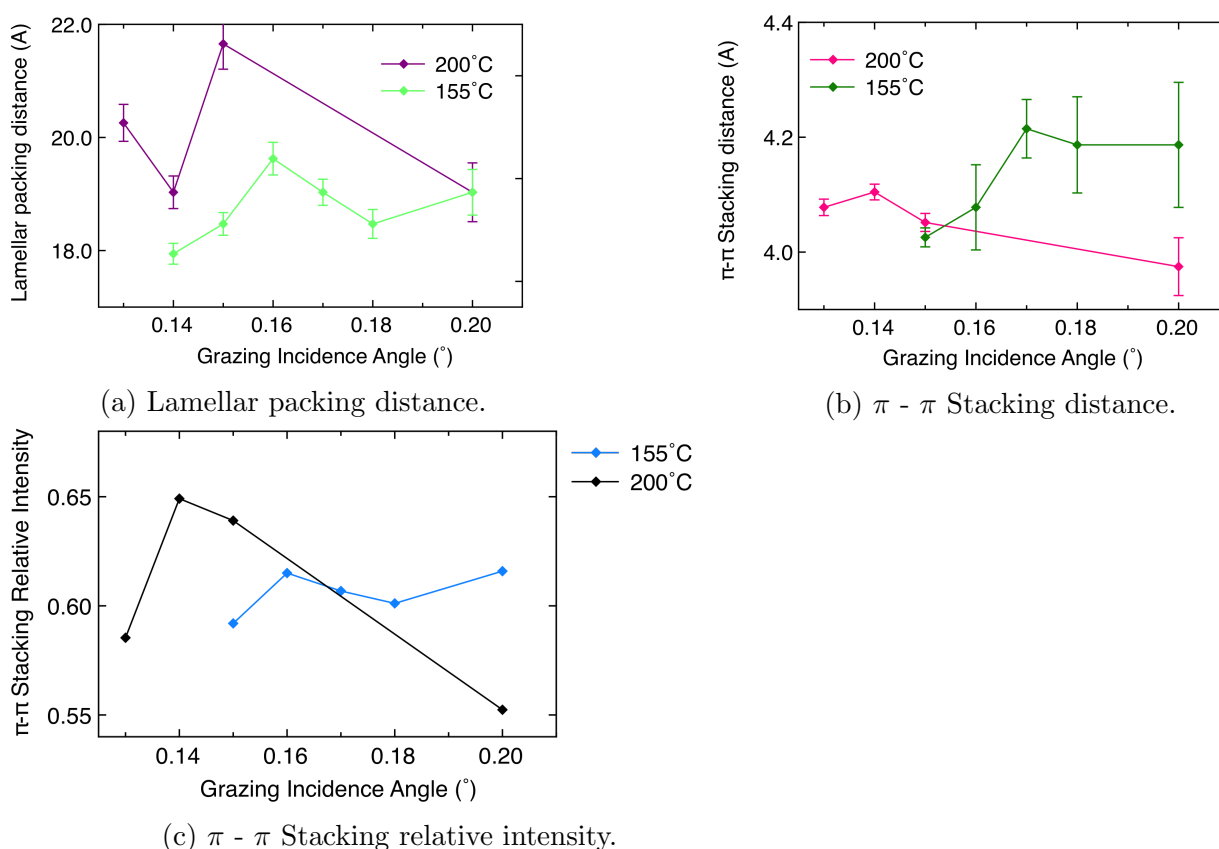


Figure 4.27: These plots show the values of the distances in Å for the two characteristic distances of the polymer, lamellar packing and the π - π stacking, obtained with $L = 2\pi/Q$, where Q is obtained by a Lorentzian fitting of the scattering curves in the out-of-plane direction for the two samples annealed at 200°C and 155°C.

Ultimately, the distances for the 75 nm samples have the same value as for the 50 nm samples presented in section 4.4.1 meaning this 15 nm thickness difference do not influence the packing distances. The intensities for the 75 nm samples are higher than in the 50 nm as it is expected to be in a thicker samples: more material to give scattering. It is also observable that scattering intensities are higher in the out-of-plane direction, as concluded in the chapter 3, so the chains are oriented preferably with the face parallel to the substrate.

4.5 Discussion - Temperature dependence in PCDTBT films

From the data presented in this chapter it is possible to see something striking. The ellipsometry curves show the existence of a characteristic temperature that can be defined as T_o (or temperature where the crystallisation starts): if the target temperature T_i for the annealing is 200°C, the film would start shrinking at a temperature $T_o \leq T_i$ (for example 180°C). Obviously, if the target temperature T_i is $\leq T_o$ (e.g. 160°C), the film would start shrinking at 160°C; in this case the shape of the ellipsometer curve (thickness vs time and temperature) will be different, a preordering phase will become noticeable (section 4.2.1). It is clear that different mechanisms contributes to the ordering of PCDTBT and they become visible when the polymer is annealed at different temperatures. At lower temperature, near the limit of the T_g , the shape of the isotherm changes once more, not corresponding anymore to an exponential decay, but to a linear one.

Studying the crystallisation activation energy for different thicknesses of PCDTBT, has also allowed to recognise two different trends for thin and thick films. The activation energy is minimum for thin films, where more of the polymer film is exposed to air therefore the polymer chains have a better mobility, which helps to suppress the crystallisation activation energy.

Analysing the GIWAXS results, a general trend suggests that the samples annealed at lower temperatures (140°C - 150°C) present the lowest scattering intensities, which is how it would be expected by observing the ellipsometry curves: the film thickness does not reach a plateau during the isotherm before the experiment is done, meaning that the polymer film did not

crystallise completely. Ellispometry curves for intermediate annealing temperatures (160°C - 170°C) reach a plateau, from which it would be expected that the maximum degree of crystallinity has been reached, because no more shrinkage occurs. Higher temperatures (180°C - 200°C) also reach a maximum shrinkage, but a following thickness expansion is observable, probably a sign that the ordering within the polymer film is diminishing once again probably for the excessive annealing time and temperature.

Regarding the location of the scattering peaks along the Q -axis in the X-rays results, there does not seem to be an appreciable difference in the lamellar or π - π stacking distances at different annealing temperatures. In some cases is shown that annealing at very high temperatures, such as 200°C disrupts the ordering as a larger distance between the chains suggests. These larger interchain distances at higher temperature observable in the out-of-plane directions might be the cause of the expansion of the films at high temperatures.

Another striking result is the absence or extremely weak scattering of the π - π stacking peaks in the in-plane direction for as-cast samples. This means that the configuration that is acquired quicker and preferentially is the flat-on orientation of the chains. In the as-cast samples, polymer chains do not tend to π -stack edge-on, but most of the π - π stacking occurring is mostly flat-on the surface which is responsible for the out-of-plane scattering. In the 3rd chapter the GIWAXS data presented in section 3.5, showed that the as-cast samples preferred orientation was out-of-plane. The annealing processes then support the edge-on orientation, as the in-plane intensity increases with temperature. For this reason, it could be possible that the edge-on orientation is thermodynamically favoured, whilst the flat-on orientation is the kinetically supported one.

Chapter 5

Expansion during the isotherms

5.1 Introduction

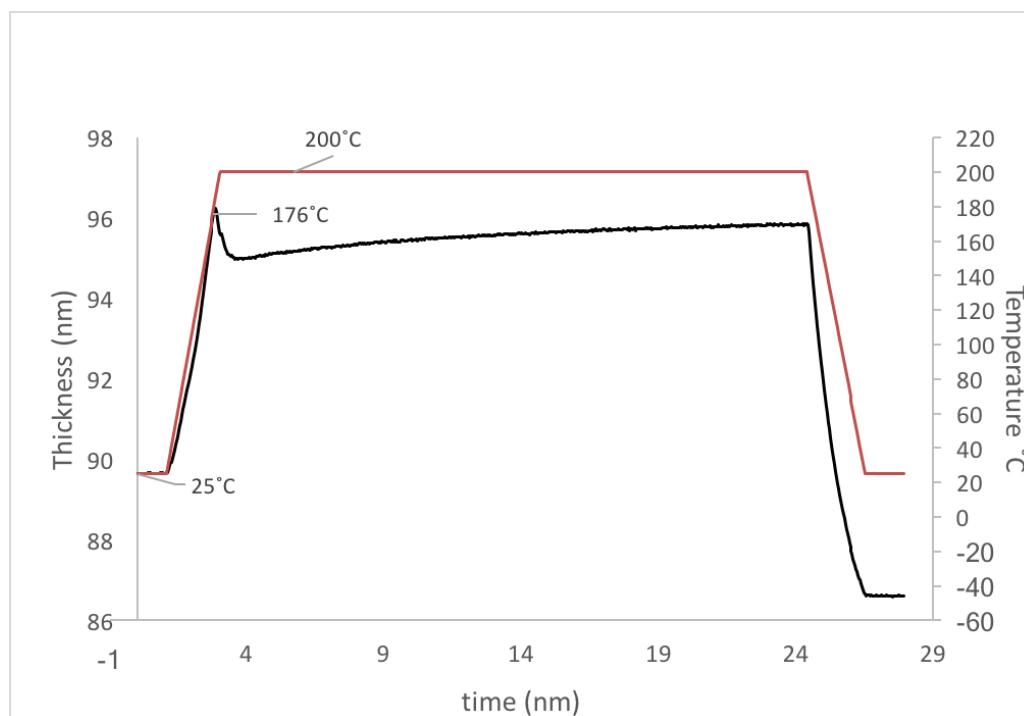


Figure 5.1: Example of a sample showing expansion during the isothermal annealing at 200°C ($T_o = 176^\circ\text{C}$)

During the isothermal annealing of PCDTBT films, in some cases it is possible to notice an expansion that follows the initial shrinking (figure 5.1). Films that show an expansion are usually the ones that are heated above the temperature T_o . As it is possible to notice from the

ellipsometry curve, the film starts to shrink at 176°C, while the temperature of the sample keeps increasing until it reaches the target temperature of 200°C. After the shrinkage to a minimum thickness, the polymer expands again spontaneously until is cooled down to 25°C.

In this chapter have been gathered all the experimental results where the film showed an expansion like the one described in figure 5.1 in order to understand the phenomenon. Usually films heated at a $T \leq T_o$ do not show any expansion, as it is possible to see from the purple curve in figure 5.2, belonging to a sample heated at 155°C ($T_o = 169^\circ\text{C}$).

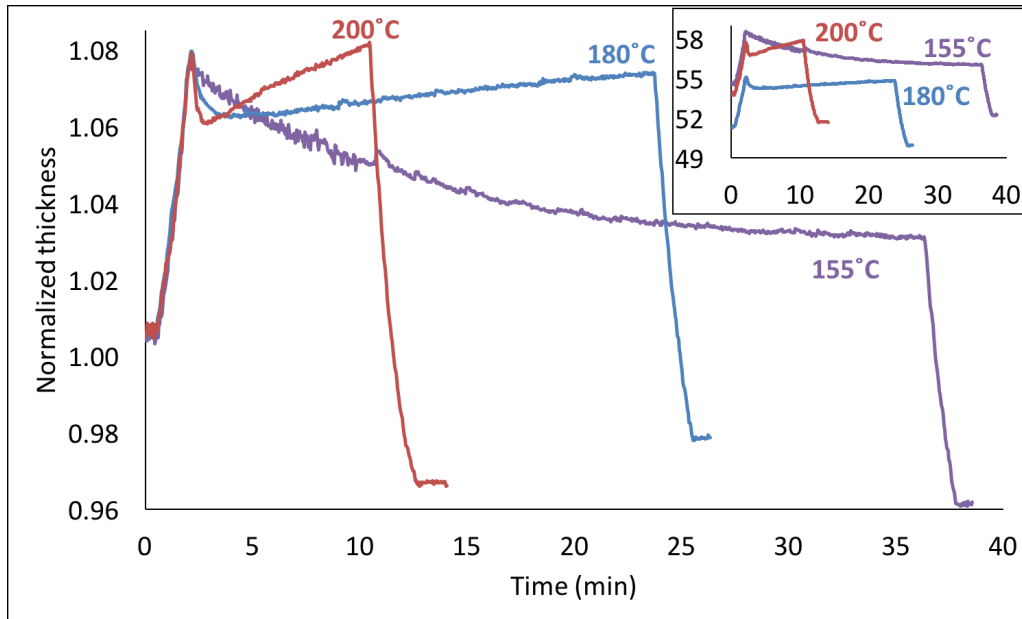


Figure 5.2: Thickness profile measured by ellipsometry for a 50 nm sample. $T_o = 169^\circ\text{C}$. It is possible to see that the film expands as the annealing temperature goes from 155°C to 200°C. In the insert are the plots with the absolute thickness value in nm on the y-axis.

In order to gain some insights, samples that showed expansion and samples that did not have been analysed with AFM and GIWAXS. It was not possible to analyse the samples at high temperatures with these two techniques, so it had been necessary to cool down the samples to room temperature before analysing them with AFM or GIWAXS. For this reason there were two ways to compare films that were subject to an expansion and films that were not:

- samples annealed for different time-lengths, *i.e.* same annealing temperatures, but cooled down before and after the expansion happened;
- samples annealed at different temperatures: T lower than T_o usually do not show any expansion. For annealing temperatures $\geq T_o$, the expansion becomes more evident in-

creasing the annealing temperature, therefore, GIWAXS, AFM and UV-vis data have been collected at different annealing temperatures, to see how the surface morphology and crystallinity of the polymer films change.

As already said at the beginning of this section, the perfect experiment would have been to analyse the sample *in situ* with AFM or GIWAXS at the annealing temperature, *e.g.* 200°C, taking images every minute or so in order to follow the ordering process at high temperatures. Because once the sample is cooled down at room temperature, the crystallinity and/or the morphology of the polymer change, so the result is not a picture of what happened at 200°C that caused the expansion. The AFM apparatus that has been used for this thesis and the GIWAXS stage could not allow an *in situ* annealing of the polymer films. The only technique that gave the possibility to take pictures of the sample at different points of the annealing curves was ellipsometry and the possibility to save the UV-vis spectra of the films. It has been possible to collect optical data of the PCDTBT films every 0.9 seconds, throughout the annealing process, obtaining information about the thickness and the absorption spectra at every point. The intensity of the signal is the value of the extinction coefficient for PCDTBT and processes such as aggregation and crystallisation changes in extinction coefficient are all to be attributed to changes in aggregation and crystallisation processes [129–131]. This experimental part has been carried out by inspiration from the work of Staniec et al. [129] where they studied the morphological change of P3HT during solvent casting, through changes in extinction coefficient measured by ellipsometry. For PCDTBT less information that correlates the absorption spectra to its morphology is available than for P3HT. The correlation between morphology and extinction coefficient is not completely clear, but an increased crystallinity should correspond to an increased a red-shift in the spectral peaks as the conjugation length of the polymer improves with the ordering [132, 133]. The correlation between crystallinity and the intensity of the extinction coefficient is a more complicated matter, due to the influence of the light scattering from the crystal structure, so it is not easy to make predictions about the degree of crystallinity from the analysis of these spectra [134].

5.2 Comparison between samples annealed for different time-lengths

In this section samples that expanded and samples that did not have been compared. The only difference is the duration of the annealing process: annealing temperatures and thickness were kept constant. It was possible to notice in chapter 4 that at high enough temperatures the expansion of the polymer increases linearly with the time and the higher the temperature the faster the process.

Three different thicknesses: 50 nm, 70 nm and 220 nm have been compared to verify the robustness of the results and the effect of the different film thickness on the ordering.

5.2.1 UV-vis spectroscopy and GIWAXS analysis of 90 nm thick films (expanded vs not expanded)

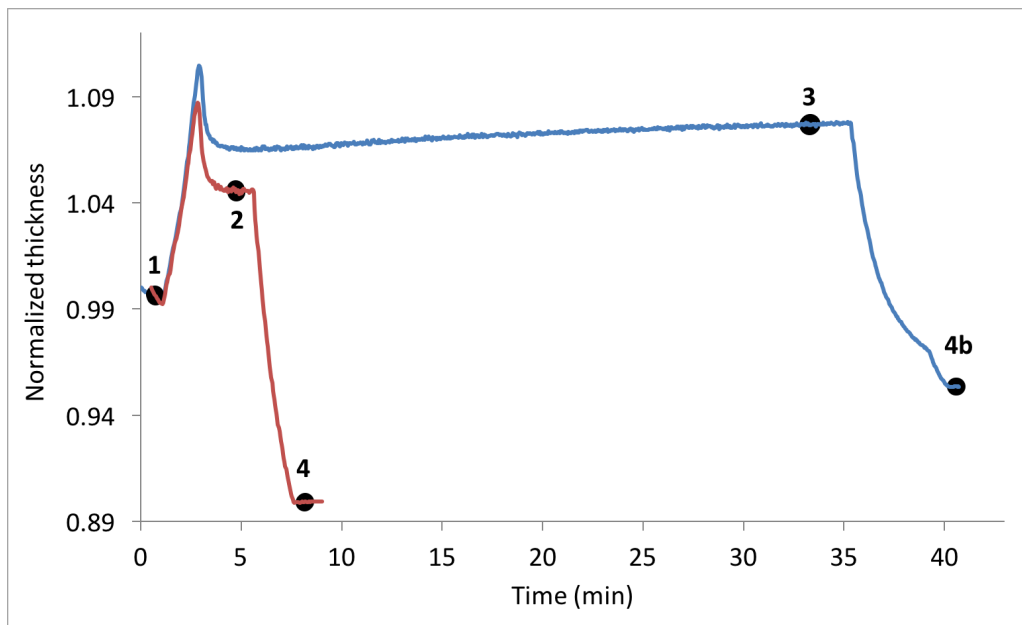


Figure 5.3: Ellipsometry thickness profiles of two 90 nm samples annealed at 200°C for a different amount of time, the red curve did not expand while the blue curve shows some expansion. They both start shrinking at 184°C, T_o .

Two 90 nm thick samples have been annealed for about 5 and 35 min and the thickness profiles are shown in figure 5.3 and the light absorption of the polymer in the UV-visible region has been studied at different points of these two curves.

The UV-visible absorption spectrum for PCDTBT is constituted by two absorption peaks: one at about 390 nm and the second at 580 nm, corresponding to two electronic transition from the ground state S_0 to two different charge-transfer like excited states S_1 and S_2 . The absorption varies depending on the temperature and state at which the polymer is (solution or thin film), this is because of the different packing of the polymer chains, generally the more the polymer is ordered and dense the higher is the absorbance of light (described in detail in chapter 2). Another important phenomenon is the red-shift of the absorption bands that indicates an increased conjugation length and better delocalisation of π orbitals in unsaturated polymers.[132, 133]

The intensity of the signal is the value of the extinction coefficient for PCDTBT and processes such as aggregation and crystallisation changes in extinction coefficient are all to be attributed to changes in aggregation and crystallisation processes [129–131]. This experimental part has been carried out by inspiration from the work of Staniec et al. [129] where they studied the morphological change of P3HT during solvent casting, through changes in extinction coefficient measured by ellipsometry. For PCDTBT is not available the same amount of information that correlates the absorption spectra to its morphology as it is for P3HT. The correlation between morphology and extinction coefficient is not completely clear, but an increased crystallinity should correspond to an increased a red-shift in the spectral peaks as the conjugation length of the polymer improves with the ordering [132, 133]. The correlation between crystallinity and the intensity of the extinction coefficient is a more complicated matter, due to the influence of the light scattering from the crystal structure, so it is not easy to make predictions about the degree of crystallinity from the analysis of these spectra [134].

What it is clear from the spectra in figure 5.4 is that the absorption is reduced when the film is at 200°C; this is because of the lower density of the material at high temperatures, compared to when the sample is at 25°C. The blue curve in figure 5.4, corresponding to the expanded film results, is blue-shifted from the yellow curve, that corresponds to the minimum value of the film thickness at 200°C (where the film is presumably the most ordered). The blue-shift corresponds to a reduced conjugation of the chains, supporting the fact that annealing at high temperatures disrupts π - π stacking in PCDTBT. Another peculiarity is the fact that the

intensity is inverted for the two peaks between the blue (expanded) and yellow (not-expanded) curves, with the presence of an isosbestic point: the expansion influences differently the two electronic transitions and the isosbestic point might indicate a transition between two phases. From figure 5.5a it is also possible to see the red-shift from the melted-quenched film (black) to the film after the isotherm (green), meaning the annealing at 200°C increased the conjugation length of the polymer, and the intensity of the highest energy peak.

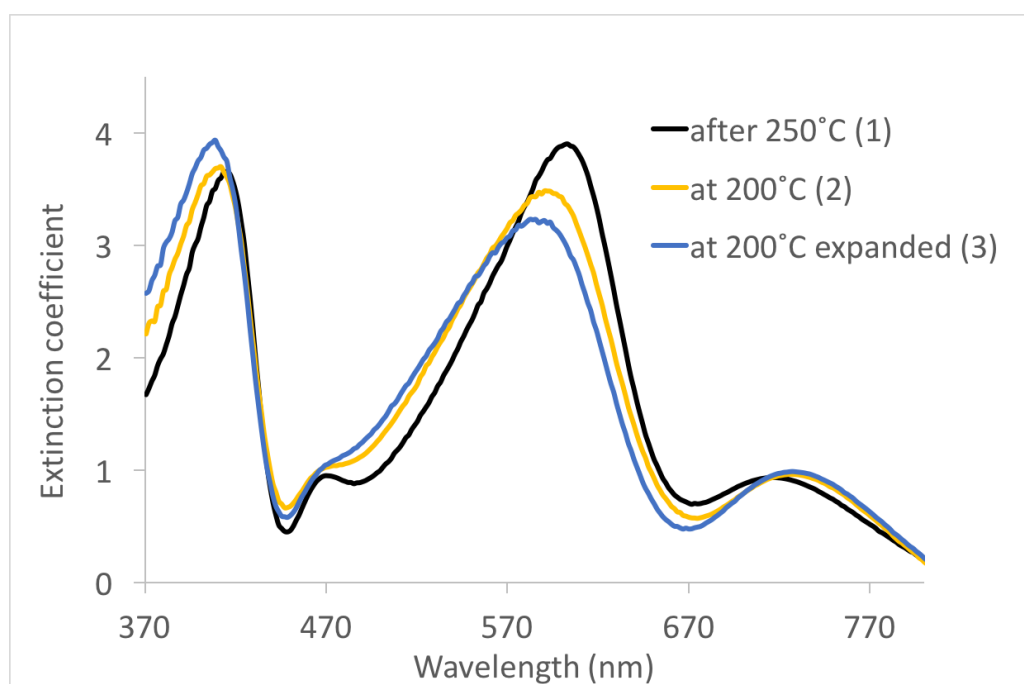
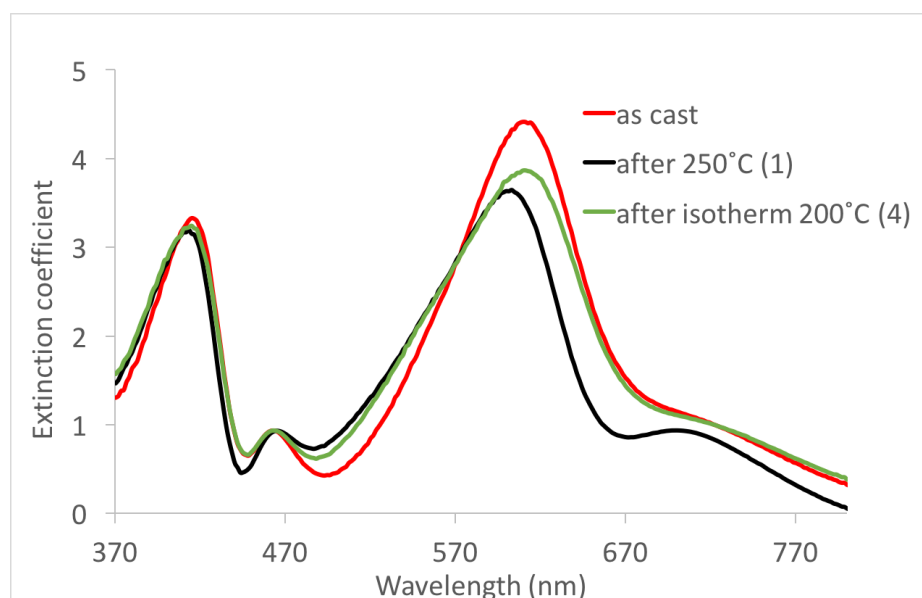
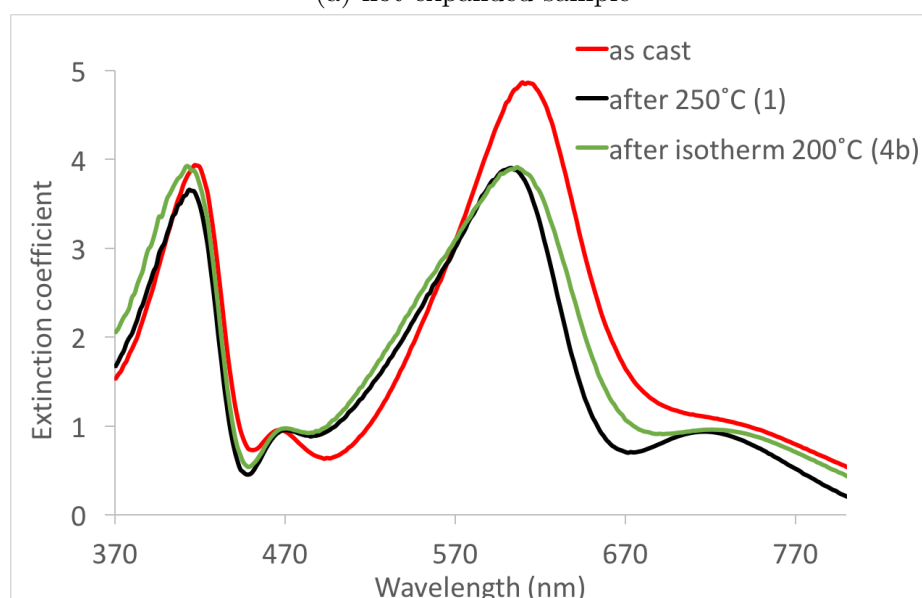


Figure 5.4: Spectra of a sample at 200°C at the 4th minute of the annealing process just after the shrinking peak (yellow), compared with a spectra taken at the 33rd minute at 200°C (blue) where the film is expanded, both compared to the spectra of the sample at 25°C after the melting-quenching (black).



(a) not expanded sample



(b) expanded sample

Figure 5.5: Absorption spectra taken at room temperature (25°C), relative to figure 5.3. Figure (a) and (b) are the comparison between the spectra of three samples after each step of the annealing protocol: an as-cast sample one day after spin-coating (red), after the melting-quenching procedure (black) and after the 200°C isotherm (light green).

The as-cast sample (red lines figure 5.5a and b) is the most red-shifted, supporting the previous finding that annealing does not improve crystallinity in PCDTBT films [71], as concluded also in chapter 3. It is possible to notice comparing the green curves in figures 5.5a and b (absorption of the film after the isotherm) that the second peak ($\lambda = 580$ nm) is higher and more red-shifted in the not-expanded sample. On the other hand, the first peak ($\lambda = 390$ nm) has the same absorbance for the three spectra of the not-expanded sample (figure 5.5a); for

the expanded sample (figure 5.5b) the 390 nm peak is the most intense for the as-cast (red spectrum) and 200°C annealed sample (green spectrum). For the as-cast the 390 nm peak is also red-shifted. We could speculate that the expansion derives from some more ordered portion of the polymer that is responsible for the enhanced intensity of the 390 nm peak. This peak is higher in intensity after the expansion, for the expanded sample (figure 5.5b) compared to its intensity for the not-expanded sample (figure 5.5a). So opposite behaviour for the two peaks in the green spectra. The higher order responsible for the 'growth' of the 390 nm peak in figure 5.5b could have impacted the ordering responsible for the 580 nm peak causing its lower intensity going from figure 5.5a to figure 5.5b. The expansion happens spontaneously at high temperatures because the polymer might be driven to achieve a different state of order with a minor potential energy or it just might be going towards a new amorphous state. Banerji *et al.* [132] studied the different moieties of PCDTBT to try to understand which moieties are responsible for which energy transfer. This is probably the right method to understand what phenomenon is causing the expansion, but the solution is not trivial. The dTBT (4,7-di(2-thienyl)-2,1,3-benzothiadiazole) moiety for example is the one responsible for the typical "camel back" shape of PCDTBT absorption spectrum.

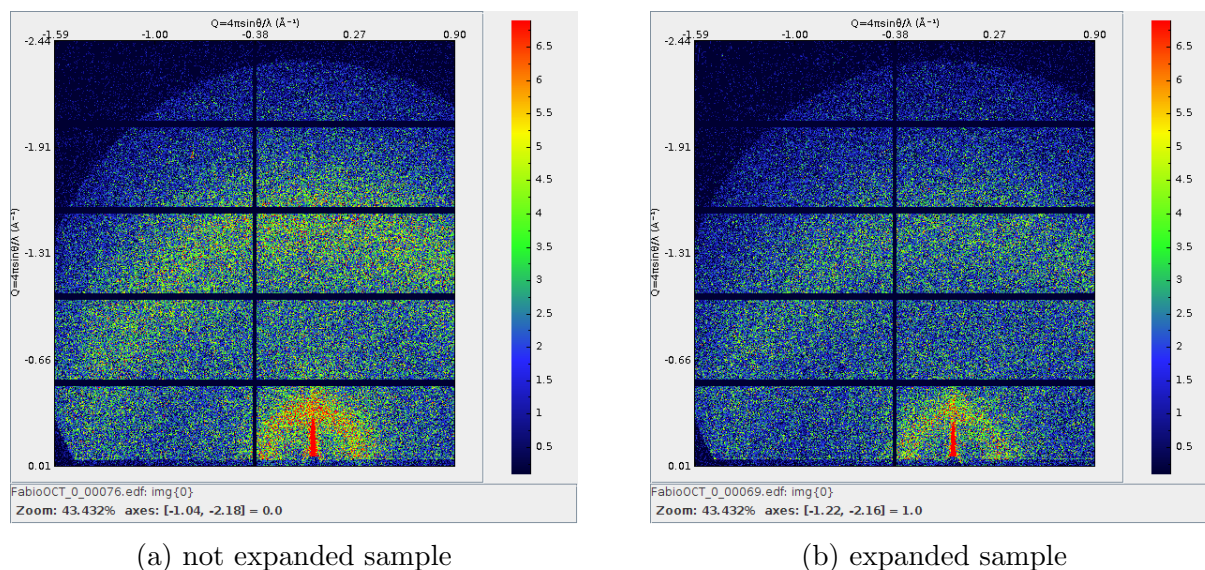


Figure 5.6: GIWAXS 2D images for the 90 nm samples annealed at 200°C (relative to ellipsometry curves in figure 5.3).

Figure 5.6 shows a comparison between 2D images taken with GIWAXS for the expanded and not-expanded samples for which ellipsometry curves are reported in figure 5.3 at the beginning

of this section. It is possible to notice the higher intensity from the not-expanded sample, but for a more detailed analysis is necessary to compare the in-plane and out-of-plane line-cuts and fitting curves in figure 5.7.

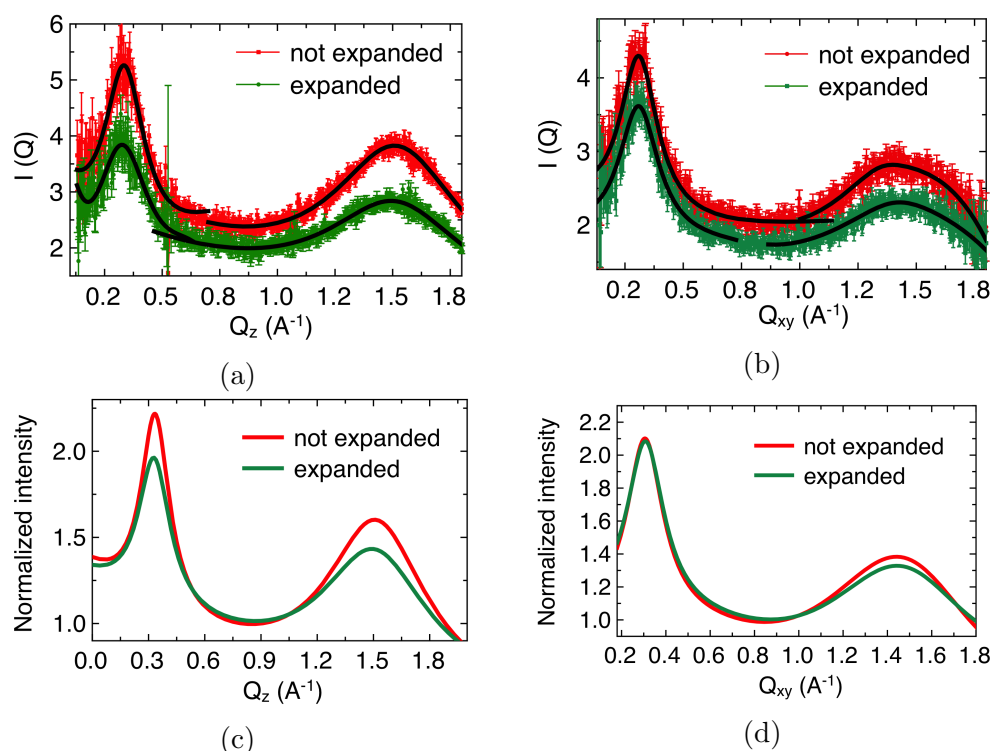


Figure 5.7: Out-of-plane (a) and in-plane (b) line-cuts for the 90 nm sample expanded (green) vs not expanded (red), of the GIWAXS data. (c) and (d) are the fitting curves for the raw data in (a) and (b)

Looking at the fitting curves for the out-of-plane direction in figure 5.7c the expanded film gives a less intense scattering than the not expanded sample, supporting once again the hypothesis that high temperature annealing is damaging for the ordering of the polymer (same conclusion of chapter 3 and [8]). Looking at the position of the peaks along the Q_z -axis (out-of-plane) in figure 5.7 there is apparently no difference between the two samples, but from the fitting parameters in table 5.1, looks like the lamellar packing peaks in the expanded sample are spaced 1 \AA more than the not expanded sample. This very little change in the out-of-plane direction, multiplied by the number of chains in a PCDTBT film, might be the explanation for the few nm expansion observable at the ellipsometry.

For the in-plane direction, the difference in Q values between expanded and not expanded samples is negligible: the Lorentzian peak fitting gave exactly the same x_0 value for the lamellar

1st peak (lamellar packing)						
	x_0 (\AA^{-1})	$\frac{2\pi}{Q}$ (\AA^{-1})	μ (\AA^{-1})	L	$I(x_0)$	Peak area
expanded	0.33 (0.002)	19 (0.1)	0.2 (0.04)	16 (3)	0.9 (0.03)	0.6 (0.1)
	0.31 (0.003)	20 (0.2)	0.1 (0.005)	31 (2)	1.0 (0.03)	0.3 (0.02)
not expanded	0.34 (0.001)	18 (0.05)	0.1 (0.01)	31 (3)	1.1 (0.02)	0.3 (0.03)
	0.31 (0.003)	20 (0.2)	0.1 (0.004)	31 (1)	1.1 (0.03)	0.3 (0.01)
2st peak (π - π stacking)						
expanded	1.50 (0.023)	4 (0.06)	0.3 (0.06)	9 (2)	0.8 (0.2)	0.8 (0.2)
	1.47 (0.014)	4 (0.04)	0.4 (0.06)	7 (1)	1.0 (0.3)	1.4 (0.5)
not expanded	1.51 (0.007)	4 (0.02)	0.3 (0.02)	10 (1)	0.9 (0.1)	0.8 (0.1)
	1.48 (0.014)	4 (0.04)	0.5 (0.06)	6 (1)	1.4 (0.4)	2.2 (0.7)

Table 5.1: Fitting parameters for the GIWAXS data shown in figure 5.7. x_0 is the position of the maximum of the Lorentzian peak on the x-axis, $2\pi/Q$ is the corresponding length to the Q -coordinate, μ the half width at half maximum of the peak, L is the coherence length and I the amplitude of the peak which counts for the scattering intensity excluded the background noise. The values in brackets are the standard errors. The first lines are the out-of-plane values, the second lines are the in-plane values.

packing peaks: distance of 20 \AA for both the samples (table 5.1). The π - π stacking peaks are very broad (low coherence length), indicating the low degree of ordering in the in-plane direction: there are fewer polymer chains oriented edge-on (in-plane signal) than oriented flat-on (out-of-plane signal). There is not much difference for the in-plane scattering intensity between the expanded and not expanded samples (figure 5.7d), slightly less π - π stacking in the expanded one.

5.2.2 AFM analysis of films annealed for different time-lengths

The atomic force microscopy analysis have been conducted on two different thicknesses, 70 nm and 220 nm, in order to see if there is any additional information attainable from a thickness comparison. All the samples have been annealed at 180°C under N₂ flux.

5.2.2.1 70 nm thick films

A series of 70 nm thick samples has been annealed for different times, from 15 min, to 650 minutes. At the end of each different annealing period, the surface morphology has been analysed with AFM in order to observe how the polymer surface changes with the progression of the expansion process. All the AFM images have been taken at 10 μm scale. Next to the AFM image, a roughness profile is reported, corresponding to the white/black line on the height image. The root mean squared roughness (RMS) is stated inside each roughness plot.

From the AFM pictures (figure 5.8) it is possible to notice a 'flattening' of the features on the surface of the film as the expansion increases. The surface morphology seems to change drastically passing from 60 to 300 min of annealing: it is possible to notice the increase in the size of the aggregates on the surface of the polymer film going from figure 5.8i (60 min) to figure 5.8k (300 min). This could mean that longer annealing times allow a better migration of material, thus an increased ordering achieved. An increased order would mean that the film becomes denser and thinner, which is not what is observed with ellipsometry.

It could be speculated that the high surface inequality of these samples could affect the ellipsometry detection of the thickness, producing in some cases an expansion. But the light-spot produced by the ellipsometer is about 2 - 3 mm in diameter, while the size of the agglomerates is 10³ smaller (about 2 μm each). 2 μm is probably too small to produce an error in the ellipsometer signal, because the oscillations in the thickness would be averaged out within the size of the light-spot on the film's surface.

Moreover, it was interesting to find out the impact of further annealing on a sample that had already been cooled down: the AFM image in figure 5.8m is from the sample annealed for 300 min at 180°C (black ellipsometry curve in figure 5.8b), which has then been cooled to 25°C

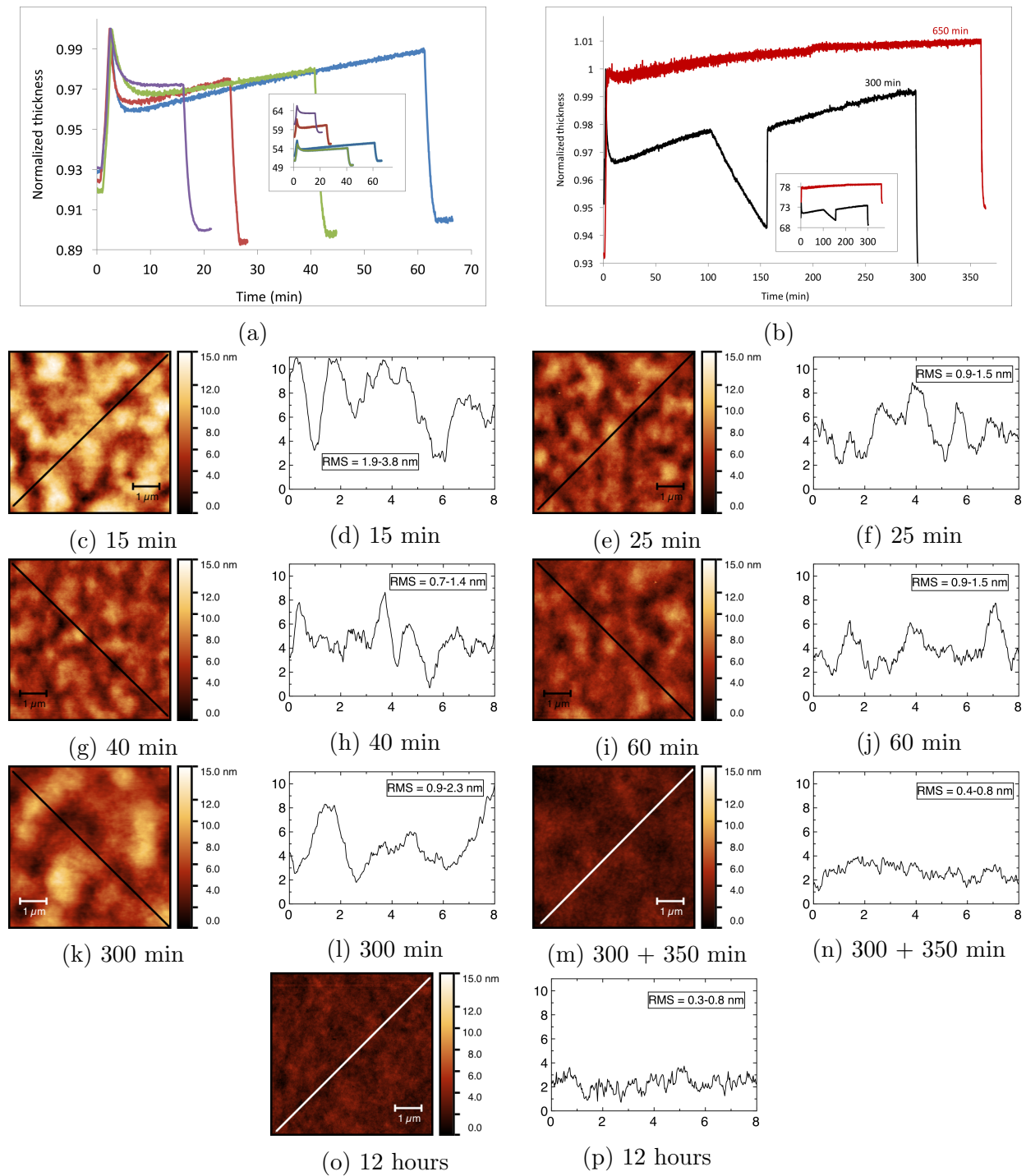


Figure 5.8: Samples annealed for different periods of time (annealing times stated in the captions). (a) and (b) report the correspondent ellipsometry curves (the inserts are the absolute thickness in nm). Figures (c) - (p) are all the AFM images taken for each sample at room temperature after the isotherm. The ellipsometry The 2D images are about $4\mu\text{m} \times 4\mu\text{m}$ and the x-axis of the roughness plots is in μm while the y-axis in nm.

and annealed again at 180°C for 350 more min, for a total of 11 hours. It is possible to see from the ellipsometry graph in figure 5.8b (red curve), that the film keeps expanding. The surface morphology for a different sample annealed this time for a total of 12 hours without

interruptions is shown in figures 5.8o (of which no ellipsometry data are available). Its surface morphology is very similar to the surface morphology of the sample annealed for 11 hours but that has been cooled down half way (figure 5.8m). Observing the surface morphologies for the two samples (figures 5.8m and 5.8o), it is possible to notice that they both look very flat, compared to the surface of the sample annealed for just 300 min (figure 5.8k).

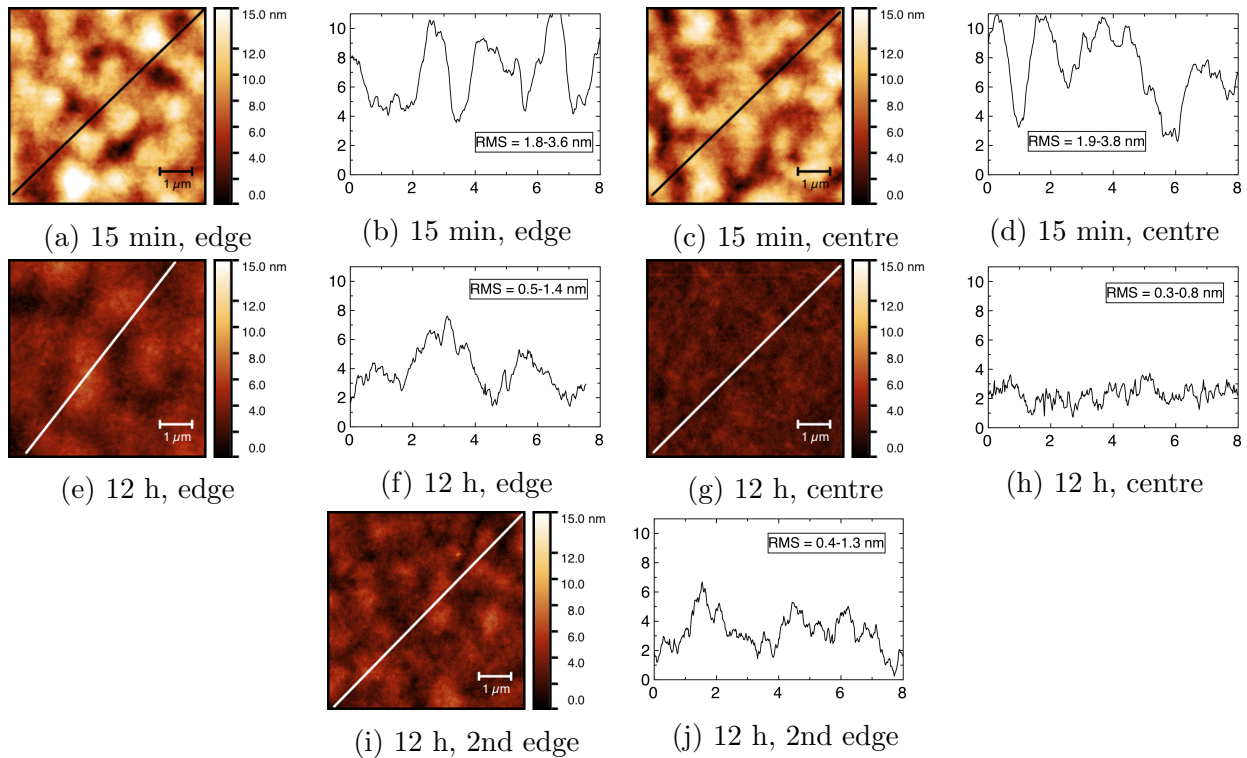


Figure 5.9: Comparison between AFM images taken at the edge and centre of the samples annealed at 15 min and for 12 hours.

The films annealed for 11 and 12 hours looked inhomogeneous at the optical microscope: thinner at the centre than near the edges of the films; therefore it has been necessary to analyse the surface morphology in different areas of the sample (figure 5.9). Two samples already shown in figure 5.8 had the surface morphology compared between the edge and the centre of the film: the sample that has been annealed for 15 min and the one annealed for 12 hour. It is possible to notice that there is no or little difference between the centre and the edge of the film for the 15 min annealed sample (figure 5.9a-c), while the morphology for the 12 hours annealed sample changes from the edge to the centre (figures 5.9e-j). For the 12-hours-annealed sample, the film looks rougher at the edges and with bigger aggregates of material. It could be possible that the proximity of the material to the edges of the substrate would aid the ordering. Another

possibility is that the material migrates towards the edges during annealing. The migration of material is a lengthy process, but it might explain why a film looks thicker near the edges while it looks less rough and thinner in the middle. In figures 5.11 and 5.12 in the next page, an absorption spectra comparison between the polymer film at different points of the ellipsometry curve in figure 5.10 is reported.

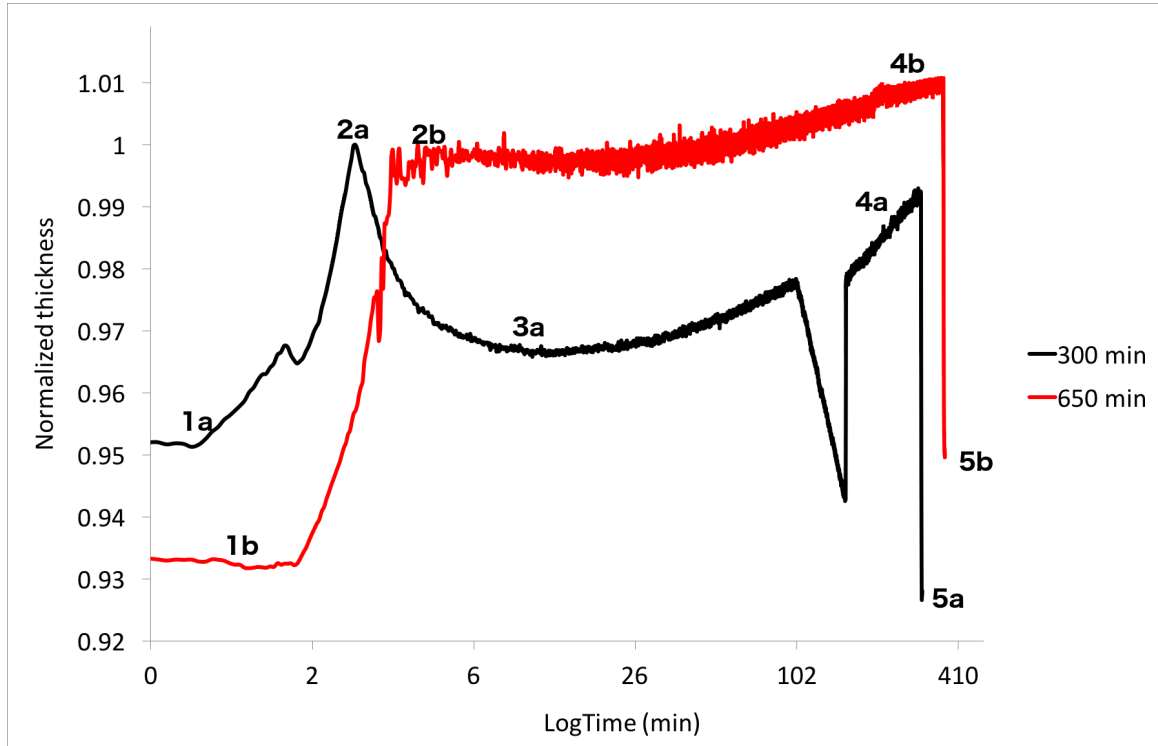


Figure 5.10: Ellipsometry curves for the 300 and 650 min annealed samples

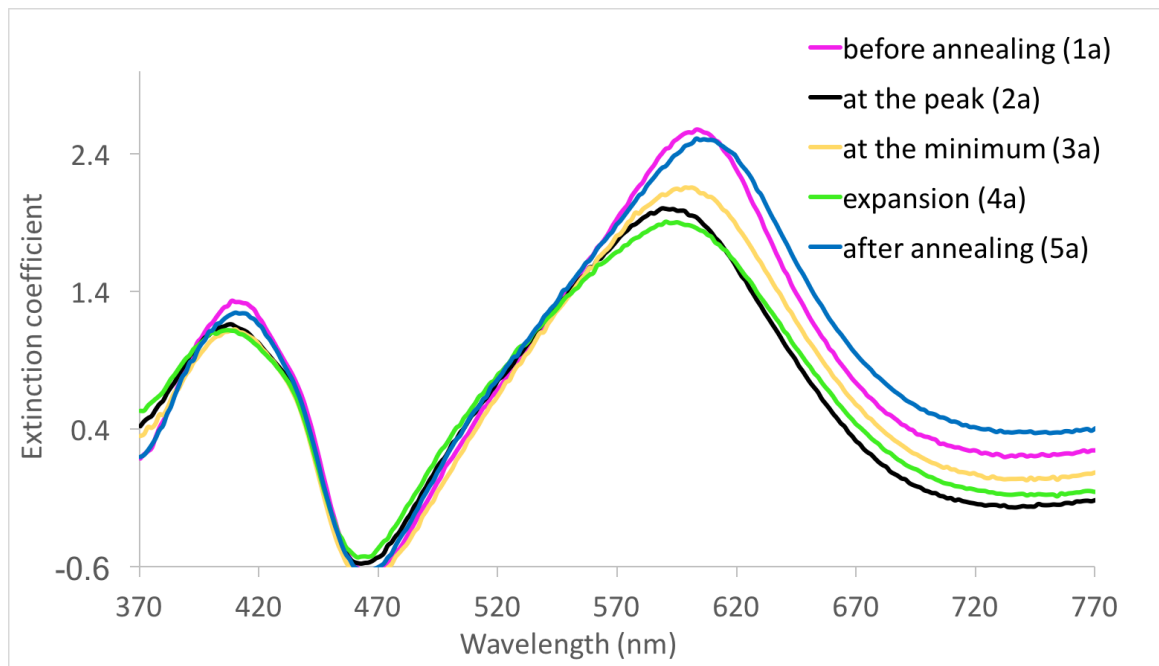


Figure 5.11: Absorption spectrum referring to the 300 min black ellipsometry curve in figure 5.10. The black spectrum in this figure, called 'at the peak' is taken at T_o so just at the beginning of the isotherm, while the yellow curve (at the minimum) is taken just after the peak, so at the minimum point of the ellipsometry curve for the 300 min sample. The green spectrum is taken from the end of the isotherm where the film is expanded.

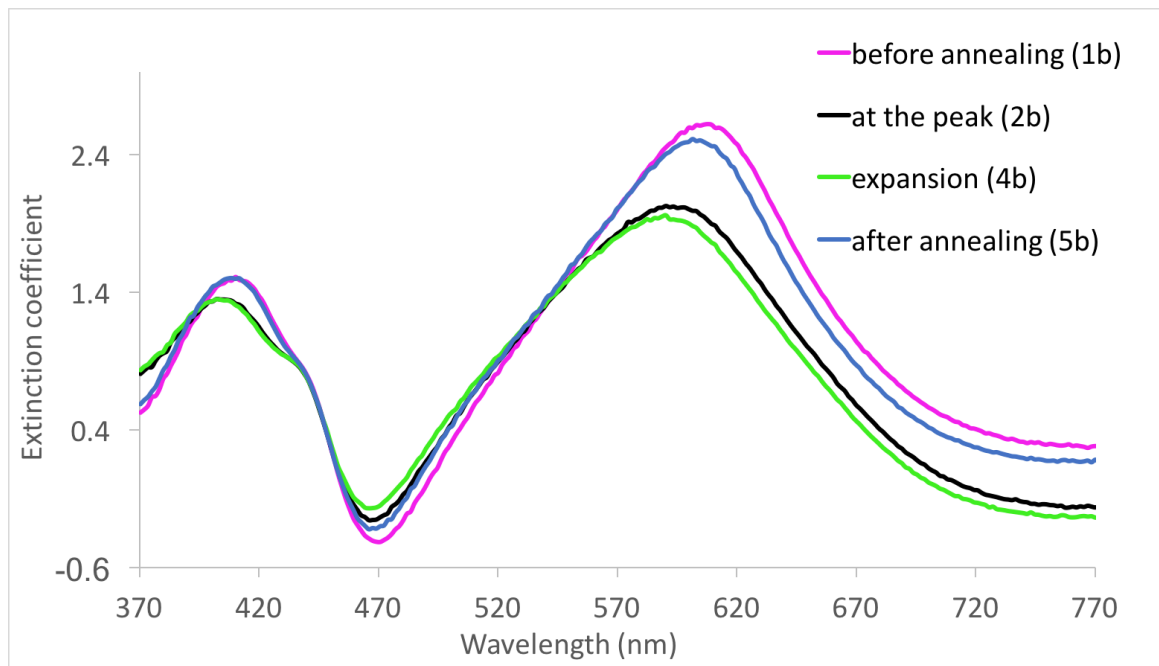


Figure 5.12: Absorption spectra referring to the 650 min red ellipsometry curves in figure 5.10. The black spectrum in this figure, called 'at the peak' is taken at T_o so just at the beginning of the isotherm. The green spectrum is taken from the end of the isotherm where the film is expanded.

It is possible to see from the absorption spectra in figures 5.11 and 5.12, as in the case of the 90 nm sample in section 5.2.1, that the expanded films (green spectra) present the lowest

absorption intensity as the thickness value suggests: the highest value in thickness corresponds to the lowest value in the density of the material. The spectra of the film at room temperature after the annealing (represented by the blue spectra in figures 5.11 and 5.12) result slightly less intense than the spectra taken at room temperature before annealing (lilac curves), suggesting the long annealing at 180°C made the film less dense.

One interesting thing is: in one case the blue curve is red-shifted compared to the lilac one (figure 5.11) and in the second case the blue curve is blue-shifted (figure 5.12). This difference matches also the difference in thickness that is visible in the ellipsometry plots in figure 5.10: the black curve indicates that the 300 min annealed film is thinner at the end of the isotherm, compared to before the annealing (value of the curve at time = 0). The ellipsometry red curve (figure 5.10) indicates that the 650 min annealed film is thicker after the isotherm, producing a blue-shifted spectrum (figure 5.12) respect to the lilac spectrum captured before annealing. The red-shift of the spectrum post-300 minutes annealing means that there is an improvement in the polymer conjugation. The blue-shifted spectrum indicates that the conjugation is worsened by the too long annealing (650 minutes). The red-shift is definitely an indication of an increased ordering, from which derives a decreased thickness at the end of the black ellipsometry curve (figure 5.10).

It is also possible to notice that the yellow curve in figure 5.11 is the one with the highest intensity and the most red-shifted curve among the spectra taken at high temperature (180°C): meaning that when the film reaches the minimum thickness in an ellipsometry experiment, in that point is effectively in the most ordered state compared to all the other points on the thickness profile.

5.2.2.2 220 nm thick films

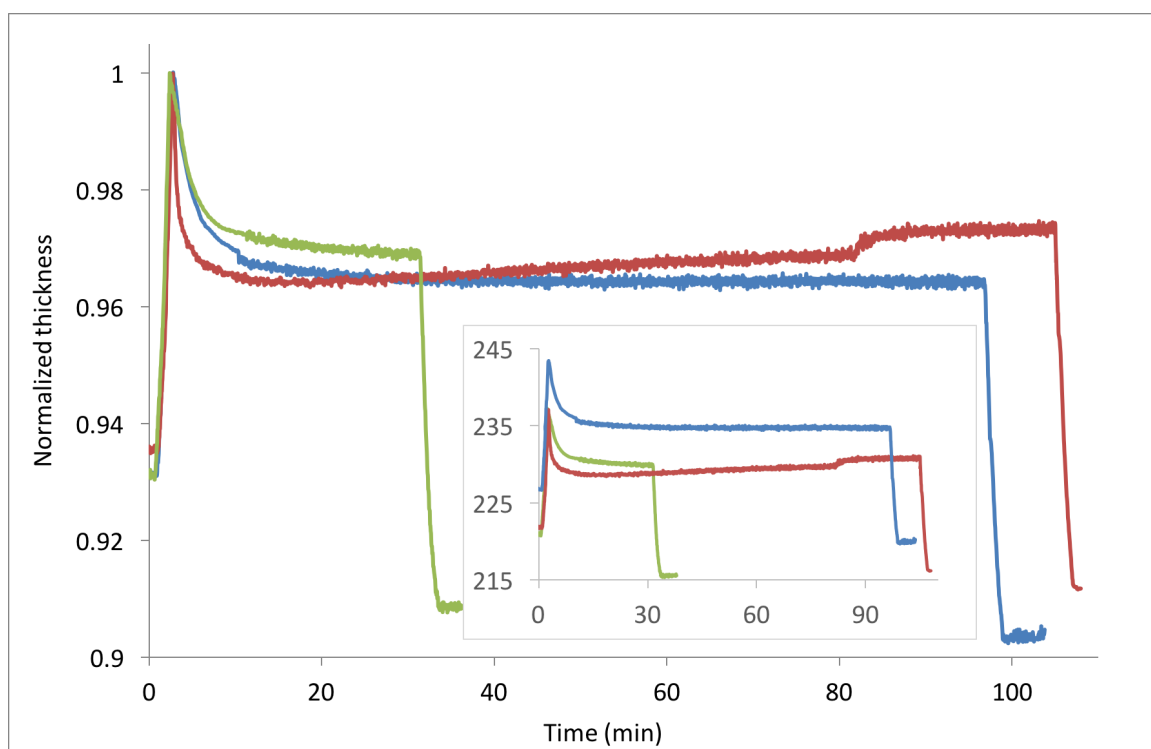


Figure 5.13: Ellipsometry for 220 nm film annealed at 30 and 100 min. Surprisingly one film expanded (red curve) and the other did not (blue). Probably because the T_o of 179°C is very close to the annealing temperature of 180°C.

Three PCDTBT samples, around 220 nm thick have been annealed at 180°C and the ellipsometry data are shown in figure 5.13. This very thick sample does not show an evident expansion, as it was the expansion for the 70 nm sample (figure 5.8a).

It has been hypothesised in section 5.2.2.1 that there might be two stable states existing in a film: one that is ordered and is responsible for the shrinkage of the film and the second is amorphous and is responsible for the expansion. It can be thought that in very thick films like this one, the percentage of amorphous phase forming from the long annealing times and high temperatures is present in less amount than in thinner films. This cannot be said with certainty, but from other ellipsometry graphs for ~ 200 nm films shown in figures 3.17 and 3.20, very little or no expansion is visible.

Moving to the AFM data in figure 5.14, it is observable that they are very similar to the AFM data shown in figure 5.8 for the 70 nm samples: the surface morphology flattens while the overall film thickness increases at longer annealing times.

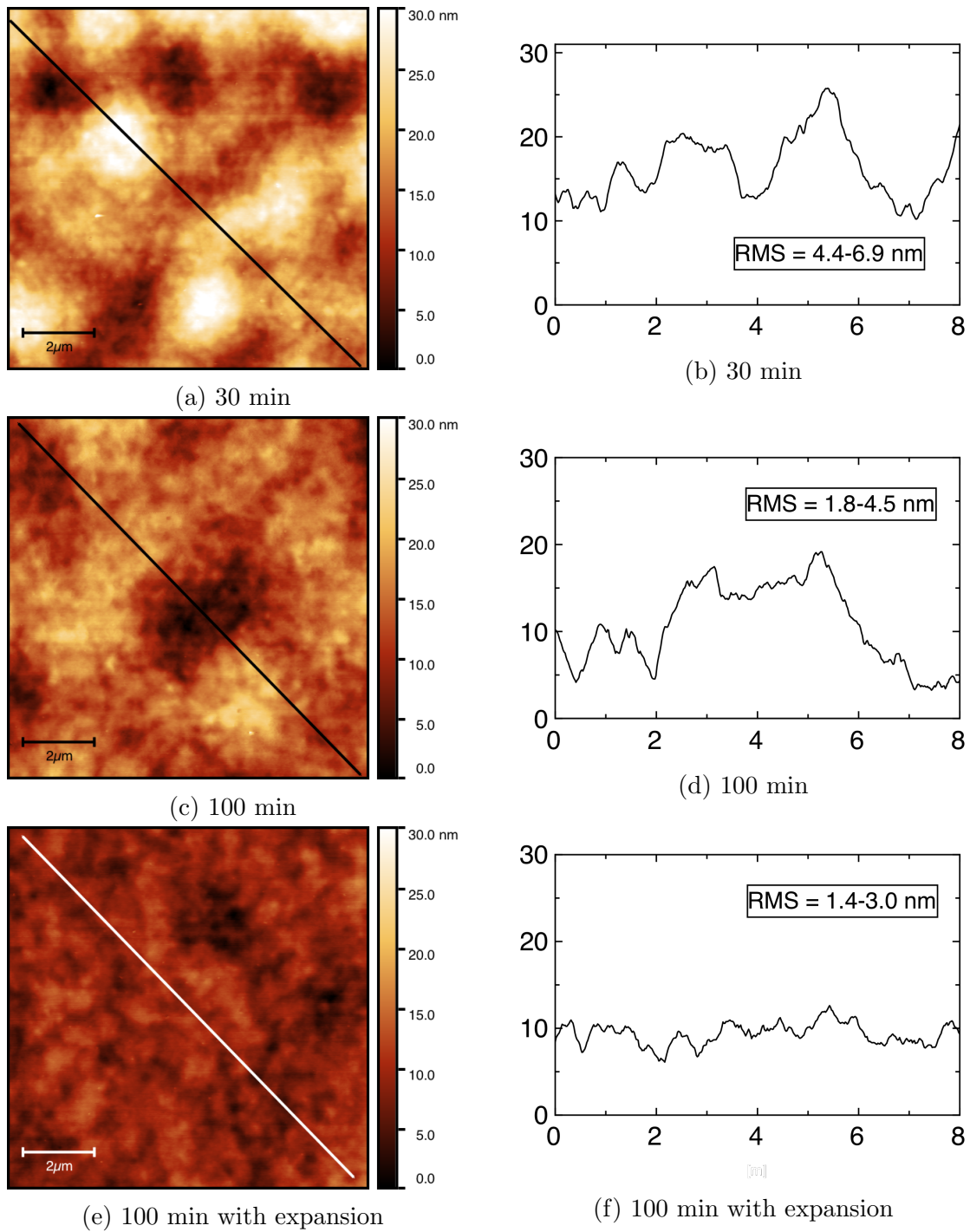


Figure 5.14: AFM results for 220 nm film annealed at 30 and 100 min. Ellipsometry data in figure 5.13.

5.3 Comparison between samples annealed at different temperatures

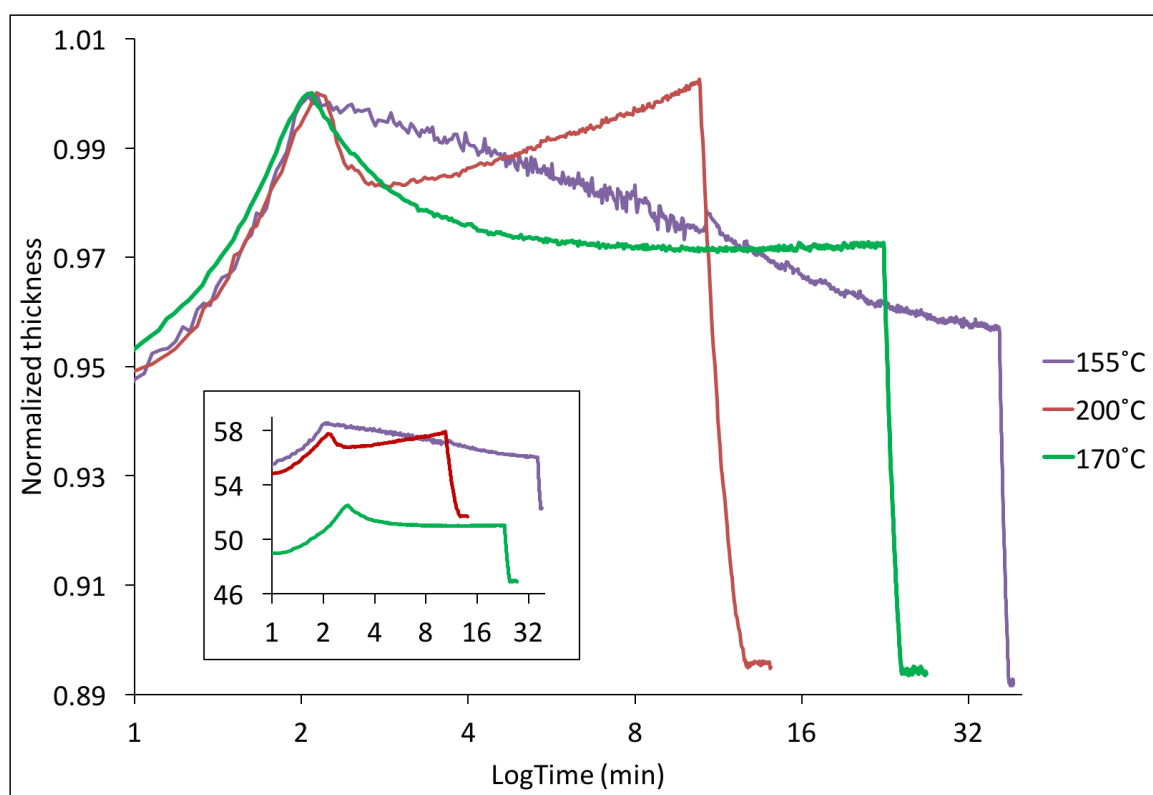


Figure 5.15: Thickness profiles measured by ellipsometry for three 50 nm PCDTBT samples annealed at three different temperatures: 155°C, 170°C and 200°C. It is possible to notice that the sample annealed at the highest temperature of 200°C (red curve) is the only one that present a conspicuous expansion following the initial shrinking. The insert contains the plots with the absolute values of thickness in nm on the y-axis.

In chapter 4 some data for samples annealed at different temperatures have been shown, it was noticed that the samples annealed at a temperature $T \geq T_o$ ($165^\circ\text{C} \leq T_o \leq 180^\circ\text{C}$) are the ones that expand. From the AFM figures in chapter 4 reported here in figure 5.16, regarding a 50 nm sample, it is possible to see that the expanded sample, the one heated at 200°C looked less rough than the not expanded one heated at 155°C, which has also more well-defined features. So one more time confirming the trend seen in this chapter, *i.e.* high temperatures causing the expansion of the film, seem to have a negative impact on the ordering of the polymer.

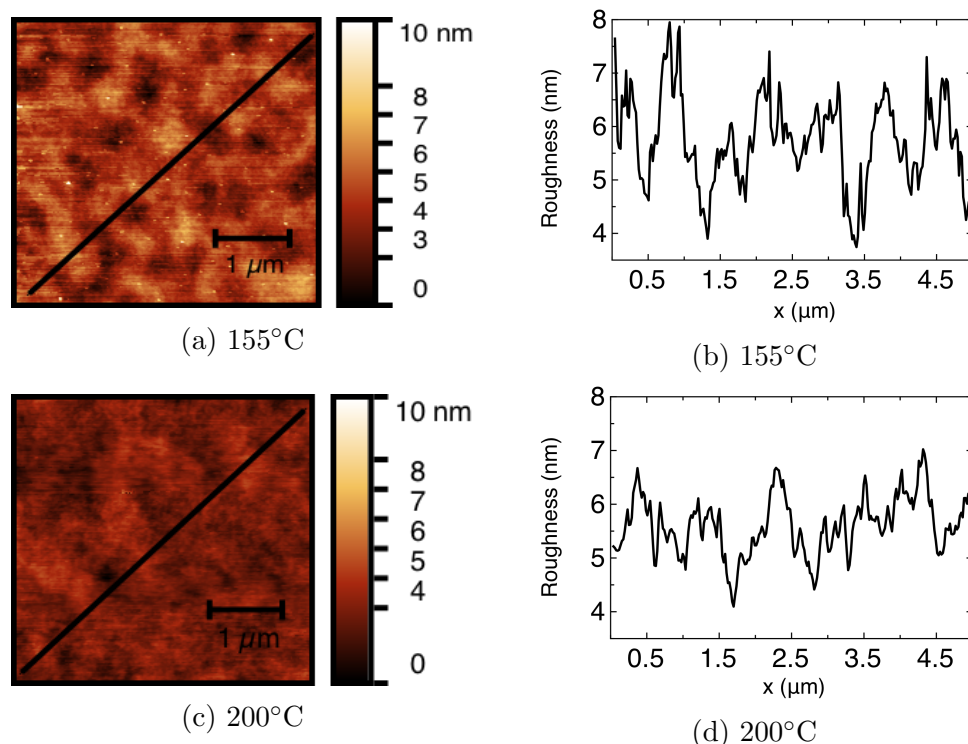


Figure 5.16: AFM images for two 50 nm PCDTBT samples annealed at 155°C and 200°C, the which ellipsometry curves are reported in figure 5.15. (a) and (b) show the surface morphology and the roughness of the sample annealed at 155°C for 30 min; (c) and (d) show the surface morphology and roughness of the sample annealed at 200°C for 15 minutes. The not expanded sample (a) presents a more evident texture on the surface.

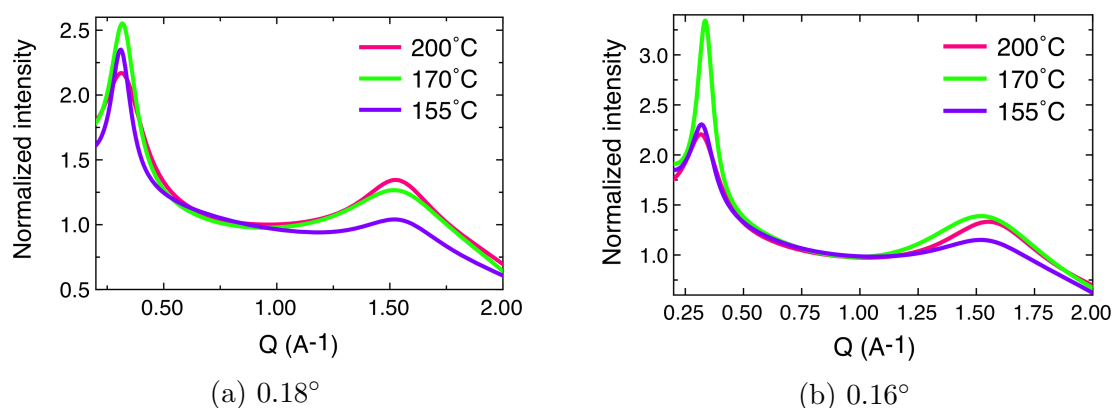


Figure 5.17: GIWAXS out-of-plane scattering curves for samples annealed at different temperatures and taken at two different grazing incidence angle.

The same 50 nm samples annealed at 200°C, 170°C and 155°C have been analysed with GIWAXS (figure 5.17), where just the 200°C thickness curve at the ellipsometer showed expansion (figure 5.15).

The GIWAXS curves do not differentiate in the same way: for $\alpha_i = 0.18^\circ$, the film that showed expansion (the one annealed at 200°C) red curve in figure 5.17a has the highest π - π stacking,

relatively to the 1st peak intensity. It might mean that the π - π stacking is the ordering that requires the longer time, as it is the weakest for the 155°C film, which is the temperature with associated the slowest kinetics. The same for $\alpha_i = 0.16^\circ$, the highest π - π stacking for the expanded sample (200°C), looking at the relative intensity of the second peak compared to the first one (figure 5.17b). From figure 5.17b is also noticeable that the π - π stacking peak is shifted to higher Q values for the 200°C sample, meaning a reduced distance. This is in agreement with what was found in chapter 4 shown in figure 4.27b: the π - π stacking length is shorter for the 200°C annealed film. The explanation for this is that the crystallisation kinetics are the slowest for an annealing temperature of 155 °C, therefore a film annealed at 200°C for roughly the same time (figure 5.15) reaches earlier an higher lever of order than a 155°C annealed film. In this case the higher level of order is represented by a more compact packing in the π - π direction.

The expansion of the ellipsometry curve for the 200°C sample might mean a decrease in the lamella order as the red scattering curve in figures 5.17a and b show: sample 200°C has the lowest lamella order peak and the highest π - π stacking peak.

5.3.1 Absorption spectra comparisons

5.3.1.1 30 nm film

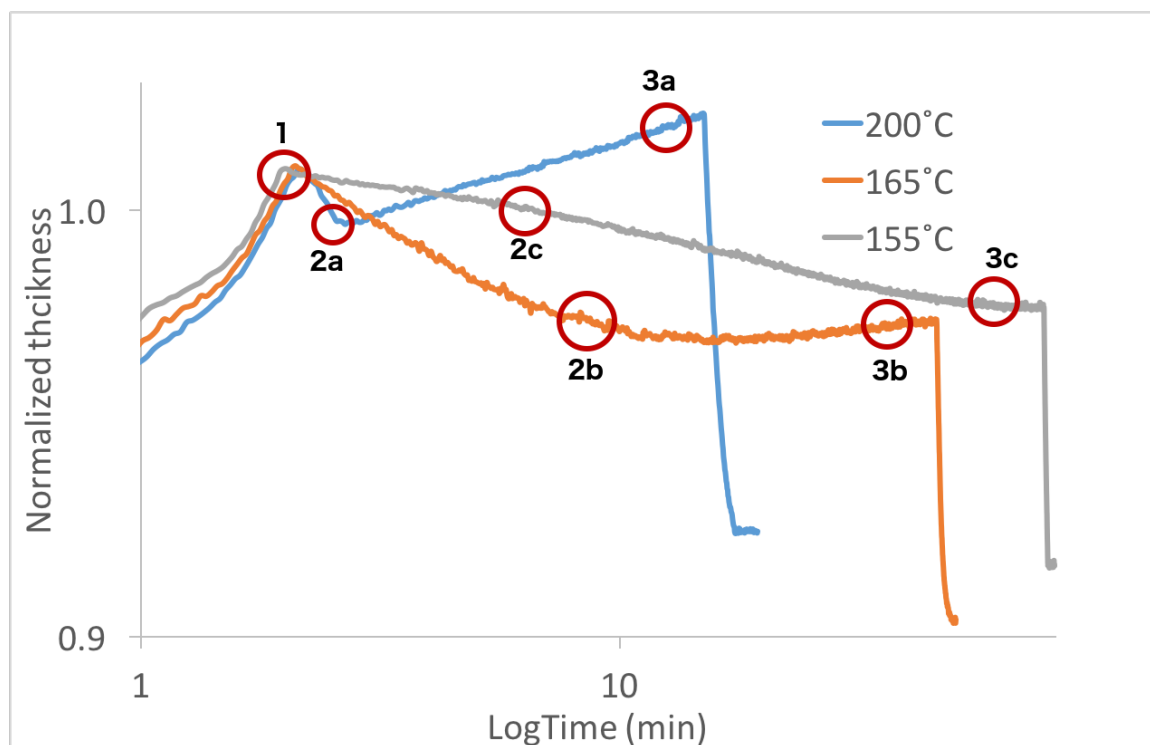
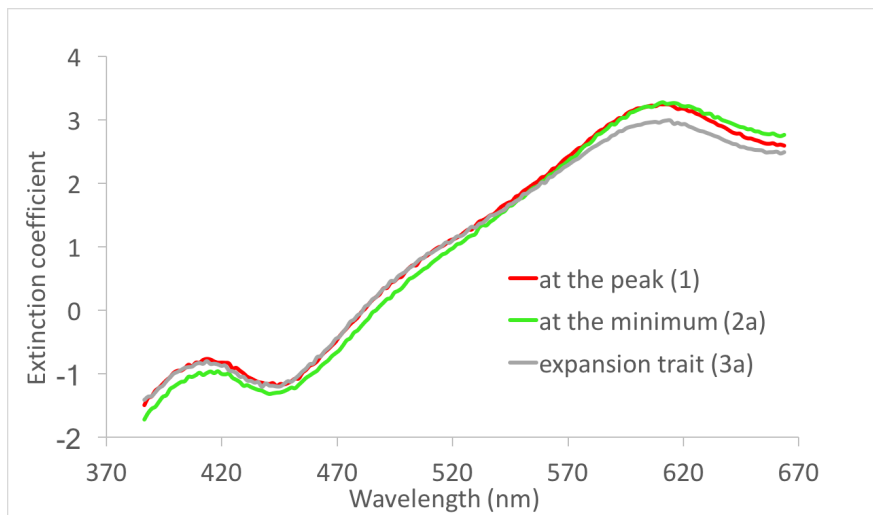
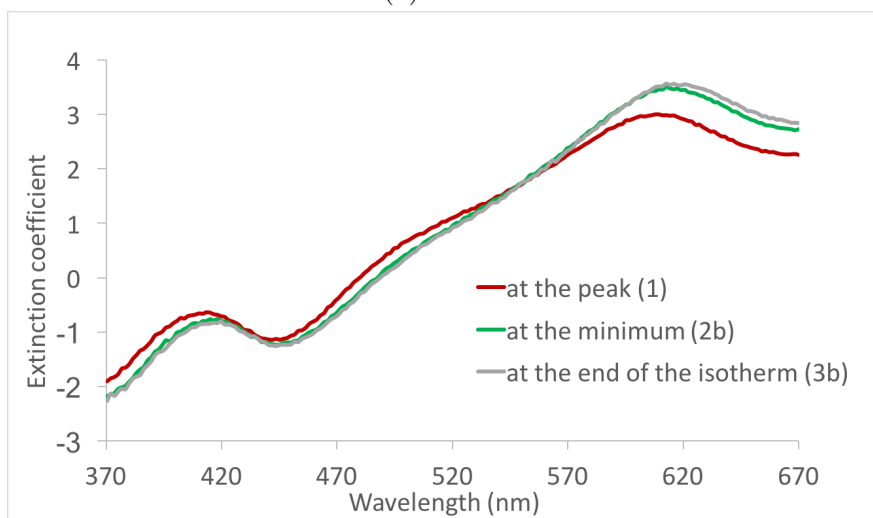


Figure 5.18: 30 nm samples annealed at different temperatures. The numbers on the ellipsometry curves correspond to the points where the absorption spectra in figure 5.19 have been taken.

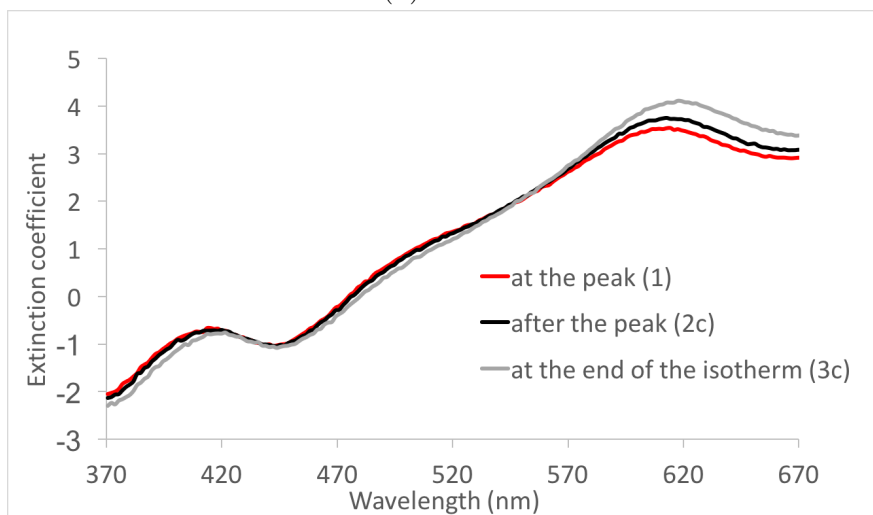
Furthermore (in figure 5.19) it is possible to check the absorption spectra for 30 nm films annealed at different temperatures, the which ellipsometry curves are shown in figure 5.18. It is possible to see how the absorption diminishes (grey spectra in figure 5.19a) with the expansion: absorbance decreasing means disruption of the crystallinity and the film becoming less dense. The 165°C annealed sample (figure 5.18), shows the least pronounced expansion: the weakest spectrum is the one taken at the peak the ellipsometer curve (number 1s), where the crystallisation has yet to happen. Then the green and grey spectra (figure 5.19b) corresponding respectively to the minimum (2b) and the end of the isotherm (3b), present higher ordering and red-shift, proving that no expansion is due to more ordering. For the 155°C sample the shrinking after T_o is very weak (figure 5.18), thus the difference in intensity between the red and black spectra in figure 5.19c is very little. At the end of the 155°C isotherm (3c), the grey spectrum in figure 5.19c shows an higher absorbance and red-shift, suggesting once again that annealing without expansion is related to more crystallinity and conjugation.



(a) 200°C



(b) 165°C



(c) 155°C

Figure 5.19: Spectra of 30 nm samples annealed at 200°C (a), 165°C (b) and 155°C (c). The spectra are very weak because of the low thickness of the films.

5.3.1.2 50 nm film

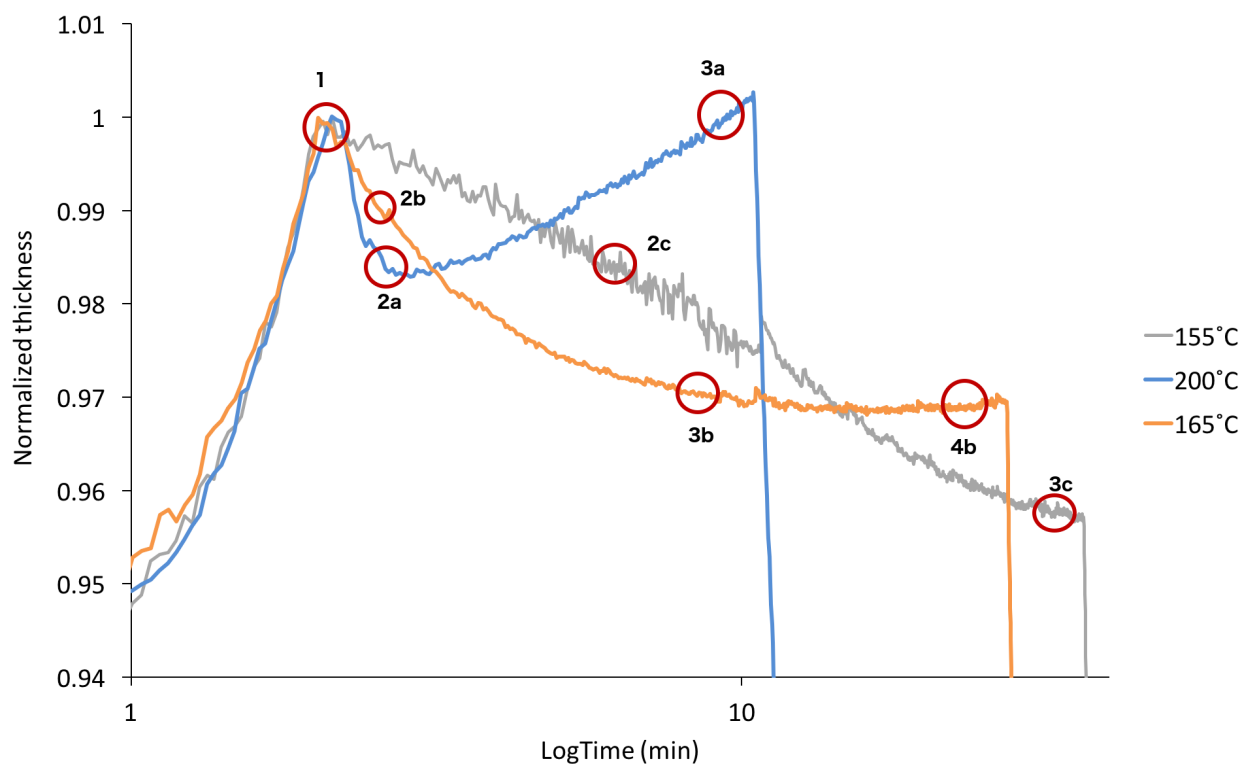


Figure 5.20: 50 nm samples annealed at different temperatures, the red circles correspond to the points of the curves where the absorption spectra below have been taken.

The same trend seen for the 30 nm film is observable for the 50 nm film (figure 5.21): highest absorption and red-shifted spectra at the end of the isotherms with no expansion. Just something unusual in the case of the 200°C (figure 5.21a), where the spectrum at the peak (1 in figure 5.20) seems to present more order than the spectrum at the minimum of the curve (2a). The minimum of the curve should represent the maximum crystallised state.

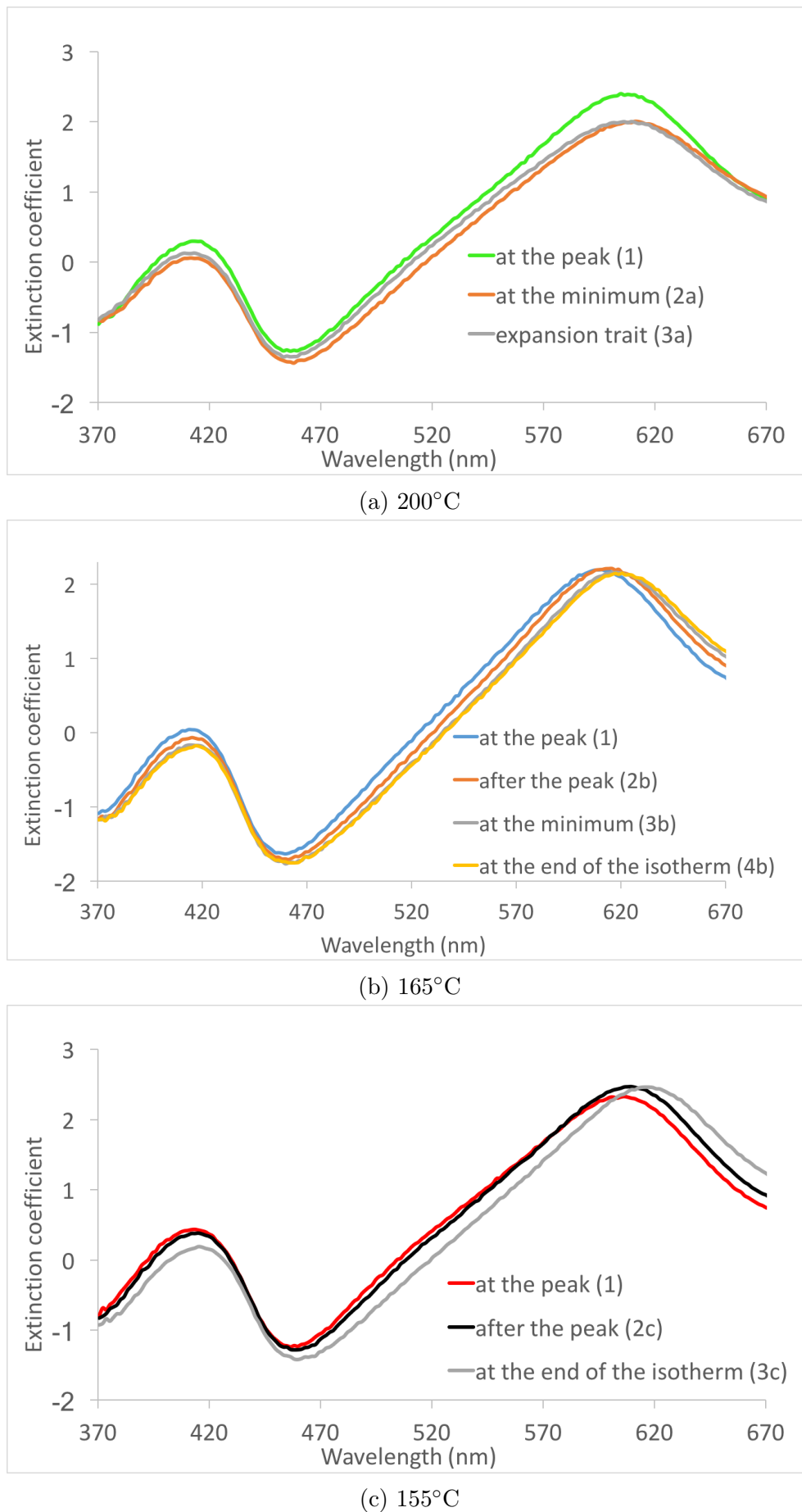


Figure 5.21: Spectra for 50 nm samples annealed at 200°C, 165°C and 155°C. The spectra are very weak because of the low thickness of the film.

5.3.1.3 77 nm film

For this 77 nm sample an annealing experiment at 220°C has been recorded. It is possible to notice the shoulder of T_o along the initial heating ramp (0 in figure 5.22b), where the shrinking surprisingly does not occur until the temperature of the sample reaches 220°C. It is surprising because usually for $T_i \geq T_o$ the shrinking starts at T_o and not T_i ($T_i = 220^\circ\text{C}$ in this case).

Looking at the absorption spectra in figure 5.23a, the highest intensities are obviously for the sample at 25°C, before and after the annealing procedure (red and light-blue curves): the thermal expansion of the material at high temperature causes the absorption to drop.

There is nothing surprising for the rest of the spectra at the other annealing temperatures, as the highest intensity is always at the end of the isotherms where no expansion happened (like the 165°C and 155°C curves figure 5.22a and b).

The only surprising thing in figure 5.22b is the absence of the expansion trait for 220°C which is a temperature higher than T_o . This absence of expansion for $T \geq 200^\circ\text{C}$ has actually been observed for other 210°C and 220°C annealed samples (chapter 4, figures 4.15, 4.16, 4.17), they present a shoulder on the heating ramp happening at T_o , then the film does not start shrinking at T_o as usual, but it proceeds until the target temperature T_i is reached.

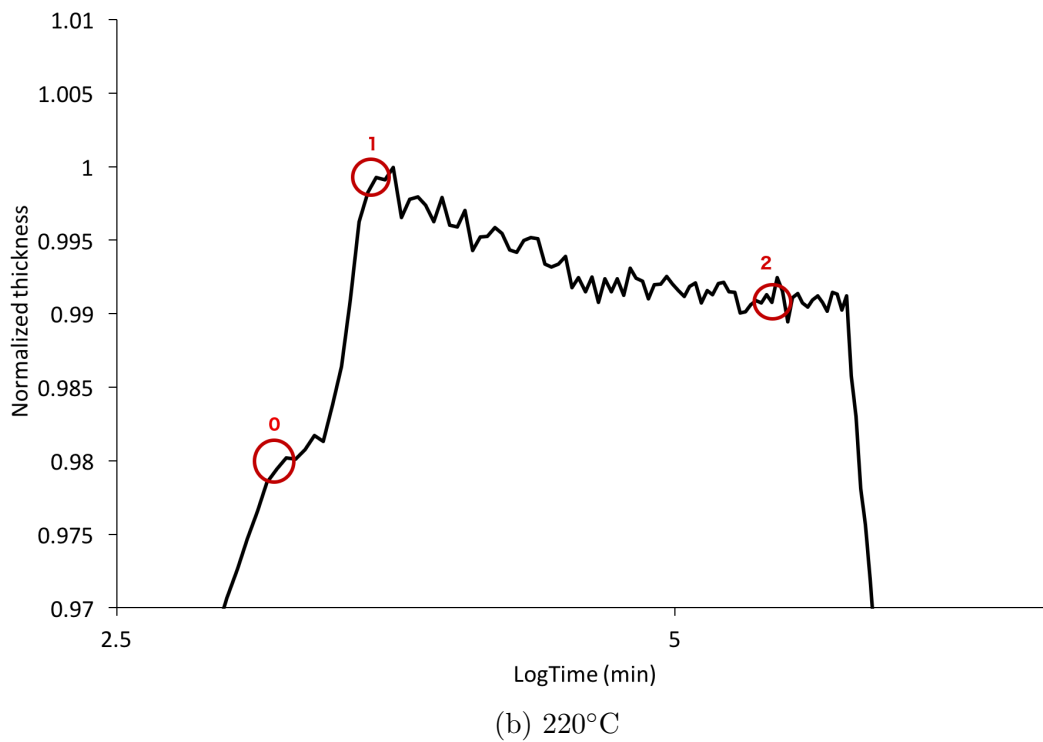
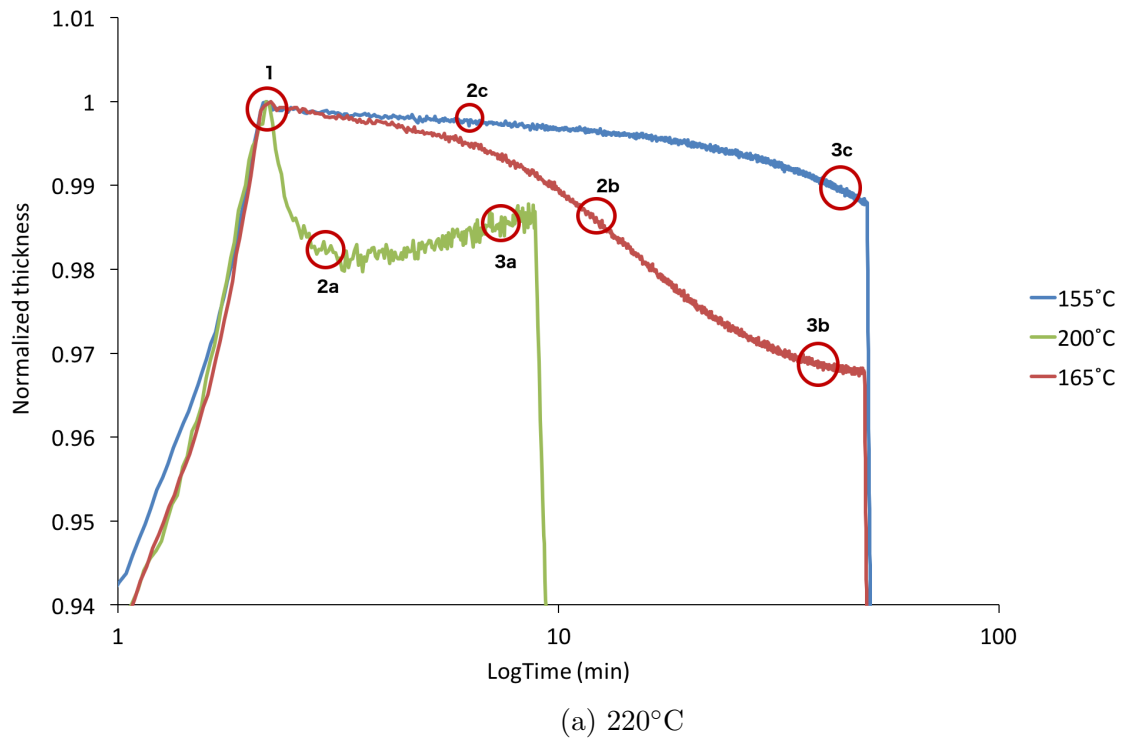
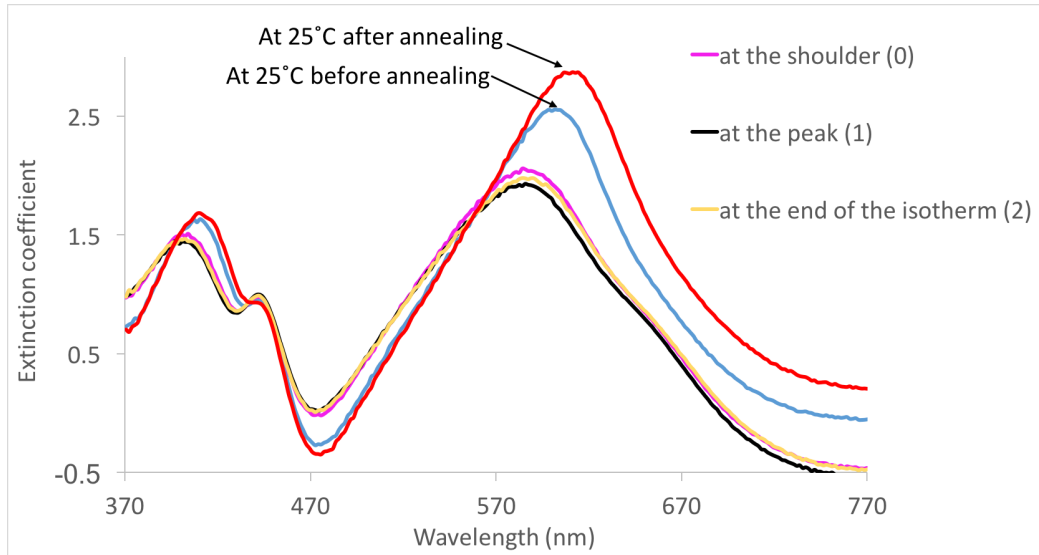
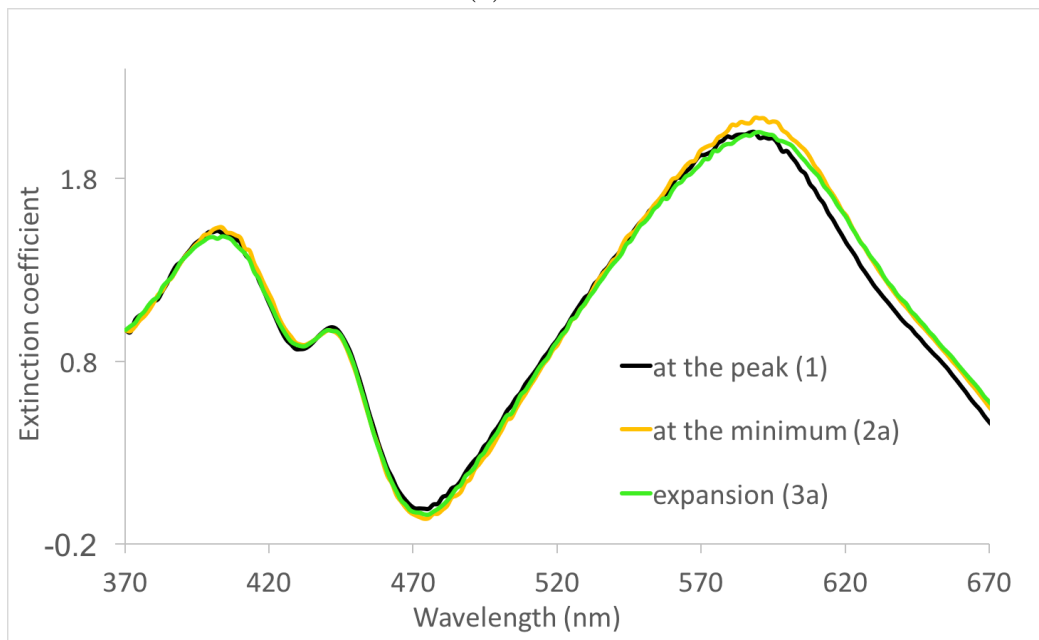


Figure 5.22: 77 nm samples annealed at different temperatures (a) and 220°C (b). The red circles correspond to the points of the curves where the absorption spectra in figures 5.24 and 5.23 have been taken.

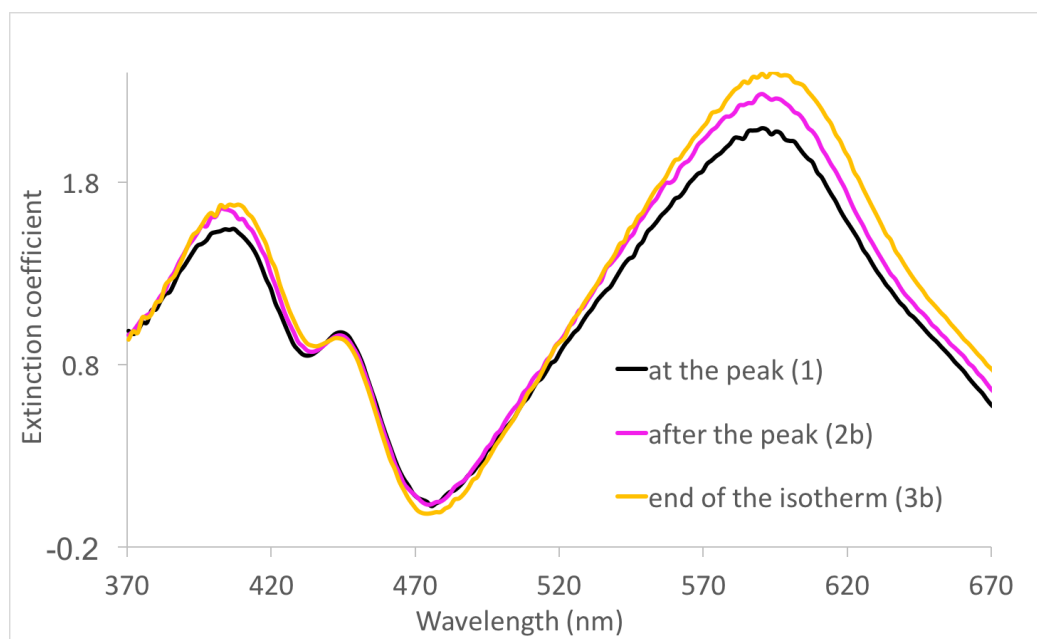


(a) 220°C

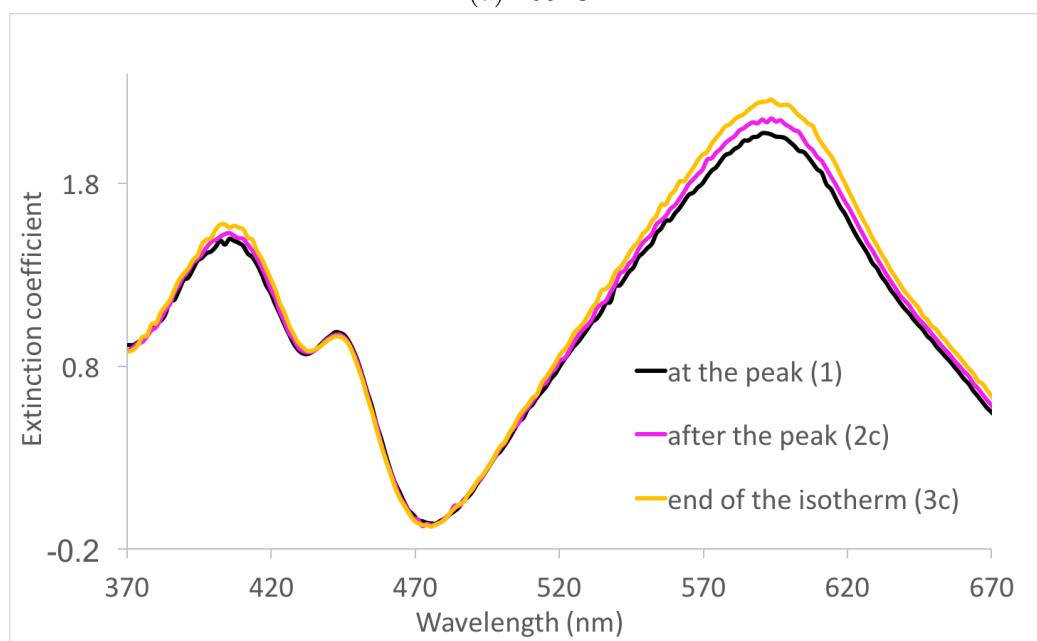


(b) 200°C

Figure 5.23: Spectra for 77 nm samples annealed at 220°C (a) and 200°C (b). The spectra are very weak because of the low thickness of the film.



(a) 165°C



(b) 155°C

Figure 5.24: Spectra for 77 nm samples annealed at 165°C (a) and 155°C (b). The spectra are very weak because of the low thickness of the film.

5.4 Discussion

The expansion noticeable in the ellipsometry experiments (following the initial ordering process), *e.g.* figure 5.1 derives theoretically (chapter 2 - section 2.1) from a decrease in material density, that provokes a reduction in the refractive index. Possible reasons that cause the expansion to happen could be:

- the initial shrinking brings the polymer to an ordered state that is thermodynamically favoured, then the higher temperatures cause the system to evolve to a new state of order that is thermodynamically stable and kinetically accessible, for $T > T_o$. Annealing processes at $T < T_o$ will not have enough energy to switch to the thermodynamically stable product, therefore they do not show any expansion. This would explain also why isotherms at $T \leq T_o$ have a different shape, with a pre-ordering phase (chapter 4 - section 4.2.1). However it is not excluded that the expansion might show up later, for longer annealing times. An important experiment to include in the further work section of this thesis (chapter 7) should look at the long time behaviour of the curves at low temperatures. It might be possible to establish a mathematical relationship between the thickness decay of the film and the annealing temperature, in order to exclude the presence of expansion at the lower temperatures.
- The thickness expansion might be due to some chemical degradation, probably loss of side chains, defects diminishing the conjugation length. In this case then, a more disordered form is hypothesised after the initial ordering phase. PCDTBT is believed to be a very stable semiconducting polymer due to its large ionization potential because of the relatively low-energy of the HOMO. PCDTBT is also inherently stable against oxidation even at relatively high temperatures and FETs fabricated with PCDTBT are stable in air at temperatures up to 150°C and stable in N₂ at temperatures up to 350°C [71]. This stability in air until 150°C coincides with the change in shape in the ellipsometry curves (chapter 4), although the annealing processes for these thesis have been carried out under N₂, it is possible that the environment was not completely sealed, that is why the change in shape happened also at higher temperatures (chapter 4).

The GIWAXS for the 90 nm sample (figure 5.7) suggests that the expansion process is a sign of a decrease in the crystallinity as the scattering rings are weaker in the expanded sample (figure 5.6b), as well as the lamella ordering peak being shifted at lower Q , suggesting the distance between chains increases by 1 Å in the expanded sample. With these results, together with findings in previous studies on PCDTBT and similar conjugated polymers it is confirmed that annealing above a certain temperature and for a certain time disrupts the crystallinity of the material. [71]

The disruption upon annealing is supported by the absorption spectra measured by ellipsometry, which are always less intense in the expanded points of the curves and typically blue-shifted. Whether the red shift in absorption is due to better interchain connection, leading to more efficient interchain delocalization, or a planarization of the polymer backbone conformation remains poorly understood. [135]

A recurrent fact in the AFM results is the flattening of the top surface of the film, indicating a reduction in roughness, but also a different aggregation state. The domains become larger when the film expands. Similar aggregation with annealing was seen in another work [71] on PCDTBT, where RMS was increasing with the aggregation size upon annealing for 15 minutes at surprisingly high temperatures 250 - 400°.

In figure 5.8 there is instead a decrease in RMS with longer annealing ≥ 300 min that provoke an expansion of the film. In figure 5.16 the aggregation is greater for the expanded sample. In figure 5.14 the 200 nm films annealed for 100 min the not expanded sample shows an increase in aggregation size, but in the expanded sample the aggregates seemed to have disrupted and the film surface to have flattened. In chapter 3, section 3.4 was shown from AFM images that annealing at 200° for about 30 minutes creates an expansion of the film, with larger aggregations and increased RMS.

It can then be concluded that high temperature annealings increase the aggregation size and roughness of PCDTBT that provoke an expansion of the PCDTBT film. For very long annealing times (above 10 hours) the RMS and probably also the aggregation sizes diminish again. Gathering all the results presented in this chapter, samples that show an expansion after the initial ordering stage:

- show a reduction and red-shift in UV-vis absorption spectra; this indicates a decreased ordering and conjugation of the polymer;
- show an higher distance of the out-of-plane features, which indicates a less dense packing: this change is very probably what is responsible for the thickness expansion seen with ellipsometry. Additionally, the expanded sample shows also a reduced coherence length mostly in the out-of-plane direction (table 5.2.1);
- a decrease in roughness at the surface of the film and a larger aggregation size, followed by a disappearance of the aggregates for long annealing times, probably above an hour. This is difficult to quantify because there have been inconsistent results.
- This expansion process happens only for films heated at $T > T_o$.

Despite the complications and inconsistencies, it is clear that high temperatures and long annealing times creates a disruption in the crystallisation of PCDTBT which provokes a thickness expansion. If the annealing of the polymer is kept at a temperature $T \leq T_o$, the crystallisation of the material improves, leading to a higher coherence length in the out-of-plane direction (table 3.1) in comparison to an amorphous sample; an as-cast sample presents still greater preferential orientation (flat-on) and chains more densely packed.

Chapter 6

Ordering as a function of thickness

6.1 Introduction

As mentioned in chapter 3, the melting and quenching procedure after the spin-coating of PCDTBT films was thought to remove most of the crystallinity from the samples. This was made in order to start an ellipsometry experiment with a completely amorphous film, so to observe the polymer ordering and studying the kinetics of the process. As discussed in the first chapter and as main title and objective of this thesis, the thickness of the film influences the kinetics and orientation of the polymer chains, which in turn, modifies the opto-electrical property of the polymer.

In this chapter, ellipsometry, GIWAXS and AFM analysis on samples with different film thickness are shown. There is a minimum thickness below which no shrinking is noticeable. In the attempt of understanding the influence of the change in thickness on the ordering process, AFM and GIWAXS analysis on different film thicknesses have been carried out, and the findings are reported in this section.

6.2 Existence of a threshold thickness

During the PhD, a numerous amount of samples with different thicknesses was prepared, ranging from 5 nm to 250 nm. Films thicker than 250 nm are difficult to prepare due to the limited

solubility of the polymer that will consequently make inhomogeneous films, as the solution will be too thick to spin coat. However, the thinnest thickness that is possible to prepare and to measure by ellipsometry is around 5 nm, for which the signal to noise ratio is already very low. Below 15 nm the film does not show any shrinking in the ellipsometry (figure 6.1). A threshold thickness below which no shrinking is occurring might exist, and if so it is around the value of 15 nm. This same value of thickness was found in the work by Taguchi *et al*, [136] where they study the morphology and growth rates for isotactic polystyrene in films from 20 nm down to 4 nm. For film thickness above 20 nm the growth rate was expressed as follows:

$$G(d) = G(\infty)(1 - a/d) \quad (6.1)$$

where $G(d)$ is the growth rate in function of the film thickness d , $G(\infty)$ is the growth rate in the bulk, and a was proposed to be the tube diameter in the reptation model of polymer dynamics, with a constant value of 6 nm. They report experimental results indicating that the diffusion process of chain molecules begins to control the crystal growth in very thin films (thinner than 15 nm), as the growth of the crystal requires the diffusion of the molecules from the melt which are distant from the growth front. When the film thickness becomes thinner than ≈ 8 nm, the growth rate dependence on the film thickness is different from that in thicker films. This might be due to reduced entanglement in very thin films and/or due to the film being less than the lamellar thickness. Hence there is a break in the $G(d)$ curve at the lamellar thickness.

Figures 6.1-6.3 show the thickness profiles for different ranges of thicknesses annealed at 180°C. It is possible to see, after the film expanded from 25°C to 180°C, that there is a negligible shrinking for very thin films, 9 and 12 nm. For thicker films the shrinkage increases proportionally with the initial thickness of the films. Generally it can be seen that both the thermal expansion from 25°C to 180°C and the successive shrinking are proportional to the initial thickness of the films. A qualitative analysis of the shrinking and expansion of the films in function of the sample thickness is presented in the next section.

It is possible to see from figures 6.1 - 6.3 that the increase in shrinking upon annealing is

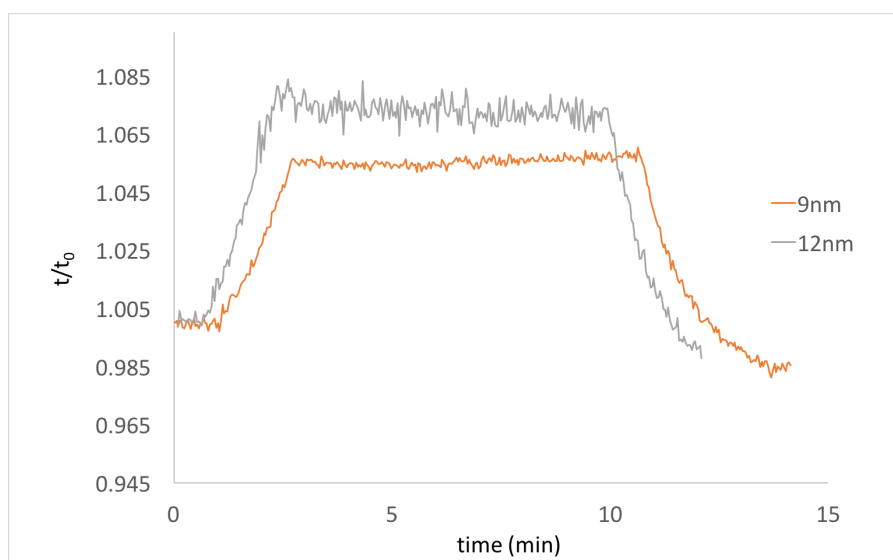


Figure 6.1: Thickness profiles for very thin films, the shrinking is not visible and the thermal expansion diminishes.

directly proportional to the thickness of the film. This is something intuitive: before doing the experiment one would expect that the amount of material that crystallises is proportional to the thickness of the film. But the question is: how much of the film is actually shrinking? What is the percentage of the film initial thickness that shrinks? Recalling the three layers model mentioned in chapter 1, [122] where there are two thin layers, the top layer influenced by the air-polymer interface and the bottom layer influenced by the polymer-substrate interface, it can be hypothesised that just the central bulk region of the film is subject to shrinking. Therefore as the thickness of the film tends to zero, the bulk region is the one that tends to zero as well, while the top and bottom layers of the film cannot be compressed any further. A logical way of thinking it, is that the film contains polymer chains that at a certain point will be completely packed with no further possibility of ordering and no further chance of occupying a smaller space. Considering that increasing the number of polymer chains will increase the number of packing defects contained within the bilayer structure suggested by Lu et al. [74], contrarily, as the film becomes very thin, the number of bilayers and packing defects will be drastically reduced. This might suggest why very thin films do not show any shrinking. The polymer chains at a certain point will be completely packed with no further possibility of ordering and no further chance of occupying a smaller space as shown for the isotactic polystyrene in the paper by Taguchi et al. [136].

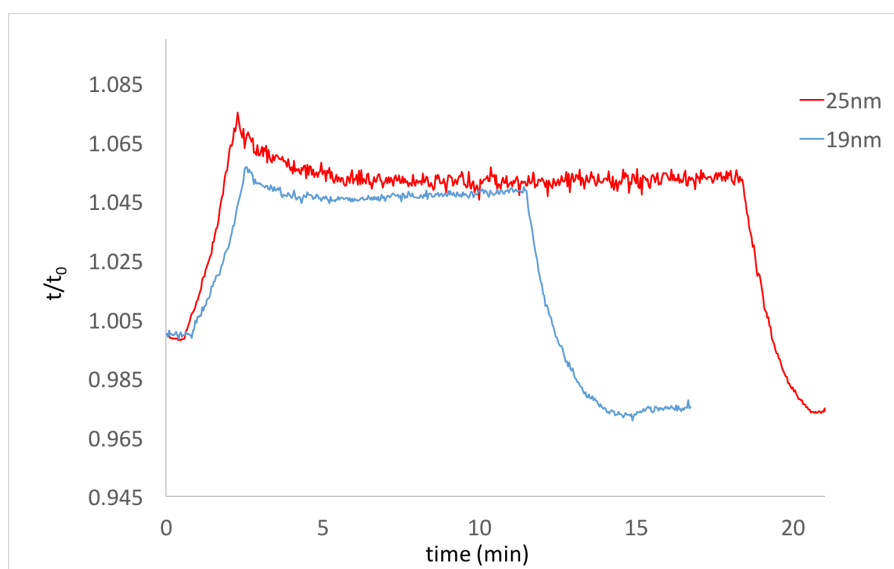


Figure 6.2: Thickness profiles for a 19 nm and a 25 nm sample. The shrinking process is now evident and the expansion increases with the thickness.

GIWAXS, AFM and ellipsometry have been used in order to understand the structure, orientation and morphology of the chains inside the film, as the total thickness was changed. The total thickness can be seen as an external constraint between the bottom and the top interface of a film. As explained in chapter 1, an interface can influence the morphology and the kinetics of the polymer chains in a thin film.

Firstly, the ellipsometry experiments are summarized in section 6.3 and from the results, it will be possible to quantify how much a film expands or shrinks as a function of its thickness.

Secondly, some GIWAXS experiments have been carried out at different thicknesses to see the scattering of a film at the critical angle (the highest scattering signal) to see if the crystalline structure changes.

Lastly, the AFM images for different film thickness are presented, to see how the surface morphology changes as a film gets thicker. The three techniques combined will help to get some insights on the impact of confinement on the ordering of PCDTBT.

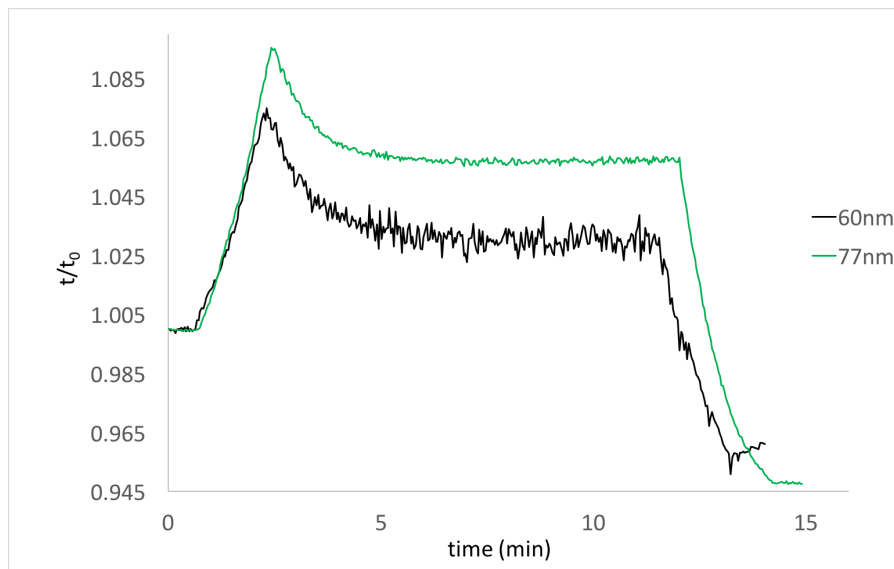


Figure 6.3: Thickness profiles for 60 and 70 nm samples, where the shrinking and the expansion keep increasing with the film thickness.

6.3 Thickness dependence of the isotherms - Ellipsometry

In this section are gathered all the ellipsometry data from the annealing of samples of different thickness. In figures 6.4 and 6.5 is plotted the initial thickness of the samples at 25°C, d_0 , against $d_{max} - d_{min}$, that is the amount the film shrinks at the annealing temperature, T_i . d_{max} is the maximum value of the thickness reached by thermal expansion from 25°C to T_i ; d_{min} is the minimum thickness reached by the sample at the annealing temperature ($T_i = 150^\circ\text{C}$, 170°C , 180°C , 200°C). This data have been plotted for the different annealing temperatures in figures 6.4 and 6.5.

It is possible to see from the plots in figures 6.4 and 6.5 that the amount a film is shrinking is directly proportional to the initial film thickness. It is possible to notice how small the shrinkage is for films below 20 nm. Generally, films until 40 nm shrank 1 nm or less, while film 100 nm thick shrank 3 or 4 nm and finally, film 200 nm thick shrank even 8-9 nm. So the percentage by which the films shrank went from 2 % of the initial thickness to almost 4 % in very thick samples. There is a need to understand what is the origin of this 2 - 4 % of space gained. The fact that the shrinkage is proportional to the initial sample thickness is interesting. The 2 % of a 5 nm sample corresponds to 0.1 nm: although the ellipsometer is a very sensitive

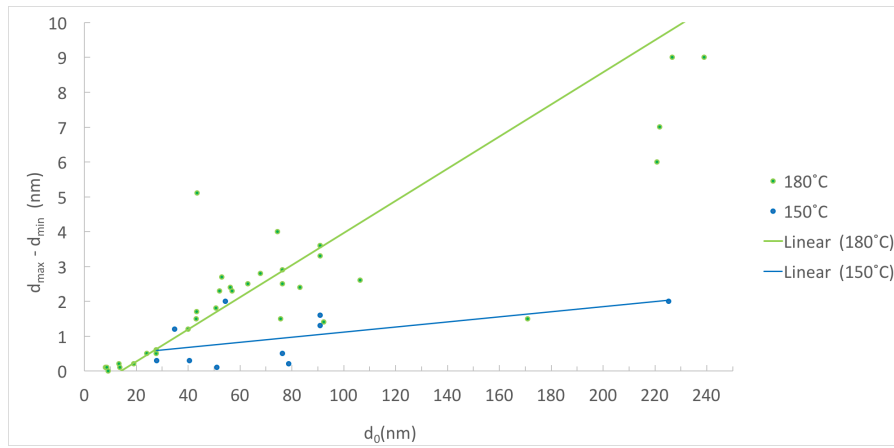


Figure 6.4: Plots of the initial thickness d_0 against the change in thickness $d_{max} - d_{min}$ occurred for 180°C and 150°C annealing isotherms. The best fits for the experimental data are plotted as straight lines.

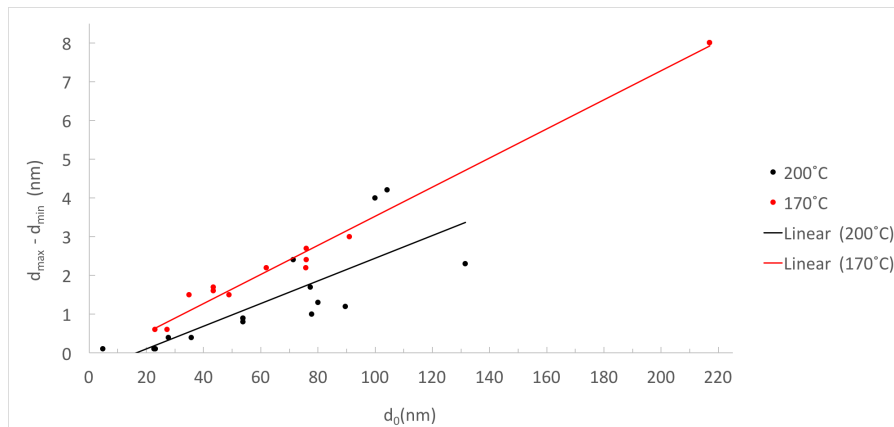


Figure 6.5: Plots of the initial thickness d_0 against the change in thickness $d_{max} - d_{min}$ occurred for 170°C and 200°C annealing isotherms. The best fits for the experimental data are plotted as straight lines.

instrument, the thickness profile for such a thin film is very noisy and not as clear as for thicker samples, so the change is approaching the sensitivity limit of the technique.

The plots in figures 6.4 and 6.5 suggest that there is a minimum thickness d_{crit} below which no shrinkage occurs ($y=0$). For temperatures of 170°C and above, the estimated values of d_{crit} are positive. However the error analysis yields estimates of the standard deviations that are of the same order of magnitude as the value for d_{crit} . The existence of a critical thickness is thus plausible, but not statistically certain.

Another important characteristic is the relationship between the initial thickness of a film and how much it expands from 25°C to the target temperature T_i . To verify this relation, d_0 ,

T ($^{\circ}\text{C}$)	Slope	Intercept	d_{crit}
200	0.03 (0.006)	- 0.48 (0.43)	16 (15)
180	0.05 (0.005)	- 0.64 (0.63)	13 (13)
170	0.04 (0.001)	- 0.22 (0.11)	5.5 (2.8)
150	0.007 (0.004)	0.39 (0.37)	-56 (61)

Table 6.1: Fitting parameters for the experimental points in figure 6.4 and 6.5. For $T = 150^{\circ}\text{C}$ is recorded the lowest slope because the films at this temperature shrink very slowly and it is difficult to say when the shrinking is really finished, so at 150°C , the minimum thicknesses recorded were not the real minimum the film could reach. Hours of annealing would have been necessary to reach the real d_{min} . The numbers in bracket are the standard deviation of the fitted values. The values for d_{crit} for 150°C and 170°C do not match with the values found for 200°C and 180°C , because the shrinking was probably not completed. Moreover, the errors on the first two temperatures are too high to have statistical certainty.

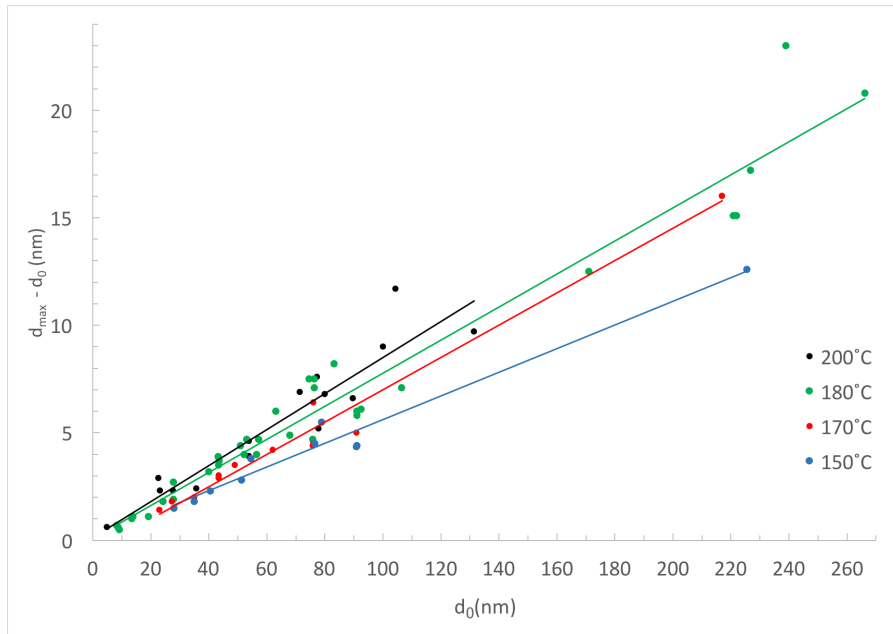


Figure 6.6: Plots of the initial thickness d_0 against the change in thickness on expansion $d_{max} - d_0$. Each point represents one ellipsometry experiment and line fittings to fit the points trends, with a different color per annealing temperature.

the initial film thickness at 25°C , has been plotted against the amount a film expands, $d_{max} - d_0$. d_{max} is the maximum thickness reached by the sample at that annealing temperature. The expansion of the film increases with the annealing temperature, as the coefficient of thermal expansion of the polymer is temperature dependent.

The coefficient of thermal expansion of the polymer film is expected to be different below and above T_g : for $T \leq T_g$ the expansion is controlled by the expansion coefficient of the glass

T ($^{\circ}\text{C}$)	Slope	Intercept
200	0.08 (0.008)	0.13 (0.59)
180	0.08 (0.003)	0.09 (0.31)
170	0.07 (0.003)	-0.52 (0.30)
150	0.05 (0.003)	0.11 (0.33)

Table 6.2: Fitting parameters for the experimental points in figure 6.6. The numbers in bracket are the standard deviation of the fitted values.

α_g and for $T \geq T_g$ by the higher expansion coefficient of the viscoelastic phase α_l . It is possible then to write an equation for the thickness difference between the polymer at 25°C and the polymer at the annealing temperature T_i :

$$d_{max}(T_i) - d_0 = \alpha_g(T_g - T_0)d_0 + \alpha_l(T_i - T_g)d_0 \quad (6.2)$$

$$\frac{d_{max}(T_i) - d_0}{d_0} = \alpha_g\Delta T_{glass} + \alpha_l(T_i - T_g) \quad (6.3)$$

Equation 6.3 is plotted in figure 6.7. The slope and the intercept will give respectively α_l and α_g , *i.e.* the value of the expansion coefficients for the viscoelastic and the glassy phases. T_i as defined in chapter 3 is the target temperature for the isotherm, where $d = d_{max}$.

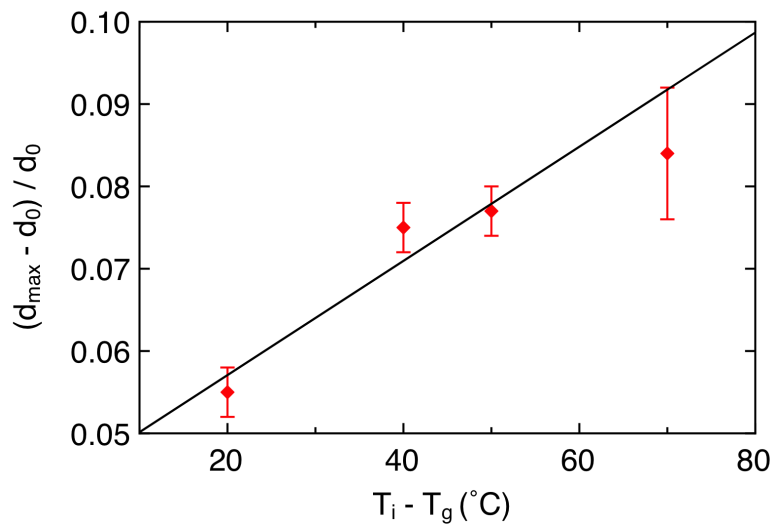


Figure 6.7: Plot of equation 6.3. The slope of this line corresponds to α_l , the expansion coefficient for the visco-elastic phase of PCDTBT; the intercept is $= \alpha_g\Delta T_{glass}$, where α_g is the expansion coefficient of the glassy phase.

Intercept	0.04 (0.005)
α_g	$3 \cdot 10^{-4} \text{ }^\circ\text{C}^{-1}$ ($4 \cdot 10^{-5}$)
Slope $\equiv \alpha_l$	$7 \cdot 10^{-4} \text{ }^\circ\text{C}^{-1}$ ($1 \cdot 10^{-4}$)

Table 6.3: Fitting parameters for the experimental points in figure 6.7 and the calculated value for α_g . The numbers in bracket are the error estimates of the calculated values.

There is an empirical relationship between the thermal coefficients of the two phases:

$$\alpha_l \approx 2.5 \cdot \alpha_g$$

α_l/α_g for PCDTBT is 2.3 which is very close.

The thermal expansion coefficients of a polymer in its visco-elastic state can also be estimated with the Boyer-Spencer rule: [simha1962]

$$\alpha_l \cdot T_g \approx 0.164$$

However the Boyer-Spencer rule often underestimates the expansion coefficient of the polymer in its visco-elastic state and the relation

$$\alpha_g \cdot T_g \approx 0.08$$

$$(\alpha_l \cdot T_g = 0.09 \text{ for PCDTBT})$$

gives often better estimates for α_l when combined with the Simha-Boyer rule: [137]

$$\alpha_l \approx 0.113 / T_g + \alpha_g = \alpha_g (0.113 + 0.08) / T_g = 0.193 / T_g$$

For our system this gives the prediction $\alpha_l = 0.193 / T_{g,\text{PCDTBT}} = 1.5 \cdot 10^{-3} \text{ }^\circ\text{C}^{-1}$ compared to the expected value of $7 \cdot 10^{-4} \text{ }^\circ\text{C}^{-1}$ that has been found here.

6.4 GIWAXS for different thicknesses

Analysing GIWAXS data for very thin films was a challenge because the low crystallinity degree of the polymer gives very weak signals, multiplied by the fact that the thinner the film is, the weaker the scattering.

In figure 6.8 is presented a comparison between as-cast samples having a different film thickness. As-cast samples are the ones that present a major difference between in-plane and out-of-plane

scattering: the annealing protocol creates a homogeneity in the orientation of the chains between flat-on and edge-on as described in section 3.5 in chapter 3. From both figures 6.8a and b it is possible to see that the smallest amount of π - π stacking is seen in the thinnest film, 20 nm, especially for the out-of plane signals, where the first scattering peak has the same intensity for 20, 40 and 90 nm films. The thinnest films are the one with the thinnest bulk region, according to the three layers model, and the fact that the thinnest film has the less relative intensity of π - π stacking might mean that the π - π stacking happens mostly in the bulk region of a film.

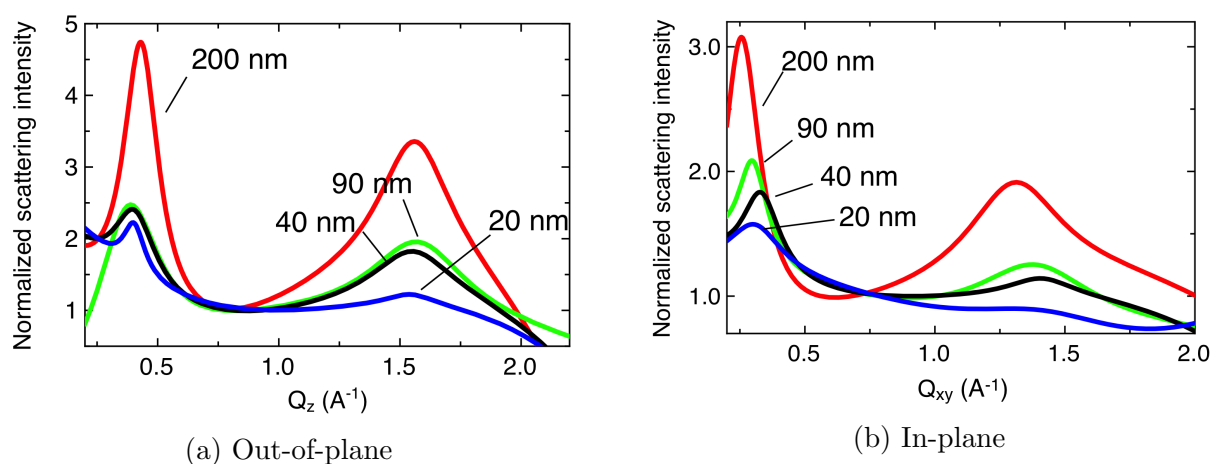


Figure 6.8: (a) and (b) are the fitting curves to the out-of-plane and in-plane scattering data for as-cast films of different thicknesses.

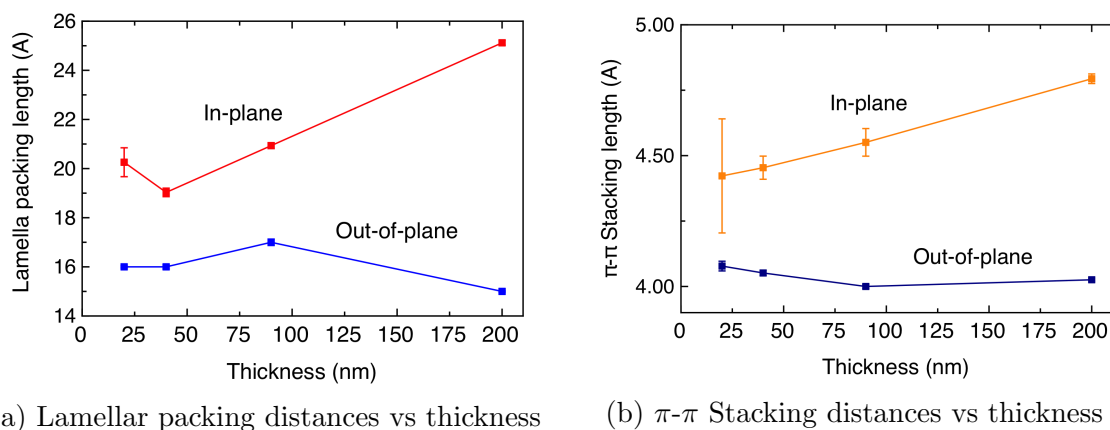


Figure 6.9: π - π stacking and lamellar packing distances thickness dependence for as-cast films. The trends are compared for the in-plane and out-of-plane geometries.

Figures 6.9a and b show a comparison of the d values for both the lamellar packing and π - π stacking for different thicknesses.

The most variation is seen in the in-plane direction. The lamellar packing distance goes from 19-20 Å in a 20 nm film to 25 Å for a 200 nm sample. The π - π stacking is ≈ 4.4 Å in a 20 nm film and ≈ 4.8 Å in a 200 nm film. Therefore there is approximately a 20 % of variation for the lamellar packing distances across the different film thicknesses and a 10 % for the π - π stacking.

For the out-of-plane direction the difference in packing lengths is less pronounced and also the thickness dependence is different. The lamellar packing goes from a maximum of 17 Å for the 90 nm film to 15 Å for the 200 nm film; the π - π stacking variation is about 4.1 Å in a 20 nm and 4.0 Å in a 200 nm film. It can be concluded that the oscillation in distances for the out-of-plane direction could just be due to experimental error.

The as-cast thickest film (200 nm) presents then the longest packing distances in the in-plane scattering curves that correspond to flat-on lamella packing and edge-on π - π stacking. While the out-of-plane scattering data, corresponding to edge-on lamella packing and edge-on π - π stacking, seem not be too much influenced by the different thickness (figures 6.9a and b).

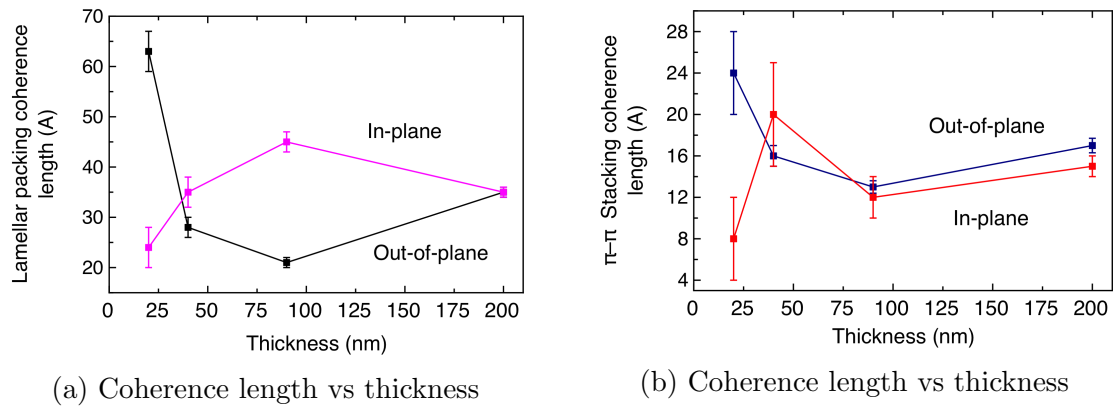


Figure 6.10: (a) and (b) show the lamellar packing and the π - π stacking coherence lengths for as cast films at different film thicknesses, both in-plane and out-of-plane.

In figures 6.10a and b is reported the trend of the coherence length as a function of the thickness. The longest coherence length (63 Å for the lamellar packing and 24 Å for the π - π stacking) is in the thinnest film (20 nm) for the out-of-plane geometry. For the in-plane direction is the opposite: the thinnest film presents the shortest coherence length (24 Å for the lamellar packing and 8 Å for the π - π stacking). This means that the thinnest films contain π - π stacking that is more densely packed, but less extended.

How it is seen in figure 6.11, the greater π - π stacking area is given by the 20 nm film, meaning

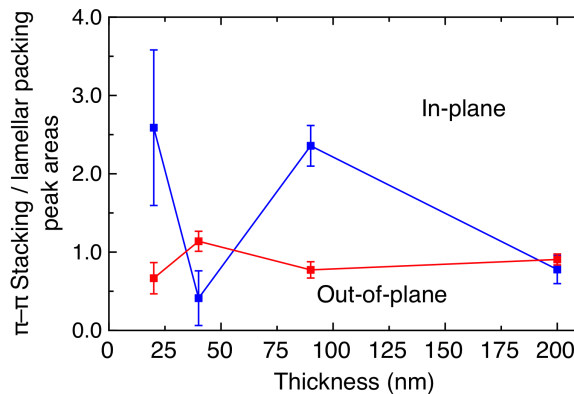


Figure 6.11: π - π Stacking relative area vs thickness for as-cast films.

the crystallinity in the thinnest film is higher, but the length-scale the crystals extend for is the shortest (lowest coherence length).

So from figure 6.11 it looks like the greater quantity of π - π stacking is present in the 20 nm and 90 nm films, and the lowest for the 40 and 200 nm films. The 40 nm film has instead the greatest π - π stacking quantity oriented out-of-plane (still from figure 6.11), although the difference in the out-of-plane direction is not very large as for the in-plane. This inconsistent

result can be attributed to the weak scattering of PCDTBT and the difficulties encountered in normalising the data.

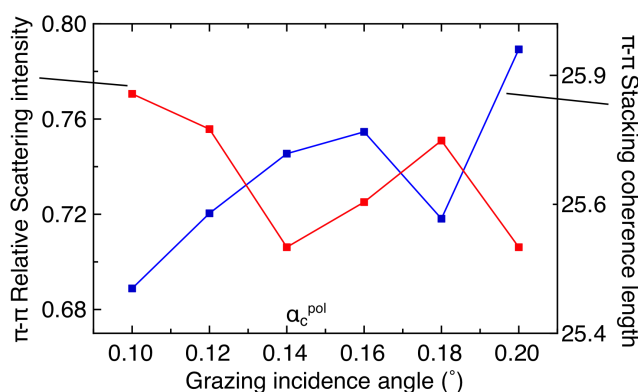


Figure 6.12: Depth profile for a 90 nm film as cast, the red line is the scattering intensity relative to the π - π stacking and the blue line is its coherence length as a function of the grazing incidence angle. Shallower angles means the surface of the film, critical angle is an average of all the film, and higher angles are closer to the substrate.

In figure 6.12 are reported the π - π stacking relative intensity (red plot) and the π - π stacking coherence length (blue plot) as functions of the grazing incident angle in a 90 nm as-cast film. The two plots show a contrasting trend as function of the depth: the lowest π - π stacking intensity is near the substrate of the film (red line), while it is reported in [8] that after annealing a PCDTBT sample, the π - π stacking becomes greater near the substrate because of the interaction with it. This is also what is shown in figure 6.13. Figure 6.13 shows the π - π

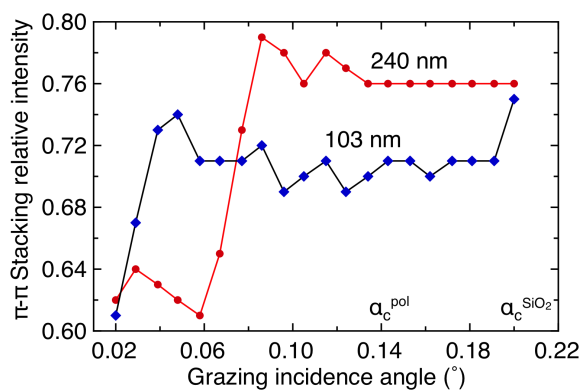


Figure 6.13: Depth profiles in the out-of-plane direction for a 103 nm and 240 nm films annealed at 180°C.

stacking relative intensity for two different film thicknesses and the trend is very much similar to the one reported in [8] for 50 and 30 nm film. Although in Wang paper the π - π stacking intensity was ≥ 1 because the lamellar structure was characterised by a second order diffraction

peak. The plot in figure 6.13 is calculated on the first order lamellar packing peak as shown in the rest of this thesis. The conclusion is that the greatest π - π stacking has been confirmed to be near the substrate in four annealed PCDTBT samples: the 30 and 50 nm from [8] and 103 nm and 240 nm here. The plots in figure 6.13 appears to be 'shifted', as in Wang's paper the 'jump' in intensities that is seen also in figure 6.13 happens about at the critical angle. This could be due to the calibration issue with the grazing incident angle. Other thing noticeable from figure 6.13 is the greatest π - π stacking for the 240 nm sample, suggesting the amount of π - π stacking relative to lamellar packing is greater in thicker samples.

1st peak (lamellar packing)						
d_0 (nm)	x_0 (\AA^{-1})	$2\pi/Q$ (\AA)	μ (\AA^{-1})	L (\AA)	$I(x_0)$	$Area$
20 _{OOIP}	0.40 (0.001)	16 (0.04)	0.05 (0.003)	63 (4)	1.6 (0.05)	0.2 (0.02)
20 _{IIP}	0.31 (0.009)	20 (0.59)	0.13 (0.002)	24 (4)	0.4 (0.08)	0.2 (0.03)
40 _{OOIP}	0.40 (0.002)	16 (0.08)	0.11 (0.006)	28 (2)	3.6 (0.13)	1.2 (0.08)
40 _{IIP}	0.33 (0.003)	19 (0.17)	0.09 (0.007)	35 (3)	0.6 (0.05)	0.2 (0.02)
90 _{OOIP}	0.38 (0.003)	17 (0.13)	0.15 (0.008)	21 (1)	4.9 (0.34)	2.3 (0.20)
90 _{IIP}	0.30 (0.002)	21 (0.12)	0.07 (0.003)	45 (2)	0.6 (0.02)	0.1 (0.01)
200 _{OOIP}	0.43 (0.001)	15 (0.03)	0.09 (0.003)	35 (1)	11 (0.30)	3.2 (0.14)
200 _{IIP}	0.25 (0.001)	25 (0.10)	0.09 (0.003)	35 (1)	1.3 (0.04)	0.4 (0.02)
2st peak (π - π stacking)						
20 _{OOIP}	1.54 (0.007)	4 (0.02)	0.13 (0.02)	24 (4)	0.4 (0.04)	0.2 (0.03)
20 _{IIP}	1.42 (0.07)	4 (0.22)	0.40 (0.18)	8 (4)	0.4 (0.31)	0.4 (0.43)
40 _{OOIP}	1.55 (0.004)	4 (0.01)	0.20 (0.02)	16 (1)	2.2 (0.17)	1.4 (0.15)
40 _{IIP}	1.41 (0.010)	4 (0.04)	0.16 (0.04)	20 (5)	0.1 (0.03)	0.1 (0.02)
90 _{OOIP}	1.57 (0.003)	4 (0.01)	0.24 (0.01)	13 (1)	2.4 (0.09)	1.8 (0.11)
90 _{IIP}	1.38 (0.002)	5 (0.05)	0.27 (0.04)	12 (2)	0.4 (0.08)	0.3 (0.08)
200 _{OOIP}	1.56 (0.002)	4 (0.01)	0.18 (0.007)	17 (1)	5.2 (0.17)	2.9 (0.16)
200 _{IIP}	1.31 (0.001)	5 (0.02)	0.21 (0.02)	15 (1)	0.4 (0.06)	0.3 (0.05)

Table 6.4: Fitting parameters for the GIWAXS data shown in figure. x_0 is the position of the maximum of the Lorentzian peak on the x -axis, $2\pi/Q$ is the corresponding length to the Q -coordinate, μ the half width at half maximum of the peak, L is the coherence length and I the amplitude of the peak which counts for the scattering intensity excluded the background noise. The values in brackets are the standard errors. The first lines are the out-of-plane values, the second lines are the in-plane values.

6.5 AFM for different thicknesses

In this section, the AFM data for different thicknesses are presented. Intermediate thicknesses to those presented, have very similar morphologies, so the one shown are the key ones.

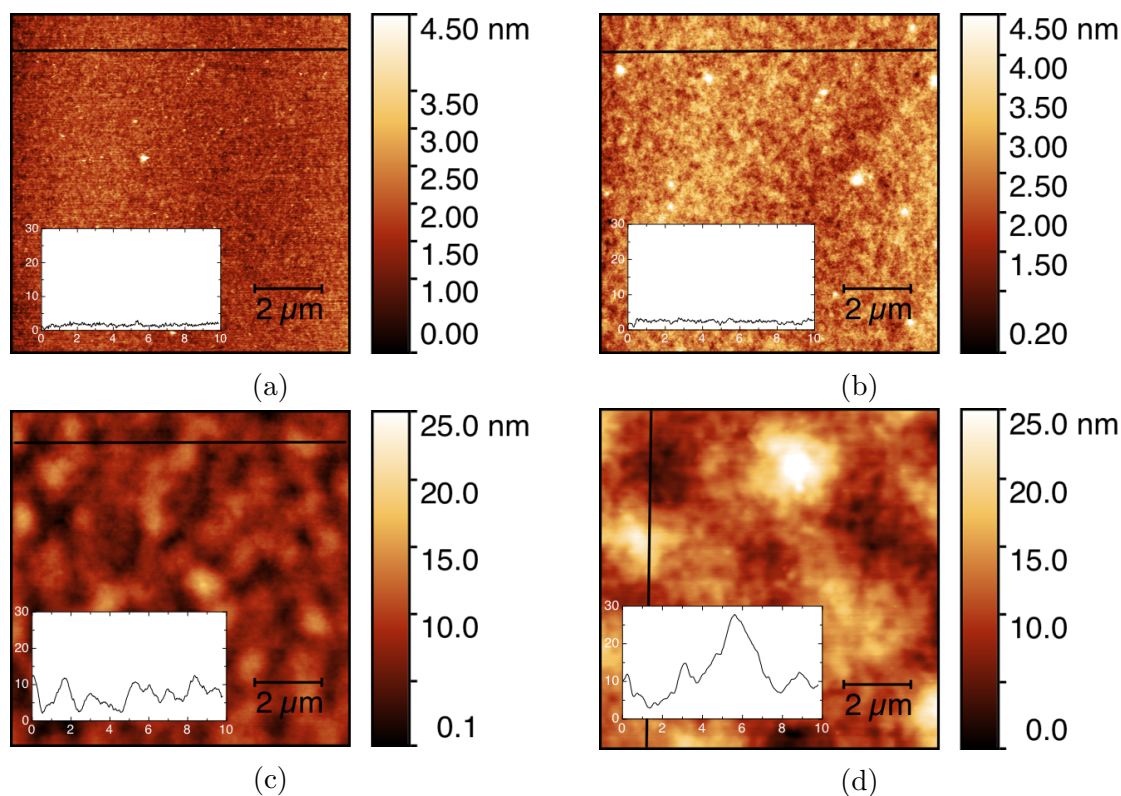


Figure 6.14: AFM images showing the difference in surface morphology for four different key thicknesses (a) 8 nm RMS = 0.4 nm, (b) 25 nm RMS = 0.5 nm, (c) 65 nm RMS = 2.5 nm, (d) 200 nm RMS = 3.9 nm. The black line in the AFM image represent where the linear profile in the inset was taken. The colour scale in the first two thicknesses ((a) and (b)), it is different from the thicker ones ((c) and (d)) for clarity. These films of different thicknesses were melted at 250°C for 4 minutes and quenched in liquid N₂. Then annealed at 180°C for an hour.

It is possible to notice from figure 6.14, the big difference in the size of the aggregates in PCDTBT between an ultrathin sample, 8 nm in figure 6.14a and a very thick sample, 200 nm in figure 6.14d. As discussed in previous sections, polymer chains in thicker films have more space to move around and they possibly can reach a better order, increasing the aggregation. The roughness and waviness of the films surfaces increases, as the aggregates size increases. If AFM images are compared for as-cast samples of different thickness (as showed in chapter 3, section 3.4), it is possible to notice that there is almost no difference between the as-cast images. After the melting and quenching step, it is already possible to see that the difference in domain sizes is proportional to the film thickness (shown in figure 6.15. Annealing the films,

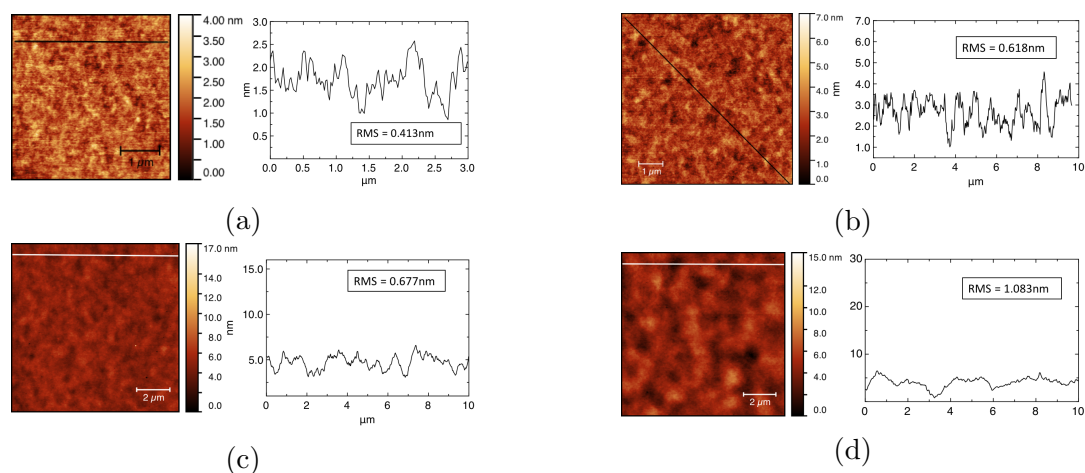


Figure 6.15: AFM height images for (a) 8 nm, (b) 40 nm, (c) 85 nm and (d) 200 nm PCDTBT films after they have been melted, as cast (a), after melted at 250°C for 4 minutes and quenched in liquid N₂.

the domain size increases with the thickness: the 200 nm film presents very large aggregates (figure 6.14d), while in the 8 nm film the aggregation state does not change. The lack of surface morphology change with annealing in the 8 nm sample, reflects what is observable with ellipsometry: no shrinkage.

6.6 Discussion - Thickness dependence of PCDTBT thin films

The influence of the film thickness has important consequences on the crystallisation of PCDTBT, which is why this thesis has been written. As explained in the chapter 1, the proximity to an interface influences the kinetics, orientation, and amount of crystallinity of a material. For PCDTBT is important to know the influence of the confinement in thin film on its crystallisation, because it influences its opto-electrical properties, hence its performance in devices. As seen from previous chapters, PCDTBT is already ordered when spin-coated onto Silicon substrates. This order is given by a preferential orientation of the chains as the lamellar packing and π - π stacking ‘facing’ the substrate (face-on). Upon melting and quenching this preferential orientation and packing is destroyed, as shown by the low scattering GIWAXS signal seen in chapter 3 - section 3.5. After this melting and quenching the film usually results thicker, signal

that the density, thus the crystallinity of the material has decreased. However, AFM images show some aggregation of material on the surface of the films: the thicker the film, the larger the aggregates. The melting and quenching apparently created some disorder at the small scale (\AA - nm order), but some order in the long range (μm).

Upon annealing between T_g and T_m of PCDTBT the films initially expand of a quantity which is proportional to the initial film thickness and the annealing temperature (plot reported in figure 6.6). The expansion stops at a temperature T_o and the film undergoes a shrinkage which is also proportional to its total thickness. However there is a minimum thickness below which no shrinking is visible. This threshold thickness is about 10 nm. Films thinner than 10 nm also do not show any aggregation in the surface morphology upon annealing. This means that the aggregates size seen from the surface morphology and the shrinking seen with ellipsometry are strictly related.

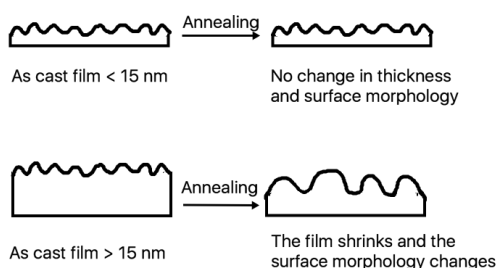


Figure 6.16: Cartoon showing the different surface morphology in very thin and very thick samples: as-cast films have the same surface morphology, but annealing causes shrinking and change in surface morphology only in films ≥ 15 nm.

The GIWAXS data presented in this chapter for as-cast samples having different thicknesses, show that generally the polymer tends to orient with flat-on π - π stacking and edge-on lamellar packing, but the film thickness has a major influence on the interchain distances of flat-on lamellar packing and edge-on π - π stacking. Flat-on (in-plane) lamellar packing goes from 20 \AA to 25 \AA (interchain distances) going from a 20 nm to a 200 nm film, while from 4.4 \AA to 4.8 \AA for edge-on (in-plane) π - π stacking. The interchain distances of the out-of-plane scattering data seem to be no very influenced by the different film thickness. The constraint does not

influence the characteristic d -spacing for flat-on π - π stacking and edge-on lamellar packing. The thinnest film (20 nm) presents though the largest out-of-plane coherence length for both lamellar and π - π stacking, meaning it is not the interchain distance changing with the thickness variation, although it is how much the flat-on ordering extends. It might be possible that in very thin films the air/polymer and substrate/polymer interfaces aid the crystallisation process, thus the higher coherence length out-of-plane. The out-of-plane scattering signal could be due to edge-on lamella and π - π stacking going from the top surface to the substrate without interruptions, how it has been explained in chapter 1 for the lamella orientation of poly(bisphenol A hexane ether) [92] where the flat-on nucleation was substrate induced.

The last observation made in this chapter was regarding the ordering as function of depth in 103 nm and 240 nm annealed films. These two samples present a π - π stacking relative scattering intensity trend similar to the one presented for 30 and 50 nm annealed PCDTBT films in Wang's paper [8]. Also in this case, the proximity to the substrate supports the better ordering at higher depths and specifically the π - π stacking, which is preferential near the substrate, rather than the lamellar packing.

Chapter 7

Discussion

7.1 Ordering as a function of thickness

It has been seen during the course of this thesis how crystallisation and surface morphology of PCDTBT are influenced by the thickness of the films and the temperatures at which they are annealed. Atomic force microscopy data on films of different thicknesses show surface morphology differences. It is clear from the AFM results that the aggregation size is the same for as-cast films of different thicknesses (figure 7.1), but increases drastically after melting-quenching (figure 7.2) and annealing (figure 7.3) as the thickness of the film increases. Films 8-20 nm thick show very little or no change in the aggregation size upon annealing. This result can be related to the lack of shrinking at ellipsometry for films less than 15 nm thick. Considering the three layers model (figure 7.4), very thin films might be constituted by a very reduced bulk region, which might be the layer where the majority of the shrinking occurs. In a recent study on P3HT films, Janasz *et al* found a similar increase in grain size with the film thickness, and the greater aggregation was accompanied by an increased charge mobility. [138]

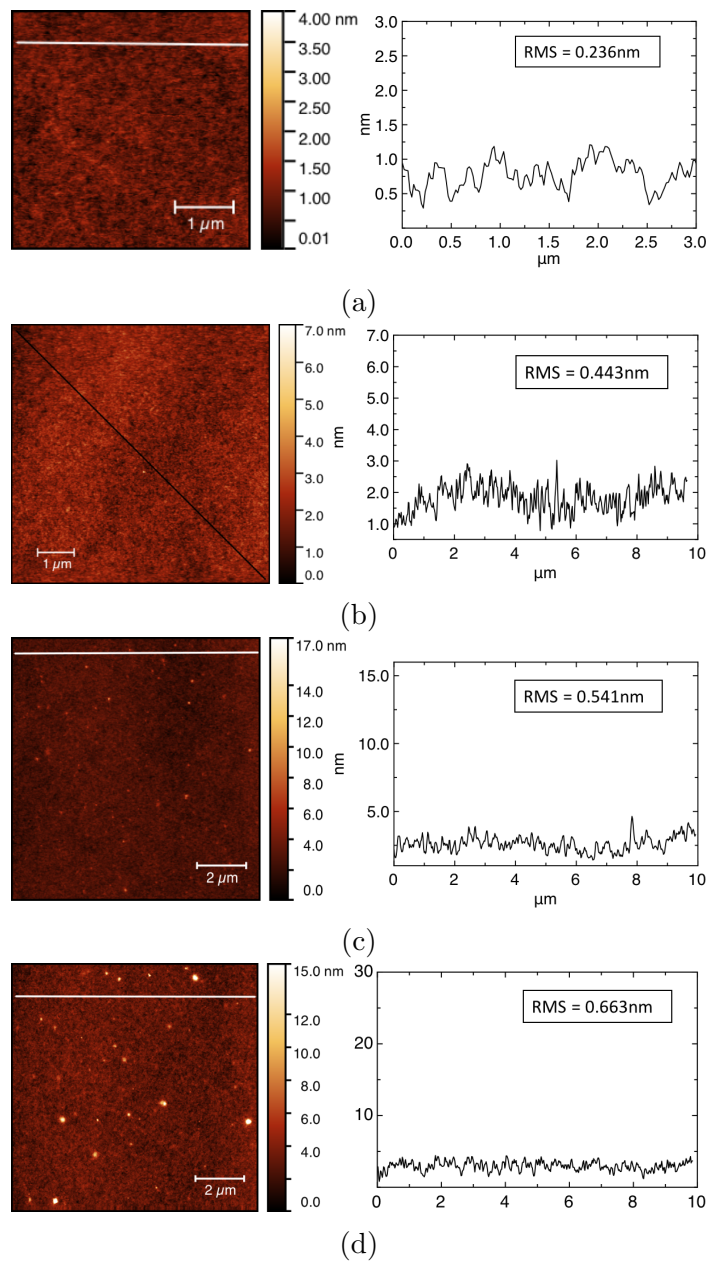


Figure 7.1: Height images for (a) 8 nm, (b) 40 nm, (c) 85 nm and (c) 200 nm as cast PCDTBT films.

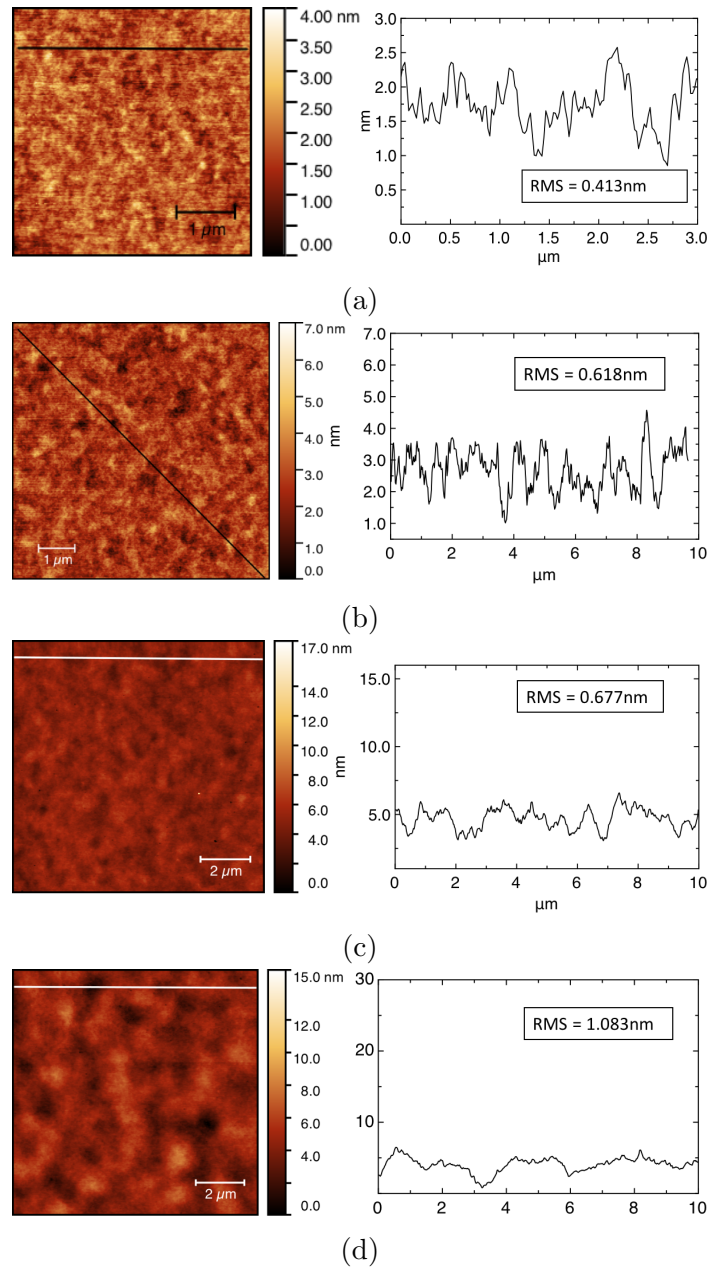


Figure 7.2: Height images for (a) 8 nm, (b) 40 nm, (c) 85 nm and (c) 200 nm melted-quenched PCDTBT films.

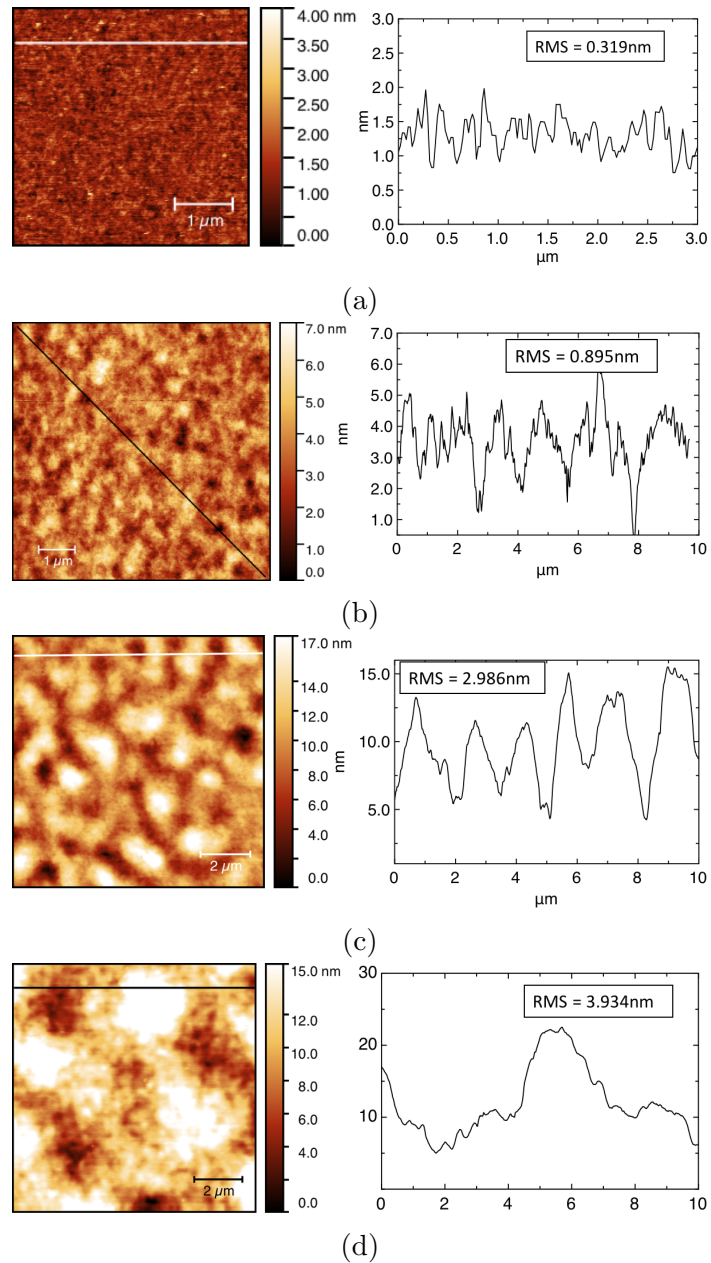


Figure 7.3: Height images for (a) 8 nm, (b) 40 nm, (c) 85 nm and (c) 200 nm PCDTBT films annealed at 180°.

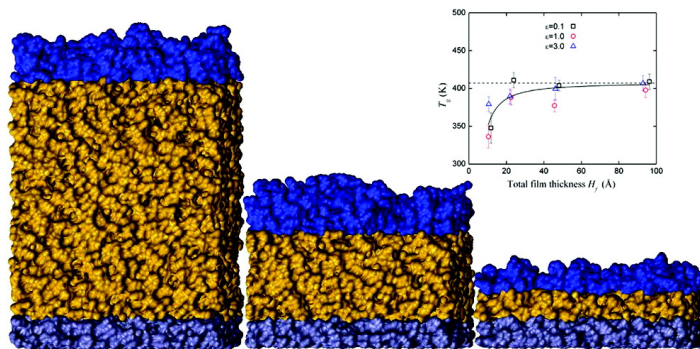


Figure 7.4: Three layers model represented from Hudzinsky *et al* molecular dynamics simulations. [139] The different colour for each region indicates different mass density and orientation of atactic-polystyrene in each layer. The inset represents the variation of T_g with the film thickness for different strengths of attraction to the substrate.

Grazing incidence X-ray scattering experiments on PCDTBT thin films, gave the following results about the packing as a function of the thickness:

- almost constant lamellar and π - π stacking intermolecular spacing in the out-of-plane scattering geometry for different film thickness in as-cast samples (schematics representing the configuration of PCDTBT molecules responsible for the out-of-plane scattering shown in figure 7.7);

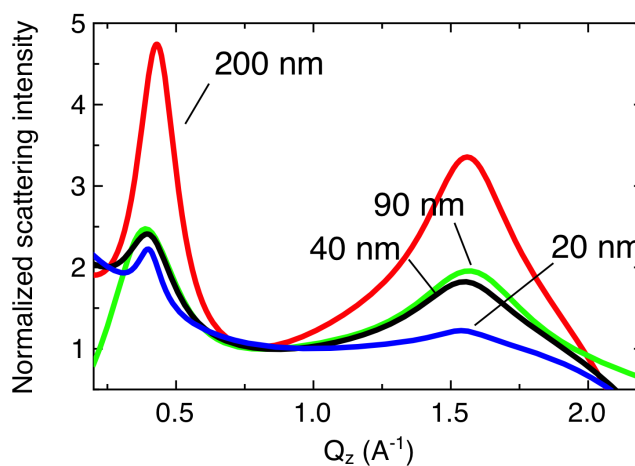


Figure 7.5: Fitting curves to the out-of-plane scattering data for different film thicknesses.

A conclusion could be drawn: the confinement in thin films is more likely to influence the percentage of crystalline material within a film, rather than changing the intermolecular packing distance. The lamellar and π - π stacking d spacings represent the characteristic distances for the molecular packing of PCDTBT which is the minimum energy configuration of the polymer

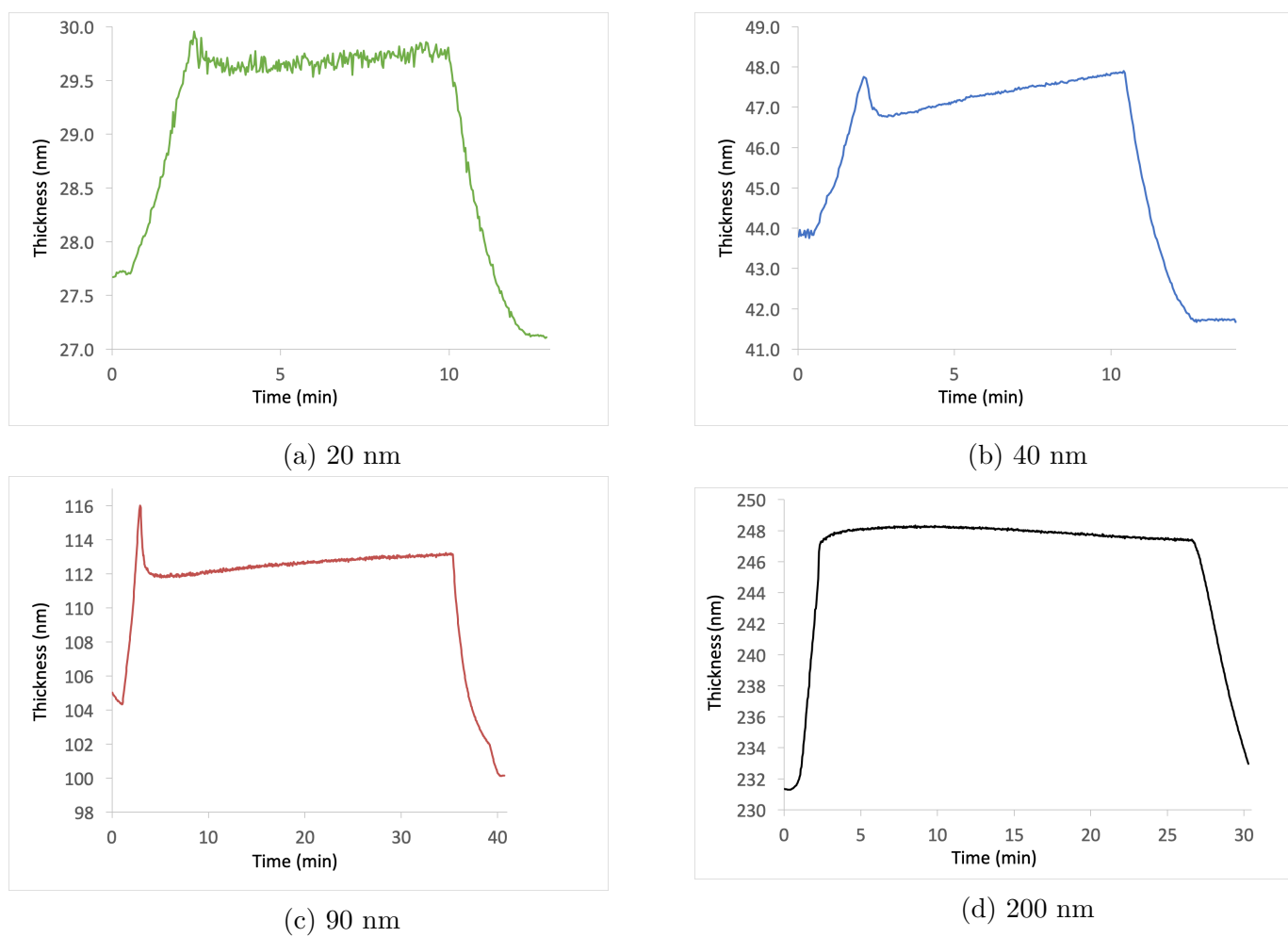


Figure 7.6: Ellipsometry data for the polymer films the which GIWAXS data are reported in figure 7.5 and 7.8

chains. A calculation of the volume fraction of the crystalline phase could be made from the thickness profiles measured by ellipsometry for different film thicknesses, in order to have a comparison for the GIWAXS data. The problem is finding accurate density values for the crystalline and amorphous phases of PCDTBT.

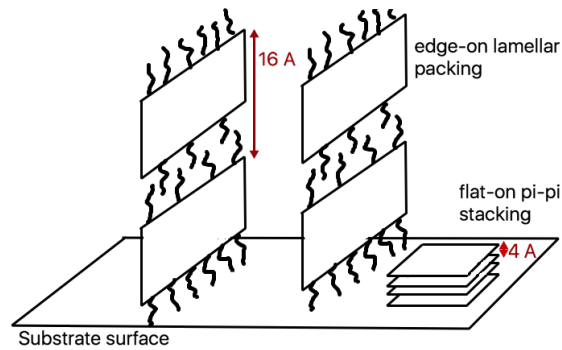


Figure 7.7: Schematics showing the molecular packing configuration of PCDTBT in thin films responsible for the GIWAXS out-of-plane scattering. The intermolecular distances are constant for different film thickness: about 16 Å for edge-on lamellar packing and 4 Å for flat-on π - π stacking.

- there is instead a remarkable Q shift in the in-plane scattering data. The flat-on lamellar packing length increases from 20 to 25 Å from the 20 nm film to the 200 nm film; the edge-on π - π stacking increases from 4.4 Å in the 20 nm film to 4.8 Å in the 200 nm film.

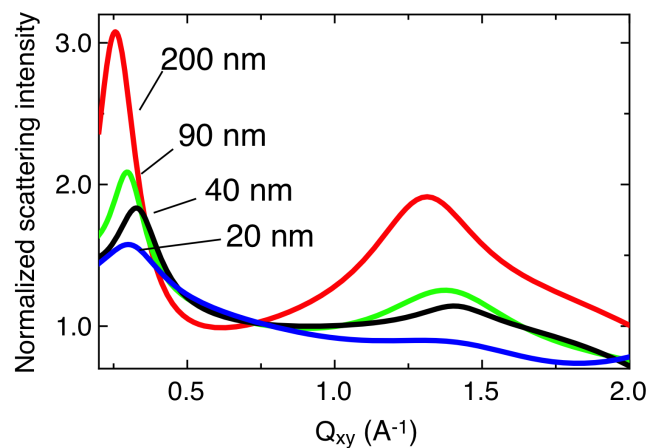


Figure 7.8: Fitting curves to the in-plane scattering data for different film thicknesses.

The constraint caused by the film thickness can be then thought to have more influence on the in plane lamellar and π - π stacking scattering peaks, which are caused by two different

orientations: the in-plane lamellar packing is caused by a flat-on configuration, while the in-plane π - π stacking is caused by an edge-on configuration (figure 7.9).

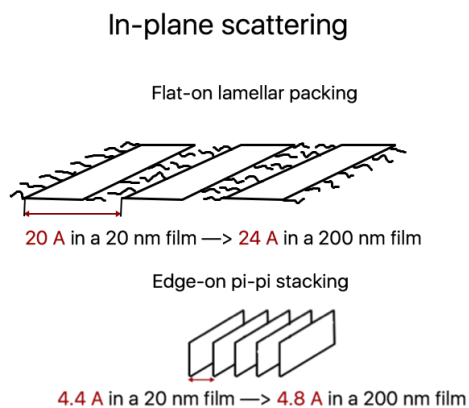


Figure 7.9: Schematics showing the molecular packing configuration of PCDTBT in thin films responsible for the GIWAXS in-plane scattering. The intermolecular distances increase with the increasing film thickness: from 20 Å to 24 Å for flat-on lamellar packing and from 4.4 Å to 4.8 Å for edge-on π - π stacking.

7.2 Ordering as a function of temperature

The annealing temperature is the second parameter that has a remarkable influence on the packing of PCDTBT as shown in chapter 3, 4 and 5.

From the GIWAXS results shown in chapter 3, as-cast PCDTBT seems to be preferentially orientated with the π - π stacking direction perpendicular (flat-on) to the substrate, as indicated by the greater scattering intensity in the out-of-plane direction. The lamellar packing (alkyl direction) is preferentially oriented perpendicular to the substrate (edge-on) giving the intense signal at around 0.33 \AA^{-1} in the out-of-plane direction (see figure 7.7).

The melting-quenching procedure reduces drastically the crystallinity of the film as seen from the very weak scattering at the critical angle. A successive isothermal annealing at 200°C for few minutes increases the crystallinity, but the orientation of the chains is different compared to the as cast film: the scattering intensity in the out-of-plane direction is reduced mainly for the π - π stacking (figure 7.10).

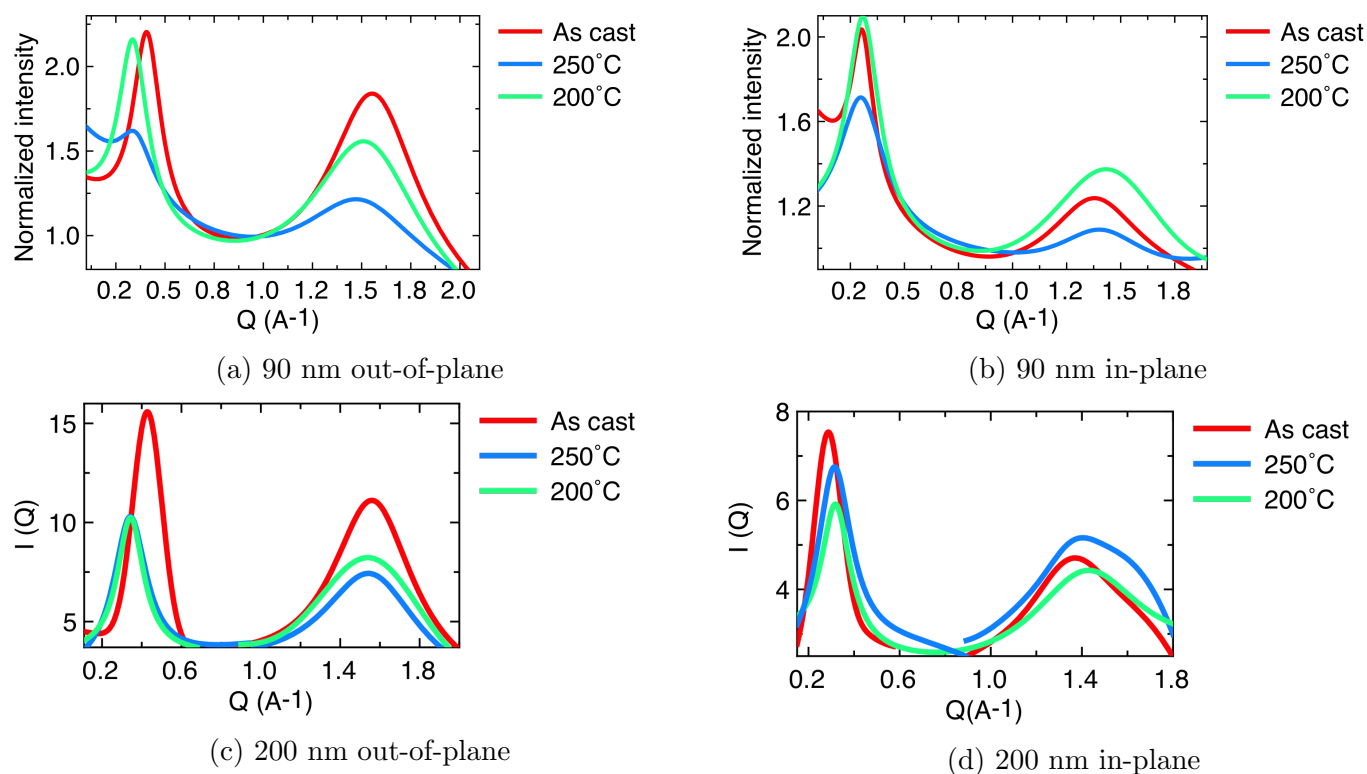


Figure 7.10: (a) and (b) show the out-of-plane and in-plane scattering data for a 90 nm PCDTBT film after each step of the thermal protocol. (c) and (d) show the out-of-plane and in-plane scattering data for a 200 nm PCDTBT film after each step of the thermal protocol.

The lamellar packing is less intense in the 200°C annealed film than in the as-cast film, but

the important difference between as-cast and annealed is the shift in Q along the out-of-plane direction. Compared to the annealed samples (both melted-quenched and isothermal annealed), the lamellar packing distance in the out-of-plane direction is 4 Å shorter in the as-cast 90 nm thick sample and 3 Å in the as-cast 200 nm thick sample. This means the melting-quenching procedure produces a film expansion which is probably due to this increased distance between backbones. As discussed in some early works on conjugated polymers, it is likely that alkyl chains start to disorder prior to any larger conformational change involving the backbones. [62, 63]

The lamellar packing oriented flat-on (parallel to the substrate) and responsible for the in-plane scattering, has instead a larger d -spacing in the as-cast samples: 1 Å more in the 90 nm thick sample and 2 Å more in the 200 nm thick sample. The flat-on π - π stacking instead (out-of-plane scattering) changes less than an Å between as-cast and annealed: shorter packing distance in the as-cast (for the 90 and 200 nm sample). The edge-on π - π stacking has instead a shorter d -spacing in the annealed sample (about 1 Å difference).

Focusing again on the difference in the scattering intensity, it seems then that annealing damages the π - π oriented face-on, as the π - π out-of-plane intensity diminishes from as-cast to annealed. Contrarily, the edge-on π - π stacking (in-plane scattering) increases in the annealed sample. Together with the shorter spacing can be concluded that annealing might be beneficial for the edge-on π - π stacking, but disrupting for the flat-on oriented π - π stacking.

This might mean that the edge-on configuration is the thermodynamically stable form, because it improves after annealing, while the flat-on is the kinetics product as it forms preferentially post spin-coating.

The edge-on lamellar packing instead, seems to be more stable upon annealing, as its amount does not change very much between as-cast and annealed, although the disorder is translated in more space between the backbones.

A similar comparison between flat-on and edge-on oriented P3HT chains and their different stability upon annealing was made in the paper by Sun X. *et al.* [140] They demonstrate that face-on oriented P3HT is less stable than the edge-on oriented one, as face-on oriented chains melt at 160°, while the edge-on ones melt at 220°.

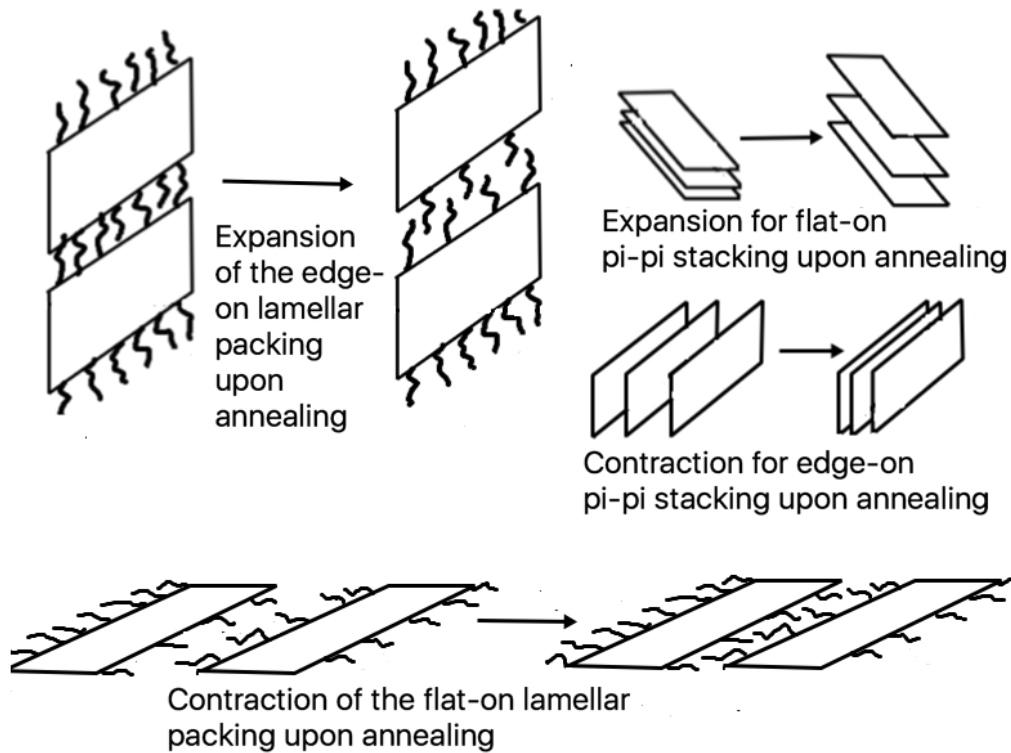


Figure 7.11: Schematics showing the molecular packing configuration of PCDTBT before and after annealing. The intermolecular distances increase upon annealing (both melting-quenching and isothermal annealing) in the out-of-plane direction, and decrease in the in-plane direction.

The PCDTBT thickness profiles measured by ellipsometry during annealing present us some curious results. This polymer does not present an induction time prior to crystallisation as observed by Ibaragi for PET, [9] but all the ellipsometry curves show the existence of a characteristic temperature (T_o) at which the polymer starts to crystallise. The value of T_o changes with the heating rate, supporting the hypothesis that this temperature marks the beginning of the crystallisation process. Annealing at lower or larger temperatures than T_o has consequences on the shape of the ellipsometry curves. Annealing above this T_o usually brings the film to expand again after the first shrinking (figure 7.12).

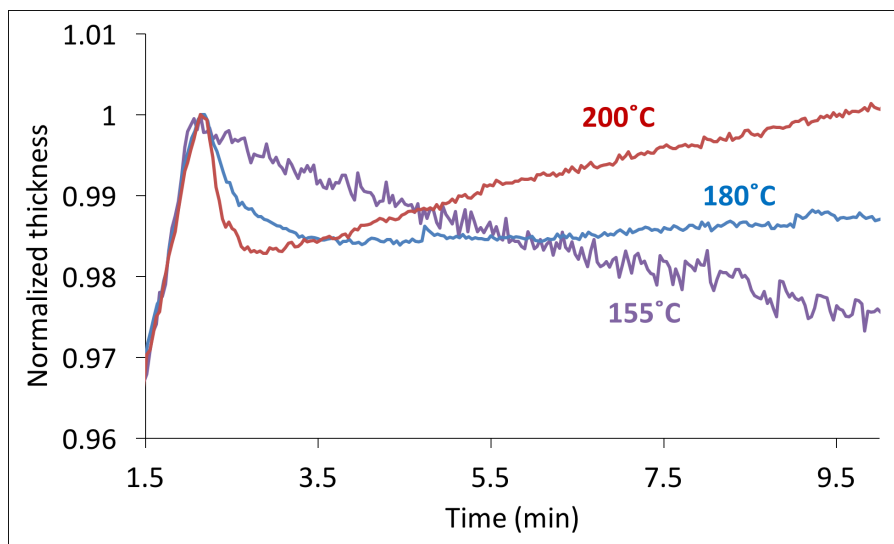


Figure 7.12: Thickness profiles measured by ellipsometry for 50 nm thick samples. The samples that show expansion are the ones that have been annealed at a temperature $\geq T_o$: 180°C and 200°C.

The second expansion discussed largely in chapter 5 is very probably due to a disruption of the crystallinity as the absorption spectra show. High annealing temperatures usually also causes a larger d -spacing in the lamellar packing, demonstrating that annealing has more influence than the space constraint on the d spacing of the polymer chains. Very high temperatures are able to create defects and disrupt the crystallinity more easily than the proximity to an interface. The other puzzling result is the flattening of the surface morphology upon annealings long enough to provoke a film expansion seen with ellipsometry. What is certain is the proof that the increase in surface aggregate size means better order, which is related to a shrinkage of the film observed with ellipsometry and a better conjugation of the backbones and increased crystallinity: as shown by increased UV-vis absorption of PCDTBT and red-shifts of the spectra.

The disruption of the out-of-plane crystallinity upon annealing at high temperatures seen in the GIWAXS results, demonstrates that the out-of-plane features (edge-on lamellar packing and flat-on π - π stacking) are the kinetically favoured conformations, while the in-plane features (flat-on lamellar packing and edge-on π - π stacking) are the thermodynamically stable features.

7.3 Conclusions

The surface morphology of the PCDTBT films changes with the thickness and the thermal protocol, getting rougher and presenting larger aggregates for thicker, longer annealed films. The key result of this study is the loss of preferential orientation of the chains post melting and quenching, shown by the fact that the scattering goes from elliptical in the as-cast films to circular in the post annealed films, as was shown also in the paper by Lu et al. [74]. The as cast films present a preferential orientation which is with the aromatic rings π - π stacking parallel to the Silicon wafer, piling up in the direction orthogonal to the film surface. This produces the out-of-plane scattering intensity at 1.45 Å. As a consequence, the lamellar packing should happen in the direction parallel to the film surface, as the lamellar and π - π stacking are orthogonal to each other. However the scattering intensity also for the lamellar packing is mostly out-of-plane in the GIWAXS data, suggesting that the lamellar packing occurs orthogonally to the film surface. This means that π - π stacking and lamella ordering do not occur at the same time, or at least not as many chains involved in the lamellar packing are also π - π stacking, probably due to the steric hindrance caused by the alkyl chains that are causing the backbones to order as bilayers, or due to the dihedral angles between the carbazole and the thiophene and between the thiophene and the benzothiadiazole [74]. There is also a great amount of amorphous material as is suggested by the diffuse nature of the scattering.

From the data presented in chapter 4 it is possible to see the existence of a characteristic temperature that can be defined as T_o , which is the temperature where the crystallisation starts. The shape of the ellipsometry isotherm is different depending if the annealing temperature is larger or lower than this crystallisation temperature. If the annealing temperature is lower than the crystallisation temperature, a preordering phase will become noticeable (section 4.2.1). It is clear that different mechanisms contribute to the ordering of PCDTBT and they become visible when the polymer is annealed at different temperatures. At lower temperature, near the limit of the T_g , the shape of the isotherm changes once more, not corresponding any more to an exponential decay, but to a linear one.

Annealing at very high temperatures, such as 200°C disrupts the ordering as a larger distance

between the chains in the GIWAXS data suggests. This causes the expansion of the films during the isotherms.

As it appears from the coherence length for the different annealing temperatures, 155°C is optimal as the coherence length for the lamellar stacking reaches 63 Å, out-of-plane. It looks like the coherence length is greater in the in-plane than out-of plane. There is also a very high coherence length in thin films of 20 nm in the out-of-plane direction, this could mean that the two interfaces help the extension of the packing. A key result from chapter 4 is the existence of a transition point for the crystallisation activation energy at around 40 nm. The activation energy linearly increases with the film thickness because relatively fewer of the polymer chains are exposed to the air interface and the bulk-like layer behaviour takes over as the film gets thicker. Above 40 nm the ordering activation energy seems to be constant as thicker films are governed by a bulk-like behaviour. The film thickness has important consequences on the crystallisation of PCDTBT. The confinement in thin films gives a preferential orientation of the chains as the lamellar packing and π - π stacking both occur in the direction perpendicular to the substrate.

Also the surface morphology is different: the thicker the film, the larger the aggregates of material on the surface. There is also a minimum thickness below which no shrinking is visible. This threshold thickness is about 10 nm. Films thinner than 10 nm also do not show any aggregation in the surface morphology upon annealing. This means that the aggregates visible on the film surface and the shrinking upon annealing are strictly related, and very likely annealing is promoting the aggregation of material.

The film thickness has a major influence on the interchain distances of flat-on lamellar packing and edge-on pi-pi stacking. Flat-on (in-plane) lamellar packing goes from 20 Å to 25 Å (inter-chain distances) going from a 20 nm to a 200 nm film, while from 4.4 Å to 4.8 Å for edge-on (in-plane) π - π stacking. The interchain distances of the out-of-plane scattering data seem to be not very influenced by the different film thickness. The constraint does not influence the characteristic d -spacing for flat-on π - π stacking and edge-on lamellar packing. The different film thickness influences mostly the coherence length for both lamellar and π - π stacking. The thinnest film (20 nm) presents the largest out-of-plane coherence length for both lamellar and

π - π stacking, meaning it is not the interchain distance changing with the thickness variation, but how much the conjugation extends.

7.4 Future Work

As explained in the discussion section of chapter 5, it would be important to verify that the films annealed at temperatures lower than the T_o , do not expand as the ones annealed at $T \geq T_o$, if they are annealed for longer periods.

Then it would be interesting to study the evolution of the crystal structures of PCDTBT films at different depths *in situ*, with GIWAXS on the film on the heating stage, in order to follow the evolution of the crystal structures upon annealing. Because the crystal structure changes as soon as the sample is cooled down, while ellipsometry for example is able to obtain information of the sample every second. With GIWAXS and AFM of used in this PhD I obtained information of films annealed at different temperatures, for different time lengths, but the results are for the film after it has been cooled down. During the annealing process the polymer chains undergo a change in orientation and packing which would be very interesting and informative to follow. The problems are to find the right AFM instrument that can work at high temperatures and X-ray equipment with fast acquisition time. In this case a synchrotron source would be necessary, due to the low crystallinity of PCDTBT, a laboratory equipment needs too lengthy acquisition time to be able to follow the packing of the film every second. The second problem in a *in situ* GIWAXS experiment might be the expansion of the film that would require a continue calibration of the X-ray beam.

Additional work can be done with a wider range of film thicknesses, possibly with more points near the threshold thickness where no shrinking is visible upon annealing, would confirm the observations made in chapter 6 of this thesis.

Another important experiment that could be used to understand the influence of the substrate on the packing of PCDTBT, would be being able to float a PCDTBT film off Si and analyse the surface structure with GIWAXS: it would correspond to the substrate/film interface structure. Further analysis could be done with polarised soft X-rays which are very useful in understanding

the orientation and packing structures in weak crystalline polymer films. This could be done also in transmission using SiN_3 as substrate, which is transparent. In transmission it will be possible to obtain information about the orientation of the structures influenced by a near interface. It will be an average of what is present at different depths, but probably changing the thickness of the films it would be possible to see the predominant packing configurations or orientations in function of the film thickness.

List of Figures

1.1	A spherulite on the left hand side and a chain-folded lamella on the right hand side. The lamella has thickness l which is typically 10 nm. A spherulite can reach several μm up to some cm in diameter, depending on the nucleation density. Figure reproduced from “Soft Condensed Matter” by Jones [20].	10
1.2	Crystallisation kinetics of PET annealed isothermally at 80°C. Figure reproduced from Imai <i>et al</i> [21].	11
1.3	Temperature dependence of the growth rate u of spherulites in i-PS, nylon-6 and TMPS. Data from different authors taken from “Methods of Experimental Physics” by Ross and Frolen [22].	11
1.4	Free energy changes of a polymer stem joining a growing crystal from the melt. Figure reproduced with permission from Jones [20].	13
1.5	Multistage model of the polymer crystal growth through a mesophase as suggested by Strobl [30]. The crystal does not grow by chain segments directly attaching to the crystal front, but from the melt are first incorporated in a thin layer with mesomorphic structure in front of the crystallite. A critical thickness is then reached and a crystal block forms by first order transition. In this last step the excess energy of the fold surface is reduced. Figure reproduced with permission from Strobl [30]	16
1.6	(a) Lamellar and (b) hexagonal packing structures typical in semiconducting polymers. Figure reproduced with permission from Chabinye [45].	17

- 1.7 In this figure is possible to distinguish three different length scales: (a) the lamellar structure that involves layers of π - stacked polythiophene backbones separated by the hexyl side chains (1.6 nm), (b) the π - π stacking distance, 0.38 nm and (c) the periodicity related to the alternation of crystalline and amorphous zones (28nm). The P3HT chains in the amorphous zones are represented as red segments. Figure reproduced with permission from Brinkmann [4]. 20
- 1.8 Absorption spectra for PCDTBT annealed at different temperatures in air (a) and under nitrogen (b). It is possible to see that the optical properties of the polymer are already influenced above 150°C in air (a). Figures reproduced with permission from Cho *et al* [71]. 21
- 1.9 X-ray Diffraction data for PCDTBT polymer films annealed and as-cast. Figure reproduced with permission from Cho *et al* [71]. 21
- 1.10 Chemical structure of benzothiazole. 22
- 1.11 (a) GIWAXS data and line-cuts out-of-plane from [75]. (b) The corresponding crystal lattice. Reprinted with permission from [75]. Copyright 2017 American Chemical Society. 23
- 1.12 (a) Molecular structure of PCDTBT and the experimental geometry of the GIWAXS (b). Figure reproduced with permission from Lu *et al* [74]. 23
- 1.13 2D GIWAXS images before (a) and after heating/cooling cycle for T_g measurement (b). (c) raw scattering data at three different grazing incidence angles in the out-of-plane direction. (d) π - π Stacking coherence length as a function of the g.i. angle, and the relative intensity changes of peaks at $q = 0.63 \text{ \AA}^{-1}$ and $q = 1.57 \text{ \AA}^{-1}$. Figure reproduced with permission from Wang *et al* [8]. 24
- 1.14 GIWAXS scattering images of PCDTBT. The images were obtained at (a) 25°C before annealing; (b) 140°C; (c) 200°C; (d) 25°C after annealing. Figure reproduced with permission from Lu *et al* [74]. 25

- 1.15 Scattering profiles along q_z . The lower seven curves have been obtained along $q_r \sim 0$ and the top two curves along $q_r = 0.15 \text{ \AA}^{-1}$. The orange 25°C curves are measured before the thermal treatment and the blue one, after the thermal treatment. Figure reproduced with permission from Lu *et al* [74]. 26
- 1.16 PCDTBT thin-film diffraction pattern, unit cell and bilayer motif. (a) Diffraction pattern obtained from the Bragg peaks shown in figure 1.15d. The filled circle corresponds to the origin. (b) The corresponding oblique real-space lattice obtained from the scattering pattern. The $\pi - \pi$ direction is normal to this plane. (c) Backbone configuration for one of possible conformations of a backbone obtained by *ab - initio* calculations. Figure reproduced with permission from Lu *et al* [74]. 27
- 1.17 Schematic of three types of liquid crystals, nematic, smectic, cholesteric. In the nematic phase the long axis of the molecules are parallel to each others. In the smectic phase, the molecules are parallel to each others and also organised in planes. In the cholesteric phase the molecules are organised in layers which are tilted forming a spiral, which gives chiral properties to this type of phase. The degree of order increases from nematic to cholesteric and the liquid becomes also more opaque. 30
- 1.18 A polymer film can be seen as constituted by three layers with different characteristics. The top air/polymer interface layer with enhanced mobility with enhanced T_g , the bottom substrate/polymer interface with hindered mobility and decreased T_g , the bulk-like layer in the middle. Figure reproduced with permission from Wang *et al* [92]. 31
- 1.19 Glass transition temperature T_g in function of the film thickness for different molecular weights of polystyrene. Figure reproduced from Keddie *et al* [10]. . . . 31

1.20	(a) Represents the T_g for three different film thicknesses, measured during cooling by ellipsometry. (b) Direct effect of $\pi - \pi$ stacking is observed on the T_g : it converges to 110°C at a film thickness of 40 nm and it does not decrease anymore. Figure reproduced from Wang <i>et al</i> [8].	32
1.21	Chemical structure of the poly(bisphenol A hexane ether) (BA-C6).	32
1.22	Measured T_g of ultrathin BA-C6 films as a function of film thickness. Differently from the curve from Keddie <i>et al</i> in here T_g increases for very thin films suggesting that the substrate influence prevails on the air/polymer interaction. Figure reproduced with permission from Wang <i>et al</i> [92].	33
1.23	(a) A bell-shaped curve shows the primary nucleation rate as a function of temperature. (b) T_{g1} is the characteristic T_g near the surface and the curve shows that the T_c will decrease. (c) T_{g3} is the characteristic T_g near the substrate and the consequent increase in T_c . (d) Shows the combination of the two. Figure reproduced with permission from Wang <i>et al</i> [92].	33
1.24	AFM images from Wang <i>et al</i> work [92]. Height images in the upper row, phase images in the lower row. Crystalline morphologies for BA-C6 are shown in these about 30 nm films crystallised for 84 hours at 45°C (a), 60°C (b), 75°C (c) and 90°C (d). It is possible to see that edge-on lamellae are visible at the surface for the lower annealing temperatures, while for higher annealing temperature, mainly flat-on lamellae are visible. The scale bar in (h) is 10 μm . Figure reproduced with permission from Wang <i>et al</i>	34
1.25	Schematic illustration proposed by Wang <i>et al</i> [92] showing the formation of flat-on lamellae in contact with the substrate. Figure reproduced with permission from Wang <i>et al</i>	35
2.1	Schematic representation of the reflected and transmitted components of the incident light-beam for a three layers system: nitrogen, PCDTBT and silicon. [111]	43
2.2	Schematic diagram of an ellipsometry experiment. The linearly polarised beam is reflected from the sample becoming elliptically polarised. [112]	46

2.3	The polariser linearly polarise the light coming from the QTH lamp and the rotating compensator introduces a phase delay of 90° producing a circularly polarised light. [111]	48
2.4	Schematic diagram of the ellipsometry experimental setup.	49
2.5	(a) Schematic representation of atomic force microscopy in tapping mode. (b) Cantilever deflection and feedback system through a laser reflected on the cantilever. (c) Schematic representation of the relation of the surface morphology with the cantilever oscillations. [114]	50
2.6	Scattering intensity in function of the scattering vector and representation of the length-scales that is possible to analyse in SAXS (larger lengthscales, 1 - 100 nm) or WAXS (shorter lengthscales, 10 - 1 Å. [115]	53
2.7	Schematic representation of the sample stage utilised on the Xeuss for the GI-WAXS experiments reported in this thesis. [115]	54
2.8	X-ray electric field intensity for incident angles above the critical angle of the polymers for two PCDTBT films, 30 nm and 50 nm thick. The plots of the electric fields represent the standing waves at different angles, produced from the interference of the incident beam with the reflected beam from the polymer-substrate interface. Figure reproduced from Wang <i>et al</i> [8].	55
2.9	Schematic diagram of the geometry for a GIWAXS experiment. Q_z is the component of the scattering vector perpendicular to the sample surface and Q_{xy} is the component lying on the sample surface. Material features that present a periodicity which is parallel to the substrate (plane xy) will show a scattering signal in the in-plane direction. Periodicity perpendicular to the substrate (along the z axis) will show scattering in the out-of-plane direction.	56
2.10	Photography of the Xeuss chamber in GIWAXS mode of the instrument at the department of chemistry, University of Sheffield. [115]	57
3.1	Differential Scanning Calorimetry of PCDTBT. No crystallisation peaks are observed.	61

3.2	Ellipsometry experiment heating up a 68 nm film from 25°C to 310°C at 5°C/min. It is possible to recognise the glass transition, T_g , the shoulder where the polymer presumably tends to order spontaneously, at the temperature T_o (it will be explained in chapter 4) and the shoulder corresponding to the melting point.	62
3.3	Heat capacity and enthalpy vs. temperature. The latent heat for melting and evaporation is modeled by a Gaussian distribution.	63
3.4	Glass transition, crystallisation and melting for PLLA films. Right panels: an example of the determination of the phase transition temperatures. Reproduced from [123] with permission of The Royal Society of Chemistry.	64
3.5	Thermal Gravimetric Analysis for PCDTBT.	65
3.6	Thickness profile (black line) of a PCDTBT film as a function of time, measured by ellipsometry. The temperature profile is represented by the red line. The difference in thickness between the beginning and the end of the experiment is due to the polymer molecules reorganising during the isothermal annealing and packing in a different conformation that occupies less space.	66
3.7	Thickness profile of the 8 nm PCDTBT film annealed at 180°C, after melting and quenching at 250°C.	67
3.8	Height images for a 8 nm film of PCDTBT as cast (a), after melting-quenching at 250°C (b), and after an isotherm at 180°C (c).	68
3.9	Height images for 40 nm PCDTBT films, as cast (a), after melting-quenching at 250°C (b) and after an isotherm at 180°C (c).	69
3.10	Height images for 85 nm PCDTBT films, as cast (a), after melting-quenching at 250°C (b) and after an isotherm at 180°C (c).	70
3.11	Height images for 200 nm PCDTBT films, as cast (a), after melting-quenching at 250°C (b) and after an isotherm at 180°C (c).	71
3.12	Thickness profile of the 90 nm PCDTBT sample heated at 200°C.	73

- 3.13 GIWAXS data verifying the thermal protocol on a 90 nm film. 2D images for an as cast sample (a), a sample that has been just melted and quenched at 250°C (b), and a sample that has been heated at 200°C (c). The two scattering rings at $Q = 0.33 \text{ \AA}^{-1}$ and the π - π stacking at $Q = 1.53 \text{ \AA}^{-1}$ correspond to the lamellar packing. 73
- 3.14 (a) and (b) show the out-of-plane and in-plane GIWAXS scattering data for a 90 nm PCDTBT film after each step of the thermal protocol. (c) and (d) are the functions that best fit the data in figures (a) and (b). The data were re-scaled, so that they could be represented on a single plot helping the comparison between the different peaks. The peaks were fitted to Gaussian functions. (a) and (b) have been created by integrating the signal intensity within delimited circular sectors centred at the beamstop, of the 2D data represented in figure 3.13. For the out-of-plane sections were taken regions 30° wide centred along Q_z , while for the in-plane data, regions 30° wide were taken along Q_{xy} with the bottom radius lying horizontally coinciding with the bottom border of the 2D image. 74
- 3.15 This figure is showing how the data fitting has been performed to obtain height and position of a scattering peak. The red squares are the line cuts taken from the GIWAXS data showed in figure 3.13. The grey lines represent the third degree polynomial and the Gaussian functions used to fit the experimental data. The black line is the sum of the two function. The distances between the polynomial and the maximum of the peaks are then the intensity at x_0 reported in table 3.1. 74
- 3.16 Schematic diagram representing the changes in the molecular ordering and spacing between an as cast and an annealed sample. 76
- 3.17 Thickness profile of the 200 nm PCDTBT sample heated at 200°C. 78

- 3.18 GIWAXS 2D images for 200 nm thick films of PCDTBT: as-cast (a), after melting and quenching at 250°C (b) and after isothermal annealing at 200°C (c). The inner scattering rings are from the lamellar packing distance, which is about 15 Å for the as-cast sample in the out-of-plane direction and 18 Å for the annealed samples. While, along the in-plane direction the distance is 22 Å for the as-cast sample and 20 Å for the annealed samples. The outer rings are from the π - π stacking distance of 4 Å in the out-of-plane direction for all the samples and 5 Å in the in-plane direction. 79
- 3.19 (a) and (b) show the out-of-plane and in-plane scattering data for a 200 nm PCDTBT film after each step of the thermal protocol. (c) and (d) are the functions that best fit the data in figures (a) and (b). 80
- 3.20 Thickness profiles for two 200 nm PCDTBT samples: with (a) and (b) without a previous melting-quenching process. (c) and (d) are the out-of-plane and in-plane scattering data for the two samples. The ellipsometry curve in (a) shows more shrinking compared to the curve for a film of the same thickness, reported in figure 3.17. The only difference between the two samples is that they have been prepared from different solutions, prepared on different dates, but material and experimental conditions were exactly the same. 82
- 3.21 Thickness profiles for three 35 nm PCDTBT samples, studying the impact on isothermal annealing for a sample that has not been previously melted and quenched (a); a sample that has been cooled on a cold piece of Si (b); and a sample normally cooled by being dipped in liquid nitrogen. 83
- 4.1 Thickness profile (black line) of a PCDTBT film as a function of time, measured by ellipsometry. The temperature profile is represented by the red line. 86
- 4.2 Ellipsometry data for 30°C/min (a), 90°C/min (b) and 130°C/min (c) heating rates. The faster the heating rate, the higher is T_o , temperature where the shrinking starts. 87

- 4.3 Ellipsometry experiment showing two isotherms at 195°C, heating rate 90°C/min.
- a) The film annealed at 195°C the first time after one melting-quenching, starts shrinking spontaneously at 166°C. In this case $T_o < T_i$ where $T_o = 166^\circ\text{C}$ and $T_i = 195^\circ\text{C}$. (b) the same sample of figure (a) has been then melted-quenched a second time and brought again at 195°C for more than 10 minutes, in this case $T_o = T_i$, the film does not start shrinking before reaching the set up temperature of 195°C 88
- 4.4 Thickness profiles measured by ellipsometry are shown for three different PCDTBT film thicknesses: 30 nm (a), 50 nm (b) and 75 nm (c). For each film thickness are reported the thickness profiles of samples annealed at three different temperatures, 155°C, 180°C and 200°C. 89
- 4.5 The shift factors have been plotted against the annealing temperatures. All the ellipsometry curves have been compared to the ellipsometry curve of the film annealed at 170°C, which has been chosen as reference temperature. That is why is highlighted in the graphs with an arrow. The red lines represent the best exponential fit for the data points. The data points for temperatures $> 185^\circ$ have not been included in the fitting because is believed they follow a different law. 92
- 4.6 Logarithmic forms of the plots in figure 4.5. 170° is the reference temperature taken in the time-temperature superposition analysis. The red lines represent the best fit to the data points and they are described by the equation $\ln(c_T) = \ln(A) + \alpha T$, where α is the slope of the linear fits. 93
- 4.7 Plot showing two trends of the crystallisation activation energy α in function of the film thickness. α varies for film thinner than 40 nm and it is constant for films thicker than 40 nm. 94

- 4.8 90 nm film thickness. (a) The normalised thickness profiles at different temperatures, as recorded by the ellipsometry. (b) The curves have been multiplied by a shift factor in order to make them overlap. (c) The curves once again multiplied by a shift factor and then 'shifted' along the x-axis, so it is possible to distinguish the three different shapes of the isotherms: 140°C is one shape, different from 150°C and 160°C, which are different from 170°C and 180°C. 95
- 4.9 75 nm film thickness. (a) and (b) The normalised thickness profiles at different temperatures, as recorded by the ellipsometry. (c) The curves have been multiplied by a shift factor in order to make them overlap. (d) The curves once again multiplied by a shift factor and then 'shifted' along the x-axis. One shape for 150°C - 155°C, a different one for 160°C - 175°C and another one for 180°C - 200°C. 97
- 4.10 60 nm film thickness. (a) and (b) The normalised thickness profiles at different temperatures, as recorded by the ellipsometer. (c) The curves have been multiplied by a shift factor in order to make them overlap. (d) The curves once again multiplied by a shift factor and then 'shifted' along the x-axis. 98
- 4.11 35 nm film thickness. (a) and (b) The normalised thickness profiles at different temperatures, as recorded by the ellipsometer. (c) The curves have been multiplied by a shift factor in order to make them overlap. 99
- 4.12 25 nm film thickness. (a) and (b) The normalised thickness profiles at different temperatures, as recorded by the ellipsometer. (c) The curves have been multiplied by a shift factor in order to make them overlap. (d) The curves once again multiplied by a shift factor and then 'shifted' along the x-axis. 100

4.13	Example of a 170°C and a 145°C isotherm for a 60 nm film, illustrating the different shape of the two curves. The 170°C (black curve) shrinks 0.04 units in 5 minutes, while at 145°C (red curve) for the same time the shrink is of 0.01 unit and then it continues a slow shrinking for a long time. It is impossible to overlap these curves completely as they both are divided in two stages, but for the 140°C the first step is much shorter than the 170°C.	101
4.14	Thickness profiles measured by ellipsometry for 35 nm films annealed at 210°C (a) and 200°C (b). (a) The change in expansivity at 110°C it is probably due to the T_g and 179°C denotes T_o : the ordering does not start at T_o but it starts when the film reaches T_i (210°C).	102
4.15	Thickness profiles measured by ellipsometry for 50 nm films annealed at 210°C (a) and 200°C (b).	102
4.16	Thickness profiles measured by ellipsometry for 75 nm films annealed at 220°C (a), 210°C (b) and 200°C (c).	103
4.17	Thickness profiles of the two 50 nm PCDTBT samples annealed at 155°C and 200°C the which AFM images are shown in figures 4.18 and 4.19	104
4.18	AFM comparison of 50 nm PCDTBT films annealed at 155°C (a) and 200°C (b). Scale: 10 μm	105
4.19	AFM comparison of 50 nm PCDTBT films annealed at 155°C (a) and 200°C (b). Scale: 2 μm	105
4.20	Raw scattering data (a,b) and fitting curves (c-e) for GIWAXS experiments on 50 nm samples annealed at 200°C, 170°C, 155°C at a grazing incident angle of 0.18°. The π - π stacking peaks in the in-plane direction are extremely weak and no fitting is possible.	107
4.21	Raw scattering data (a,b) and fitting curves (c-e) for GIWAXS experiments on 50 nm samples annealed at 200°C, 170°C, 155°C at a grazing incident angle of 0.16°	109

4.22	Raw scattering data (a,b) and fitting curves (c-e) for GIWAXS experiments on 50 nm samples annealed at 200°C, 170°C, 155°C at a grazing incident angle of 0.14°	111
4.23	75nm out-of-plane and in-plane for two different incident angles 0.14° and 0.15°.	114
4.24	75nm out-of-plane (a) and in-plane (b), grazing angle of 0.14° for 200°C and 0.16° for 155°C. The black lines correspond to the Lorentzian fitting of the peaks, the values with the error estimates are reported in table.	115
4.25	Fitting plots for the two temperatures out-of-plane line-cuts.	116
4.26	Out-of-Plane scattering intensities, comparison between the two temperatures, absolute intensities as function of the incidence angles (a,b), indicating the critical angles in the two samples.	116
4.27	These plots show the values of the distances in Å for the two characteristic distances of the polymer, lamellar packing and the π - π stacking, obtained with $L = 2\pi/Q$, where Q is obtained by a Lorentzian fitting of the scattering curves in the out-of-plane direction for the two samples annealed at 200°C and 155°C. .	117
5.1	Example of a sample showing expansion during the isothermal annealing at 200°C ($T_o = 176^\circ\text{C}$	121
5.2	Thickness profile measured by ellipsometry for a 50 nm sample. $T_o = 169^\circ\text{C}$. It is possible to see that the film expands as the annealing temperature goes from 155°C to 200°C. In the insert are the plots with the absolute thickness value in nm on the y-axis.	122
5.3	Ellipsometry thickness profiles of two 90 nm samples annealed at 200°C for a different amount of time, the red curve did not expand while the blue curve shows some expansion. They both start shrinking at 184°C, T_o	124

- 5.4 Spectra of a sample at 200°C at the 4th minute of the annealing process just after the shrinking peak (yellow), compared with a spectra taken at the 33rd minute at 200°C (blue) where the film is expanded, both compared to the spectra of the sample at 25°C after the melting-quenching (black). 126
- 5.5 Absorption spectra taken at room temperature (25°C), relative to figure 5.3. Figure (a) and (b) are the comparison between the spectra of three samples after each step of the annealing protocol: an as-cast sample one day after spin-coating (red), after the melting-quenching procedure (black) and after the 200°C isotherm (light green). 127
- 5.6 GIWAXS 2D images for the 90 nm samples annealed at 200°C (relative to ellipsometry curves in figure 5.3). 128
- 5.7 Out-of-plane (a) and in-plane (b) line-cuts for the 90 nm sample expanded (green) vs not expanded (red), of the GIWAXS data. (c) and (d) are the fitting curves for the raw data in (a) and (b) 129
- 5.8 Samples annealed for different periods of time (annealing times stated in the captions). (a) and (b) report the correspondent ellipsometry curves (the inserts are the absolute thickness in nm. Figures (c) - (p) are all the AFM images taken for each sample at room temperature after the isotherm. The ellipsometry The 2D images are about 4 μ m x 4 μ m and the x-axis of the roughness plots is in μ m while the y-axis in nm. 132
- 5.9 Comparison between AFM images taken at the edge and centre of the samples annealed at 15 min and for 12 hours. 133
- 5.10 Ellipsometry curves for the 300 and 650 min annealed samples 134

- 5.11 Absorption spectrum referring to the 300 min black ellipsometry curve in figure 5.10. The black spectrum in this figure, called 'at the peak' is taken at T_o so just at the beginning of the isotherm, while the yellow curve (at the minimum) is taken just after the peak, so at the minimum point of the ellipsometry curve for the 300 min sample. The green spectrum is taken from the end of the isotherm where the film is expanded. 135
- 5.12 Absorption spectra referring to the 650 min red ellipsometry curves in figure 5.10. The black spectrum in this figure, called 'at the peak' is taken at T_o so just at the beginning of the isotherm. The green spectrum is taken from the end of the isotherm where the film is expanded. 135
- 5.13 Ellipsometry for 220 nm film annealed at 30 and 100 min. Surprisingly one film expanded (red curve) and the other did not (blue). Probably because the T_o of 179°C is very close to the annealing temperature of 180°C. 137
- 5.14 AFM results for 220 nm film annealed at 30 and 100 min. Ellipsometry data in figure 5.13. 138
- 5.15 Thickness profiles measured by ellipsometry for three 50 nm PCDTBT samples annealed at three different temperatures: 155°C, 170°C and 200°C. It is possible to notice that the sample annealed at the highest temperature of 200°C (red curve) is the only one that present a conspicuous expansion following the initial shrinking. The insert contains the plots with the absolute values of thickness in nm on the y-axis. 139
- 5.16 AFM images for two 50 nm PCDTBT samples annealed at 155°C and 200°C, the which ellipsometry curves are reported in figure 5.15. (a) and (b) show the surface morphology and the roughness of the sample annealed at 155°C for 30 min; (c) and (d) show the surface morphology and roughness of the sample annealed at 200°C for 15 minutes. The not expanded sample (a) presents a more evident texture on the surface. 140

5.17	GIWAXS out-of-plane scattering curves for samples annealed at different temperatures and taken at two different grazing incidence angle.	140
5.18	30 nm samples annealed at different temperatures. The numbers on the ellipsometry curves correspond to the points where the absorption spectra in figure 5.19 have been taken.	142
5.19	Spectra of 30 nm samples annealed at 200°C (a), 165°C (b) and 155°C (c). The spectra are very weak because of the low thickness of the films.	143
5.20	50 nm samples annealed at different temperatures, the red circles correspond to the points of the curves where the absorption spectra below have been taken. . .	144
5.21	Spectra for 50 nm samples annealed at 200°C, 165°C and 155°C. The spectra are very weak because of the low thickness of the film.	145
5.22	77 nm samples annealed at different temperatures (a) and 220°C (b). The red circles correspond to the points of the curves where the absorption spectra in figures 5.24 and 5.23 have been taken.	147
5.23	Spectra for 77 nm samples annealed at 220°C (a) and 200°C (b). The spectra are very weak because of the low thickness of the film.	148
5.24	Spectra for 77 nm samples annealed at 165°C (a) and 155°C (b). The spectra are very weak because of the low thickness of the film.	149
6.1	Thickness profiles for very thin films, the shrinking is not visible and the thermal expansion diminishes.	155
6.2	Thickness profiles for a 19 nm and a 25 nm sample. The shrinking process is now evident and the expansion increases with the thickness.	156
6.3	Thickness profiles for 60 and 70 nm samples, where the shrinking and the expansion keep increasing with the film thickness.	157
6.4	Plots of the initial thickness d_0 against the change in thickness $d_{max} - d_{min}$ occurred for 180°C and 150°C annealing isotherms. The best fits for the experimental data are plotted as straight lines.	158

- 6.5 Plots of the initial thickness d_0 against the change in thickness $d_{max} - d_{min}$ occurred for 170°C and 200°C annealing isotherms. The best fits for the experimental data are plotted as straight lines. 158
- 6.6 Plots of the initial thickness d_0 against the change in thickness on expansion $d_{max} - d_0$. Each point represent one ellipsometry experiment and line fittings to fit the points trends, with a different color per annealing temperature. 159
- 6.7 Plot of equation 6.3. The slope of this line corresponds to α_l , the expansion coefficient for the visco-elastic phase of PCDTBT; the intercept is $= \alpha_g \Delta T_{glass}$, where α_g is the expansion coefficient of the glassy phase. 160
- 6.8 (a) and (b) are the fitting curves to the out-of-plane and in-plane scattering data for as-cast films of different thicknesses. 162
- 6.9 $\pi - \pi$ stacking and lamellar packing distances thickness dependence for as-cast films. The trends are compared for the in-plane and out-of-plane geometries. . . 162
- 6.10 (a) and (b) show the lamellar packing and the $\pi - \pi$ stacking coherence lengths for as cast films at different film thicknesses, both in-plane and out-of-plane. . . 164
- 6.11 π - π Stacking relative area vs thickness for as-cast films. 164
- 6.12 Depth profile for a 90 nm film as cast, the red line is the scattering intensity relative to the $\pi - \pi$ stacking and the blue line is its coherence length as a function of the grazing incidence angle. Shallower angles means the surface of the film, critical angle is an average of all the film, and higher angles are closer to the substrate. 165
- 6.13 Depth profiles in the out-of-plane direction for a 103 nm and 240 nm films annealed at 180°C. 165

- 6.14 AFM images showing the difference in surface morphology for four different key thicknesses (a) 8 nm RMS = 0.4 nm, (b) 25 nm RMS = 0.5 nm, (c) 65 nm RMS = 2.5 nm, (d) 200 nm RMS = 3.9 nm. The black line in the AFM image represent where the linear profile in the inset was taken. The colour scale in the first two thicknesses ((a) and (b), it is different from the thicker ones ((c) and (d)) for clarity. These films of different thicknesses were melted at 250°C for 4 minutes and quenched in liquid N₂. Then annealed at 180°C for an hour. 167
- 6.15 AFM height images for (a) 8 nm, (b) 40 nm, (c) 85 nm and (d) 200 nm PCDTBT films after they have been melted, as cast (a), after melted at 250°C for 4 minutes and quenched in liquid N₂. 168
- 6.16 Cartoon showing the different surface morphology in very thin and very thick samples: as-cast films have the same surface morphology, but annealing causes shrinking and change in surface morphology only in films ≥ 15 nm. 169
- 7.1 Height images for (a) 8 nm, (b) 40 nm, (c) 85 nm and (c) 200 nm as cast PCDTBT films. 172
- 7.2 Height images for (a) 8 nm, (b) 40 nm, (c) 85 nm and (c) 200 nm melted-quenched PCDTBT films. 173
- 7.3 Height images for (a) 8 nm, (b) 40 nm, (c) 85 nm and (c) 200 nm PCDTBT films annaled at 180°. 174
- 7.4 Three layers model represented from Hudzinsky *et al* molecular dynamics simulations. [139] The different colour for each region indicates different mass density and orientation of atactic-polystyrene in each layer. The inset represents the variation of T_g with the film thickness for different strenghts of attraction to the substrate. 175
- 7.5 Fitting curves to the out-of-plane scattering data for different film thicknesses. . 175
- 7.6 Ellipsometry data for the polymer films the which GIWAXS data are reported in figure 7.5 and 7.8 176

- 7.7 Schematics showing the molecular packing configuration of PCDTBT in thin films responsible for the GIWAXS out-of-plane scattering. The intermolecular distances are constant for different film thickness: about 16 Å for edge-on lamellar packing and 4 Å for flat-on π - π stacking. 177
- 7.8 Fitting curves to the in-plane scattering data for different film thicknesses. . . . 177
- 7.9 Schematics showing the molecular packing configuration of PCDTBT in thin films responsible for the GIWAXS in-plane scattering. The intermolecular distances increase with the increasing film thickness: from 20 Å to 24 Å for flat-on lamellar packing and from 4.4 Å to 4.8 Å for edge-on π - π stacking. 178
- 7.10 (a) and (b) show the out-of-plane and in-plane scattering data for a 90 nm PCDTBT film after each step of the thermal protocol. (c) and (d) show the out-of-plane and in-plane scattering data for a 200 nm PCDTBT film after each step of the thermal protocol. 179
- 7.11 Schematics showing the molecular packing configuration of PCDTBT before and after annealing. The intermolecular distances increase upon annealing (both melting-quenching and isothermal annealing) in the out-of-plane direction, and decrease in the in-plane direction. 181
- 7.12 Thickness profiles measured by ellipsometry for 50 nm thick samples. The samples that show expansion are the ones that have been annealed at a temperature $\geq T_o$: 180°C and 200°C. 182

List of Tables

3.1	Fitting parameters for the GIWAXS data shown in figure 3.14. x_0 is the position of the maximum of the Lorentzian peak on the x-axis, $2\pi/Q$ is the corresponding length to the Q -coordinate, μ the half width at half maximum of the peak, L is the coherence length and I the amplitude of the peak which counts for the scattering intensity excluded the background noise. The values in brackets are the standard errors. The first lines are the out-of-plane values, the second lines are the in-plane values.	75
3.2	Fitting parameters for the GIWAXS data shown in figure 3.19. x_0 is the position of the maximum of the Lorentzian peak on the x-axis, $2\pi/Q$ is the corresponding length to the Q -coordinate, μ the half width at half maximum of the peak, L is the coherence length and I the amplitude of the peak which counts for the scattering intensity excluded the background noise. The values in brackets are the standard errors. The first lines are the out-of-plane values, the second lines are the in-plane values.	81
4.1	Fitting parameters for the GIWAXS data shown in figure 4.20 for a grazing angle of 0.18° . The values in brackets are the standard errors. The first lines are the out-of-plane values, the second lines are the in-plane values.	108
4.2	Fitting parameters for the GIWAXS data shown in figure 4.21 for a grazing angle of 0.16° . The values in brackets are the standard errors. The first lines are the out-of-plane values, the second lines are the in-plane values.	110

- 4.3 Fitting parameters for the GIWAXS data shown in figure 4.22 for a grazing angle of 0.14° . The values in brackets are the standard errors. The first lines are the out-of-plane values, the second lines are the in-plane values. 112
- 4.4 Fitting parameters for the GIWAXS data shown in figure 4.24. The values in brackets are the standard errors. The first lines are the out-of-plane values, the second lines are the in-plane values. 115
- 5.1 Fitting parameters for the GIWAXS data shown in figure 5.7. x_0 is the position of the maximum of the Lorentzian peak on the x-axis, $2\pi/Q$ is the corresponding length to the Q -coordinate, μ the half width at half maximum of the peak, L is the coherence length and I the amplitude of the peak which counts for the scattering intensity excluded the background noise. The values in brackets are the standard errors. The first lines are the out-of-plane values, the second lines are the in-plane values. 130
- 6.1 Fitting parameters for the experimental points in figure 6.4 and 6.5. For $T = 150^\circ\text{C}$ is recorded the lowest slope because the films at this temperature shrink very slowly and it is difficult to say when the shrinking is really finished, so at 150°C , the minimum thicknesses recorded were not the real minimum the film could reach. Hours of annealing would have been necessary to reach the real d_{min} . The numbers in bracket are the standard deviation of the fitted values. The values for d_{crit} for 150°C and 170°C do not match with the values found for 200°C and 180°C , because the shrinking was probably not completed. Moreover, the errors on the first two temperatures are too high to have statistical certainty. 159
- 6.2 Fitting parameters for the experimental points in figure 6.6. The numbers in bracket are the standard deviation of the fitted values. 160
- 6.3 Fitting parameters for the experimental points in figure 6.7 and the calculated value for α_g . The numbers in bracket are the error estimates of the calculated values. 161

- 6.4 Fitting parameters for the GIWAXS data shown in figure. x_0 is the position of the maximum of the Lorentzian peak on the x-axis, $2\pi/Q$ is the corresponding length to the Q -coordinate, μ the half width at half maximum of the peak, L is the coherence length and I the amplitude of the peak which counts for the scattering intensity excluded the background noise. The values in brackets are the standard errors. The first lines are the out-of-plane values, the second lines are the in-plane values. 166

Bibliography

- (1) Mayer, A. C.; Scully, S. R.; Hardin, B. E.; Rowell, M. W.; McGehee, M. D. *Materials Today* **2007**, *10*, 28–33.
- (2) Geoghegan, M.; Hadziioannou, G., *Polymer Electronics*; Oxford University Press: 2013, p 272.
- (3) He, C.; Germack, D. S.; Joseph Kline, R.; Delongchamp, D. M.; Fischer, D. A.; Snyder, C. R.; Toney, M. F.; Kushmerick, J. G.; Richter, L. J. *Solar Energy Materials and Solar Cells* **2011**, *95*, 1375–1381.
- (4) Brinkmann, M. *Journal of Polymer Science Part B: Polymer Physics* **2011**, *49*, 1218–1233.
- (5) Lim, J. A.; Liu, F.; Ferdous, S.; Muthukumar, M.; Briseno, A. L. *Materials Today* **2010**, *13*, 14–24.
- (6) Collins, B. A.; Cochran, J. E.; Yan, H.; Gann, E.; Hub, C.; Fink, R.; Wang, C.; Schuetfort, T.; McNeill, C. R.; Chabinye, M. L.; Ade, H. *Nature materials* **2012**, *11*, 536–43.
- (7) Noriega, R.; Rivnay, J.; Vandewal, K.; Koch, F. P. V.; Stingelin, N.; Smith, P.; Toney, M. F.; Salleo, A. *Nature materials* **2013**, *12*, 1038–44.
- (8) Wang, T.; Pearson, A. J.; Dunbar, A. D. F.; Staniec, P. A.; Watters, D. C.; Coles, D.; Yi, H.; Iraqi, A.; Lidzey, D. G.; Jones, R. A. L. *The European physical journal. E, Soft matter* **2012**, *35*, 9807.
- (9) Ibaragi, M. The very early stage of the crystallization of thin PET films studied by ellipsometry, AFM and grazing incidence X-ray scattering., Sheffield, 2015.

- (10) Keddie, J. L.; Jones, R. A. L.; Cory, R. A. *Europhysics Letters (EPL)* **1994**, *27*, 59–64.
- (11) Deribew, D.; Pavlopoulou, E.; Fleury, G.; Nicolet, C.; Renaud, C.; Mougner, S.-J.; Vignau, L.; Cloutet, E.; Brochon, C.; Cousin, F.; Portale, G.; Geoghegan, M.; Hadziioannou, G. *Macromolecules* **2013**, *46*, 3015–3024.
- (12) Woo, C. H.; Piliago, C.; Holcombe, T. W.; Toney, M. F.; Fréchet, J. M. J. *Macromolecules* **2012**, *45*, 3057–3062.
- (13) Sirringhaus, H.; Wilson, R. J.; Friend, R. H.; Inbasekaran, M.; Wu, W.; Woo, E. P.; Grell, M.; Bradley, D. D. C.; Sirringhaus, H.; Wilson, R. J.; Friend, R. H. *Applied Physics Letters* **2000**, *77*, 406–408.
- (14) Jimison, L. H.; Toney, M. F.; McCulloch, I.; Heeney, M.; Salleo, A. *Advanced Materials* **2009**, *21*, 1568–1572.
- (15) Agostinelli, T.; Lilliu, S.; Labram, J. G.; Campoy-Quiles, M.; Hampton, M.; Pires, E.; Rawle, J.; Bikondoa, O.; Bradley, D. D. C.; Anthopoulos, T. D.; Nelson, J.; Macdonald, J. E. *Advanced Functional Materials* **2011**, *21*, 1701–1708.
- (16) Keivanidis, P. E.; Clarke, T. M.; Lilliu, S.; Agostinelli, T.; MacDonald, J. E.; Durrant, J. R.; Bradley, D. D. C.; Nelson, J. *Journal of Physical Chemistry Letters* **2010**, *1*, 734–738.
- (17) Joseph Kline, R.; McGehee, M. D.; Toney, M. F. *Nature Materials* **2006**, *5*, 222–228.
- (18) Zhang, X.; Man, X.; Han, C. C.; Yan, D. *Polymer* **2008**, *49*, 2368–2372.
- (19) Terrill, N. J.; Fairclough, P. A.; Towns-Andrews, E.; Komanschek, B. U.; Young, R. J.; Ryan, A. J. *Polymer Communications* **1998**, *39*, 2381–2385.
- (20) Jones, R. A. L., *Soft condensed matter*; Oxford University Press: 2002; Vol. 6.
- (21) Imai, M.; Kaji, K.; Kanaya, T.; Sakai, Y. *Physical Review B* **1995**, *52*, 696–704.
- (22) Ross, G.; Frolen, L. *Methods of Experimental Physics*, Vol. 16B., 1980.
- (23) Hoffman, J. D.; Davis, G. T. *Journal of research of the National Bureau of Standards section A - Physics and chemistry* **1975**, *79A*, 613–617.

- (24) Strobl, G. R., *The Physics of Polymers: Concepts for Understanding Their Structures and Behavior*; Springer: 2007, p 532.
- (25) Painter, P. C.; Coleman, M. M., *Fundamentals of polymer science: an introductory text*; Technomic: 1994.
- (26) Miyano, K. *Phys. Rev. Lett.* **1979**, *43*, 51–54.
- (27) Miyano, K. *The Journal of Chemical Physics* **1979**, *71*, 4108–4111.
- (28) Keller, A. *Journal of Materials Science* **1994**, *29*, 2579–2604.
- (29) Ostwald, W. *Z. phys. Chem* **1897**, *22*, 306.
- (30) Strobl, G. *Reviews of Modern Physics* **2009**, *81*, 1287–1300.
- (31) Olmsted, P. D.; Poon, W. C. K.; Mcleish, T. C. B.; Terrill, N. J.; Ryan, A. J. *Physical Review Letters* **1998**, *373*.
- (32) Donald, A. M.; Windle, A. H.; Hanna, S., *Liquid crystalline polymers*; Cambridge University Press: 2006.
- (33) Fritz, S. E.; Martin, S. M.; Frisbie, C. D.; Ward, M. D.; Toney, M. F. *Journal of the American Chemical Society* **2004**, *126*, 4084–4085.
- (34) Prosa, T. J.; Winokur, M. J.; Moulton, J.; Smith, P.; Heeger, A. J. *Macromolecules* **1992**, *25*, 4364–4372.
- (35) DeLongchamp, D. M.; Kline, R. J.; Lin, E. K.; Fischer, D. A.; Richter, L. J.; Lucas, L. A.; Heeney, M.; McCulloch, I.; Northrup, J. E. *Advanced Materials* **2007**, *19*, 833–837.
- (36) Rabolt, J.; Hofer, D.; Miller, R.; Fickes, G. *Macromolecules* **1986**, *19*, 611–616.
- (37) Stepanyan, R.; Subbotin, A.; Knaapila, M.; Ikkala, O.; ten Brinke, G. *Macromolecules* **2003**, *36*, 3758–3763.
- (38) Kawana, S.; Durrell, M.; Lu, J.; Macdonald, J. E.; Grell, M.; Bradley, D. D. C.; Jukes, P. C.; Jones, R. A. L.; Bennett, S. L. *Polymer* **2002**, *43*, 1907–1913.
- (39) Grell, M.; Bradley, D. D. C.; Ungar, G.; Hill, J.; Whitehead, K. S. *Macromolecules* **1999**, *32*, 5810–5817.

- (40) Chen, S. H.; Chou, H. L.; Su, A. C.; Chen, S. A. *Macromolecules* **2004**, *37*, 6833–6838.
- (41) Chen, S.; Su, A.; Su, C.; Chen, S. *Macromolecules* **2005**, *38*, 379–385.
- (42) Österbacka, R.; An, C. P.; Jiang, X.; Vardeny, Z. V. *Science* **2000**, *287*, 839–842.
- (43) Sirringhaus, H.; Brown, P. J.; Friend, R. H.; Nielsen, M. M.; Bechgaard, K.; Langeveld-Voss, B. M. W.; Spiering, A. J. H.; Janssen, R. A. J.; Meijer, E. W.; Herwig, P.; de Leeuw, D. M. *Nature* **1999**, *401*, 685–688.
- (44) Street, R.; Northrup, J.; Salleo, A. *Physical Review B* **2005**, *71*, 165202.
- (45) Chabinyk, M. L. *Polymer Reviews* **2008**, *48*, 463–492.
- (46) Chang, J.-F.; Clark, J.; Zhao, N.; Sirringhaus, H.; Breiby, D. W.; Andreasen, J. W.; Nielsen, M. M.; Giles, M.; Heeney, M.; McCulloch, I. *Phys. Rev. B* **2006**, *74*, 115318.
- (47) Kline, R. J.; McGehee, M. D.; Kadnikova, E. N.; Liu, J.; Frchet, J. M. J.; Toney, M. F. *Macromolecules* **2005**, *38*, 3312–3319.
- (48) Zen, A.; Saphiannikova, M.; Neher, D.; Grenzer, J.; Grigorian, S.; Pietsch, U.; Asawapirom, U.; Janietz, S.; Scherf, U.; Lieberwirth, I., et al. *Macromolecules* **2006**, *39*, 2162–2171.
- (49) Sirringhaus, H.; Brown, P. J.; Friend, R. H.; Nielsen, M. M.; Bechgaard, K.; Spiering, A. J. H. **1999**, 685–688.
- (50) DeLongchamp, D. M.; Vogel, B. M.; Jung, Y.; Gurau, M. C.; Richter, C. A.; Kirillov, O. A.; Obrzut, J.; Fischer, D. A.; Sambasivan, S.; Richter, L. J., et al. *Chemistry of materials* **2005**, *17*, 5610–5612.
- (51) Chang, J.-F.; Sun, B.; Breiby, D. W.; Nielsen, M. M.; Sölling, T. I.; Giles, M.; McCulloch, I.; Sirringhaus, H. *Chemistry of Materials* **2004**, *16*, 4772–4776.
- (52) Geer, R.; Shashidhar, R. *Physical Review E* **1995**, *51*, R8.
- (53) Geer, R.; Shashidhar, R.; Thibodeaux, A.; Duran, R. *Physical review letters* **1993**, *71*, 1391.
- (54) Knaapila, M.; Lyons, B. P.; Kisko, K.; Foreman, J. P.; Vainio, U.; Mihaylova, M.; Seeck, O. H.; Pålsson, L.-O.; Serimaa, R.; Torkkeli, M., et al. *The Journal of Physical Chemistry B* **2003**, *107*, 12425–12430.

- (55) Knaapila, M.; Stepanyan, R.; Lyons, B. P.; Torkkeli, M.; Hase, T. P.; Serimaa, R.; Güntner, R.; Seeck, O. H.; Scherf, U.; Monkman, A. P. *Macromolecules* **2005**, *38*, 2744–2753.
- (56) Knaapila, M.; Stepanyan, R.; Lyons, B. P.; Torkkeli, M.; Monkman, A. P. *Advanced Functional Materials* **2006**, *16*, 599–609.
- (57) Zhang, Y.; Mukoyama, S.; Mori, K.; Shen, D.; Yan, S.; Ozaki, Y.; Takahashi, I. *Surface Science* **2006**, *600*, 1559–1564.
- (58) Zhao, N.; Botton, G. A.; Zhu, S.; Duft, A.; Ong, B. S.; Wu, Y.; Liu, P. *Macromolecules* **2004**, *37*, 8307–8312.
- (59) Wu, Y.; Liu, P.; Ong, B. S.; Srikumar, T.; Zhao, N.; Botton, G.; Zhu, S. *Applied Physics Letters* **2005**, *86*, 142102.
- (60) Olsen, B. D.; Jang, S.-Y.; Lüning, J. M.; Segalman, R. A. *Macromolecules* **2006**, *39*, 4469–4479.
- (61) Jones, R. A. L., *Polymers at surfaces and interfaces*; Cambridge University Press: 1999.
- (62) Ballauff, M. *Angewandte Chemie International Edition* **1989**, *28*, 253–267.
- (63) Steuer, M.; Hörth, M.; Ballauff, M. *Journal of Polymer Science Part A: Polymer Chemistry* **1993**, *31*, 1609–1619.
- (64) Liu, Y.-X.; Chen, E.-Q. *Coordination Chemistry Reviews* **2010**, *254*, 1011–1037.
- (65) Clarke, T. M.; Ballantyne, A. M.; Nelson, J.; Bradley, D. D. C.; Durrant, J. R. *Advanced Functional Materials* **2008**, *18*, 4029–4035.
- (66) Marsh, R. A.; Hodgkiss, J. M.; Albert-Seifried, S.; Friend, R. H. *Nano letters* **2010**, *10*, 923–30.
- (67) Mihailetschi, V.; Xie, H.; deBoer, B.; Koster, L.; Blom, P. *Advanced Functional Materials* **2006**, *16*, 699–708.
- (68) Wu, P.-T.; Xin, H.; Kim, F. S.; Ren, G.; Jenekhe, S. A. *Macromolecules* **2009**, *42*, 8817–8826.
- (69) Prosa, T. J.; Winokur, M. J.; McCullough, R. D. *Macromolecules* **1996**, *29*, 3654–3656.

- (70) Mardalen, J.; Samuelsen, E.; Gautun, O.; Carlsen, P. *Synthetic Metals* **1992**, *48*, 363–380.
- (71) Cho, S.; Seo, J. H.; Park, S. H.; S, B.; Leclerc, M.; Heeger, a. J. *Advanced Materials* **2010**, *22*, 1253–1257.
- (72) Blouin, N.; Michaud, A.; Gendron, D. *Journal of the American Chemical Society* **2008**, 732–742.
- (73) Blouin, N.; Michaud, A.; Leclerc, M. *Advanced Materials* **2007**, *19*, 2295–2300.
- (74) Lu, X.; Hlaing, H.; Germack, D. S.; Peet, J.; Jo, W. H.; Andrienko, D.; Kremer, K.; Ocko, B. M. *Nature communications* **2012**, *3*, 795.
- (75) Wang, H. W.; Pentzer, E.; Emrick, T.; Russell, T. P. *ACS Macro Letters* **2014**, *3*, 30–34.
- (76) Szarko, J. M.; Guo, J.; Liang, Y.; Lee, B.; Rolczynski, B. S.; Strzalka, J.; Xu, T.; Loser, S.; Marks, T. J.; Yu, L.; Chen, L. X. *Advanced Materials* **2010**, *22*, 5468–5472.
- (77) Zhao, K.; Khan, H. U.; Li, R.; Su, Y.; Amassian, A. *Advanced Functional Materials* **2013**, *23*, 6024–6035.
- (78) Shao, B.; Vanden Bout, D. A. *Journal of Materials Chemistry C* **2017**, *5*, 9786–9791.
- (79) Hwang, I.; Beaupré, S.; Leclerc, M.; Scholes, G. D. *Chemical Science* **2012**, *3*, 2270–2277.
- (80) Kawanabe, Y.; Moule, A. J.; Faller, R. *J. Chem. Eng. Data* **2014**, *10*, 2982–2986.
- (81) Grell, M.; Redecker, M.; Whitehead, K. S.; Bradley, D. D.; Inbasekaran, M.; Woo, E. P. *Liquid Crystals* **1999**, *26*, 1403–1407.
- (82) Grell, M.; Bradley, D. D.; Inbasekaran, M.; Woo, E. P. *Advanced Materials* **1997**, *9*, 798–802.
- (83) Calvert, P. *Nature* **1996**, *384*, 311–312.
- (84) Zheng, X.; Rafailovich, M.; Sokolov, J.; Strzhemechny, Y.; Schwarz, S.; Sauer, B.; Rubinstein, M. *Physical Review Letters* **1997**, *79*, 241–244.
- (85) Jones, R. A. L.; Kumar, S.; Ho, D.; Briber, R.; Russell, T. *Nature* **1999**, *400*, 146–149.

- (86) Frank, B.; Gast, A. P.; Russell, T. P.; Brown, H. R.; Hawker, C. *Macromolecules* **1996**, *29*, 6531–6534.
- (87) Lin, E. K.; Kolb, R.; Satija, S. K.; Wu, W.-l. *Macromolecules* **1999**, *32*, 3753–3757.
- (88) Zheng, X.; Sauer, B.; Van Alsten, J.; Schwarz, S.; Rafailovich, M.; Sokolov, J.; Rubinstein, M. *Physical Review Letters* **1995**, *74*, 407–410.
- (89) DeMaggio, G.; Frieze, W.; Gidley, D.; Zhu, M.; Hristov, H.; Yee, A. *Physical Review Letters* **1997**, *78*, 1524–1527.
- (90) Reiter, G. *EPL (Europhysics Letters)* **1993**, *579*.
- (91) Kawana, S.; Jones, R. A. L. *The European physical journal. E, Soft matter* **2003**, *10*, 223–30.
- (92) Wang, Y.; Chan, C.-M.; Ng, K.-M.; Li, L. *Macromolecules* **2008**, *41*, 2548–2553.
- (93) Lin, E. K.; Kolb, R.; Satija, S. K.; Wu, W.-l. *Macromolecules* **1999**, *32*, 3753–3757.
- (94) Vanroy, B.; Wu, M.; Napolitano, S. **2013**.
- (95) Fang, A.; Haataja, M. *Physical Review E* **2014**, *89*, 022407.
- (96) Chan, C.; Li, L., *Intrinsic Molecular Mobility and Toughness of Polymers II*; Kausch, H.-H., Ed.; Advances in Polymer Science, Vol. 188; Springer-Verlag: Berlin/Heidelberg, 2005, pp 1–41.
- (97) Wang, Y.; Ge, S.; Rafailovich, M.; Sokolov, J.; Zou, Y.; Ade, H.; Lüning, J.; Lustiger, A.; Maron, G. *Macromolecules* **2004**, *37*, 3319–3327.
- (98) Harmandaris, V. A.; Daoulas, K. C.; Mavrantzas, V. G. *Macromolecules* **2005**, *38*, 5796–5809.
- (99) Mansfield, K. F.; Theodorou, D. N. *Macromolecules* **1990**, *23*, 4430–4445.
- (100) Mansfield, K. F.; Theodorou, D. N. *Macromolecules* **1991**, *24*, 4295–4309.
- (101) Theodorou, D. N. *Macromolecules* **1989**, *22*, 4578–4589.
- (102) Despotopoulou, M. M.; Frank, C. W.; Miller, R. D.; Rabolt, J. F. *Macromolecules* **1996**, *29*, 5797–5804.

- (103) Despotopoulou, M. M.; Miller, R. D.; Rabolt, J. F.; Frank, C. W. *Journal of Polymer Science Part B: Polymer Physics* **1996**, *34*, 2335–2349.
- (104) Zhang, Y.; Lu, Y.; Duan, Y.; Zhang, J.; Yan, S.; Shen, D. *Journal of Polymer Science Part B: Polymer Physics* **2004**, *42*, 4440–4447.
- (105) Napolitano, S.; Wu, M. **2006**, 5967–5970.
- (106) Massa, M. V.; Dalnoki-Veress, K.; Forrest, J. a. *The European physical journal. E, Soft matter* **2003**, *11*, 191–8.
- (107) Porzio, W.; Scavia, G.; Barba, L.; Arrighetti, G.; Milita, S. *European Polymer Journal* **2011**, *47*, 273–283.
- (108) Joshi, S.; Grigorian, S.; Pietsch, U.; Pingel, P.; Zen, A.; Neher, D.; Scherf, U. *Macromolecules* **2008**, *41*, 6800–6808.
- (109) Joshi, S.; Pingel, P.; Grigorian, S.; Panzner, T.; Pietsch, U.; Neher, D.; Forster, M.; Scherf, U. *Macromolecules* **2009**, *42*, 4651–4660.
- (110) Ren, Y.; Gao, H.; Hu, W. **2012**, *51*, 1548–1557.
- (111) Sun, J. Ellipsometry tutorial.
- (112) www.jawoollam.com/resources/ellipsometry-tutorial/what-is-ellipsometry. What Is Ellipsometry?
- (113) A., J. F.; H.E., W., *Fundamentals of Optics*; McGraw-Hill: 1976.
- (114) Ong, H. G.; Wang, J. In *Physical and Chemical Properties of Carbon Nanotubes*, Suzuki, S., Ed.; InTech: Rijeka, 2013; Chapter 14.
- (115) Xenocs Training Slides.
- (116) Parratt, L. *Phys. Rev.* **1954**, *95*, 359.
- (117) Wang, J.; Bedzyk, M. J.; Caffrey, M. *Science* **1992**, *258*, 775–778.
- (118) Factor, B. J.; Russell, T. P.; Toney, M. F. *Macromolecules* **1993**, *26*, 2847–2859.
- (119) Macdonald, J. E.; Durell, M.; Trolley, D.; Lei, C.; Das, A.; Jukes, P. C.; Geoghegan, M.; Higgins, A. M.; Jones, R. A. L. *Radiation Physics and Chemistry* **2004**, *71*, 811–815.

- (120) Pearson, A. J.; Wang, T.; Dunbar, A. D. F.; Yi, H.; Watters, D. C.; Coles, D. M.; Staniec, P. A.; Iraqi, A.; Jones, R. A. L.; Lidzey, D. G. *Advanced Functional Materials* **2014**, *24*, 659–667.
- (121) Kim, J. H.; Jang, J.; Zin, W.-C. *Macromolecular Rapid Communications* **2001**, *22*, 386–389.
- (122) Wang, Y.; Rafailovich, M.; Sokolov, J.; Gersappe, D.; Araki, T.; Zou, Y.; Kilcoyne, A. D. L.; Ade, H.; Marom, G.; Lustiger, A. **2006**, *028303*, 1–4.
- (123) Spiece, J.; Martinez-Tong, D. E.; Sferrazza, M.; Nogales, A.; Napolitano, S. *Soft Matter* **2015**, *11*, 6179–6186.
- (124) Zhang, F.; Baralia, G. G.; Nysten, B.; Jonas, A. M. *Macromolecules* **2011**, *44*, 7752–7757.
- (125) Zhao, J.; Yin, X.; Shi, J.; Zhao, X.; Gutmann, J. S. *Journal of Physical Chemistry C* **2011**, *115*, 22347–22353.
- (126) Wang, T.; Pearson, A. J.; Dunbar, A. D. F.; Staniec, P. A.; Watters, D. C.; Yi, H.; Ryan, A. J.; Jones, R. A. L.; Iraqi, A.; Lidzey, D. G. *Advanced Functional Materials* **2012**, *22*, 1399–1408.
- (127) Sperati, C. A.; Franta, W. A.; Starkweather, H. W. *Journal of the American Chemical Society* **1953**, *75*, 6127–6133.
- (128) Zen, A.; Saphiannikova, M.; Neher, D.; Grenzer, J.; Grigorian, S.; Pietsch, U.; Asawapirom, U.; Janietz, S.; Scherf, U.; Lieberwirth, I.; Wegner, G. *Macromolecules* **2006**, *39*, 2162–2171.
- (129) Staniec, P. A.; Parnell, A. J.; Dunbar, A. D. F.; Yi, H.; Pearson, A. J.; Wang, T.; Hopkinson, P. E.; Kinane, C.; Dalgliesh, R. M.; Donald, A. M.; Ryan, A. J.; Iraqi, A.; Jones, R. A. L.; Lidzey, D. G. *Advanced Energy Materials* **2011**, *1*, 499–504.
- (130) Wang, T.; Dunbar, A. D. F.; Staniec, P. A.; Pearson, A. J.; Hopkinson, P. E.; MacDonald, J. E.; Lilliu, S.; Pizzey, C.; Terrill, N. J.; Donald, A. M.; Ryan, A. J.; Jones, R. A. L.; Lidzey, D. G. *Soft Matter* **2010**, *6*, 4128.

- (131) Amrutha, S. R.; Jayakannan, M. *Journal of Physical Chemistry B* **2008**, *112*, 1119–1129.
- (132) Banerji, N.; Gagnon, E.; Morgantini, P.-Y.; Valouch, S.; Mohebbi, A. R.; Seo, J.-H.; Leclerc, M.; Heeger, A. J. *The Journal of Physical Chemistry C* **2012**, *116*, 11456–11469.
- (133) Scharsich, C.; Fischer, F. S. U.; Wilma, K.; Hildner, R.; Ludwigs, S.; Köhler, A. **2015**, *submitted*, submitted.
- (134) Shepilov, M. P.; Petrovskii, G. T.; Zhilin, A. A.; Dymshits, O. S.; Golubkov, V. V. *Journal of Optical Technology* **2006**, 590–595.
- (135) Peet, J.; Cho, N. S.; Lee, S. K.; Bazan, G. C. *Macromolecules* **2008**, *41*, 8655–8659.
- (136) Taguchi, K.; Miyaji, H.; Izumi, K.; Hoshino, A.; Kokawa, R. *Journal of Macromolecular Science, Part B* **2002**, *B41*, 1033–1042.
- (137) Mark, J. E. *Physical Properties of Polymers Handbook* **2007**.
- (138) Janasz, L.; Gradzka, M.; Chlebosz, D.; Zajaczkowski, W.; Marszalek, T.; Kiersnowski, A.; Ulanski, J.; Pisula, W. *Langmuir* **2017**, *33*, 4189–4197.
- (139) Hudzinskyy, D.; Lyulin, A. V.; Baljon, A. R.; Balabaev, N. K.; Michels, M. A. *Macromolecules* **2011**, *44*, 2299–2310.
- (140) Sun, X.; Ren, Z.; Liu, J.; Takahashi, I.; Yan, S. *Langmuir* **2014**, *30*, 7585–7592.